ALMA MATER STUDIORUM
UNIVERSITÀ DI BOLOGNA

Dipartimento di Fisica e Astronomia

DOTTORATO DI RICERCA IN
ASTROFISICA

Ciclo XXXIII

Tesi di Dottorato

INTERPLAY BETWEEN RELATIVISTIC AND THERMAL PLASMA IN RELAXED GALAXY CLUSTER

Presentata da:
Alessandro Ignesti

Supervisore:
Prof.ssa Myriam Gitti

Coordinatore di Dottorato:
Prof. Francesco Rosario Ferraro

Co-supervisore:
Dr. Gianfranco Brunetti

Esame finale anno 2021

Settore Concorsuale: 02/C1 – Astronomia, Astrofisica, Fisica della Terra e dei Pianeti
Settore Scientifico Disciplinare: FIS/05 – Astronomia e Astrofisica

THIS THESIS WORK WAS DONE AS PART OF THE RESEARCH ACTIVITY OF THE ISTITUTO DI RADIOASTRONOMIA - ISTITUTO NAZIONALE DI ASTROFISICA (BOLOGNA)

Alla mia famiglia

"If you trust in yourself..and believe in your dreams...and follow your star...you'll still get beaten by people who spent their time working hard and learning things and weren't so lazy."

Sir Terry Pratchett

"In the beginning the Universe was created. This had made many people very angry and has been widely regarded as a bad move."

Douglas Adams

"Great work is 80% idea and 80% execution."

Sir John Hegarty

"Se la vita ha un senso deve essere quello dell'umorismo."

Leonardo Ortolani

Abstract

Doctor of Philosophy

Interplay between relativistic and thermal plasma in relaxed galaxy clusters

by Alessandro IGNESTI

Galaxy clusters are complex ecosystems, where galaxies with powerful active galactic nuclei, thermal plasma, magnetic fields, and cosmic rays can interact and flourish in spectacular astrophysical phenomena. Decades of studies have investigated these systems, and as the boundaries of our knowledge were pushed forward, new questions emerged awaiting to be answered.

The main focus of this Thesis is the interplay between the relativistic and thermal plasma of the intra-cluster medium. The study of the intra-cluster medium (ICM) allows to understand the way energy is injected from large scale dynamics and dissipated in different channels. These channels include viscous heating and the generation of non-thermal components that, eventually, generate diffuse radio emission. Furthermore, studying the ICM provides complementary insights into the physics of cluster galaxy evolution. We mainly focus on the case of relaxed galaxy clusters, where the connection between the central, massive, radio-loud galaxies and the diffuse radio emission is still unclear. In this context, we investigate also the interactions between the ICM and the cluster galaxies. The cornerstone of our works is a multi-wavelength analysis based on radio and X-ray observations, which features brand-new Low-Frequency Array (LOFAR) observations and new approaches to the study of the spatial correlation between these emissions.

We anticipate here the highlights of our work:

- ◇ A comprehensive study of the spatial correlation between diffuse non-thermal radio and thermal X-ray emission, that unveiled an intrinsic difference between disturbed and relaxed clusters. For the latter, we provide novel constraints on the possible role of the central active galactic nuclei (AGN) and relativistic protons in the origin of diffuse radio emission;
- ◇ New observational evidences that the life-time of old radio electrons in cluster radio galaxies is longer than expected. This is in line with other studies based on low frequency radio observations. Overall, these evidences affect our view of the life-cycle of relativistic plasma in galaxy clusters;
- ◇ A pilot study of the radio and X-ray emission of a jellyfish galaxy, that provided new insights into the physics of cluster galaxy evolution via ram-pressure stripping.

In addition to these results, the original software and numerical procedures developed to carry out our studies constitute an important part of the Ph.D. Thesis.

The Thesis is structured as follow:

- ◇ In **Chapter 1** we provide an introduction to the physics of relaxed clusters, of the ICM which pervades them, and of its complex interplay with the cluster galaxies and the non-thermal, radio-emitting plasma;
- ◇ In **Chapter 2** we explore the connection between the thermal and non-thermal plasma in order to investigate the origin of radio mini-halos. We started by studying the spatial correlation between radio and X-ray emission in a sample of 7 relaxed clusters, then we used our results to explore the scenario of a pure hadronic origin of the radio emission;
- ◇ In **Chapter 3** we introduce the potential of LOFAR for our studies by presenting its scientific projects and the implications of low-frequency observations for the study of galaxy clusters;
- ◇ In **Chapter 4** we present the architecture of the LOFAR-Planck online automated catalog, a brand-new tool which we developed as part of the LOFAR Survey Key Project to manage the future, statistical studies of large sample of diffuse radio sources made possible by LOFAR;
- ◇ In **Chapter 5** we present our studies of the so-called Kite radio source in the Abell 2626 galaxy cluster. Due to the presence of four symmetric arcs, the origin of this radio source has been a puzzle for years. We investigated its nature by exploiting radio (LOFAR, JVLA and GMRT) and X-ray (*Chandra* and *XMM-Newton*) observations;
- ◇ In **Chapter 6** we explore the rich environment of the relaxed galaxy cluster 2A0335+096 with our proprietary LOFAR data and archival X-ray observations. We study the central galaxy, which shows evidence of radio-mode AGN feedback associated with ICM sloshing and diffuse radio emission, and the head-tail galaxy GB6 B0335+096, which stands out in the new LOFAR data due to its Mpc-long radio tail;
- ◇ In **Chapter 7** we present a detailed study of the jellyfish galaxy JW100 in the galaxy cluster Abell 2626. Investigating this object allowed us to study how the interaction with the ICM can dramatically impact on the galaxy evolution. We carried out a radio and X-ray study of this galaxy and we discuss the results in light of the most recent studies in this field;
- ◇ In **Chapter 8** we summarize the highlights of this Thesis and we discuss the future developments;
- ◇ In **Appendix A** we present in details PT-REX, the software we developed to evaluate the spatial correlation between extended emission at different wavelengths which was used for our studies;

◇ ◇ ◇

The results obtained during the Ph.D. project and presented in this Thesis have been published in the following refereed publications:

1. *"The mystery of the Kite radio source in Abell 2626: insights from new Chandra observations"* by **A. Ignesti**, M. Gitti, G. Brunetti, E. O'sullivan, C. Sarazin, K.W. Wong. 2018, Astronomy&Astrophysics 610, A89

2. *"GASP XXIII: A jellyfish galaxy as an astrophysical laboratory of the baryonic cycle"* by B. M. Poggianti, **A. Ignesti**, M. Gitti, A. Wolter, F. Brighenti, A. Biviano, K. George, B. Vulcani, M. Gullieuszik, A. Moretti, R. Paladino, D. Bettoni, A. Franchetto, Y. L. Jaffé, M. Radovich, E. Roediger, N. Tomičić, S. Tonnesen, C. Bellhouse , J. Fritz, A. Omizzolo, 2019, The Astrophysical Journal, 887

3. *"Radio and X-ray connection in radio mini-halos: Implications for hadronic models"* by **A. Ignesti**, G. Brunetti, M. Gitti, S. Giacintucci, 2020, Astronomy & Astrophysics, 640, A37

4. *"Highly ordered magnetic fields in the tail of the jellyfish galaxy JO206"* by A. Müller, B. Poggianti , C. Pfrommer , B. Adebahr , P. Serra , **A. Ignesti** , M. Sparre , M. Gitti , R. Dettmar , B. Vulcani , A. Moretti , Nature Astronomy 2020, doi: https://doi.org/10.1038/s41550-020-01234-7

5. *"The great Kite in the sky: A LOFAR observation of the radio source in Abell 2626"* by **A. Ignesti**, T. Shimwell, G. Brunetti, M. Gitti, H. Intema, R. J. van Weeren, M. J. Hardcastle, A. O. Clarke, A. Botteon, G. Di Gennaro, M. Brüggen, I. Browne, S. Mandal, H. J. A. Röttgering, V. Cuciti, F. de Gasperin, R. Cassano, A. M. M. Scaife , 2020, Astronomy & Astrophysics, 643, A172

6. *"Very Large Array observations of the mini-halo and AGN feedback in the Phoenix cluster"* by R. Timmerman, R. J. van Weeren, M. McDonald, **A. Ignesti**, B. R. McNamara, J. Hlavacek-Larrondo, H. J. A. Röttgering, 2021, Astronomy & Astrophysics, 646, A38

Contents

List of Figures

List of Tables

List of Abbreviations

AGN	**A**ctive **G**alactic **N**ucleus
BCG	**B**rightest **C**luster **G**alaxy
CMB	**C**osmic **M**icrowave **B**ackground
CRe	**C**osmic **R**ays **e**lectrons
CRp	**C**osmic **R**ays **p**rotons
GMRT	**G**iant **M**etrowave **R**adio **T**elescope
ICM	**I**ntra-**C**luster **M**edium
ISM	**I**nter-**S**tellar **M**edium
JVLA	Karl G. **J**ansky **V**ery **L**arge **A**rray
LOFAR	**LO**w-**F**requency **AR**ray
LoTSS	LOFAR **T**wo-metre **S**ky **S**urvey
MH	**M**ini **H**alo
MCptp	**M**onte **C**arlo **p**oint-**t**o-**p**point
MUSE	**M**ulti **U**nit **S**pectroscopic **E**xplorer
ptp	**p**oint-**t**o-**p**oint
RMS	**R**oot **M**ean **S**quare
SFR	**S**tar **F**ormation **R**ate
SKA	**S**quare-**K**ilometer **A**rray
SMptp	**S**ingle-**M**esh **p**oint-**t**o-**p**point
VLA	**V**ery **L**arge **A**rray

Physical Constants

Speed of Light	c_0	$= 3\times10^{10}$ cm s^{-1}
Proton rest mass	m_p	$= 1.66\times10^{-24}$ g
Electron rest mass	m_e	$= 9.11\times10^{-28}$ g
Gravitational constant	G	$= 6.67\times10^{8}$ cm^3 g^{-1} s^{-2}
Boltzmann constant	k	$= 1.38\times10^{-16}$ erg K^{-1}
Parsec	pc	$= 3.09 \times 10^{18}$ cm
Year	yr	$= 3.16\times10^{7}$ s
Solar mass	$M_\odot$	$= 2\times10^{33}$ g
Planck constant	h	$= 6.63 \times 10^{-27}$ erg s

Chapter 1

The ecosystem of relaxed galaxy clusters

1.1 Galaxy clusters

Galaxy clusters are large structures composed by dark matter ($\sim$ 85%) and baryons ($\sim$ 15%), with masses that can reach up to 10^{15} $M_{\odot}$ within linear sizes of a few Mpc (e.g., Kravtsov and Borgani, 2012). The dark matter provides the gravitational well where a fraction of the baryons ($\sim$ 2%) can collapse, forming stars and galaxies. The remaing fraction ($\sim$ 13%) can be found in the form of hot and rarefied gas, with typical temperature $T = 10^7 - 10^8$ K and density $n = 10^{-4} - 10^{-3}$ cm^{-3}, called intra-cluster medium (ICM), that fills the entire cluster volume (e.g., Sarazin, 1986). Galaxy clusters are of key importance of astrophysical studies because they are the crossways of cosmology and astrophysics (e.g., Borgani, 2006). From the cosmological point of views, galaxy clusters are probes to study the formation and evolution of large-scale structures (e.g., Voit, 2005). By studying their distribution and mass-function in the Universe, we can reconstruct the structure of the cosmic web and the history of the mergers that lead to the formation of the largest and most massive structures (Figure 1.1).

From the astrophysical point of view, galaxy clusters are closed-box environments in which we can study the interactions between galaxies, the formation of the most massive galaxies, the history of the star formation in galaxies (due to the fact that the byproducts are retained in the cluster gravitational well), and a plethora of phenomena produced by the interactions between the cluster galaxies and the ICM. Galaxy clusters are also remarkable systems to study the physics of cosmic rays (CR) acceleration. First, the hierarchical formation process provide an energy budget that is channeled in the acceleration of these particles. Furthermore, due to their sizes, galaxy cluster are efficient storehouses of CRs, which manifest as large-scale diffuse radio emission.

1.1.1 Formation of galaxy clusters

According to the current picture of structure formation in the Universe, galaxy clusters are produced starting from the gravitational collapse of primordial, random density fluctuations, whose existence is proved by the studies of the cosmological micro-wave background (CMB) (Bennett et al., 1996; Planck Collaboration et al., 2011a). Once that the collapse started, matter is accumulated and grows via a hierarchical sequence of accretion of smaller systems (e.g., Press and Schechter, 1974;

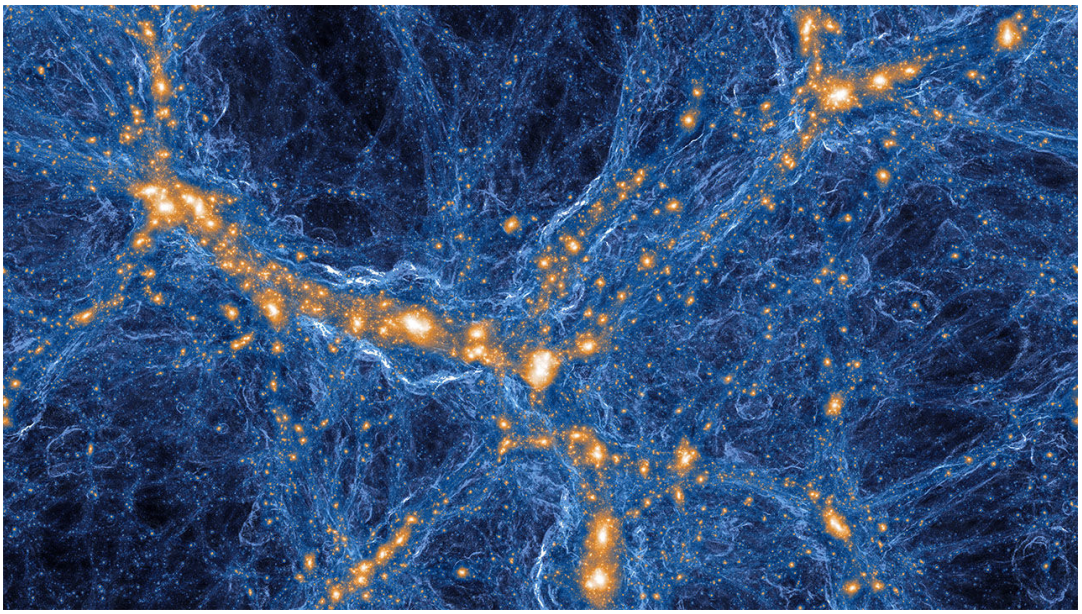

Figure 1.1: Composite image, from the TNG100-1 simulation, which overlays a projection of the dark matter density with the output of the cosmological shock finder, here used to derive the average Mach number of shocks along each line of sight. All the gravitationally collapsed structures (in orange/white) are surrounded by successive shock surfaces (blue) which encode their formation histories (Pillepich et al., 2018).

Blumenthal et al., 1984; Kaiser, 1986; Kaiser, 1991). These structures grow over cosmic time into today massive clusters of galaxies (e.g., Voit, 2005, for a review).

There are two different regimes of growth of the perturbations, which are linear and non-linear. The two regimes are defined by the magnitude of the density fluctuation (or overdensity):

$$\delta = \frac{\rho - \langle\rho\rangle}{\langle\rho\rangle} \tag{1.1}$$

where $\langle\rho\rangle = \frac{3H(z)^2}{8\pi G}$ is the mean mass density of the Universe.

For $\delta \ll 1$ the fluctuation is in the linear regime, which can be treated analytically (e.g., Peebles, 1980; Peebles, 1993). Galaxy clusters are instead highly non-linear ($\delta \gg 1$) objects, and this requires more complex approaches for studying the evolution of perturbations in this particular regime. Specifically, this regime is studied by the means of large N-body simulations, such as the Millenium (Springel et al., 2005) and the Illustris (Vogelsberger et al., 2014) simulations. Interestingly, the clusters galaxies share a similar destiny by interacting gravitationally between them ending in large, massive galaxies sitting at the center of the cluster's gravitational well.

The hierarchical accretion of sub-clusters entails that the in-fallling sub-clumps of matter enter the cluster producing a complex network of shocks. This gravitationally driven shocks can heat the diffuse gas to the virial temperature of the potential well that confines it (e.g., Voit, 2005, for a review), thus producing clusters with almost self-similar entropy profiles (e.g., Voit, Kay, and Bryan, 2005; Ghirardini et al., 2017).

1.1.2 Mass of galaxy clusters

The total binding mass is a fundamental parameter to understand the physics of galaxy clusters because it sets their gravitational energy budgets that, ultimately, drives both the dynamical interaction with other clusters and the evolution of the cluster components. Historically, several methods have been developed to estimate the cluster mass:

◇ *Virial mass:* Under the assumption of virial equilibrium, the cluster mass can be estimated by knowing the position and redshift of a high enough number of member galaxies:

$$M \simeq \frac{\sigma_{\rm gal}^2 R_V}{G} \tag{1.2}$$

where $\sigma_{\rm gal}$ is the radial velocity dispersion of cluster galaxies, R_V is the virial radius of the cluster and $G = 6.67 \cdot 10^{-8}$ cm^3 g^{-1} s^{-2} is the gravitational constant. This simple approach, which is based on the strong (and not always verified) assumption of virial equilibrium, led to the first observational evidence of the existence of the dark matter in the Coma cluster (Zwicky, 1933). They found that the viral mass was larger by a factor ~ 10 than the sum of the mass of the galaxies, hence an additional, and invisible, component was necessary to explain the observation;

◇ *Hydrostatic equilibrium:* Under the assumption that the pressure force is balanced by the gravitational force given by a spherical distribution of gas (i.e., the thermal component of the ICM, which we discuss in more details in the following section), the pressure profile is:

$$\frac{dP_{\rm gas}}{dr} = -\rho_{\rm gas}\frac{d\phi}{dr} = -\rho_{\rm gas}\frac{GM(<r)}{r^2} \tag{1.3}$$

where $P_{\rm gas}$ and $\rho_{\rm gas}$ are the pressure and mass density of the gas, ϕ is the gravitational potential of the binding mass and $M(<r)$ indicates the total mass within the radius r. Therefore, by assuming the cluster gas as a perfect gas, the pressure equilibrium lead to:

$$M(<r) = -\frac{rkT_{\rm gas}}{G\mu m_p}\left(\frac{d\ln\rho_{\rm gas}}{d\ln r} + \frac{d\ln T_{\rm gas}}{d\ln r}\right) \tag{1.4}$$

where k is the Boltzmann constant, $\mu = 0.6$ is the mean molecular mass, m_p is the rest proton mass and $T_{\rm gas}$ is the gas temperature, which can be derived from X-ray observations (e.g., Ettori et al., 2013, for a review);

◇ *Gravitational lensing:* As the highest mass concentrations in the Universe, galaxy clusters are extremely efficient gravitational lenses. Their matter distorts background-galaxy images with an intensity that increases from the outskirts to the inner regions. The most massive galaxy clusters produce the strongest distortions, leading to the formation of "gravitational arcs" (Figure 1.2), or to the formation of systems of multiple images of the same source. Smaller masses (e.g., sub-clusters) produce weaker distortions, which can be only measured statistically, that are impressed on the shape of distant galaxies that lie on the sky at large angular distances from the cluster centers. The combination of these lensing regimes can be used to map the mass distribution in galaxy clusters (e.g., Meneghetti et al., 2010; Hoekstra et al., 2013);

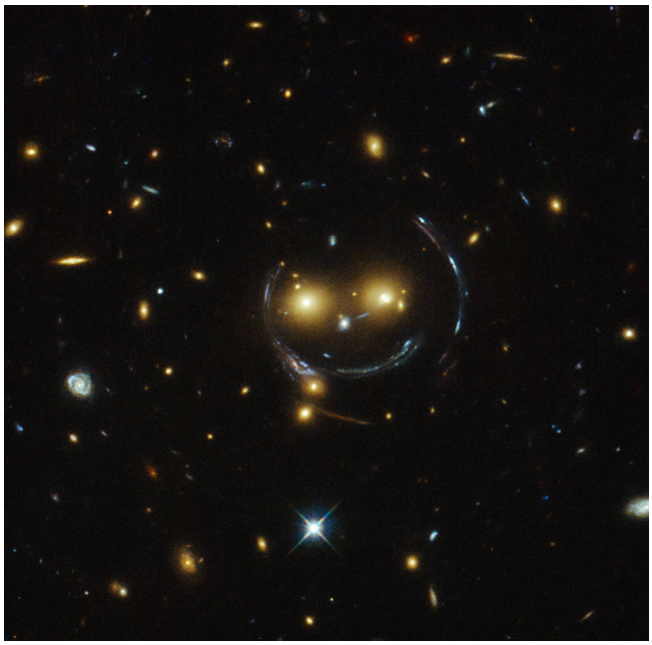

Figure 1.2: Einsten-ring captured by the Hubble telescope. Credit: NASA & ESA

◇ *Dynamical analysis:* When a large number of redshift measurements is available, the total mass can be inferred from the dynamical analysis of member galaxies. This can be obtained by fitting the velocity dispersion data to the solution of the Jeans equations (e.g., Binney and Tremaine, 1987), which describes the "flow" of a set of particles through phase-space in response to the acceleration induced by a gravitational potential Φ:

$$n\nabla\Phi = -n\bar{v}\cdot\nabla\bar{v} - \nabla\sigma^2 \tag{1.5}$$

where n is the number density of the galaxies, $\bar{v}$ is the mean velocity and σ the velocity dispersion. With respect to the virial mass method, the Jeans analysis permits to test different models of mass profiles to reproduce the gravitational potential Φ inferred by the observations (e.g., Biviano, 2002, for a review). Alternatively, the mass can be inferred using the "caustic technique". In the line-of-sight velocity v.s. projected radius diagram, cluster galaxies distribute in a characteristic trumpet shape. The edges of the trumpet are called caustic and, under the assumption of spherical symmetry, they trace the escape velocity profile of the cluster, thus they can be used to determine the cluster mass profile (Diaferio and Geller, 1997);

◇ *Scaling relations:* As a consequence of the hierarchical formation driven by the gravity, galaxy clusters have physical properties, such as the gas temperature, that are expected to scale with the mass and redshift of the dark matter halo because they mostly depend on the depth of the potential well. This induces a connection between the thermal energy budget of a cluster and its gravitational mass, which manifests as a series of scaling relations between the total mass and several observable quantities. Three correlations are particularly important, i.e. the X-ray luminosity-temperature, mass-temperature, and X-ray luminosity-mass relations, which are described by power-law functions (e.g.,

Giodini et al., 2013; Mantz et al., 2016; Ettori, Lovisari, and Sereno, 2020). Scaling relations are powerful tool that allow to derive the cluster mass more readily than the other methods, but first they must be calibrated carefully.

In order to test and calibrate the relations, it is necessary to compare, for small samples, the cluster masses, which can be measured through the methods described above, with the their properties, which can be inferred from the ICM X-ray emission or the Sunyaev-Zel'dovich effect (see Section 1.2.3). The calibrated relations permit, in turn, to derive the binding mass for larger samples of objects based on quantities that are more easily observed, such as the X-ray luminosity. Deviations from the scaling relations can indicate that non-gravitational processes, such as galaxy formation/feedback, may be a significant contributor to the global energy budget in clusters.

Given the variety of the methods, the total mass of galaxy clusters can be reconstructed by combining the different probes. However, it is necessary to account for the intrinsic biases of each of these analysis. X-ray based methods assume the hydrostatic equilibrium and the spherical symmetry of the systems, thus they can fail for disturbed clusters. On the contrary, the lensing analysis probes the cluster total mass, including the dark matter component, without basing on strong assumptions such as the equilibrium state of the clusters, i.e. the lens. However, this technique measures the projected mass instead of the 3D mass, and, thus, it is more sensitive than X-ray methods to projection effects, such as triaxiality and additional concentrations of mass along the line of sight. Given the richness and the quality of the current observations, nowadays it is possible to minimize the biases by exploiting rich datasets ranging from X-ray, to optical, to radio wavelengths (e.g., Sereno et al., 2017; Tchernin et al., 2018).

1.2 The intra-cluster medium

The ICM is composed of thermal plasma, which is heated during the collapse into the gravitational well, and non-thermal components, such as cosmic rays (CRs) and magnetic field, which represent a minor but non negligible fraction of the total energy budget and affect the micro-physics of the ICM as a whole. The interplay between these components give rise to a plethora of physical effects that end in a multi-wavelength emission, which ultimately allows us to study and diagnose the ICM. The principal processes, which are summarized in Table 1.1, includes X-ray thermal emission, non-thermal radio emission, the Faraday effect, and the Sunyaev-Zel'dovich (SZ) effect. Each of these processes provide us a different point-of-view on the ICM, thus multi-wavelenths analysis are required to fully understand the complete picture.

1.2.1 Microphysics

For the typical ICM temperature and density ($T \simeq 10^7 - 10^8$ K, $n \simeq 10^{-3} - 10^{-4}$ cm^{-3}), the mean free path of the ICM electrons is (Spitzer, 1956):

$$\lambda_e \simeq \frac{3^{3/2}(kT_e)^2}{4\pi^{1/2} n_e e^4 \ln\Lambda} \simeq 23 \left(\frac{T_e}{10^8\ \mathrm{K}}\right)^2 \left(\frac{n_e}{10^{-3}\ \mathrm{cm}^{-3}}\right)^{-1} \mathrm{kpc} \tag{1.6}$$

Table 1.1: Summary of the physical processes resulting from the interactions of thermal plasma and cosmic rays with the other components. We report their bolometric functional form without showing the spectral dependencies (from Rudnick, 2019).

	Thermal plasma	Cosmic rays
Thermal plasma	Bremsstrahlung (X-ray) $[n_e n_p T^{0.5}]$ H- and He-like line emission	π_0 decay (γ-ray) $[n_p n_{\rm CRp}]$
Magnetic field	Faraday rotation (radio) $[n_e B]$	Synchrotron (radio) $[n_{\rm CRe} B^2]$
Cosmic Microwave Background	SZ effect (mm) $[n_e T]$	Inverse Compton (X-ray) $[n_{\rm CRe} T^4_{\rm CMB}]$

where $\ln\Lambda \simeq 38$ is the ratio of largest to smallest impact parameters for the collisions. In comparison, the Larmor gyroradius-scale is (Braginskii, 1965):

$$\lambda_L \simeq 3 \times 10^{-12} \left(\frac{kT}{10\ \mathrm{keV}}\right) \left(\frac{B}{\mu\mathrm{G}}\right)^{-1}\ \mathrm{kpc} \tag{1.7}$$

where $B \sim \mu$G is the ICM magnetic field.

This defines $\lambda_e \gg \lambda_L$, thus implying that the ICM is a weakly-collisional plasma. In this regime, plasma instabilities and kinetic effects play important roles in regulating microphysical properties (e.g., Brunetti and Lazarian, 2011; Santos-Lima et al., 2014). Specifically, in the ICM the ratio between Coulomb collision frequency and plasma frequency is of the order of $\sim 10^{-16}$, thus the wave-particle interactions are potentially more important than Coulomb collisions in driving the ICM properties.

This has important implications. First of all, the importance of micro-instabilities and collisionless kinetic processes in the ICM opens to the possibility that a fraction of the gravitational energy budget could be channeled into electromagnetic fluctuations and particle acceleration mechanisms on much smaller scales, with fundamental implications for the dynamics of CRs (e.g. Brunetti and Jones, 2014, for a review). Furthermore, due to the fact that wave-particles interactions can mediate momentum exchange more efficiently than Coulomb particle-particle interactions, ICM behaves like a fluid that can be described with a reasonable approximation through the hydro or MHD frameworks (e.g., Santos-Lima et al., 2017, and references therein).

Therefore the sound speed is $c_s = \sqrt{\gamma P/\rho} \simeq 520\sqrt{kT/(1\ \mathrm{keV})} \simeq 1000$ km s^{-1}, where $\gamma = 5/3$ is the adiabatic factor, and P and ρ are the ICM pressure and mass density, implying a crossing-time, τ_c:

$$\tau_c = \frac{L}{c_s} \simeq \frac{1\ \mathrm{Mpc}}{1000\ \mathrm{km\ s^{-1}}} \simeq 1\ \mathrm{Gyr} \tag{1.8}$$

This is shorter than the cluster life-time, thus it entails the ICM is an efficient "memory-foam mattress" of cluster physics, i.e. it can store, and show, a wealth of hydrodynamical features that trace both the dynamical interactions that take place into the cluster, such as merging, minor merging or processing of cluster galaxies, and the

episodes of feedback by central active galactic nuclei (AGNs). These hydrodynamical features include the wakes of the infalling objects, as well as the interfaces between the host ICM and the atmosphere of the infalling object. Furthermore, the cluster dynamics can be traced by merger shocks, bow shocks, and sloshing motions of the ICM (e.g., Markevitch and Vikhlinin, 2007; Roediger et al., 2013).

1.2.2 The thermal view

The most important diagnostic of the ICM thermal plasma properties is its X-ray emission. Thanks to the very low density and high temperature of the electrons, the ICM is optically thin and it is in a state of collisional equilibrium established between the electrons and the heavy ions. As a consequence, the ICM mainly emits in the X-ray band due to a combination of line emission from K- and L-shell transitions of heavy ions (iron being the most prominent) and thermal X-ray bremsstrahlung, whose emissivity is:

$$\epsilon(T,\nu) \simeq 6.8 \times 10^{-38} n_e n_i T^{-1/2} Z^2 g_{ff} e^{-\frac{h\nu}{kT}} \text{ erg s}^{-1} \text{ cm}^{-3} \tag{1.9}$$

where n_e and n_i are, respectively, the electrons and ions particle density, T and Z are the temperature and metallicity of the plasma and g_{ff} is the free-free Gaunt factor, which absorbs the quantum correction to the classical Maxwell energy distribution function (e.g., Sarazin, 1986). The emission is dominated by H and He and has its peak around 1 keV. The sharp exponential cut-off of the spectrum permits to reliably estimate the temperature of the emitting plasma.

The line-to-continuum ratio permits to measure the abundances of the heavy elements in the ICM, whereas the Fe-L lines can be used as an additional thermometer for low-temperature environments. The blending of thermal bremsstrahlung, recombination, collisional emission lines, and re-ionization taking place in the ICM of the ICM can be summarized by the cooling function $\Lambda(T) = lT^{\alpha}$ (Sutherland and Dopita, 1993), where for thermal bremsstrahlung $l \simeq 2.5 \times 10^{-27}$ and $\alpha = 1/2$. The resulting emissivity can be defined as:

$$\epsilon(T) = n_e n_p \Lambda(T) \text{ erg s}^{-1} \text{ cm}^{-3} \tag{1.10}$$

For galaxy clusters, the typical X-ray luminosity is $10^{43} - 10^{45}$ erg s^{-1}, thus making them one of the most luminous X-ray sources in the sky that have been studied since the advent of the first X-ray observatories such as *UHURU* (e.g., Gursky et al., 1971).

The β-model

The strong dependence of the ICM emission on the gas density permits to use the X-ray surface brightness to infer the 3D distribution of the thermal gas. Under the assumption that gas and galaxies are in equilibrium in the same potential, where the galaxy mass profile is (King, 1962):

$$\rho_{\text{gal}}(r) = \frac{\rho_{\text{gal},0}}{\left[1 + \left(\frac{r}{r_c}\right)^2\right]^{3/2}} \tag{1.11}$$

where $\rho_{\rm gal}$ is the galaxy density, $\rho_{\rm gal,0}$ is its central value, and r_c is the core radius, it is possible to demonstrate that the density profile of an isothermal gas, $n_{\rm gas}$, can be described as:

$$\frac{n_{\rm gas}(r)}{n_{\rm gas,0}} = \left[\frac{\rho_{\rm gal}(r)}{\rho_{\rm gal,0}}\right]^{\beta} \tag{1.12}$$

where $n_{\rm gas,0}$ is the central particle density and $\beta = \mu m_p \sigma_r^2 / kT \simeq 2/3$ is the ratio between thermal and gravitational energy (Cavaliere and Fusco-Femiano, 1976; Cavaliere and Fusco-Femiano, 1978) .

This relation can be re-written in the so-called β-model:

$$n_{\rm gas}(r) = n_{\rm gas,0}\left[1 + \left(\frac{r}{r_c}\right)^2\right]^{-\frac{3}{2}\beta} \tag{1.13}$$

Under the assumption that the X-ray emission is dominated by the thermal bremsstrahlung, this density profile defines an emissivity profile $\epsilon_c(r,T) = n_e n_i \Lambda(T) \propto n_{\rm gas}(r)^2 T^{1/2}$ that can be then converted into a surface brightness profile by using the Abel transformation:

$$I(b) = 2\int_r^{+\infty} \frac{\epsilon(r) r {\rm d}r}{\sqrt{r^2 - b^2}} \tag{1.14}$$

where $I(b)$ is the surface brightness observed at the projected radius b.

Therefore, the X-ray surface brightness, $I_{\rm X}$, can be linked directly to the gas density profile as:

$$I_{\rm X}(b) = n_{\rm gas,0}^2 r_c \Lambda(T) B(3\beta - 0.5, 0.5)\left[1 + \left(\frac{b}{r_c}\right)^2\right]^{\frac{1}{2}-3\beta} \tag{1.15}$$

where B is the Beta function $B(x,y)$ (e.g., Ettori, 2000).

This simple model hence permits to derive the parameters that describe the density profile by studying the observed $I_{\rm X}$ profile. The β-model has been successfully used to study and model the first X-ray observations of galaxy clusters made with *Einstein* and *ROSAT* (e.g., Jones and Forman, 1984). Later, more detailed observations made with *Chandra* and *XMM-Newton* made clear two limitations of this model (Arnaud, 2009), i.e. an over-estimate of the density for $r >> r_c$, and the fact that clusters are not isothermal, thus making the model physically inconsistent. Nevertheless, this straightforward and flexible method is still largely used to infer the main characteristics of the ICM in a first approximation.

Relaxed clusters are characterized by an enhancement of $I_{\rm X}$ in the central region, which also show a significantly lower temperature (i.e. a not-negligible temperature gradient in the cluster). Therefore, the X-ray emission from the core results inadequately described by the β-model, which, due to the assumption of the King model, inherently produces a centrally flat density profile. Spectrally, the central region of these clusters is well approximated by a two-temperature model, where the inner temperature represents the multiphase status of the core and the outer temperature is a measure of the ambient gas temperature. To account for that, the β-model needs

to be extended to a two-phase gas emission modeled as a *double* β-model. This addition, which entails a more complex physical treatment to infer the ICM properties (e.g., Xue and Wu, 2000; Ettori, 2000), has proven to effectively model the X-ray surface brightness of relaxed clusters (e.g., Hudson et al., 2010; Giacintucci et al., 2017).

X-ray emission as tracer of the cluster dynamic

Thanks to the exceptional quality of the observations provided by the last generation of X-ray satellites *Chandra* and *XMM-Newton*, the morphology of the thermal X-ray emission has been the principal probe of the dynamical state of the clusters (e.g., Markevitch and Vikhlinin, 2007; Laganá, Durret, and Lopes, 2019, and references therein). Recently, the new X-ray observatory *eROSITA* (Predehl et al., 2020), which thanks to its large field of view (1 degree) and special scanning mode provides exceptionally uniform and deep X-ray image covering, is delivering new remarkable insights into the dynamics of galaxy clusters (Churazov et al., 2020; Ghirardini et al., 2020).

The dynamical state can be discriminated based on the morphological paremeters, i.e. centre shift, power ratios, concentration parameter (e.g., Parekh et al., 2015; Rossetti et al., 2016), and spectral signatures, such as the central entropy and cooling time, and entropy ratio of the X-ray emission (e.g., Cavagnolo et al., 2009; Hudson et al., 2010). We can identify two main extreme cases of dynamical state (Figure 1.3). On the one side there are the relaxed, cool-core clusters, which are dynamically relaxed clusters characterized by a regular morphology, peaked X-ray emission, and low specific entropy at their centres. This class of clusters is the main focus of this Thesis, thus it is introduced in details in the following section.

On the other side, there are the merging clusters, which are characterized by irregular morphology, substructures in their X-ray brightness distribution and high central entropy. The impact velocity, $v_{\rm imp}$, of two clusters with mass M_1 and M_2 at a distance d can be estimated as:

$$v_{\rm imp} = 2930 \sqrt{\left(\frac{M_1 + M_2}{10^{15}\ {\rm M}_\odot}\right)\left(\frac{d}{1\ {\rm Mpc}}\right)\left[\frac{1 - \frac{d}{d_0}}{1 - \left(\frac{b}{d_0}\right)^2}\right]}\ {\rm km\ s^{-1}} \tag{1.16}$$

where b is the impact parameter and d_0 is the initial distance (e.g., Sarazin, 2002). The order of magnitude of the velocity, combined with the typical masses of galaxy clusters, entails that the merger between clusters of galaxies are the most energetic events in the Universe, capable of releasing energies up to $\sim 10^{63} - 10^{64}$ erg during one cluster crossing time of $\sim$ 1 Gyr (e.g., Markevitch and Vikhlinin, 2007). This huge amount of kinetic energy is mostly converted into heat by large scale shock waves traveling through the ICM with low Mach number $\mathcal{M}$ =3-5, and is ultimately dissipated through large scale turbulent motions of the gas. During their propagation, shock waves compress and heat the gas producing an increase in the X-ray surface brightness and temperature in correspondence of the shock front. However, shock waves are actually difficult to observe. Shocks with such low Mach numbers are expected to produce relatively small density jumps ($\rho_2/\rho_1 = 4\mathcal{M}^2/\mathcal{M}^2 + 3$), implying that they can be visible only if they have not moved yet to the very external regions of the cluster where the X-ray emission is dominated by the background. Furthermore, shocks are detectable only if they are moving along the plane of the

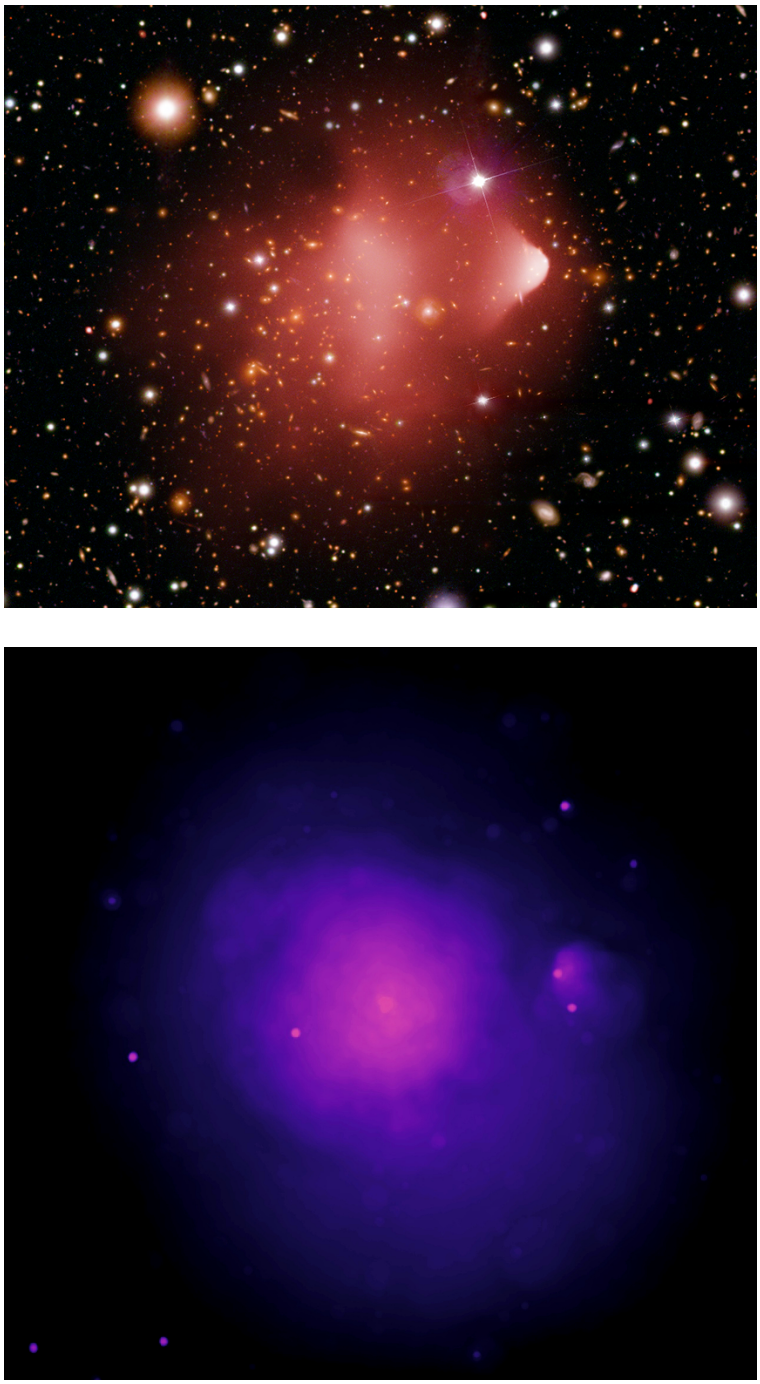

Figure 1.3: Comparison between X-ray morphology of merging and relaxed clusters. Top: Composed optical and X-ray image of the disturbed "bullet" cluster (Credits https://chandra.harvard.edu/photo/2008/bullet/); Bottom: Smoothed X-ray image of the relaxed cluster Abell 2626. The structure toward west is not related to the cluster but is instead produced by the jellyfish galaxy JW100 (see Chapter 7).

sky, otherwise their observable effects can be smoothed by projection effects.

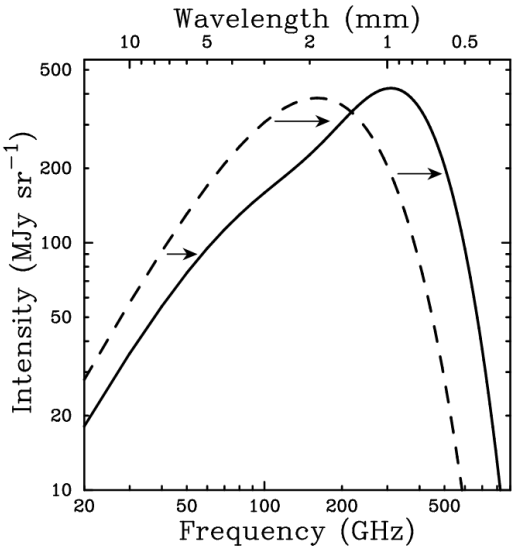

Figure 1.4: The CMB spectrum, undistorted (dashed line) and distorted by the SZ effect (solid line), illustrated is for a fictional cluster 1000 times more massive than a typical massive galaxy cluster (Carlstrom, Holder, and Reese, 2002).

1.2.3 The Sunyaev-Zel'dovich effect

The Sunyaev-Zel'dovich (SZ) effect is a small distortion of the Cosmic Microwave Background (CMB) spectrum caused by the Inverse Compton (IC) scattering of the CMB photons with the electrons of the hot ICM (Sunyaev and Zeldovich, 1972). When a low-energy CMB photon encounters an high-energy ICM electron, the former gains energy via IC process, its frequency increases and it is blue-shifted. The characteristic spectral signature of the SZ effect is a decrease in the CMB intensity at frequencies $\leq$218 GHz and an increase at higher frequencies (Figure 1.4).

For a thermal distribution of electrons n_e, the change in the background CMB intensity, $I_{\rm CMB}$, is $\delta I_{\rm CMB}/{\rm I_{CMB}} \propto I_{\rm CMB} y_e \sim 10^{-5} - 10^{-4}$, where y_e is the Compton parameter, which provides the integrated electron pressure of the ICM along the line of sight:

$$y_e = \frac{\sigma_T}{m_e c^2} \int_0^{+\infty} n_e T_e dl \tag{1.17}$$

where σ_T is the Thomson cross-section, m_e is the electron mass and T_e is the electron temperature.

For a source extended over a solid angle Ω, such as a galaxy cluster, the integrated Compton paramter is:

$$Y = \int_\Omega y_e d\Omega \propto \frac{1}{D_A^2} \int_0^{+\infty} dl \int_A n_e T_e dA \tag{1.18}$$

where D_A is the angular diameter distance and A is the are on the plane of the sky.

The SZ signal integrated over the solid angle of the cluster provides the sum of the electrons weighted by temperature, which is a measure of the total thermal pressure/energy of the cluster. Under the hypothesis of isothermal gas, Y results

tightly related to the total mass of the cluster:

$$Y D_A^2 \propto T_e \int n_e dV \propto M_{\rm gas} T_e \propto f_{\rm gas} M_{\rm tot} T_e \tag{1.19}$$

where $f_{\rm gas}$ is the fraction of the mass in form of ICM.

The connection between the integrated SZ signal and the total mass has been specifically proven in Planck Collaboration et al. (2011b), where the $Y_{500} - M_{500}$ correlation is derived. The 500 subscript indicates that the quantities are computed within R_{500}, i.e. the radius within which the average density is 500 times the critical density of the Universe at the cluster redshift. In order to test the validity of SZ effect as proxy of the cluster mass, the SZ-based estimates were compared with those obtained with deep *XMM-Newton* observation. The results of 23 months of Planck observations are reported in the PSZ2 catalog (Planck Collaboration et al., 2016), the largest SZ-selected sample of galaxy clusters, and the deepest systematic all-sky survey of galaxy clusters. The PSZ2 catalog provides SZ-based masses within R_{500} for 1203 clusters with identified counterparts in external data sets, thus it is an unmatched tool for statistical studies.

1.2.4 The non-thermal view

Magnetic field

The last decades of radio observations have proven that the ICM is magnetized and filled with relativistic particles, highlighted by the presence of large-scale radio emission. These studies have revealed that the ICM magnetic field has a typical strength of ~ 1 μG, but it can rise up to 10-20 μG at the center of relaxed clusters, with important effect on energy transport in the ICM (e.g., Ryu et al., 2012, and references therein).

The reference method to measure the magnetic field in galaxy clusters is the Faraday rotation measure (RM). When a linearly polarized radiation passes through a magnetised plasma, the left and right circularly polarized rays propagate with different velocities. This leads to a rotation of the polarization angle proportional to the wavelength λ of $\Delta\Phi = {\rm RM}\lambda^2$, where:

$${\rm RM} = 812 \int_0^L \frac{n_e}{\rm cm^{-3}} \cdot \frac{B_\parallel}{\mu{\rm G}} \times \frac{dl}{\rm kpc} \ {\rm rad\ m^{-2}} \tag{1.20}$$

where $B_\parallel$ is the component of the magnetic field along the line-of-sight and L is the depth of the magnetised screen.

RM measures, which are made possible by the serendipitous presence of polarized source behind the ICM magnetic field, i.e. the magnetized screen, have permitted to derive the magnetic field profile of galaxy clusters, as well as the global value, finding that it can be well described in terms of the gas density as $B(r) \propto n_{\rm gas}(r)^\eta$ (e.g., Bonafede et al., 2010).

The origin and the evolution of cluster-scale magnetic field is still a matter of studies. From a theoretical point of view, the first cosmic seed fields ($B \sim 10^{-34} - 10^{-10}$ G) can be generated in the very early Universe during inflation and first-order

phase transitions (Widrow et al., 2012). Indeed, by studying the deflection due to magnetic field of CR cascade produced by TeV blazars, it has been possible to set the upper limits on the primordial magnetic field at the epoch of the CMB to $B < 10^{-10}$ G (Neronov and Vovk, 2010). Later on, structure formation can cause further amplification via a small-scale turbulent dynamo in two main phases, exponential growth of the magnetic field in the kinematic regime, and non-linear growth and stretching of the coherence scales (e.g., Subramanian, Shukurov, and Haugen, 2006; Pakmor, Marinacci, and Springel, 2014). Galactic activity can yield further localized seeding, while further amplification in cluster outskirts might be produced via the magnetothermal instability or instabilities driven by cosmic rays accelerated by shocks (e.g., Völk and Atoyan, 2000; Brüggen, 2013). At higher redshifts ($z \simeq 2$), star formation should be able to induce small-scale dynamo by injecting turbulence from supernova explosions (Beck et al., 2013). Furthermore, the existence of high-redshift ($z \sim 0.7 - 0.8$) diffuse synchrotron sources points out a rapid evolution of the magnetic field strength, which permits to constrain the micro-physics of the ICM (Di Gennaro et al., 2020). Cosmological simulations provide a valuable tool to combine the different components and to model the evolution of magnetic fields from the scale observed in the CMB up to the values observed today (e.g., Vazza et al., 2014, and references therein).

Cosmic rays

Cosmological shock waves and turbulence driven in the ICM during the process of hierarchical cluster formation work as accelerator of cosmic ray electrons (CRe) and protons (hadrons or CRp). In addition, clusters host other accelerators of CRs, ranging from ordinary galaxies (especially as a byproduct of star formation) to AGN and, potentially, regions of magnetic reconnection (e.g., Brunetti and Jones, 2014, and references therein).

The propagation of CRs injected in the ICM is mainly determined by diffusion and convection, hence the time necessary for CRs to diffuse over distances L is $\tau \simeq (1/4)L^2/D$, where D is the diffusion coefficient, which can have a maximum value of $\sim 10^{31}$ cm^2 s^{-1} (Brunetti and Jones, 2014). For CRs with energies $E \gtrsim$Gev, the life-time, $\tau \sim p/(dp/dt)$, is limited by energy losses, that varies for CRe and CRp:

- For CRe, energy losses are dominated by ionization and Coulomb losses at low energy, and by synchrotron emission and Inverse Compton at high energy. The resulting life-time, τ_e, can be described by:

$$\tau_e \simeq 4 \times \left\{ \frac{1}{3} \left(\frac{\gamma}{300} \right) \left[\left(\frac{B}{3.2\ \mu\mathrm{G}} \right)^2 + (1+z)^4 \right] + \left(\frac{n_{th}}{10^{-3}} \right) \left(\frac{\gamma}{300} \right)^{-1} \left[1.2 + \frac{1}{75} \ln \left(\frac{\gamma/300}{n_{th}/10^{-3}} \right) \right] \right\}^{-1} \mathrm{Gyr} \tag{1.21}$$

  where n_{th} is the density of the thermal plasma protons. For CRe with energies $E \sim 5$ GeV, i.e. those that are responsible of the observed radio emission, the radiative age is commonly computed by neglecting Coulomb losses:

$$\tau_e \simeq 3.2 \times 10^{10} \frac{B^{1/2}}{B^2 + B^2_{\mathrm{CMB}}} \left[\nu (1+z) \right]^{-1/2} \ \mathrm{yrs} \tag{1.22}$$

where ν is the observed frequency in MHz, B and $B_{\rm CMB}$ are in units of μG, and the latter is the CMB equivalent magnetic field $B_{\rm CMB} = 3.25(1+z)^2$ μG, which is used to quantify the Inverse Compton energy losses;

◇ For CRp, the main channel of energy losses due to inhelastic proton-proton collisions with the thermal ICM protons, which set a life-time, τ_p of:

$$\tau_p \simeq \frac{1}{c n_{th} \sigma_{pp}} \ {\rm s} \tag{1.23}$$

where σ_{pp} is the inclusive proton-proton cross-section.

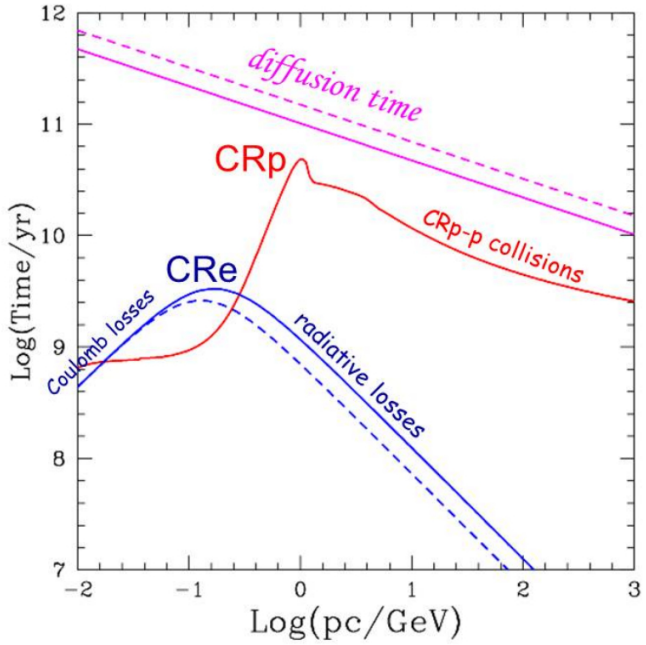

Figure 1.5: Life-time as function of the energy of CRp (red) and CRe (blue, lower curves) in the ICM at redshift $z = 0$, compared with the CR diffusion time on Mpc scales (magenta, upper curves). Dashed and continuous lines represent the estimates derived for an ICM magnetic filed of, respectively, 1 and 3 μG (Brunetti and Jones, 2014).

The comparison between τ_e, τ_p, and the diffusion time-scale over Mpc scale (Figure 1.5) points out two interesting implications. On the one hand, the long lifetimes of CRp against energy losses in the ICM, and their likely slow diffusive propagation through the disordered ICM magnetic field in the large size of galaxy clusters, make clusters efficient storehouses for cosmic rays. The consequent accumulation of CRs inside clusters occurs over cosmological times, with the potential implication that a non-negligible amount of the ICM energy could be in the form of relativistic, non-thermal particles. On the other hand, the existence of Mpc-scale radio sources (e.g., van Weeren et al., 2019), which we describe in the following Section, adds a complexity to the puzzle. Indeed for particles with a radiative times of $\sim 10^7 - 10^8$ yrs, such as the CRe producing the observed emission, the simple diffusion can not explain the scales at which these particles are observed emitting radio waves, thus additional processes are necessary to explain the observations (Brunetti and Jones, 2014, for a review).

Diffuse radio sources

Diffuse radio sources are the principal evidence of the presence of magnetic field and CRs in the ICM. In general, we define "diffuse" any kind of emission that is not directly connected to a galaxy. Diffuse sources have in common a synchrotron radio emission, with a spectrum $S \propto \nu^{\alpha}$, with a characteristics steep-spectrum emission ($\alpha < -1$). Here we present a taxonomy of diffuse radio sources (van Weeren et al., 2019, and references therein):

- ◇ Radio halos: extended sources that follow the ICM distribution. This class includes giant and mini radio halos. These source are observed at the center of the clusters, with roundish shapes. Their sizes goes from hundred of kpc (mini) to Mpc scales (giant), and generally they do not show polarized emission. Combined radio and X-ray studies made clear that giant and mini-halos flourish in different environments, where the the former are generally observed in disturbed clusters and the latter in relaxed ones (e.g., Cassano et al., 2010; Kale et al., 2015). Giant radio halos are though to originate from re-acceleration mechanisms powered by merger-induced turbulence (Brunetti and Jones, 2014, for a review). A more detailed discussion of mini-halos (MH) is provided in Section 1.3.4;

- ◇ Radio relics: elongated radio sources observed at the periphery of dynamically-disturbed clusters. They can extend up to Mpc scales and are highly polarized (e.g., van Weeren et al., 2019, for a review). These sources are thought to originate from the acceleration (or re-acceleration) of electrons at the shock waves propagating in the ICM. In fact a connection with shocks is observed in many cases (e.g., Brunetti and Jones, 2014; van Weeren et al., 2019, for reviews);

- ◇ Revived AGN fossil plasma sources: extended sources tracing AGN radio plasma that has somehow been re-energized through processes in the ICM, unrelated to the radio galaxy itself. These sources have shown a plethora of features, both in terms of radio spectral properties and position in the cluster (e.g., de Gasperin et al., 2017; Mandal et al., 2020), that makes difficult to outline a common process for their origin. The main observational properties that the sources have in common is the AGN origin of the plasma, and their ultra-steep radio spectra ($\alpha < -2$).

Cluster radio galaxies

In addition to the diffuse emission related to the ICM, the radio emission in galaxy clusters can be due to the presence of radio galaxies, associated both to the star formation or the AGN. Here we report a brief overview of the different classes of radio galaxies commonly observed in galaxy clusters:

- ◇ Brightest central galaxies (BCG): the most massive and luminous elliptical galaxies in the present day Universe (e.g., Lauer et al., 2014, for a review). They are typically located at the center of galaxy clusters, near the bottom of the cluster's gravitational potential well, with small peculiar velocities relative to the cluster mean. Most of them are radio-loud (e.g., Burns, 1990), and the radio emission is mainly due to the AGN activity. However, there is strong observational evidence that star formation is not negligible, especially in relaxed clusters (e.g., Donahue et al., 2015). The radio morphology BCG is generally characterized by a single pair of anti-parallel jets of relativistic plasma ejected

from the central AGN (e.g., Begelman, Blandford, and Rees, 1984). However, a small fraction ($\sim$ 10%) of them show a more "exotic" morphology with multiple jets and complex wing-like structures. The origin of these sources, which take the name of X- or Z-shaped sources is still debated and often related to the presence of binary black holes, or more complex interactions between the radio jets and the galactic environment (e.g., Wirth, Smarr, and Gallagher, 1982; Gopal-Krishna et al., 2012);

- ◇ Tailed galaxies: galaxy clusters host the so-called tailed radio galaxies, FR I (Fanaroff and Riley, 1974) sources where the large scale, low-brightness emission is bent by the environmental pressure (thermal or ram-pressure) in the same direction, forming structures similar to tails. These radio galaxies are classified, in turn, into two classes, which are narrow-angle tailed sources (NAT), with small angles between the tails (O'Dea and Owen, 1985), and wide-angle tailed sources (WAT), with a larger angle between the tails (e.g., Feretti and Venturi, 2002);

- ◇ Normal galaxies: for those galaxies whose energy output is not dominated by the AGN, the main source of radio emission is the star formation (e.g., Condon, 1992, for a review). Specifically, the radio emission arises from synchrotron emission of CRe released by supernovae, with a typical spectral index $\alpha \simeq -0.7$, and free-free radiation of HII regions, with a flatter spectral index ($\alpha \simeq -0.1$). However, the interactions with the ICM can dramatically impact on the star formation, and hence the radio properties, of these galaxies. We discuss this in the following section.

1.2.5 Cluster galaxies and their interplay with the ICM

The possibility that the evolution of the cluster galaxies is affected by the cluster environments was suggested immediately after the first detection of ICM (Gursky et al., 1971). Since then, this interplay has been often invoked to explain the evolution with the redshift of the populations of cluster galaxies, in particular the decrease of S0 galaxies and the increase of spiral and star-forming galaxies at higher redshift (Figure 1.6, e.g., Poggianti et al., 1999; Fasano et al., 2000).

The dominant process is considered to be the ICM ram pressure stripping that is able to remove gas from the galaxies in their first infall in the cluster (Boselli and Gavazzi, 2006). The condition for gas loss is that the ram-pressure overcome the gravitational bound, and can be expressed as:

$$\rho_{\rm ICM} v_{\rm gal}^2 = 2\pi G \Sigma_{\rm s} \Sigma_{\rm g} \tag{1.24}$$

where $\Sigma_{\rm s}$ and $\Sigma_{\rm g}$ are the surface density of stars and gas, respectively, $\rho_{\rm ICM}$ is the ICM mass density, and $v_{\rm gal}$ the in-fall velocity of the galaxy. The characteristic signatures of ram pressure-processed galaxies are hydrogen deficiency, truncated gaseous disks, and asymmetrical HI and Hα emission. The most extreme examples of galaxies undergoing strong ram pressure are the so called jellyfish galaxies (Fumagalli et al., 2014; Smith et al., 2010; Ebeling, Ma, and Barrett, 2014), objects that show extra-planar, unilateral debris visible in the optical/UV light and striking tails of Hα ionised gas.

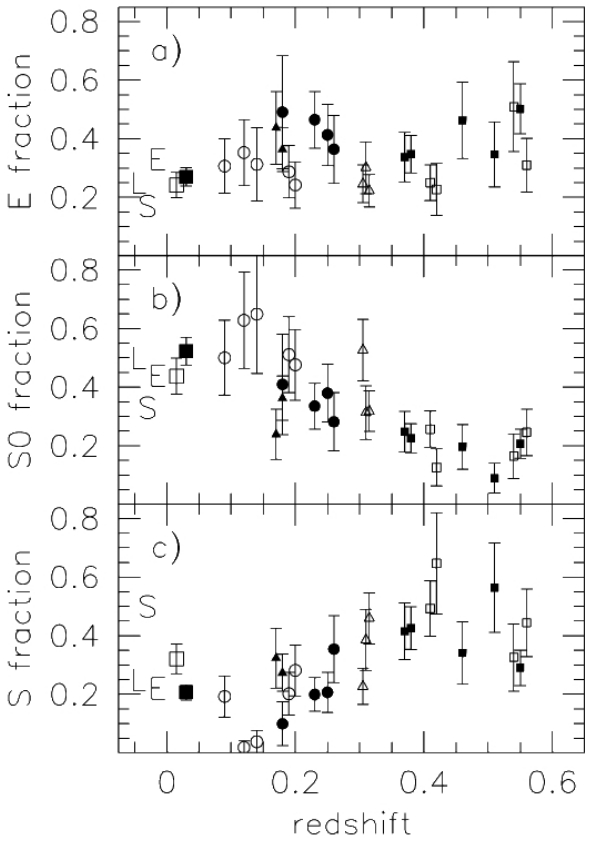

Figure 1.6: Distribution of elliptical, S0 and spiral galaxies with the redshift (Fasano et al., 2000).

The effects of ICM ram pressure has been studied by the means of both the multi-wavelength observations and the numerical simulations, finding that it is able to dramatically impact on the galaxy evolution by abruptly quenching the star formation (see van Gorkom, 2004, for a review). However, it has been suggested that this interaction could lead also to "ram pressure-induced" bursts of star formation by enhancing the compression, and the subsequent collapse, of ISM cold gas (e.g., Gavazzi et al., 1995). A fascinating, and currently studied, possibility is that the impact of the ICM could be closely related to the dynamical state of the cluster. Cluster-(sub)cluster merging can give rise to bulk motions, shocks and temperature structures within the ICM that can increase the efficiency of the stripping. In support of this, recent studies found that the extended structures of jellyfish galaxies can be used as proxy to determine the dynamics of cluster collisions (Ebeling and Kalita, 2019).

1.3 Relaxed galaxy clusters

In this Thesis we explore the physics of the interplay between the thermal and non-thermal processes taking place in relaxed clusters. In the following, we introduce the main actors of these ecosystems.

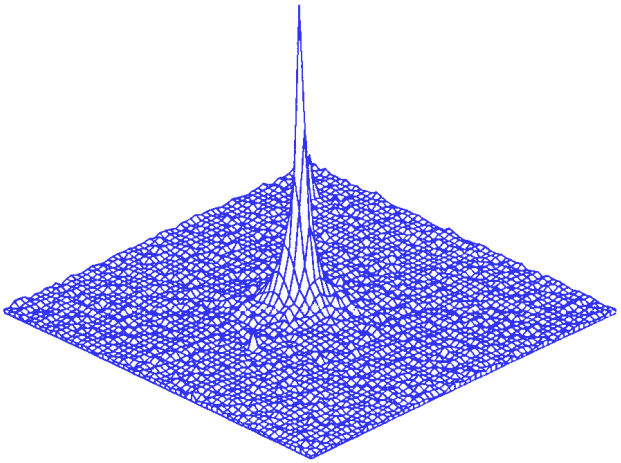

Figure 1.7: 3D representation of the X-ray surface brightness of the Abell 478 galaxy clusters by *ROSAT* HRI. The cooling region in this cluster extends up to 200 kpc, incorporating most of the prominent peak (1 pixel=60 kpc, adapted from White et al., 1994)

1.3.1 Physiology of the cool core

In dynamically-relaxed clusters, i.e. those that have not been subjected to major mergers in a time $\tau \sim 3$ Gyr, the ICM can cool down, lose energy and deposit at the center of the gravitational well. Hence, in the region within few hundred kpc from the center of the cluster the local increase of density heavily impacts on the cooling time of the thermal gas, which can be expressed as (Sarazin, 1988):

$$t_{\rm cool} = \frac{\gamma}{\gamma - 1} \frac{kT}{\mu X n_e \Lambda(T)} \simeq 8.5 \times 10^{10} \left(\frac{n_e}{10^{-3}}\right)^{-1} \left(\frac{T}{10^8\ {\rm K}}\right)^{\frac{1}{2}} \ {\rm yrs} \qquad (1.25)$$

where γ is the adiabatic factor, $\mu \simeq 0.6$ is the mean molecular weight and $X \simeq 0.71$ is the hydrogen mass fraction.

In the physical conditions found in the central region of relaxed clusters, $t_{\rm cool}$ can result significantly short. Specifically, within $R_{\rm cool}$, which is the radius at which $t_{\rm cool} \simeq 3$ Gyr, the cooling becomes so efficient that, in absence of an external heating, the mean temperature and pressure at the center of relaxed clusters can decrease dramatically, forming the so-called cool core. Following the drop of central pressure, larger and larger masses of gas begin to flow down at the center of the cluster due to the pressure of the overlying gas, ending in a significant mass flow called *cooling flow* (Fabian, Canizares, and Boehringer, 1994). The result is an evident decrease of temperature and increase of gas density within $R_{\rm cool}$ (e.g., Hudson et al., 2010), which, from an observational point of view, produces an extremely high X-ray luminosity ($\sim 10^{45}$ erg s^{-1}) and a characteristic peaked surface brightness profiles (Figure 1.7). As described in Section 1.2.2, the cooling emission is mainly due to thermal bremsstrahlung and line emission. In the cold ($kT < 2$ keV), high-density cool cores the line emission dominates the X-ray emission and permits precise measures of the gas temperature and metallicity (e.g., Sarazin, 1986; Peterson and Fabian, 2006).

The efficiency of the cooling process can be expressed by the amount of matter which crosses $R_{\rm cool}$ and flows towards the center, that is the mass inflow rate $\dot{M}$.

The cooling mass inflow rate can be estimated from the luminosity $L_{\rm cool}$, which is in turn inferred from the X-ray observations, associated with the cooling region. By assuming that $L_{\rm cool}$ is all due to the radiation of the total thermal energy of the gas plus the pdV work done on the gas as it enters, it is connected to the $\dot{M}$ as (e.g., Fabian, Canizares, and Boehringer, 1994):

$$L_{\rm cool} = \frac{5}{2}\frac{\dot{M}}{\mu m_p} kT \tag{1.26}$$

Generally $L_{\rm cool}$ is $\sim$ 10% of the total X-ray luminosity, i.e., $\sim 10^{43}$-10^{44} erg s^{-1}. Typical values of $\dot{M}$ are around 100 M$_\odot$ yr^{-1}, which represents an huge amount of cold gas deposited onto the central galaxy, and, as we discuss in the following section, is one of the biggest controversies of the cooling flow model.

However, the simple cooling flow scenario has been severely challenged by the observations over the years (e.g., Peterson and Fabian, 2006, for a review). The enormous mass deposition predicted by X-ray observations has not been confirmed by optical observations, that instead found that both the star formation and the molecular gas mass in the BCG are, in general, order of magnitudes below the expectations (e.g., McNamara and O'Connell, 1989; Edge, 2001; McDonald et al., 2018). A noticeably exception in this sense is the Phoneix cluster, for which McDonald et al. (2013) reports a star formation rate $\sim$ 800 M$_\odot$ yr^{-1}, which would consume a 30-40% of the predicted cooling flow. Furthermore, X-ray spectral analysis carried out with the Reflection Grating Spectrometer on the *XMM-Newton* observatory revealed that the gas in the central region does not cool at the rates predicted by the cooling flow model (e.g., Peterson et al., 2003). These evidence have pointed out that the cooling has to be balanced by some sort of heating process taking place in the ICM (for a review Peterson and Fabian, 2006; McNamara and Nulsen, 2007; McNamara and Nulsen, 2012; Gitti, Brighenti, and McNamara, 2012, and references therein).

A distinguishing characteristic of cool core clusters is the presence of warm, optical line-emitting filaments of gas extending from the BCG (e.g., Hu, Cowie, and Wang, 1985; Olivares et al., 2019, and references therein). Typically observed in Hα, this warm gas has been shown to correlate with several properties of the cool core, such as cooling rate and cluster entropy. However, their origin is debated (e.g., McDonald, 2011). They could be produced by cooling of ICM stimulated by the bouyancy of a cavity in the ICM (McNamara et al., 2016) or by the chaotic cold accretion (Gaspari, Ruszkowski, and Oh, 2013). In the first model the filaments are drifting away from the AGN dragged by a buoyant cavity. In the second scenario the filaments are falling into the black hole, and no associated cavity is expected. In both scenarios, molecular filaments are deeply related to the evolution of the central galaxy, thus are important pieces of the cool core puzzle. Finally, it is interesting mentioning that central molecular filaments share several similarities, both in terms of spectral and thermal properties, with stripped molecular filaments observed in jellyfish galaxies (e.g., Werner et al., 2013; Poggianti et al., 2019b), thus suggesting that these objects are produced by similar physical processes.

Figure 1.8: Composite image of the center of Hydra A with the radio (red), optical (green), and X-ray (blue) emissions (Kirkpatrick et al., 2009).

1.3.2 The role of AGN feedback

The heating process invoked to explain the fallacies of the cooling flow model could be explained by the non-gravitational energy input supplied by supernovae and AGNs. Whereas supernovae are essential in the process of enrichment of the ICM to the metallicity level observed (Domainko et al., 2004), they are energetically insufficient to balance the cooling (e.g., Borgani et al., 2002). On the contrary, the AGNs, which are powered by accretion of material onto a black hole, could provide the energy to balance the cooling (e.g., Fabian, 2012, and references therein). Specifically, the matter falling onto a black hole releases an energy of the order of $E_{\rm BH} = \eta Mc^2$, where $\eta \simeq 0.1$ is the efficiency. For supermassive black holes of masses $\sim 10^9$ $M_\odot$, the amount of energy released during their formation and growth is of the order of $E_{\rm BH} \sim 2 \times 10^{62}$ erg, which represent a significant energy budget for heating processes in the cool cores.

The most spectacular evidence of the impact of the AGN on the surrounding medium is represented by the almost ubiquitous presence of X-ray cavities at the center of relaxed clusters (e.g., Hlavacek-Larrondo et al., 2012; Shin, Woo, and Mulchaey, 2016). These structures are associated with radio-loud central galaxy (e.g., Mittal et al., 2009) whose non-thermal radio jets and lobes fill them with radio-emitting plasma (Figure 1.3.2). This association has been pointed out as evidence of that the

AGN "radio-mode" feedback can deeply affect the surrounding ICM (e.g., McNamara and Nulsen, 2007; Gitti, Brighenti, and McNamara, 2012; Bîrzan et al., 2020, for reviews). In order to understand how deeply the feedback unfolds in the ICM, it is crucial to estimate the energies involved in this process. The mechanical energy "stored" in the X-ray cavities, which reasonably is equal to (or slightly lower than) the energy which was necessary to form them, can be inferred directly from the X-ray observations. Under the assumptions of pressure equilibrium between the cavity and the ICM and of adiabatic motion of the cavity, the total energy $E_{\rm cav}$ would correspond to the work necessary to displace the gas, hence:

$$E_{\rm cav} = E_{\rm int} + pV = \frac{\gamma}{\gamma - 1} pV \tag{1.27}$$

where $E_{\rm int}$ is the internal energy of the cavities, γ is the adiabatic index, which depends on the contents of the cavities ($\gamma = 4/3$ for relativistic plasma or $\gamma = 5/3$ for thermal plasma), p is the external pressure, which can be inferred with the X-ray spectral analysis, and V is the cavity volume, which can be assumed based on the morphology of the cavity.

To compute the cavity power $P_{\rm cav}$ the mechanical energy has to be divided by a characteristic time-scale, which can be buoyancy time, the crossing time given by the local speed of sound, or the time required to the gas to fill the displaced volume (e.g., Bîrzan et al., 2008). The three estimates, although they are all consistent within a factor ~ 2, provides estimate of the characteristic time of a few 10^7 yrs, thus resulting in a $P_{\rm cav} \simeq 10^{42-44}$ erg s^{-1} that is consistent with the cooling luminosity ($L_{\rm cool} \simeq 10^{43}$-$10^{44}$ erg s^{-1}). The study of the correlation between $P_{\rm cav}$ and $L_{\rm cool}$, observed in both clusters and groups (e.g., Bîrzan et al., 2008; O'Sullivan et al., 2011b; Hlavacek-Larrondo et al., 2015; Kolokythas et al., 2018), permitted to constrain the properties of the cavities and proved that their energy release is able to balance the cooling. Moreover, observing that in some clusters $P_{\rm cav}$ largely exceeds $L_{\rm cool}$ (e.g., Rafferty et al., 2006) suggested that the heating could take place in violent burst.

Having found that the two processes are "energetically consistent" naturally poses the question of how the energy can be channeled from the cavities to the ICM. Based on both observations and numerical simulations, the emerging picture is that the energy budget of the cavities is dissipated in several forms while they are arising in the gravitational well, such as turbulence produced during the motion of these structures (e.g., McNamara and Nulsen, 2007), and the non-thermal pressure provided by the cosmic rays, originally stored in the radio plasma within the cavity, which would be released when the radio bubble reach an equilibrium with the external ICM (e.g., Fujita and Ohira, 2013; Jacob and Pfrommer, 2017a; Jacob and Pfrommer, 2017b; Ehlert et al., 2018). Finally, part of the energy injected by the AGN would be channeled also in form of cocoon shocks with Mach number $\sim 1 - 2$, which arise from the same dramatic AGN outbursts that produces the cavities, and warm-up the ICM by releasing their kinetic energy (e.g., McNamara et al., 2000; Fabian et al., 2006).

The discovery of clusters hosting several systems of cavities (e.g., Fabian et al., 2006; Kokotanekov et al., 2018) suggested a cyclic nature of the AGN feedback. The

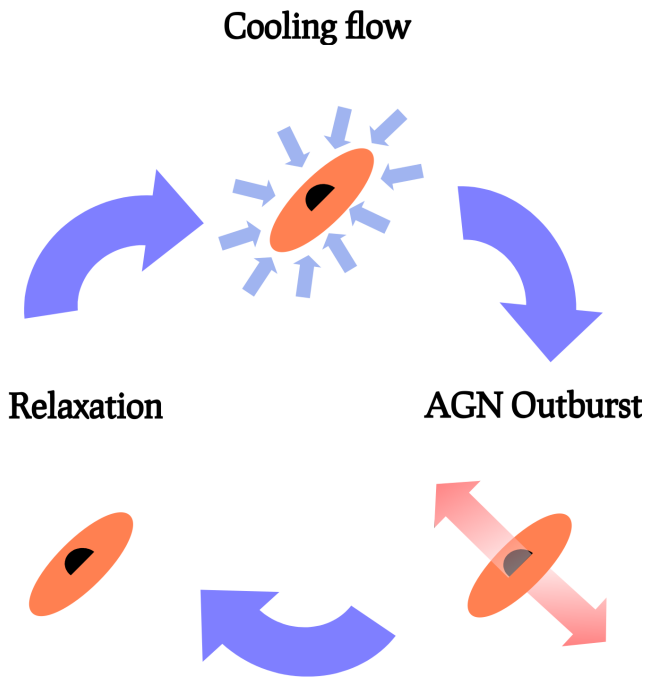

Figure 1.9: Sketch of the three phases of the self-regulated AGN feedback loop.

general picture envisions a "self-regulated AGN feedback loop" (Figure 1.9) structured in three phases (McNamara and Nulsen, 2012). While the cooling is unopposed, the mass flow deposits large amount of gas onto the central galaxy, which ends fueling the super massive black hole. As a result, the accretion initiates a phase of intense AGN activity that can result in the release of energy in the ICM. The AGN feedback can effectively balance the cooling, thus interrupting the mass inflow and, hence, the fueling of the AGN itself. Once the AGN activity phase ends because of the lack of fuel, the system reaches a relaxed phase in which both the cooling and the heating are quenched. However, if this relaxed phase persists, the cooling flow can start again, thus resuming the cycle. This cycle, which can both regulate the thermal balance of the ICM and induce the circulation of gas and metals on the scales of several hundreds of kpc (e.g., Liu et al., 2018, for recent results), represent an essential factor of the evolution of the cluster and the galaxies in it.

Nevertheless, the nature of the mechanism that convey the energy from the black hole to the ICM is complex and not yet fully understood. Great hopes in addressing these questions are placed in the advances that will be made possible with the incoming *Athena* telescope, whose large collection area and high energy resolution will allow to deeply investigate the micro-physics of the ICM, both in terms of thermal and dynamical properties, in the surroundings of the AGN (Croston et al., 2013).

1.3.3 Origin and results of the cool core sloshing

Despite their name, relaxed clusters are not completely idle, on the contrary they can be subject to minor, dynamical interactions that can drive kinetic energy in the gas at different scales. The most prominent example in the central regions is provided by the sloshing of the gas (Markevitch and Vikhlinin, 2007) and it can deeply affect both the ICM properties and the evolution of cluster galaxies. The sloshing of the cool core can be set in motion by infall of large dark matter sub-clumps following

minor mergers (e.g., ZuHone, Zavala, and Vogelsberger, 2019), or by ram-pressure slingshot following the passage of a sub-cluster with large impact parameter within a larger structure (e.g., Hallman and Markevitch, 2004), and it can persists for several Gyrs.

From the observational point of view, sloshing clusters are characterized by a striking, spiral pattern of density discontinuities in the ICM X-ray emission (Figure 1.10) which can extend from the inner regions (< 100 kpc) up to the virial radius of the cluster (e.g., Rossetti et al., 2013; Walker et al., 2020). This (spectacular) feature is produced by the oscillation of the dense structures, which generates contact discontinuities with the surrounding flows. The oscillation frequency, ω, can be estimated as:

$$\omega = \omega_k \sqrt{\frac{3}{5} \frac{d\ln(s)}{d\ln(r)}} \tag{1.28}$$

where $\omega_k = \sqrt{\sigma}/r$ is the Keplerian orbital frequency, r is the radius and s is the entropy index (Owers, Nulsen, and Couch, 2011).

The displaced gas, in result of the oscillating motion, acquires angular momentum and hence, instead of falling back radially, it forms a spiral. The contact discontinuities are called *cold fronts* and, on the contrary of shocks, are characterized by a pressure equilibrium between the two surfaces. Cold fronts have been widely observed in clusters (e.g., Ghizzardi, Rossetti, and Molendi, 2010; Botteon, Gastaldello, and Brunetti, 2018), thus providing evidence that minor dynamical events are common during the cluster life.

Cold fronts are remarkable probes of the ICM micro-physics (e.g., Zuhone and Roediger, 2016, for a review). The temperature jump across these fronts implies that either thermal conduction is intrinsically weak in galaxy clusters (e.g., ZuHone, Markevitch, and Brunetti, 2011), or the magnetic field is oriented parallel to the front surfaces, restricting conduction across the front (e.g., ZuHone et al., 2013a). Finally, the developing (or not) of Kelvin-Helmotz instabilites along the cold front permit to infer further constraints on the ICM viscosity and magnetic field (e.g., Walker et al., 2017).

The ICM sloshing can affect the evolution of relaxed clusters. It can have an important role in determining the thermal evolution of the cluster core. It brings the cold gas of the core into contact with hot gas, possibly facilitating a transfer of heat between these phases, either via mixing of the hot and cold gas or by heat conduction (ZuHone, Markevitch, and Johnson, 2010). This raises the possibility that sloshing may be partially responsible for balancing the cooling in the cores of galaxy clusters. Indeed numerical simulations proved that gas mixing and the conduction of heat between the hot and cold phases in the cluster core raises the temperature and the entropy of the core, and, in the absence of radiative cooling, could potentially eliminate the cool core entirely (e.g., ZuHone et al., 2013a). Moreover, by moving the central gas, the sloshing can spread the heavy elements from the center outwards, thus altering the metallicity gradients and, hence, the local radiative cooling efficiency (e.g., Sanders, Fabian, and Taylor, 2005; Fabian et al., 2006; Simionescu et al., 2010; Ghizzardi, De Grandi, and Molendi, 2014). Finally, the sloshing can affect both the cluster galaxies, by producing over-dense regions in which the stripping is more efficient, and the BCG, by altering the cooling flow onto it, i.e. the fueling of the

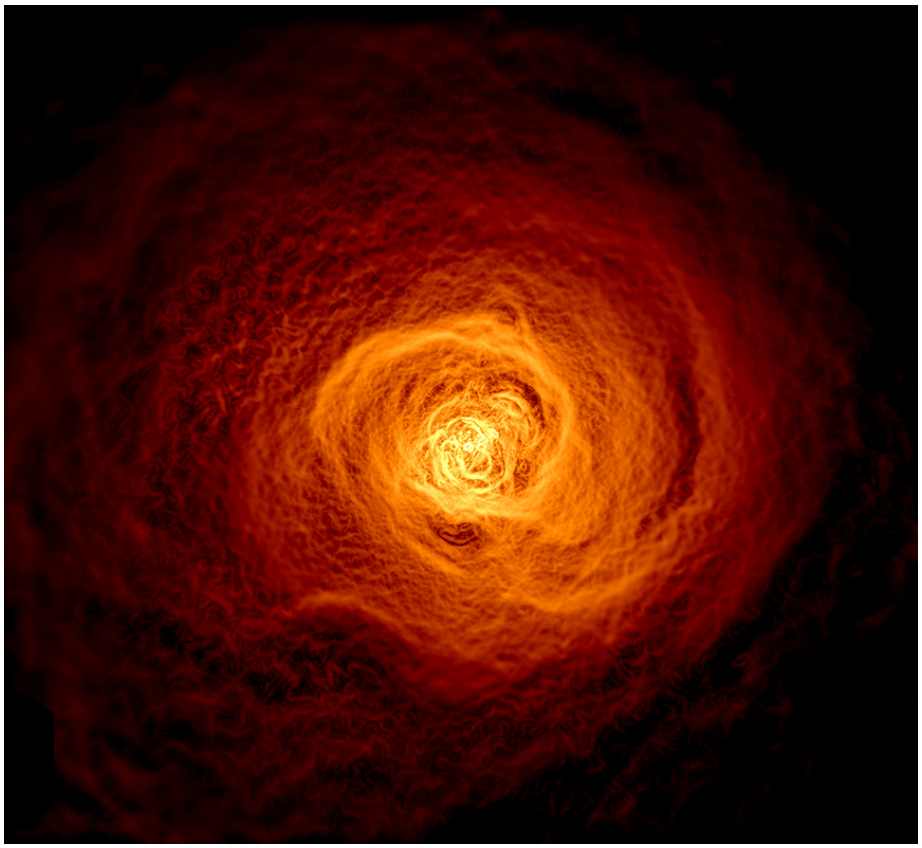

Figure 1.10: Image of the *Chandra* X-ray observation of the Perseus cluster filtered with the gaussian gradient magnitude method. The image reports the surface brightness gradients, hence highlighting the sloshing pattern in the cluster (Walker et al., 2017).

central AGN (Pasini et al., 2019, for a recent result).

1.3.4 Radio mini-halos

Massive, relaxed clusters often host diffuse radio emission with a steep ($\alpha < -1$) spectrum at their center, the so-called radio mini-halos (MH, classified for the first time in Feretti and Giovannini, 1996). In Figure 1.11 we report one of the first images of the MH in the Persues cluster, which is considered the archetype of this kind of sources. The radio emission, whose emissivity is generally higher than that of giant radio halos ($\sim$ 50 times, Cassano, Gitti, and Brunetti, 2008; Murgia et al., 2009), has been observed surrounding the central radio galaxy and extending generally up to $\sim$100-150 kpc (e.g., van Weeren et al., 2019, and the references therein). Recently, the discovery of very steep spectrum ($\alpha < -2$) emission on large scale ($\sim$ 500 kpc) around a number of MHs (Savini et al., 2018; Savini et al., 2019) suggested the possibility that low-energy CRe could be actually diffused on large scales also in relaxed cluster. At higher frequency, the radio emission is mostly confined within the cool cores of the clusters, thus outlining a connection between the non-thermal ICM components and the thermal plasma (e.g., Rizza et al., 2000; Gitti, Brunetti, and Setti, 2002; Mazzotta and Giacintucci, 2008; Giacintucci et al., 2014a). This intrinsic connection is supported by the correlations observed between global radio and X-ray luminosities (Bravi, Gitti, and Brunetti, 2016; Gitti et al., 2015; Gitti et al., 2018; Giacintucci et al., 2019; Richard-Laferrière et al., 2020). At the present time, we know 23

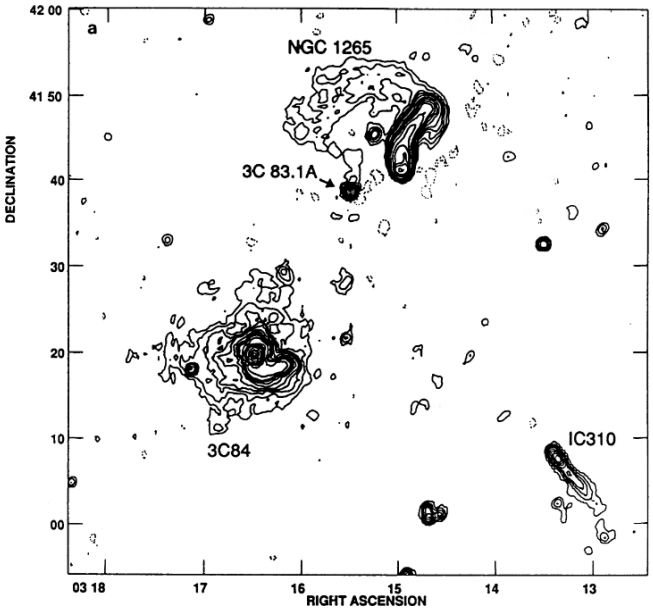

Figure 1.11: VLA image at 330 MHz of the Perseus cluster from Burns et al. (1992).

MHs, observed in almost all the massive cool-core clusters (the incidence is $\sim$ 80% for $M_{500} > 6 \cdot 10^{14}\ M_{\odot}$, Giacintucci et al., 2017), but current and future facilities, like Low-Frequency ARray (LOFAR) and the Square Kilometre Array (SKA), may have the potential to discover up to 10^4 new MHs (Gitti et al., 2018).

The origin of CRe in the MH volume is still debated. Two possible scenarios have been proposed. One is the leptonic scenario, where the CRe, possibly injected by the active galactic nucleus (AGN) of the central radio galaxy, are re-accelerated by ICM turbulence. In this scenario the turbulence in the cool cores may be injected by the dynamics of the gas cooling in the central region (e.g., Gitti, Brunetti, and Setti, 2002), by the AGN itself during so-called "radio-mode" AGN feedback (see Section 1.3.2), or by the gas dynamics driven by the cold fronts (e.g., ZuHone et al., 2013b).

The other scenario is the hadronic one, where CRe are produced by collisions between CRp and the thermal protons of the ICM (Pfrommer and Enßlin, 2004), with a cascade:

$$p + p \rightarrow \pi^0 + \pi^- + \pi^+ + \text{anything}$$

$$\pi^0 \rightarrow \gamma\gamma$$

$$\pi^{\pm} \rightarrow \mu^{\pm} + \nu_{\mu}(\bar{\nu}_{\mu})$$

$$\mu^{\pm} \rightarrow e^{\pm} + \bar{\nu}_{\mu}(\nu_{\mu}) + \nu_e(\bar{\nu}_e)$$

Once the CRp are released into the cluster, most likely by the central AGN (e.g., Blasi and Colafrancesco, 1999), they can diffuse on the scale of the observed radio emission due to their longer radiative times ($\tau_{\rm CRp} \simeq 10^{10}$ yr $>> \tau_{\rm CRe} \simeq 10^8$ years, see Section 1.2.4). The most striking feature of this scenario is the expected γ-ray diffuse emission that would be produced by the same collisions that inject the CRe.

This latter mechanism was originally proposed also to explain the Mpc-scale radio emission of giant radio halos (e.g., Blasi and Colafrancesco, 1999), but the lack of clear detection from the Fermi telescope ruled out this possibility (Brunetti, Zimmer, and Zandanel, 2017, and references therein). As we are going to discuss in Chapter 2, the γ-ray emission that would be generated in the cool cores falls below the current observational limits, thus leaving this possibility open for MH. On the other hand, hadronic models cannot explain the large scale emission with very steep spectrum that has been detected by LOFAR surrounding a number of MH (Savini et al., 2018; Savini et al., 2019). Turbulent re-acceleration models have predicted steep-spectrum, large-scale emission in minor mergers (e.g. Cassano et al., 2010; Brunetti and Jones, 2014). Therefore, if MH are hadronic, it is possible that in these cases we are looking at MH surrounded by a region where CRe are re-accelerated by the dissipation of energy injected by minor mergers.

Despite the debate on their origin, it is undeniable that the properties of MHs are rooted into those of the hosting cool core and the central AGN, thus they can be proxy of the internal physics of relaxed clusters. On the one hand, from the study of the continuum radio emission we can infer the properties of ICM magnetic field and cosmic rays, which locally affect the micro-physics and, thus, the thermal processes that regulate the thermal balance of the cool core (e.g., Fujita and Ohira, 2013; Jacob and Pfrommer, 2017a). At the same time, both the hadronic and leptonic processes show that their main "ingredients", i.e. streaming cosmic rays or ICM turbulence, can both explain the origin of the diffuse radio emission and, to a certain extent, the heating of the cool core (e.g., Jacob and Pfrommer, 2017b; Zhuravleva et al., 2014, respectively). Therefore, following the fascinating possibilities that MHs would be a probe of the process that balance the ICM cooling, great effort will be spent in the next years, thanks to present and incoming radio telescope such as the LOFAR and the SKA, to expand the current statistic of MH and push further these studies (Gitti et al., 2018).

◇ ◇ ◇

In this Thesis, unless stated differently, we adopted a ΛCDM cosmology with $H_0 = 70$ km s^{-1}Mpc^{-1}, $\Omega_M = 1 - \Omega_\Lambda = 0.3$. We define the radio spectrum $S \propto \nu^\alpha$ where S is the observed radio flux density at frequency ν. The values are reported with a 1σ confidence error.

Chapter 2

The connection between radio and X-ray emission in relaxed clusters

Based on Ignesti et al., 2020, A&A, 640, A37

2.1 Introduction

As discussed in Chapter 1.3.4, the two scenarios (leptonic or hadronic) proposed to explain the origin of diffuse radio emission share two common aspects: the possible role played by the AGN as the source of relativistic particles and the physical connection between the CRe and thermal plasma (as background medium for the turbulence or targets for CRp collisions). This connection is expected to induce a spatial correlation between the radio, I_R, and X-ray, I_X, surface brightness. In re-acceleration models the I_R-I_X correlation is sensitive to the way turbulence is generated in the thermal background plasma and relativistic particles are accelerated and transported in that turbulence. On the contrary, the correlation is particularly straightforward in the case of secondary models, where the thermal plasma, which generates the X-ray emission, also provides the targets for the inelastic collisions with the CRp that produce the secondary electrons emitting in the radio band. In this latter case, a super-linear scaling between radio and X-ray brightness is generally expected.

Radio and X-ray correlations can be studied through the point-to-point connection between radio and X-ray surface brightness. The importance of this correlation has been discussed in the case of giant radio halos (e.g., Govoni et al., 2001; Brunetti, 2004; Pfrommer, 2008; Donnert et al., 2010; Brunetti and Jones, 2014). For these sources, it is generally observed a sub-linear scaling between the two quantities, as $I_R \propto I_X^k$, with $k \leq 1$ (Govoni et al., 2001; Feretti et al., 2001; Giacintucci et al., 2005; Vacca et al., 2010; Hoang et al., 2019).

Similar considerations apply to the case of MHs, and thus following this idea, in this Chapter we explore, for the first time, the connection between I_R and I_X surface brightness for a sample of MHs, which we describe in the following section. Exploring these correlations potentially provides important information on the origin of these sources and their connection with the central AGN.

In this Chapter we adopted ΛCDM cosmology, with $H_0 = 73$ km s^{-1} Mpc^{-1}, $\Omega_m = 1 - \Omega_\Lambda = 0.27$, and we define the synchrotron spectrum as $S \propto \nu^{-\alpha}$.

Table 2.1: Physical properties of the clusters analyzed in this work.

Cluster name	RA_{J2000}	DEC_{J2000}	z	M_{500}	R_{500}	R_{MH}	$L_{X,R_{500}}$
2A0335+096	03 38 44.4	+09 56 34	0.035	$2.3^{+0.2}_{-0.3}$	0.92	70	4.4 ± 0.5
RBS 797	09 47 00.2	+76 23 44	0.345	$6.3^{+0.6}_{-0.7}$	1.16	120	41.9 ± 5.4
Abell 3444	10 23 54.8	-27 17 09	0.254	$7.6^{+0.5}_{-0.6}$	1.27	120	28.3 ± 4.0
MS 1455.0+2232	14 57 15.1	+22 20 34	0.258	$3.5^{+0.4}_{-0.4}$	0.98	120	21.1 ± 2.2
RXC J1504.1-0248	15 04 05.4	-02 47 54	0.215	$7.0^{+0.6}_{-0.6}$	0.98	140	68.4 ± 7.0
RX J1532.9+3021	15 32 53.8	+30 20 58	0.345	$4.7^{+0.6}_{-0.6}$	1.04	100	41.6 ± 4.5
RX J1720.1+2637	17 20 12.6	+26 37 23	0.164	$6.3^{+0.4}_{-0.4}$	1.24	140	17.2 ± 1.7

From left to right: Cluster name; J2000 hexadecimal coordinates; Redshift; Total mass and radius at a mean over-density of 500 with respect to the cosmological critical density at redshift z in units of 10^{14} $M_{\odot}$ and Mpc, respectively; Average radius of the diffuse emission in units of kpc defined as $R_{MH} = \sqrt{R_{max} \times R_{min}}$ where R_{max} and R_{min} are the maximum and minimum radius as derived from the 3σ iso-contour emission; Bolometric X-ray luminosity measured within R_{500} expressed in units of 10^{44} erg s^{-1}. The values are taken from Giacintucci et al. (2017) and references therein.

2.2 Cluster sample

We selected a sample of targets based solely on the quality of the radio and X-ray data. In order to reliably evaluate the I_R-I_X correlation, we searched for relaxed clusters with deep and well-resolved radio images in the literature, and deep archival *Chandra* observations. The sample is composed of seven MHs, we report the physical properties in Table 2.1, and the details of the radio images and archival X-ray observations in Table 2.2. Below we present a brief morphological description of each cluster of the sample and of the previous literature results:

- ◇ *2A0335+096:* The MH was first imaged at 1.4 GHz and 5.5 GHz by Sarazin, Baum, and O'Dea (1995). The MH morphology in our images, obtained from the same radio data (see Giacintucci et al., 2019, for details), is consistent with the structure previously mapped. The central radio galaxy is a core-dominated, double-lobe source and another patch of extended emission, which is interpreted as a fossil lobe from an older AGN outburst, is detected at $\sim 25''$($\sim$18 kpc) from the cluster center. The MH surrounds this structure extending for $\sim 100''$ ($\sim$ 70 kpc). In the X-ray band we observe two cavities, which coincide with the radio lobes, and a cold front located at $\sim$40 kpc from the center. The region inside the cold front shows a number of small, dense gas blobs that may be the shred of a cooling core disturbed by either Kelvin-Helmotz instabilities or intermittent AGN activity. All of these properties relate to processes that may act to disrupt or destroy any cooling flow (Mazzotta, Edge, and Markevitch, 2003; Sanders, Fabian, and Taylor, 2009). The cluster hosts a head-tail radio galaxy whose radio tail is close to the MH with a projected distance of $\sim$ 90 kpc. This suggests the possibility that the close-by passage of the galaxy may have played a role in the injection of both CRe and turbulence in the ICM.

◇ *RBS 797:* This cluster shows radio emission on three different scales. VLA observations at 4.8 GHz at high resolutions ($\sim 0.4''$) revealed the presence of a pair of jets connected to the central galaxy, oriented in the north-south direction and extended for ∼15 kpc. On the larger scale, the radio emission observed at 1.4 GHz coincides with a striking system of cavities extending for ∼26 kpc in the east-west direction observed by *Chandra* in the X-ray band. The misalignment of the cavities with respect to the inner jet system suggests that the central AGN had different cycles of activity with the jets oriented in different directions (Gitti, Feretti, and Schindler, 2006; Gitti et al., 2013). Finally, the cluster shows diffuse radio emission with a roughly spherical morphology and a radius of ∼100 kpc (Gitti, Feretti, and Schindler, 2006; Doria et al., 2012). We excluded the region of the cavities from the analysis of the MH.

◇ *Abell 3444:* The MH was reported first by Venturi et al. (2007) and then confirmed in Giacintucci et al. (2019). The BCG at the center of the low-entropy cool core does not show jets (Giacintucci et al., in prep.). The morphology of the radio emission seems orthogonal to the X-ray emission, with the I_R decreasing rapidly eastward.

◇ *MS 1455.0+2232:* The MH is composed of a central region and a tail located at the southeast. The northern part of the MH is delimited by a cold front. The cluster, along with RX J1720.1+2637, has been reported by Mazzotta and Giacintucci (2008) as a first evidence of the connection between cold fronts and MHs.

◇ *RXC J1504.1-0248:* This cluster is characterized by an extreme X-ray luminosity ($L_{bol} = 4.3 \cdot 10^{45}\ h_{70}^{-1}$ erg s^{-1}), of which more the 70% is radiated inside the cool core region. The exceptional X-ray luminosity suggests that we are observing AGN-ICM interactions taking place in extreme conditions. The MH surrounds the BCG, extending for ∼140 kpc, and it has a spectral index of $\alpha = 1.2$. The cluster also shows a pair of cold fronts located inside the radio emitting region that highlight the presence of ongoing sloshing processes (Giacintucci et al., 2011).

◇ *RX J1532.9+3021:* The *Chandra* observation shows a pair of cavities associated with the BCG and a cold front located at ∼65 kpc from the center, partially associated with one of the cavities (Hlavacek-Larrondo et al., 2013). The MH appears more extended toward the northeast, with a radius of $\sim$ 180 kpc, following the morphology of the X-ray surface brightness. Giacintucci et al. (2014b) estimated the total spectral index of the diffuse radio emission $\alpha = 1.2$ by combining observations at 325 MHz, 610 MHz, 1.4 GHz, and 4.9 GHz.

◇ *RX J1720.1+2637*: This cluster was the first relaxed system in which sloshing cold fronts were revealed by *Chandra* (Mazzotta et al., 2001) as well as one of the first two clusters in which a connection between MH and cold fronts was reported (Mazzotta and Giacintucci, 2008). The MH consists of a bright central region that contains most of its flux density, and a fainter, arc-shaped tail elongated for ∼230 kpc, and it is delimited by the cold front. Giacintucci et al. (2014a) combined several radio observations spanning from 0.317 to 8.44 GHz to obtain a detailed spectral index map of the MH. They observed that the spectral index varies within the MH. The central region shows $\alpha \simeq 1$, whereas the tail shows $\alpha \simeq$2-2.5. ZuHone et al. (2015) demonstrated via numerical

simulations that the CRe in the tail could be efficiently re-accelerated by the turbulence injected at the edge of the cold front.

2.3 Data analysis

2.3.1 Data preparation

The radio images used in this work have been presented in literature (see list of references in Table 2.2). The images were obtained from high-sensitivity, pointed radio observations with the Very Large Array (VLA) at 1.4 and 5.5 GHz and the Giant Metrewave Radio Telescope (GMRT) at 0.3 and 0.6 GHz. All observations used to produce our MH images have a good sampling of the *uv* plane at short antenna spacings, which ensures the detection of large-scale emission (above the image sensitivity) on scales significantly larger than the measured extent of the MH (for details see Giacintucci et al., 2017, their Table 10 and Figure 12). To enhance the diffuse emission, a weighting scheme close to natural weighting was typically adopted during the data imaging. Furthermore, the MH sizes do not appear to correlate with the signal-to-noise ratio of the radio images (Giacintucci et al., 2017, Section B), thus ensuring that the measured extent is not biased by the image sensitivity. Besides a good *uv* coverage at short spacings, the observations also have a sufficiently high resolution to disentangle the central radio galaxy from the surrounding diffuse emission. Higher resolution images, showing the smaller scale emission associated with the central galaxy, are also presented in the previous works. Nevertheless, to avoid any possible contamination of the radio galaxy emission into the diffuse MH, we masked the central region of each MH using an appropriate mask with a size larger than the radio beam (see Section 2.3.2).

Concerning the X-ray images, we retrieved the *Chandra* observations of the clusters from the archive[1] to produce the X-ray images and to derive the physical quantities of the thermal ICM. When it was possible, we collected multiple observations to improve the sensitivity of our analysis. The datasets were reprocessed with CIAO v.4.9 and corrected for known time-dependent gain and charge transfer inefficiency problems following techniques similar to those described in the *Chandra* analysis threads[2]. To filter out strong background flares, we also applied screening of the event files. We used CALDB v.4.7.8 blank-sky background files normalized to the count rate of the source image in the 9-12 keV band to produce the appropriate background image for each observation. We produced the exposure-corrected, background-subtracted brightness maps in the energy range 0.5-2.0 keV. We used this energy band because it is where the thermal ICM emission and *Chandra* sensitivity are at their maximum, thus it assures an optimal count statistic for the analysis using our data. We masked the X-ray point sources embedded in the cluster emission. The final X-ray images with the radio contours and the masks are presented in Section 2.3.2.

2.3.2 Monte Carlo point-to-point analysis

Govoni et al. (2001) performed a point-to-point analysis of the radio and X-ray emission for a sample of clusters hosting giant radio halos. In their work they adopted a

[1] http://cxc.harvard.edu/cda/
[2] http://cxc.harvard.edu/ciao/threads/index.html

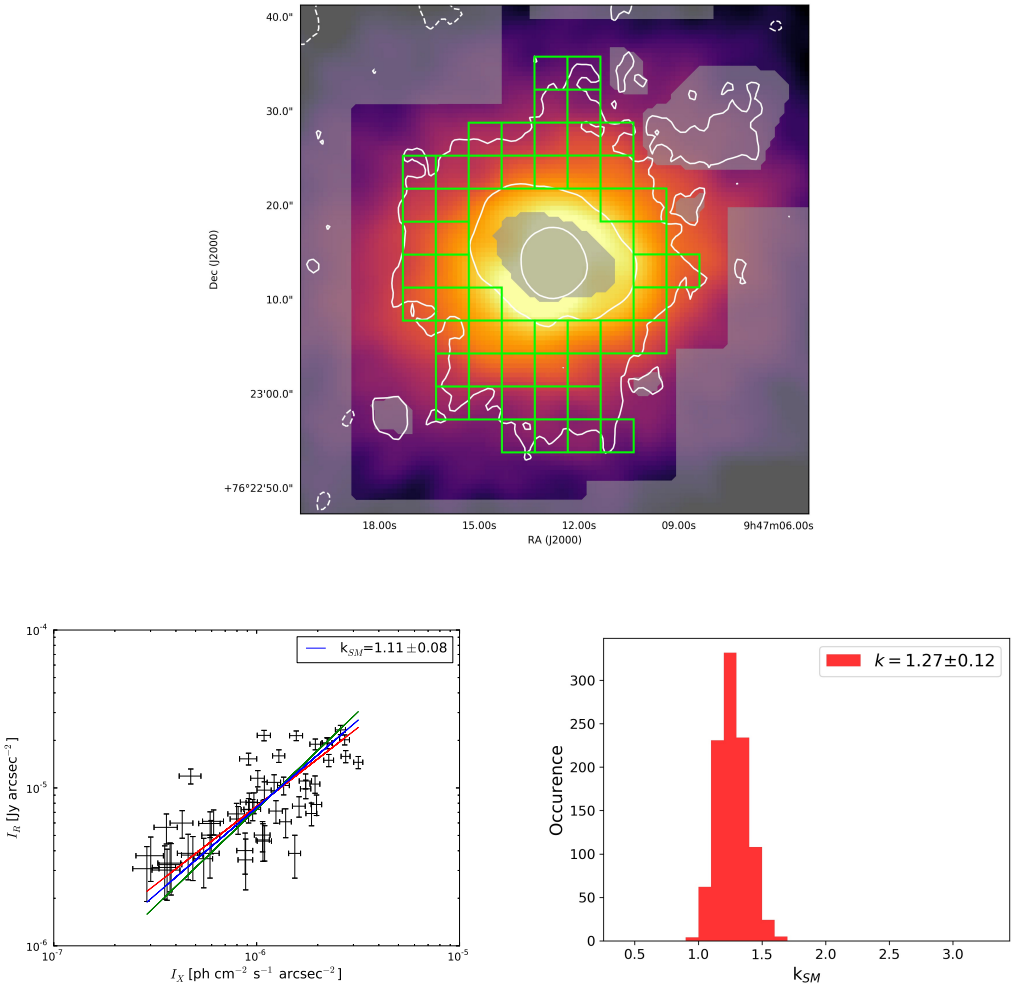

Figure 2.1: Top: *Chandra* image of the RBS 797 cluster with the contours at the -3, 3, 24, 96σ levels of the radio emission at 1.4 GHz (Doria et al., 2012). The resolution of the radio maps is 3″x3″ and 1σ = 10 μJy beam^{-1}. Shown in green is a random mesh that samples the emission above the 3σ level with cells of 4″x4″ size. The central cavities and the external sources were masked (gray) and, therefore they were excluded from the sampling. Bottom-left: I_R vs. I_X plot where each point corresponds to a cell of the sampling mesh. The red and green lines are, respectively, the best-fit power law estimated for (I_R | I_X) and (I_X | I_R). The blue line is their bisector power law. The value of k_{SM} is reported in the legend ; Bottom-right: Histogram of the distribution of values of k_{SM} produced by the Monte Carlo point-to-point analysis with 1000 cycles. The best estimate of k is reported in the legend with the associated 1σ error.

Table 2.2: Archival radio and X-ray observations used in this work.

Radio observations				
Cluster name	Reference	Frequency [GHz]	Beam [arcsec×arcsec]	RMS [μJy beam^{-1}]
2A0335+096	1	1.4	23.0×22.0	56
		5.5	18.5×16.0	16
RBS 797	2	1.4	3.0×3.0	10
Abell 3444	1	0.6	8.0×8.0	58
		1.4	8.0×8.0	35
MS 1455.0+2232	3	0.6	6.0×5.0	50
RXC J1504.1-0248	4	0.3	11.3×10.4	75
RX J1532.9+3021	5	1.4	3.4×2.9	15
RX J1720.1+2637	6	0.6	7.8×6.1	30
X-ray observations				
Cluster name		Chandra Obs ID		Total exposure time [ks]
2A0335+096		919, 7939, 9792		106
RBS 797		7902		40
Abell 3444		9400		37
MS 1455.0+2232		4192		92
RXC J1504.1-0248		17197, 17669, 17670		109
RX J1532.9+3021		14009		88
RX J1720.1+2637		3224, 4361		50

References of the radio maps: (1) Giacintucci et al. (2019) (2) Doria et al. (2012) and Gitti et al. (2013) (3) Mazzotta and Giacintucci (2008) (4) Giacintucci et al. (2011) (5) Giacintucci et al. (2014b) (6) Giacintucci et al. (2014a)

single grid of cells to sample the diffuse radio emission. Here we extend the single-mesh point-to-point (SMptp) analysis introduced in Govoni et al. (2001). The case of MHs is more difficult than that of giant, well-resolved, radio halos, because of the small number of independent beams sampling the surface brightness. Furthermore, the sampling scale that allows the maximum number of cells is the angular resolution of the image itself. However, using grids with cells as small as the beam of the image could generate biases in the analysis of the spatial correlations, because contiguous cells are not statistically independent.

For these reasons, we developed a new method to carry out spatial correlation analysis of poorly-resolved sources, the Monte Carlo point-to-point (MCptp) analysis, which basically is the combination of several cycles of SMptp analysis based on a randomly generated grids tailored to the diffuse radio emission. By fitting the values of I_R and I_X^k as $I_R \propto I_X^k$, each cycle produced a different estimate of the k index (k_{SM}). Eventually, these measurements are combined to obtain a more reliable estimate of the real scaling. For this reason, we developed a Python script, PT-REX, to perform the SMptp and the MCptp analysis. We report the details of the code in Appendix A, where we also discuss its usage and limitations. For this work, we combined 1000 SMptp iterations for each cluster, where we sampled the radio emission above the

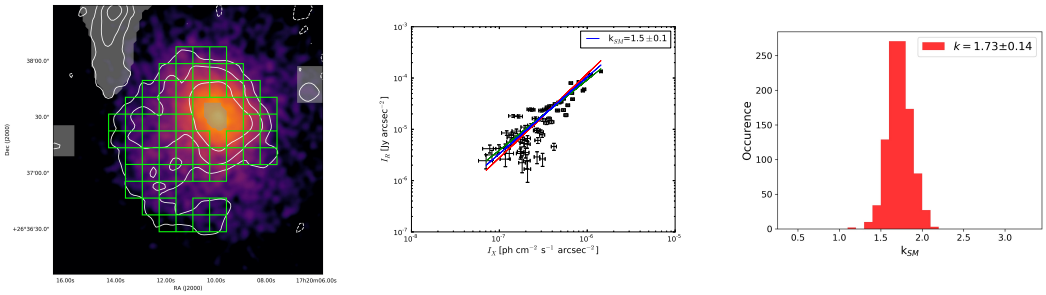

Figure 2.2: RXJ1720.1+2637 .

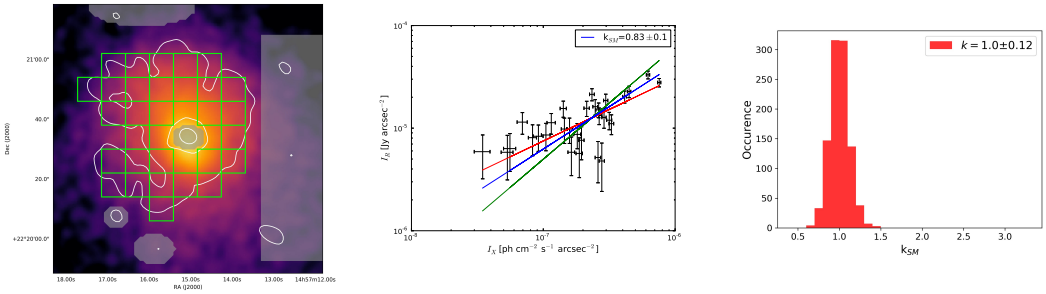

Figure 2.3: MS 1455.0+2232 .

3σ level, and we used the BCES bisector fit (Akritas and Bershady, 1996) to estimate the correlation.

Sampling of the diffuse radio emission

In Figures 2.2-2.7 we report for each cluster of the sample (with the exception of RBS 797, which is reported in Figure 2.1) the contours of the radio emission and the mask used for the analysis overlapped on the X-ray image. We also present a random mesh generated during the MCptp analysis, the corresponding SMptp analysis, and the distribution of k produced by the MCptp analysis. The resolution and the noise of each map are reported in Table 2.2. For each object we report:

- ◇ Left: X-ray surface brightness map smoothed with a 1.5″ gaussian, with the contours of the radio map at the -3, 3, 24, 96σ levels (white), the mask used in the analysis (gray), and a random sampling mash (green). The cell size matches the angular resolution of the radio image;
- ◇ Center: I_R versus I_X obtained from the presented mesh. The red, green, and blue lines are, respectively, the best-fit slopes obtained with the BCES for (I_X | I_R), (I_R | I_X), and the bisector. The estimated value of k_{SM} is reported in the label;
- ◇ Right: Distribution of indexes k produced after 1000 iterations of MCptp analysis.

Contaminations of the central source in SMptp analysis

In order to test that the adopted masking is sufficient to contain the contamination of the central radio source in our analysis, we present here a comparison of the SMptp

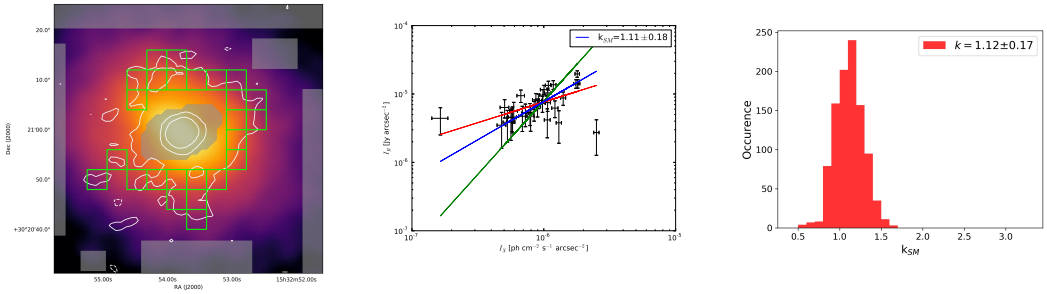

Figure 2.4: RX J1532.9+3021 .

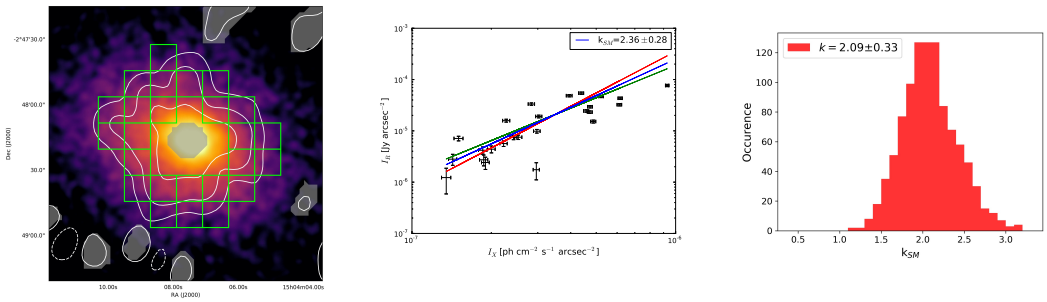

Figure 2.5: RXC J1504.1-0248 .

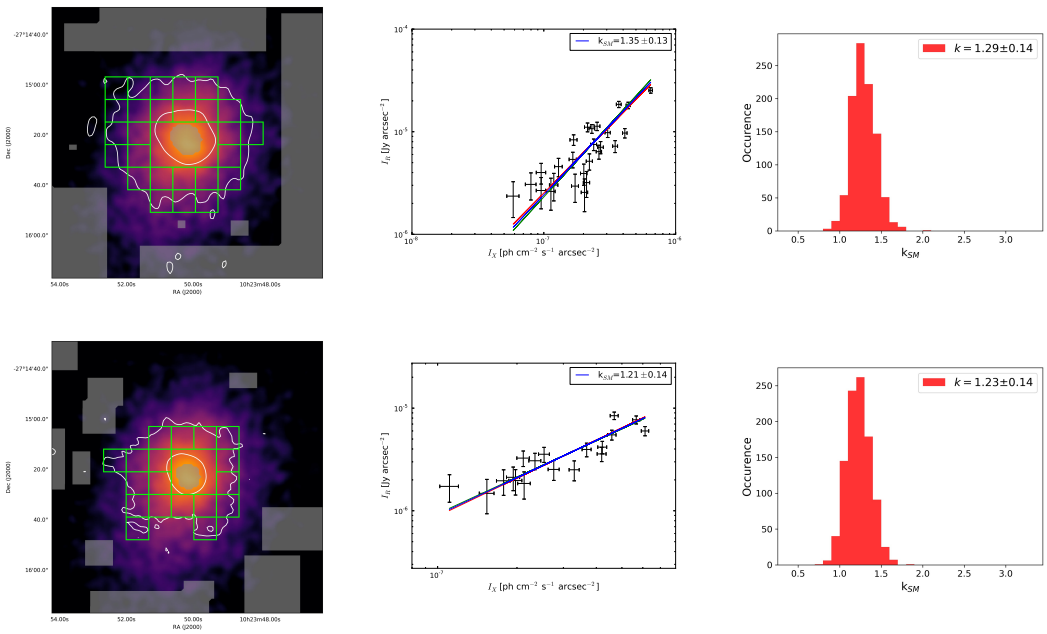

Figure 2.6: Abell 3444 at 610 MHz (top) and 1.4 GHz (bottom) .

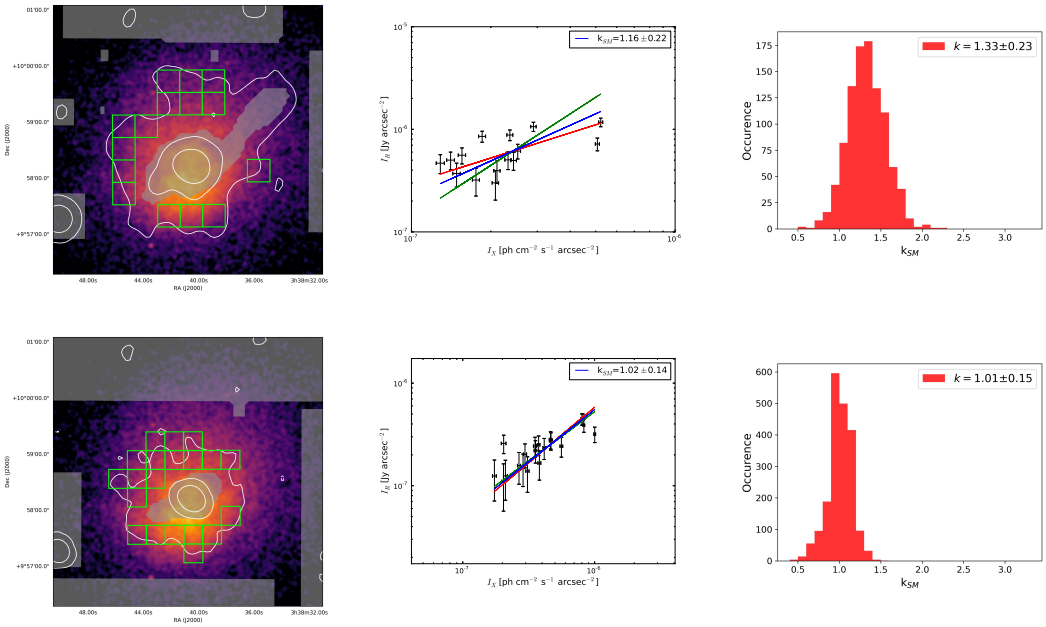

Figure 2.7: 2A03335+096 at 1.4 GHz (top) and 5.5 GHz (bottom) .

analysis for two of our objects after the subtraction of the central source, namely clusters RX J1532.9+3021 and RXC J1504.1-0248. We selected RXC J1504.1-0248 because it hosts the most luminous radio sources of our sample, therefore it should be the most sensitive to possible contaminations. In the two observations, the central sources were first imaged by selecting only baselines longer than, respectively, 10 and 15 kλ. The clean components were then subtracted from the uv-data to obtain images of the diffuse emission alone.

In Figure 2.8 we present the images before and after the subtraction with the same color-scale and surface brightness levels and the same resolution reported in Table 2.2, and the corresponding SMptp analysis performed on the subtracted images by using the same grids presented in Section 2.3.2. We found that, for each cluster, the two estimates of k obtained with the two different approaches are consistent within the errors. Therefore, for the aims of this work the central source can be masked instead of subtracted.

2.4 Results

We performed the MCptp analysis with 1000 cycles on each MH of the sample. For each cluster, we set the size of the cells to match the resolution of the radio map and we set the I_R minimum threshold for the brightness measured in each cell (flux/cell area) to 3σ. We excluded the region of the radio-filled cavities from the analysis for 2A0335+096, RBS 797 and RX J1532.9+3021.

We found clear evidence of a spatial correlation between the radio and X-ray emission. To further corroborate this result, we ran the Spearman test for each cluster, finding statistical dependence $\rho_s > 0.6$ and two-sided significance levels of deviation from zero $P_c < 2 \cdot 10^{-2}$. We also tested if the sampling size may affect the results of the MCptp. We tried to vary the size of the cells from the $1\times$ beam size

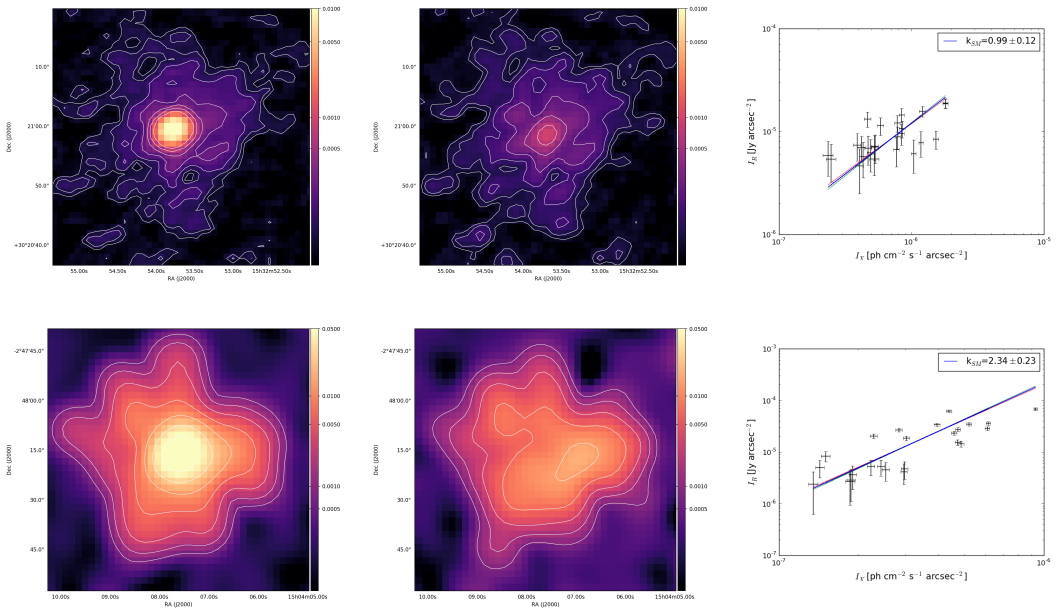

Figure 2.8: Top: RX J1532.9+3021, before (left) and after the subtractions (center). The contours are at 2, 4, 8, 16, 32, and 64 × 22 μJy beam^{-1}. The plot (right) is the result of the SMptp analysis performed on the subtracted image with the same grid presented in Section 2.3.2; Bottom: RXC J1504.1-0248, before (left) and after the subtractions (center). The contours are at 2, 4, 8, 16, 32, and 64 × 0.9 mJy beam^{-1}. The plot (right) is the result of the SMptp analysis performed on the subtracted image with the same grid presented in Section 2.3.2.

Table 2.3: Results of the MCptp analysis.

Cluster name	k
2A035+096 [1.4 GHz]	1.33 ± 0.23
2A035+096 [5.5 GHz]	1.01 ± 0.15
RBS 797	1.27 ± 0.12
Abell 3444 [0.6 GHz]	1.29 ± 0.14
Abell 3444 [1.4 GHz]	1.23 ± 0.14
MS 1455.0+2232	1.00 ± 0.12
RXC J1504.1-0248	2.09 ± 0.33
RX J1532.9+3021	1.12 ± 0.17
RX J1720.1+2637	1.73 ± 0.14

to 1.5×beam size, finding that the increment of the cell size does not produce significant differences in the results. For the whole sample we estimate k$\geq$ 1 and for the two cases with radio observations at two frequencies we do not find a significant variation of k with frequency (Table 2.3).

2.4.1 Mini vs Giant halos

We note that the values of k we find for MHs are, generally, larger than 1. This is interesting because it is different from the sub-linear or linear scalings ($k \leq 1$) that are reported in the literature for giant radio halos (Figure 2.9, where we report the results presented in Govoni et al., 2001; Feretti et al., 2001; Giacintucci et al., 2005; Vacca et al., 2010; Hoang et al., 2019; Xie et al., 2020; Botteon et al., 2020; Rajpurohit

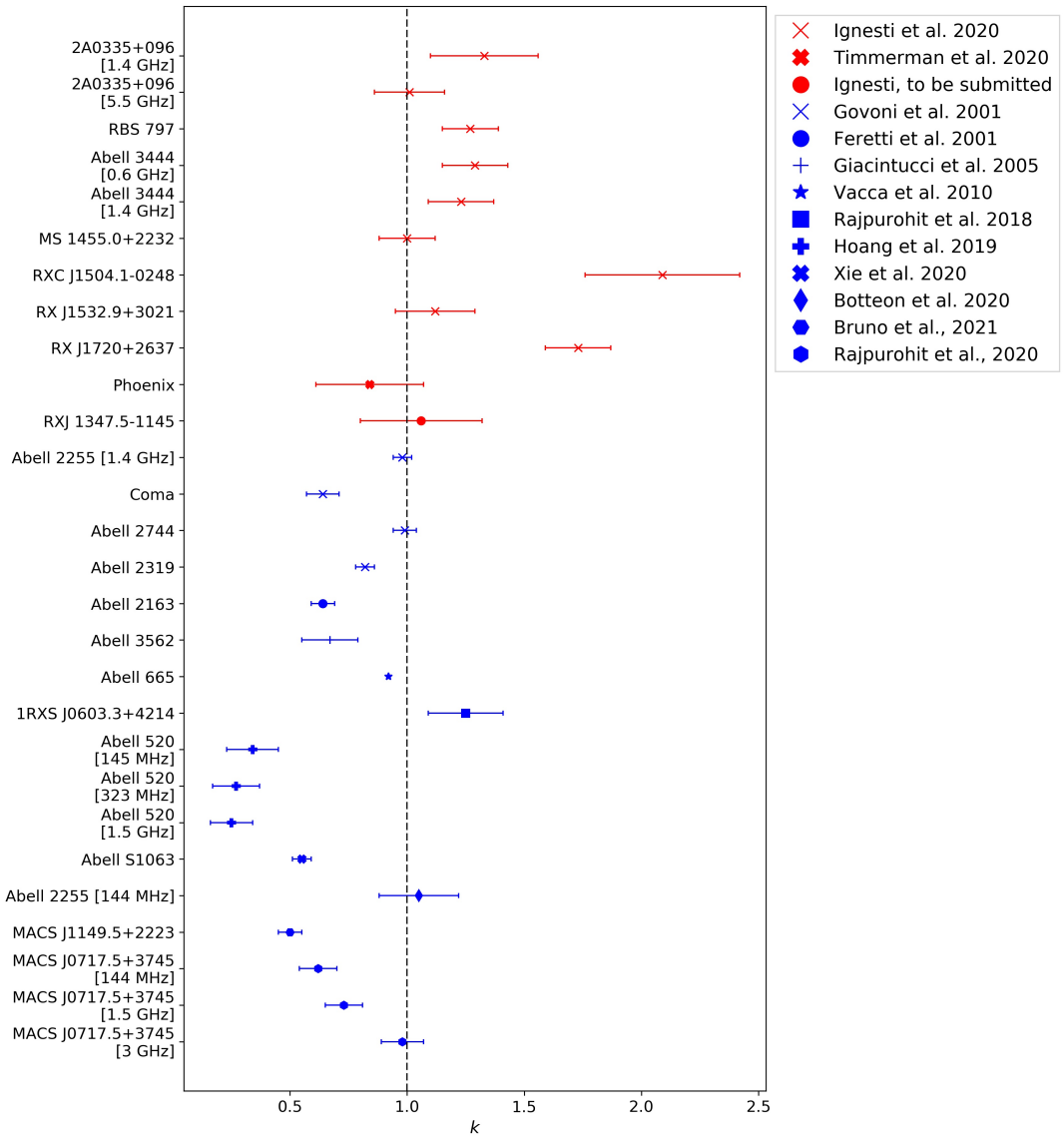

Figure 2.9: Distribution of index k for MH (red) and giant halos (blue) reported in literature. The horizontal, dashed line points out the $k = 1$ threshold.

et al., 2020; Bruno et al., 2021).[3] We observe that the medians of the two distribution are only marginally consistent, with $k = 1.27 \pm 0.34$ for MH and $k = 0.74 \pm 0.28$ for giant halos.

The slope of this spatial correlations basically describes the distribution of magnetic field and CRe in the thermal ICM, thus it may suggest an intrinsic difference in the origin and dynamics of the CRs , or a different entanglement of magnetic field and CRs, between relaxed and perturbed clusters. Specifically, the super-linear correlation observed in MH indicates that the distribution of CRe is peaked at the center of these clusters, thus suggesting a central origin of these particles. On the contrary, the sub-linear scaling observed in giant halos may indicates that the CRe in these clusters have diffused on scales larger than these of the thermal plasma. A fascinating outcome of this results would be a new criteria to discriminate between

[3]The only exception is 1RXS J0603.3+4214 (Rajpurohit et al., 2018).

the two classes of radio sources. However, a re-analysis of the cases of giant radio halos adopting our procedure is required for a more quantitative statement.

2.5 Implications for hadronic models

The study of radio and X-ray brightness distribution provides important information on the origin of diffuse radio sources and on the model parameters (e.g., Govoni et al., 2001; Brunetti, 2004; Pfrommer, 2008; Brunetti and Jones, 2014). In this work we focus on the hadronic model (See Chapter 1.3.4). The super-linear scaling between I_R and I_X for MHs suggests that the number density of emitting electrons rapidly declines from the center to the external regions. One possibility is that CRp propagate from the central AGN and generate secondary particles which emit the observed radio emission. As we will show in the following, in this scenario the observed radio and X-ray spatial correlation can constrain the model parameters, including the CRp luminosity of the AGN and the magnetic fields in the MH volume. We note, however, that steep I_R profiles can also be explained by pure leptonic models (e.g., Gitti, Brunetti, and Setti, 2002, for the MH in the Perseus cluster), which are not analyzed in this work.

2.5.1 Model framework

In the context of a pure hadronic scenario, we assume the central AGN as the primary source of CRp, which are injected with a rate of

$$Q(p) = Q_0 p^{-\delta}, \tag{2.1}$$

where p is the proton momentum for which we assumed a power-law distribution in momentum as typically assumed for CR sources in the ICM (Brunetti and Jones, 2014, for a theoretical discussion).

We assume a diffusive propagation of CR on scales much larger than the coherent scale of the magnetic field in the ICM, ($>>$10 kpc, e.g., Brunetti and Jones, 2014). In this case, the time required for a particle to diffuse up to the observed MH radius, R_{MH}, is $\tau = R_{MH}^2/4D_0$, where D_0 is the spatial diffusion coefficient. In this work we assumed a diffusion coefficient D_0 that does not depend on CRp energy. The resulting spectrum of CRp as a function of momentum, distance, and time is:

$$N_p(p, r, t) = \frac{1}{2\pi^{3/2} r} \frac{Q(p)}{D_0} \int_{r/r_{max}}^{\infty} e^{-y^2} dy, \tag{2.2}$$

where r is the distance from the source and $r_{max} = \sqrt{4D_0 t}$ is the distance reached by CRp in an interval of time t (e.g., Blasi and Colafrancesco, 1999). In this work we assume the simplified case where stationary conditions for CRp distribution are established. These conditions are generated by the interplay of diffusion and injection from the central AGN and are valid under the following assumptions:

- ◇ CRp diffuse on a MH scale on a timescale that is considerably smaller than the timescale of the energy losses of CRp with energy $\sim$ 100 GeV ($\sim 10^{10}$ yr, e.g., Brunetti and Jones, 2014); this condition selects a minimum value of the spatial diffusion coefficient (see Section 2.5.2 for details).
- ◇ The CRp injection rate from the AGN, L_{CRp}, is fairly constant when averaged and sampled on a sufficiently long timescale (smaller than the diffusion time)

of about 100 Myr or longer. We note that this also includes the possibility of an AGN duty-cycle, provided that its timescale is considerably smaller than the diffusion time.

Assuming stationary conditions, Eq. 2.2 gives the stationary solution

$$N_p(p,r) = \frac{1}{4\pi r}\frac{Q(p)}{D_0}. \tag{2.3}$$

While they are diffusing over the cluster volume, CRp with kinetic energy above 300 MeV (e.g., Brunetti, Zimmer, and Zandanel, 2017) interact with the ICM thermal protons in the cool core, for which we assumed a β-model distribution described in Chapter 1.2.2:

$$n_{\rm th}(r) = n_0 \left[1 + \left(\frac{r}{r_{\rm c}}\right)^2\right]^{-\frac{3}{2}\beta}, \tag{2.4}$$

where n_0 is the central proton density, $r_{\rm c}$ is the core radius, and β describes the ratio between thermal and gravitational energy of the plasma (e.g., Cavaliere and Fusco-Femiano, 1976).

As a result of these interactions, secondary particles, that is, π^0, positrons, and electrons, are continuously injected into the cluster volume (e.g., Blasi and Colafrancesco, 1999; Pfrommer and Enßlin, 2004; Brunetti and Blasi, 2005). We follow the procedures in Brunetti, Zimmer, and Zandanel (2017, their Section 3.4) to calculate the injection spectrum of secondary electrons and positrons, $Q_e^{\pm}(p,t)$, and calculate the spectrum of electrons and positrons, $N_e^{\pm}(p,t)$, assuming the stationary conditions:

$$N_e^{\pm}(p,t) = \frac{1}{\sum_{\rm rad,\,i}\left|\frac{{\rm d}p}{{\rm d}t}\right|}\int_p Q_e^{\pm}(p,t)\,p\,dt, \tag{2.5}$$

where $\left|{\rm d}p/{\rm d}t\right|_{\rm rad,\,i}$ are the radiative and Coulomb losses, and:

$$\begin{aligned} Q_e^{\pm}(p,t) =& \frac{8\beta'_\mu m_\pi^2 n_{\rm th} c^2}{m_\pi^2 - m_\mu^2}\int_{E_{\rm min}}\int_{p_*}\frac{{\rm d}E_\pi {\rm d}p}{E_\pi \bar{\beta}_\mu}\beta_p N_p(p,t) \\ &\times \frac{{\rm d}\sigma^{\pm,0}}{{\rm d}E}\left(E_\pi, E_p\right) F_e\left(E_e, E_\pi\right) \end{aligned} \tag{2.6}$$

where $\bar{\beta}_\mu = \sqrt{1 - m_\mu^2/\bar{E}_\mu^2}$, $\bar{E}_\mu = 1/2E_\pi(m_\pi^2 - m_\mu^2)/(\beta'_\mu m_\pi^2)$, $\beta'_\mu = 0.2714$, and $d\sigma^{\pm,0}/dE$ is the differential inclusive cross-section for the production of charged and neutral pions (we assume the cross-section in Brunetti, Zimmer, and Zandanel, 2017). $F_e\left(E_e, E_\pi\right)$ is given in Brunetti and Blasi (2005):

$$\begin{aligned} &F_e(E_e,E_\pi) = \frac{5}{12} - \frac{3}{4}\lambda_\pi^2 + \frac{1}{3}\lambda_\pi^3 - \frac{P_\pi}{2\beta_\pi}\left[\frac{1}{6} - \left(\beta_\pi + \frac{1}{2}\right)\lambda_\pi^2 + \left(\beta_\pi + \frac{1}{3}\right)\lambda_\pi^3\right] \\ &\text{for } \frac{\gamma_\pi}{c}(1+\beta_\pi)^2 > \frac{m_\pi^2 + m_\mu^2}{2m_\pi E_e} \end{aligned} \tag{2.7}$$

and:

$$F_e(E_e, E_\pi) = \frac{\lambda_\pi^2 \beta_\pi}{(1-\beta_\pi)^2}\left[3 - \frac{2}{3}\lambda_\pi\left(\frac{3+\beta_\pi^2}{1-\beta_\pi}\right)\right] - \frac{P_\pi}{1-\beta_\pi}\left\{\lambda_\pi^2(1+\beta_\pi)\right.$$
$$\left. - \frac{2\lambda_\pi^2}{1-\beta_\pi}\left[\frac{1}{2} + \lambda_\pi(1+\beta_\pi)\right] + \frac{2\lambda_\pi^3(3+\beta_\pi^2)}{3(1-\beta_\pi)^2}\right\} \tag{2.8}$$
$$\text{for } \frac{\gamma_\pi}{c}(1+\beta_\pi)^2 \leq \frac{m_\pi^2 + m_\mu^2}{2m_\pi E_e}$$

where $\lambda_\pi = 2m_\pi^2 E_e/(m_\pi^2 + m_\mu^2)E_\pi$, and:

$$P_\pi = -\frac{1}{\beta_\pi}\frac{m_\pi^4}{m_\pi^4 - m_\mu^4}\left\{4 - \left[1 + \left(\frac{m_\mu}{m_\pi}\right)^2\right]^2\right\}. \tag{2.9}$$

The secondary CRe injected into the ICM magnetic field, $B(r)$, can generate, in turn, synchrotron radio emission with an emissivity:

$$\begin{aligned} j_R(\nu, r) &= \sqrt{3}\frac{e^3}{m_e c^2}\int_0^{\pi/2}\sin^2\theta \mathrm{d}\theta \int N_e^{\pm}(p) F\left(\frac{\nu}{\nu_c}\right)\mathrm{d}p \\ &\propto N_p(p,r) n_{\rm th}(r)\frac{B(r)^{1+\alpha}}{B(r)^2 + B_{\rm CMB}^2}\nu^{-\alpha} \\ &\propto \frac{1}{4\pi r}\frac{Q(p)}{D_0} n_{\rm th}(r)\frac{B(r)^{1+\alpha}}{B(r)^2 + B_{\rm CMB}^2}\nu^{-\alpha} \end{aligned} \quad , \tag{2.10}$$

where $F\left(\frac{\nu}{\nu_c}\right)$ is the synchrotron kernel (e.g., Rybicki and Lightman, 1979), $B_{\rm CMB} = 3.25(1+z)^2$ μG is the cosmic microwave background (CMB) equivalent magnetic field and the spectral index is $\alpha \simeq \delta/2$ (Brunetti, Zimmer, and Zandanel, 2017, and references therein).

We assumed that the ICM magnetic field radial profile scales with the gas density profile, $n_{\rm th}(r)$, as:

$$B(r) = B_0\left[\frac{n_{\rm th}(r)}{n_0}\right]^\eta, \tag{2.11}$$

where η is the parameter that describes the scaling and n_0 is the central gas density (Eq. 2.4).

We follow the procedures in Brunetti, Zimmer, and Zandanel (2017) to calculate the injection spectrum of neutral pions:

$$Q_\pi^0(E_\pi, t) = n_{\rm th} c \int_{p_*} \mathrm{d}p N_p(p,t)\beta_p \frac{d\sigma^{\pm,0}}{dE}(E_p, E_\pi). \tag{2.12}$$

Then the γ-ray emissivity produced by the π_0 decay is:

$$\begin{aligned} j_\gamma(r) &= 2\int_{E_{\rm min}}^{E_{max}} \frac{Q_\pi^0(E_\pi, t)}{\sqrt{E_\pi^2 - {m_\pi}^2 c^4}}\mathrm{d}E_\pi \\ &\propto N_p(p,r) n_{\rm th}(r) \\ &\propto \frac{1}{4\pi r}\frac{Q(p)}{D_0} n_{\rm th}(r) \end{aligned} \tag{2.13}$$

which produces a large-scale γ-ray halo surrounding the AGN.
Finally, due to the spherical symmetry of our model, radio and γ-ray emissivities can be straightforwardly converted into a surface brightness profile by integrating along the line of sight:

$$I_{R,\gamma}(b) = \frac{1}{2\pi} \int_b^{+\infty} \frac{r j_{R,\gamma}(r)}{\sqrt{r^2 - b^2}} dr \tag{2.14}$$

where $I_{R,\gamma}(b)$ is the surface brightness at the projected distance b obtained by integrating the emissivity $j_{R,\gamma}(r)$ along the line of sight.
In this pure, hadronic framework, from the ratio of Eq. 2.10 and Eq. 2.13 we can derive a relation between radio and γ-ray emission as

$$\frac{L_\gamma}{L_R} \simeq A(\alpha) < \frac{B^2 + B_{CMB}^2}{B^{\alpha+1}} >, \tag{2.15}$$

where $A(\alpha)$ is function of the spectral index and the quantities are averaged in the emitting volume.

Equation 2.15 shows that for a source with an observed L_R, which is assumed to be generated only by secondary electrons, a larger (smaller) γ-ray luminosity is predicted for weaker (stronger) magnetic fields. This is simply because for weaker (stronger) magnetic fields a larger (smaller) number of secondary electrons is necessary to explain the observed radio luminosity, which also implies a larger (smaller) number of CR that generate the neutral pions and the γ-rays.

2.5.2 Application to a sub-sample of MHs

The model presented in Sec.t 2.5.1 is based on spherical symmetry. For this reason we select only the most roundish MHs of our sample, namely RBS 797, RXC J1504.1-0248, RX J1532.9+3021, and Abell 3444, for which we could extend our assumption of spherical symmetry. Specifically, our model depends on a set of physical parameters:

- ◇ CRp injection spectrum;
- ◇ number density of thermal targets;
- ◇ ICM magnetic field;
- ◇ AGN CRp luminosity.

In the hadronic framework the spectrum of CRp can be constrained from the radio spectrum of MHs as $\delta \simeq \alpha/2$. Due to the spherical symmetry of the clusters, we could infer the parameters that describe the distribution of thermal plasma inside the MHs (n_0, β and r_c, see Chapter 1.2.2) from the observed I_X profile as (e.g., Sarazin, 1986):

$$I_x(r) = \sqrt{\pi} n_0^2 r_c \Lambda(T) \frac{\Gamma(3\beta - 0.5)}{\Gamma(3\beta)} \left[1 + \left(\frac{r}{r_c}\right)^2\right]^{\frac{1}{2} - 3\beta} \tag{2.16}$$

where $\Lambda(T)$ is the cooling function that describes the emissivity of a plasma with a temperature T that we measured from the X-ray spectra (Sutherland and Dopita, 1993). The best-fit parameters are reported in Table 2.4. The remaining model parameters to constrain are, thus, the AGN CRp luminosity and the magnetic field in the ICM. In the following we describe in detail the steps of our analysis. We report

Table 2.4: Parameters of the $n_{\rm th}$ profile estimated within $R_{\rm MH}$.

Cluster name	n_0 [10^{-3} cm^{-3}]	r_c [kpc]	β
RBS 797	21.0	26.9	0.6
Abell 3444	14.5	24.1	0.5
RXC J1504.1-0248	15.9	22.2	0.5
RX J1532.9+3021	21.9	23.0	0.6

From left to right: Cluster name; Central proton density; Core radius; β index (Eq. 2.4).

the results of this analysis in Table 2.6.

ICM magnetic field implied by the $I_{\rm R}$-$I_{\rm X}$ correlation

In the case of spherical symmetry, the radial profile of the ratio $I_{\rm R}/I_{\rm X}$ depends on the magnetic field model (Eqs. 2.10, 2.11, and 2.15). Specifically, the values of the index k in Sect. 2.4 constrain a range of values for the couples B_0-η. Therefore, for each cluster, we calculated numerically the $I_{\rm R}$ within the MH radius (Table 2.1) by testing a wide range of combinations B_0-η, then we compared them with the observed $I_{\rm X}$ to estimate the corresponding k-index. In Figure 2.10 we report the numerical estimates compared with the observed k for each cluster. For RBS 797 the spectral index of the diffuse emission was not measured unambiguously (Doria et al., 2012), therefore we tested two extreme possibilities, $\alpha = 1.1$ ($\delta = 2.2$) and $\alpha = 1.5$ ($\delta = 3.0$).

We found that for a given value of k, larger values of B_0 are obtained for larger values of η. As a reference value, we assumed $\eta = 0.5$, which is the case where magnetic field energy scales linearly with thermal energy for isothermal ICM. Under this assumption, we constrain central values of the magnetic field of 11.8$\pm$4.8 and 18.5$\pm$5.5 μG for RBS 797 assuming α=1.1 and $\alpha = 1.5$, 18.8$\pm$5.5 μG for Abell 3444, and we derive a lower limit of 14.5 μG for RX J1532.9+3021.

A value of $\eta = 0.5$ is inconsistent with the case of RXC J1504.1-0248, whose steep scaling ($k \simeq 2$) is reproduced only by a peaked spatial distribution of the magnetic field ($0.6 < \eta < 1.3$). On the one hand, by assuming a steeper profile for the magnetic field ($\eta = 1$), we estimate a central magnetic field $B_0 = 20.0 \pm 18.5$ μG. On the other hand, assuming η=0.5 would require a CRp density radial profile steeper than the $\propto 1/r$ profile of the stationary solution (Eq. 2.3) to produce a final $I_{\rm R}$ as peaked in the center as the observed one. This case would imply a more complicated situation, including (1) a non-constant CRp luminosity of the central AGN showing a significant enhancement across the duty cycle, or (2) that the diffusion time that is necessary for CRp to cover the MH scale is longer than (i) the AGN activity timescale, and/or (ii) the energy losses of CRp.

Considerations on the diffusion coefficient D_0

In our model the luminosity of the radio emission depends on the ratio Q_0/D_0, and thus assuming a value of D_0 has consequences on the estimate of CRp injection amplitude, Q_0, and, ultimately, on the AGN CRp luminosity necessary to reproduce the

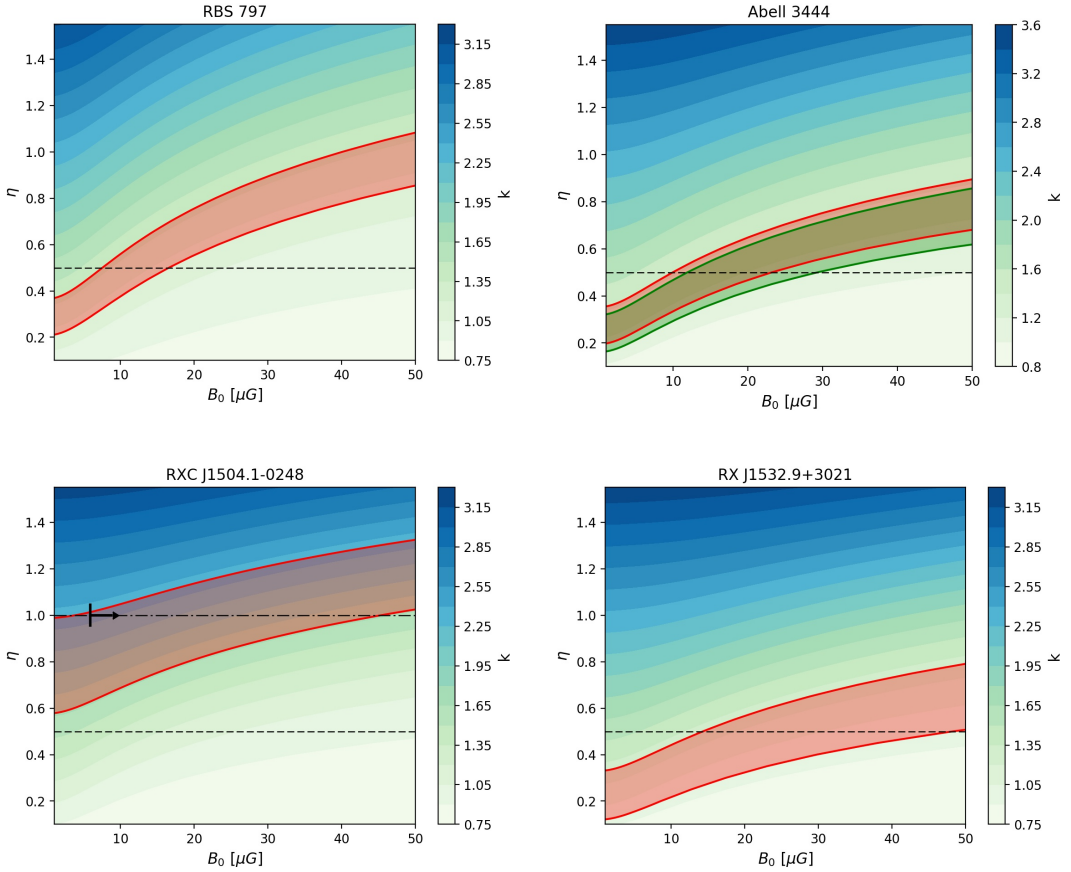

Figure 2.10: Parameter spaces of k-index for the spherical MHs. The red lines locate the 1-σ confidence interval for k measured for each MH. For RBS 797 we report the result obtained with $\alpha = 1.1$. For Abell 3444 we report in red the result at 610 MHz and in green the result at 1.4 GHz. The horizontal, dashed line points out the level $\eta = 0.5$ that reproduces the equilibrium between thermal and non-thermal energy. For RXC J1504.1-0248 we report the $\eta = 1$ level with the black dash-dotted line and the lower limit derived from the Fermi-LAT observation presented in Dutson et al. (2013). The lower limits for B_0 for the other clusters are below 1 μG and they are reported in Table 2.7.

observed radio emission.

Specifically, higher values of D_0 result in a higher Q_0 and $L_{\rm CRp}$. We assumed that CRp can diffuse on the MH scale on timescales that are shorter than the CRp cooling time. This cooling time is dominated by CRp-p collisions and is of the order of several Gyrs (Brunetti and Jones, 2014). More quantitatively, the condition is that the optical depth due to CRp-thermal proton collision calculated on a MH scale is $\tau \simeq \sigma_{\rm pp} n_{\rm th} L$, where $\sigma_{\rm pp} = 32$ mBarn is the cross-section of the collision and L is the spatial scale. As the CRp diffuse in the ICM, they move within different thermal densities, which contribute to the total optical depth as $d\tau = \sigma_{\rm pp} n_{\rm th}(r(t)) c dt$, where $r(t) = \sqrt{4 D_0 t}$. Therefore, the time $t_{\rm max}$ required to dissipate all the injected CRp in the thermal plasma within $R_{\rm MH}$ can be derived by imposing that the total optical depth is

$$\tau = c \sigma_{\rm pp} n_0 \int_0^{t_{\rm max}} \left[1 + \left(\frac{R_{\rm MH}}{r_c} \sqrt{\frac{t}{t_{\rm max}}} \right)^2 \right]^{-\frac{3}{2}\beta} dt = 1, \qquad (2.17)$$

where n_0, r_c , and β are the parameters that describe the β-model for each cluster.

Table 2.5: Diffusion coefficients.

Cluster	$D_0^{1\,\mathrm{Gyr}}$	D_0^{min}	t_{max}
RBS 797	6.9	1.1	6.4
Abell 3444	13.8	1.1	12.3
RXC J1504.1-0248	15.0	1.3	11.4
RX J1532.9+3021	10.5	0.9	12.1

From left to right: Cluster name; Diffusion coefficients that allows the diffusion of CRp within R_{MH} in 1 Gyr and that assures the complete dissipation of CRp within R_{MH} in units of 10^{29} cm^2 s^{-1}; Time in Gyr required to dissipate all the injected CRp within R_{MH} by adopting D_0^{min}.

For a given t_{max}, the associated diffusion coefficient is $D_0^{\mathrm{min}} = R_{\mathrm{MH}}^2/4t_{\mathrm{max}}$. In Table 2.5 we report the diffusion coefficients that we estimated for each MH.

This gives a lower limit to the CRp luminosity and an upper limit to the timescale for diffusion, which is shown to be longer than the timescale of cosmological cluster evolution. Assuming a larger value of the diffusion coefficient allows the diffusion of CRp on the MH scale, i.e. the establishing of a stationary CRp distribution, on shorter timescales, and entails that a higher L_{CRp} is required to reproduce the observed radio emission. Therefore, as a reference value, we assumed a coefficient that allows the diffusion of CRp over the MH radius in 1 Gyr ($D_0^{1\,\mathrm{Gyr}}$), which we report in Table 2.5 and Table 2.6 with the corresponding L_{CRp}. We note that adopting D_0^{min}, instead of $D_0^{1\,\mathrm{Gyr}}$, results in values of L_{CRp} that are a factor of $D_0^{\mathrm{min}}/D_0^{1\,\mathrm{Gyr}} \simeq 0.1$ lower that the values that we report. The γ-ray luminosity does not change, because it depends, instead, on the ratio Q_0/D_0, which is constrained by the observed radio luminosity.

Constraints on the AGN CRp luminosity

Once the scaling between the magnetic field and the thermal density is constrained by the observed scaling between I_{R} and I_{X}, we can derive the CRp luminosity of the central AGN that is required to substain the observed radio luminosity of MHs. The AGN luminosity, L_{CRp}, is

$$L_{\mathrm{CRp}} = \int_{p_{0.2\,\mathrm{GeV}}} Q_0 p^{-\delta} \sqrt{c^2p^2 + m_{\mathrm{p}}^2c^4}\,dp, \tag{2.18}$$

where m_{p} is the proton mass and $p_{0.2\,\mathrm{GeV}}$ is the momentum for which the kinetic energy, pc, is 0.2 GeV. We note that for $\delta < 3$ the exact choice of the minimum energy is not relevant for the final result.

In order to obtain the value of Q_0 to compute L_{CRp} (Eq. 2.18) we matched the observations with the I_{R} profiles predicted by our model. We estimated the synchrotron emissivity numerically with Eq. 2.10 by following the formalism presented in Sect. 2.5.1 and by assuming the $B(r)$ configurations that we constrained in Sect. 2.5.2. The radio emission depends on the ratio Q_0/D_0 (Eq. 2.10), therefore we estimated Q_0, and thus L_{CRp}, by assuming a diffusion coefficient D_0^{1Gyr} for which the

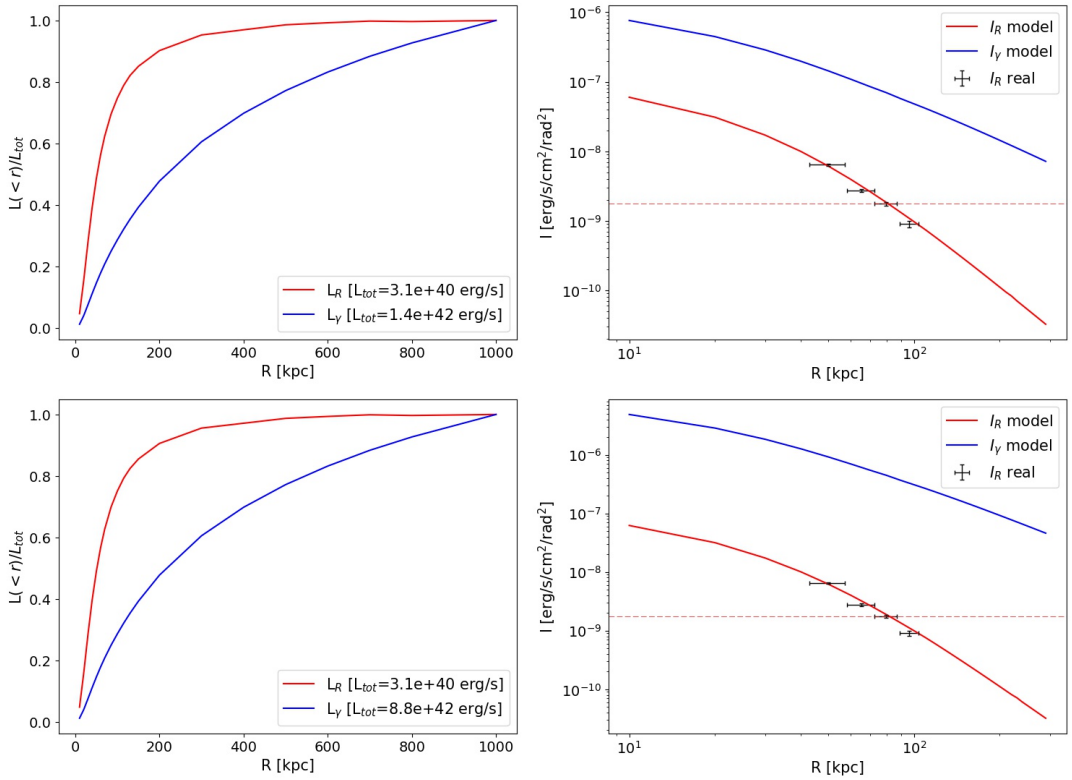

Figure 2.11: Results for RBS 797 for δ=2.2 (top) and δ=3.0 (bottom). Left: Integrated radio (red) and γ-ray (blue) luminosity; Right: Radio (red) and γ-ray (blue) surface brightness. We report the observed I_R profile and the 3σ level of the observation (dashed red line).

diffusion time of CRp in the MH is $\tau = R^2_{MH}/4D_0$=1 Gyr. This implies an optimistic diffusion coefficient and consequently a upper bound to the L_{CRp} that is required by the model. In Section 2.5.2 we discuss the consequences of different assumptions, including the scenario of total dissipation of CRp within R_{MH}, which entails the lower bound for L_{CRp} in our model. Finally we compared them with the observed I_R profiles measured in circular bins with the same resolution of the radio maps. We report in Table 2.6 the parameters adopted and the results obtained. We estimate that the AGN L_{CRp} required in our model to reproduce the observed radio emission is 10^{44}-10^{46} erg s^{-1} (see Section 2.5.2). In Figs. 2.11, 2.12, and 2.13 for each cluster we report the integrated radio luminosity and the surface brightness radial profiles, predicted and observed, at the observed frequency.

2.5.3 Resulting γ-rays emission and comparison with current and future observations

In the previous sections we used the I_R-I_X scaling to derive constraints on the model parameters. In this section we check if the γ-ray fluxes are consistent with current observational limits. We calculated numerically the γ-ray emission produced by the π_0 decay described in Sect. 2.5.1 within the same physical boundaries adopted in Sect. 2.5.2 by implementing numerically Eq. 2.13. However, the approximation of thermal density adopted to reproduce the MH volume (Eq. 2.4) could extrapolate incorrectly the thermal density beyond R_{MH}. Therefore, to calculate the total γ-ray luminosity we used a double β-model to better describe the radial decline of the thermal gas density beyond R_{MH}.

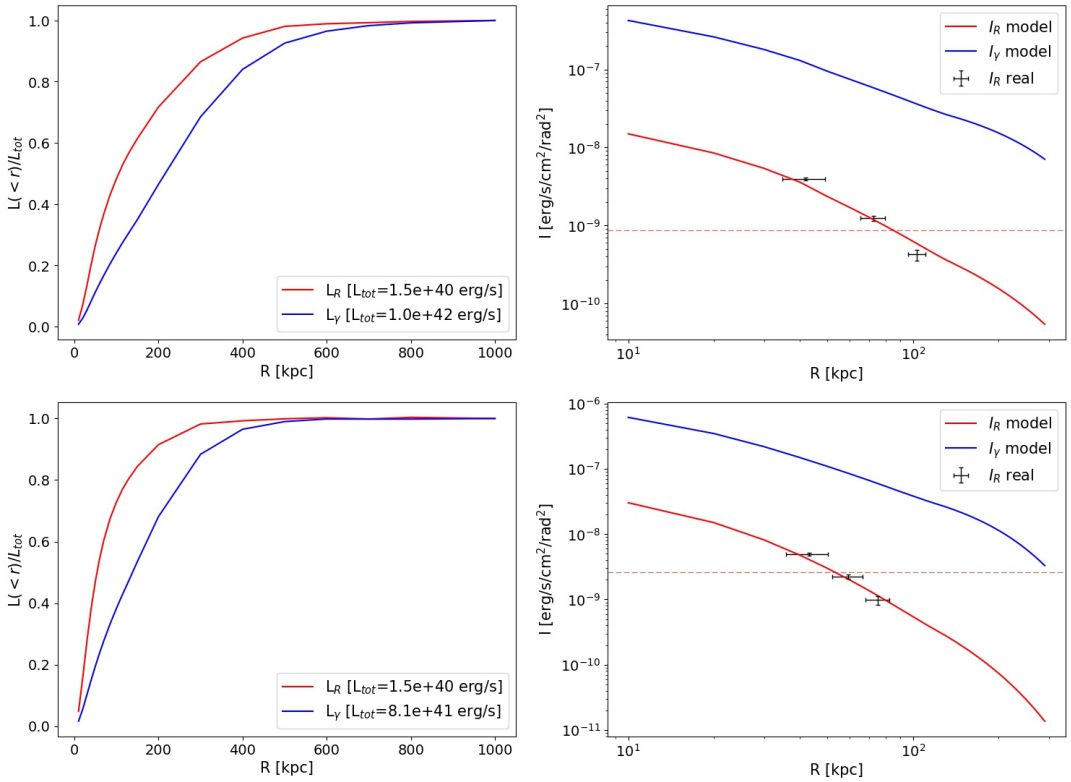

Figure 2.12: Results for Abell 3444 at 1.4 GHz (top) and RX J1532.9+3021 (bottom). For the latter, we report reference values of $L_{\rm R}$ and L_γ derived from the upper limit of the magnetic field (Table 2.6). Left: Integrated radio (red) and γ-ray (blue) luminosity. Right: Radio (red) and γ-ray (blue) surface brightness. We report the observed $I_{\rm R}$ profile and the 3σ level of the observation (dashed red line).

Table 2.6: Parameters of the hadronic model.

Cluster name	$D_0^{1\,\rm Gyr}$ [cm^2 s^{-1}]	$\rm R_\gamma$ [kpc]	δ	B_0 [μG]	η	Q_0/D_0	$L_{\rm CRp}^{>0.2\,\rm GeV}$ [erg s^{-1}]	$S_\gamma^{>1\rm Gev}$ [erg s^{-1} cm^{-2}]
RBS 797	$6.9{\cdot}10^{29}$	650	2.2	11.8±4.8	0.5	1.7	$1.5{\cdot}10^{44}$	$1.3{\cdot}10^{-14}$
			3.0	18.5±5.5	0.5	$1.6{\cdot}10^{-9}$	$8.1{\cdot}10^{45}$	$2.1{\cdot}10^{-14}$
Abell 3444	$1.4{\cdot}10^{30}$	400	2.6	18.5±5.5	0.5	$1.1{\cdot}10^{-5}$	$4.2{\cdot}10^{44}$	$7.3{\cdot}10^{-15}$
RXC J1504.1-0248	$1.5{\cdot}10^{30}$	320	2.5	20.0±18.5	1.0	$4.4{\cdot}10^{-3}$	$4.2{\cdot}10^{45}$	$9.4{\cdot}10^{-14}$
				10.0	1.0	$1.5{\cdot}10^{-2}$	$1.4{\cdot}10^{46}$	$3.3{\cdot}10^{-13}$
				1.0	1.0	2.2	$2.0\cdot10^{48}$	$4.7\cdot10^{-11}$
RX J1532.9+3021	$1.1{\cdot}10^{30}$	300	2.4	>14.5	0.5	$7.1{\cdot}10^{-3}$	$<1.2\cdot10^{45}$	$<5.2\cdot10^{-15}$

From left to right: Cluster name; Diffusion coefficient for which CRp reach $R_{\rm MH}$ in 1 Gyr; Radius in which 85% of γ-rays are emitted; Index of the CRp injection spectrum (Eq. 2.1); Central magnetic field (Eq. 2.11); Slope between the ICM magnetic field and the thermal plasma (Eq. 2.11); Normalization of non-thermal emissivity, in units of $\left[\left(\frac{\rm g\,cm}{\rm s}\right)^\delta {\rm cm}^{-2}\right]$ (Eq. 2.1); AGN CRp luminosity ; γ-ray flux expected from the total emitting region inside R_γ.

In Table 2.6 we report the radius containing 85% of the γ-ray emission and the

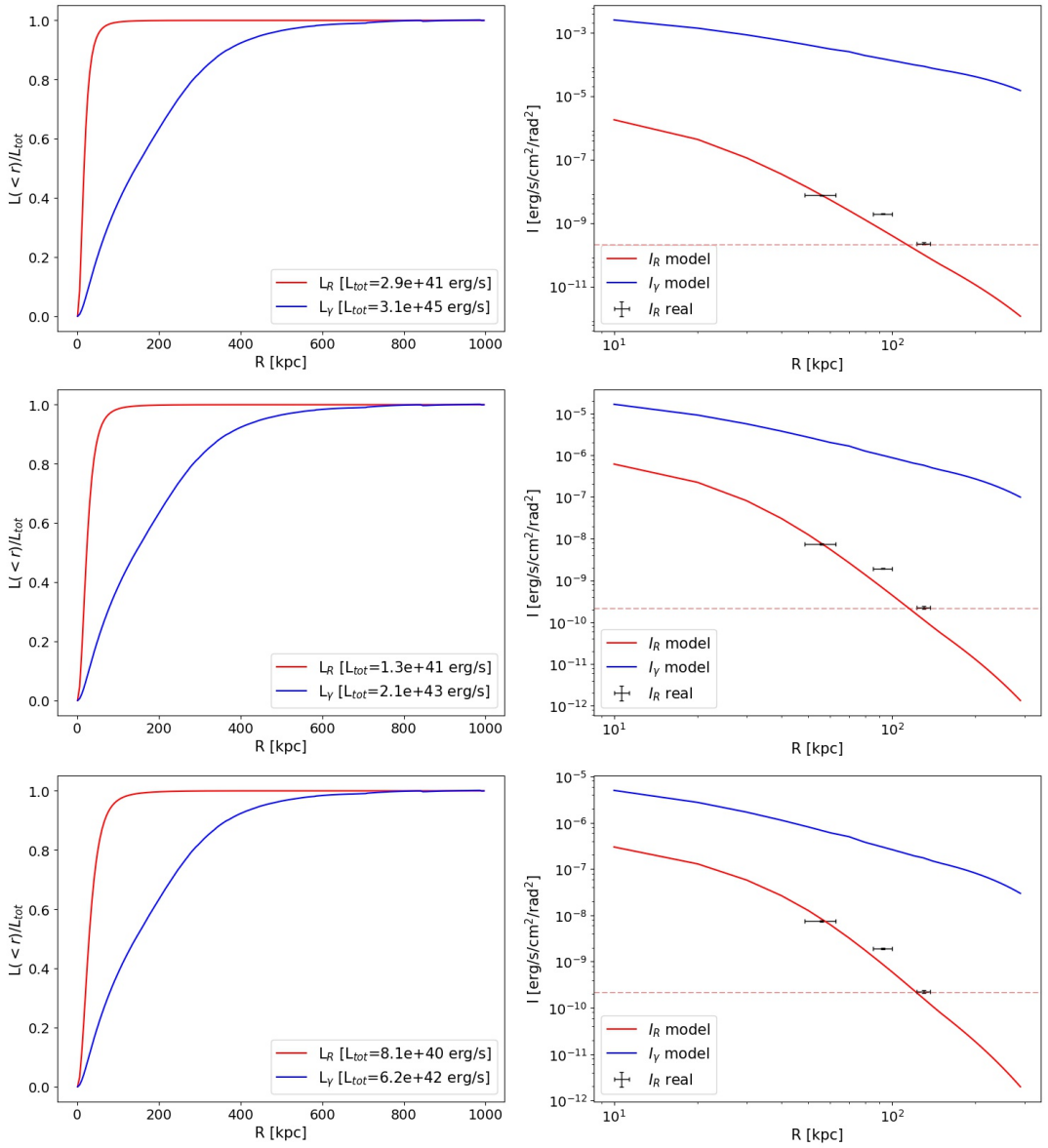

Figure 2.13: Results for RXC J1504.1-0248 with $B_0 = 1$ μG (top), $B_0 = 10$ μG (middle), and $B_0 = 20$ μG (bottom). Left: Integrated radio (radio) and γ-ray (blue) luminosity; Right: Radio (red) and γ-ray (blue) surface brightness. We report the observed I_R profile and the 3σ level of the observation (dashed red line). We limited the profile up to R_{MH} to avoid possible contamination by field sources (see Section 2.3.2).

γ-ray flux. Figures 2.11, 2.12, and 2.13 report the integrated γ-ray luminosity and surface brightness radial profiles at 1 GeV. The radio and γ-ray halos differ in terms of size, because the j_R (Eq. 2.10) declines faster than j_γ (Eq. 2.13). According to our results, the γ-ray halos extend beyond the cooling region, which contains instead almost the totality of the radio emission. In the case of RXC J1504.1-0248, the value of B_0 is poorly constrained from the analysis presented in Sect. 2.5.2 (B_0=20.0$\pm$18.5 μG). Therefore, for this cluster we compute L_{CRp} and the γ-ray emission assuming three values of the central magnetic field, namely B_0 =1.0, 10.0, 20.0 μG. We note that assuming $B_0 > 20$ μG would produce results close to the case $B_0 = 20.0$ μG (Eq. 2.15).

Diffuse γ-ray emission from galaxy clusters has never been firmly detected, so

Table 2.7: Fermi lower limits for the central magnetic field B_0.

Cluster name	η	$B_{0,\mathrm{min}}$ [μG]
RBS 797	0.3	0.5
"	0.5	0.7
Abell 3444	0.3	0.8
"	0.5	0.8
RXC J1504.1-0248	1.0	5.9
RX J1532.9+3021	0.3	0.5
"	0.5	0.8

From left to right: Cluster name; Magnetic field configuration (see Eq. 2.11); Lowest central magnetic field B_0 allowed by Fermi detection limit.

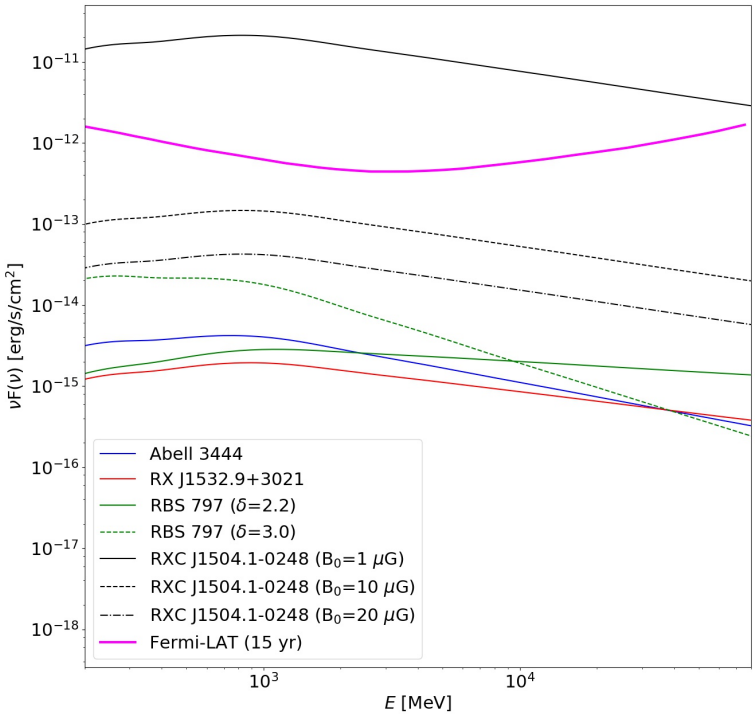

Figure 2.14: Predicted γ-rays spectrum for the MHs for parameters reported in Table 2.6 compared with the Fermi-LAT 15 yr detection limit.

we tested the consistency of our model with the observational constraints. This is shown in Figure 2.14, where we compare the expected γ-ray emission, computed with the parameters reported in Table 2.6, with the Fermi-LAT detection limit after 15 years. In general, we find that the γ-ray fluxes predicted for the four MHs are below the Fermi-LAT detection limit, hence our model constrained from the I_R-I_X scaling does not violate the current non-detection of diffuse γ-ray emission.

The Fermi-LAT detection limits can also be used to infer complementary limits to the central magnetic field B_0 in our model, because in our model a fainter magnetic field will result in stronger γ-ray emission (Eq. 2.15). For RBS 797, Abell 3444, and RX J1532.9+3021 we used the results of the Fermi-LAT 15yr observations as constraints, whereas for RXC J1504.1-0248 we used the limit obtained by Dutson et al. (2013) with the Fermi-LAT. In Table 2.7 we report the limits inferred for the configurations of ICM magnetic field and $L_{\rm CRp}$ constrained by our results. The Fermi-LAT detection limit provides lower limits below 1 μG for RBS 797, Abell 3444, and RX J1532.9+3021. On the contrary, for RXC J1504.1-0248 the lower limit is 5.9 μG, due to the higher γ-ray emissivity predicted by our model.

2.6 Discussion and summary

In this work we have carried out, for the first time, a systematic study of the spatial connection between thermal and non-thermal ICM components in relaxed clusters. Here we summarize and discuss our results.

2.6.1 New scaling relation for MHs

The most important result of our work comes from the study of the spatial correlation between non-thermal radio and thermal X-ray brightness for a sample of seven MHs. We extended the strategy based on a single grid, which has been applied to giant radio halos, by including a Monte Carlo approach in the generation of the grid. This approach allows us to avoid the biases generated by the relatively small ($\sim$20-30) number of independent radio beams that cover the emission of MHs (after excluding the regions contaminated by discrete sources).

We found evidence of a spatial correlation between $I_{\rm R}$ and $I_{\rm X}$, where the radio emission is generally more peaked than the thermal emission, thus indicating that the ICM non-thermal components are more concentrated around the central AGN. Our result further confirms the connection between thermal and non-thermal ICM components in MHs, which has already been claimed by previous works that studied the correlations between radio and X-ray luminosity (Gitti et al., 2015; Kale et al., 2015; Bravi, Gitti, and Brunetti, 2016; Gitti et al., 2018; Giacintucci et al., 2019) and the morphological connection between cold fronts and MHs (Mazzotta and Giacintucci, 2008).

Furthermore, the values of k that we measure for MHs differ from the case of radio halos reported in the literature, where a sub-linear or linear scaling is generally found (Govoni et al., 2001; Feretti et al., 2001; Giacintucci et al., 2005; Vacca et al., 2010; Hoang et al., 2019). This may suggest an intrinsic difference in the nature of these radio sources, and, hence, that the $I_{\rm R}$-$I_{\rm X}$ can represent a new criteria to discriminate between the two kind of diffuse radio emission. However, further test including large samples of giant and mini halos are now necessary to prove this. The steep decline of the radio emission in MHs also suggests that secondary particles injected at the center by the AGN play a role, both directly or as seed particles re-accelerated by other mechanisms.

2.6.2 Comparison with hadronic models

We have considered a simple, reference hadronic model based on the injection of CRp by the central AGN. The model is a pure hadronic scenario without including the effect of re-acceleration. Furthermore, we assume that the combination of CRp injection and diffusion generates stationary conditions in the ICM. We note that this simple scenario connecting the AGN activity and the MH has already been proposed to explain the origin of the Perseus MH (e.g., Boehringer and Morfill, 1988; Pfrommer and Enßlin, 2004) and, in general, to evaluate the effect of CRp-driven streaming instability on the heating of the cool cores and the connection with the formation of MHs (e.g., Fujita and Ohira, 2013; Jacob and Pfrommer, 2017a; Ehlert et al., 2018).

We compared the observed scalings between I_R and I_X with our simple model to infer combined constraints on the AGN CRp luminosity and the ICM magnetic field, in terms of its central value B_0 and the index of scaling with the gas density η. We selected the four MHs of our sample with a roundish shape for which it is possible to assume spherical symmetry in 3D. In this case, constraints deriving from point-to-point correlations are similar to those deriving from the azimuthally averaged brightness profile. Specifically, we derived B_0 in the range 10-40 μG assuming $\eta = 0.5$, where smaller values of B_0 would require smaller values of η, and a $L_{CRp} = 10^{44}$-$10^{46} (D_0 / D_0^{1\,Gyr})$ erg s^{-1}, where we assumed a $D_0^{1\,Gyr}$ that allows the diffusion of CRp in the MH volume in 1 Gyr.

We stress that, although these results are based on the assumption of stationary conditions, they are obtained by sampling spatial scales of a few 100 kpc and consequently they do not depend significantly on local variations. As a consequence, we expect that only a strong violation of stationary conditions can affect our conclusions.

The values of B_0 that we found are consistent, although slightly larger than the values reported by Carilli and Taylor (2002) for relaxed clusters. An independent observational test of pure hadronic models, where the AGN plays the main role in the injection of the primary CRp, would thus result from detailed studies of the Faraday rotation measure and depolarization of the discrete radio sources embedded in the cluster core or in background (e.g., Bonafede et al., 2011).

γ-ray emission

The unavoidable consequence of a hadronic scenario is the production of γ-rays with a luminosity that is close to the CRp luminosity of the AGN, where the γ-ray luminosity depends on the model parameters. In Sect. 2.5.3 we calculated the γ-ray emission under the assumption of the parameters reported in Table 2.6. The expectations do not violate Fermi upper limits (Figure 2.14). We found that smaller B_0 produce a larger γ-ray luminosity, whereas larger D_0 entail larger L_{CRp} and fulfill the stationary conditions for the CRp distribution in shorter timescales. The Fermi-LAT detection limit allowed us to provide a lower limit for the central magnetic field, which we report in Table 2.7. The I_γ profile is broader than the I_R profile (Figs. 2.11, 2.12, and 2.13), although for the parameters used in Sect. 2.5.2 we find that the radius where 85% of the emission is produced is larger than the core radius of the cluster.

Observation tests and limitations

The MH size predicted by our model depends on our assumptions on the diffusion coefficient (see Section 2.5.2). Large diffusion coefficients produce MHs that extend beyond the radius measured by current observations (Figs. 2.11, 2.12, and 2.13). Deeper observations of the MHs of our sample will allow us to test whether the emission can extend on larger scales or is more confined, for example within the region defined by cold fronts (e.g., Mazzotta and Giacintucci, 2008). These tests will allow us to understand whether additional mechanisms, such as turbulent re-acceleration, are necessary to explain observations (ZuHone et al., 2013b).

One of the main caveats in our analysis is the assumption of stationary conditions. On the one hand, these are justified by the fact that in a cooling time the CRp can diffuse on scales similar to or larger than that of MHs. On the other hand, the duty cycles of AGN last for $10^7 - 10^8$ years (Morganti, 2017), thus the MHs would be powered by numerous bursts of injection of CRp, whose diffusion scale is $r_{\rm max} = \sqrt{4 D_0 t}$, with t being the look-back time for the single burst. Consequently, stationary conditions also imply that the phase of the interplay between the AGN and MH is much longer than a single burst of activity of the AGN, thus, the MH results from the integrated effect of many bursts and AGN active phases.

However, if the system has recently experienced unusually powerful AGN activity (injection of CRp), the resulting spatial distribution of CRp would be steeper than in our approximation. This would also result from a scenario where the $L_{\rm CRp}$ of the AGN active phases decreases with look-back time. The case of RX1504 where a very steep trend between radio and X-ray brightness is found, might suggest that the system had very strong CRp activity in the last 100 Myr or so.

2.6.3 Future prospects

We observed a difference in the distribution of radio and X-ray emission between mini and giant halos. At the same time, our analysis made clear that reliably evaluating the $I_{\rm R}$-$I_{\rm X}$ correlation MH halos requires a different approach than that used for giant halos. Therefore, to confirm the different behavior that we observed, the Monte Carlo point-to-point analysis and BCES fitting procedure presented in this work should be extended to a large sample of targets, including both mini and giant radio halos. In this spirit, we are going to make publicly available the PT-REX code (Ignesti in preparation, see Appendix A), which includes both the SMptp and MCptp routines used in this work, as well as several statistical methods to evaluate the $I_{\rm R}$-$I_{\rm X}$.

The estimates provided by our model could act as constraints for future theoretical work aimed at addressing the connection between AGN feedback and cooling flow quenching. Our results suggest that simple hadronic models can still match the main observations of MHs. Further studies are now required to address the implications of secondary production of electrons in the presence of ICM turbulence, and the implications of interplay with the leptonic models in general in the origin of the diffuse radio emission. The incoming Athena X-ray observatory will play a crucial role in these studies by providing an unprecedented spectral resolution. In particular, by combining radio images and Athena X-ray Integral Field Unit (X-IFU,

Barcons et al., 2017) observations in a point-to-point analysis, we will be able to explore the spatial connection between the energy of CRe and the ICM turbulence.

The study of radio emission in galaxy clusters will greatly benefit from the present and new radio observatories, such as LOFAR and SKA, that could potentially observe thousands of new sources. As mentioned in Chapter 1.3.4, LOFAR observations are already showing that relaxed clusters can host diffuse, ultra-steep spectrum emission extending far beyond the sloshing region, suggesting a more complex scenario involving "gentle" CRe re-acceleration due to ICM turbulence on large scales (Savini et al., 2018; Savini et al., 2019). In this case, follow-up studies of point-to-point brightness distribution based on our approach open up the possibility of discriminating the contribution of hadronic collisions (pure hadronic or re-accelerated secondaries) from that of turbulent re-acceleration of primary seeds, because the two regimes should produce different scalings. By probing the steep spectrum emission on larger scales at lower frequencies, we may expect to observe a flattening of the radio and X-ray scaling, similar to what is observed in giant radio halos.

In the following Chapter we introduce LOFAR in details, and we discuss its potential to revolutionize our understandings of diffuse radio sources.

Chapter 3

The LOFAR revolution

3.1 The LOw-Frequency ARray

LOFAR,the LOw Frequency ARray (van Haarlem et al., 2013), is a new generation interferometer operated by ASTRON and spread all over Europe (Figure 3.1). It is the largest pathfinder of the SKA at low frequencies, accounting about 20,000 dipole antennas. LOFAR observes the sky in the frequency range 10-240 MHz (corresponding to wavelengths of 30-1.2 m), entering an uncharted observational window of the electromagnetic spectrum with unprecedented resolution and sensitivity. LOFAR offers high-resolution, sub-arcsecond observation, thanks to the the longest European baseline, while the densely populated core, i.e. with plenty of short baselines, allows to recover, at the same time, very extended emission in the sky. The effectively all-sky coverage of the dipoles gives LOFAR a large field-of-view (FoV), essential for surveying purposes. We report the LOFAR performances at different frequencies in Table 3.2. This makes LOFAR a versatile instrument with potential breakthroughs in many fields of astrophysics.

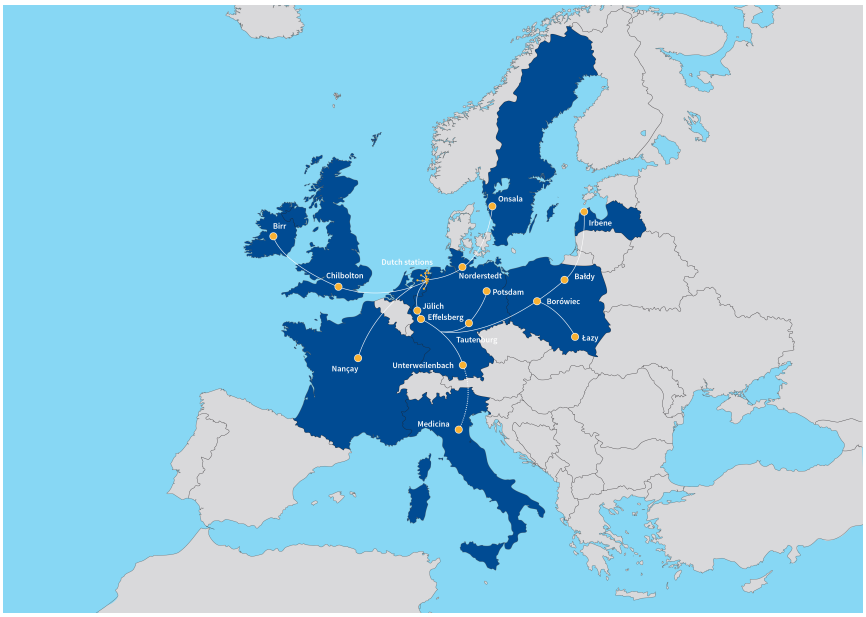

Figure 3.1: The LOFAR stations.

LOFAR comprises 52 individual stations distributed mainly on the northern part of Europe. The majority of these stations, 38 in total, are located in the Netherlands, and form the LOFAR Dutch array. The remaining 14 stations are built in Germany (6), the UK (1), France (1), Sweden (1), Poland (3), Ireland (1) and Latvia (1). The

Freq. (MHz)	λ (m)	D (m)	$A_{\rm eff}$ (m^2)	$FWHM$ (deg)	FOV (deg^2)	D (m)	$A_{\rm eff}$ (m^2)	$FWHM$ (deg)	FOV (deg^2)	D (m)	$A_{\rm eff}$ (m^2)	$FWHM$ (deg)	FOV (deg^2)
		NL Inner				NL Outer				EU			
15	20.0	32.25	1284.0	39.08	1199.83	81.34	4488.0	15.49	188.62	65.00	3974.0	19.39	295.36
30	10.0	32.25	848.9	19.55	299.96	81.34	1559.0	7.75	47.15	65.00	2516.0	9.70	73.84
45	6.67	32.25	590.2	13.02	133.31	81.34	708.3	5.16	20.96	65.00	1378.0	6.46	32.82
60	5.00	32.25	368.5	9.77	74.99	81.34	399.9	3.88	11.78	65.00	800.0	4.85	18.46
75	4.00	32.25	243.6	7.82	47.99	81.34	256.0	3.10	7.55	65.00	512.0	3.88	11.81
		NL core				NL Remote				EU			
120	2.50	30.75	600.0	4.75	17.73	41.05	1200.0	3.56	9.95	56.50	2400.0	2.59	5.25
150	2.00	30.75	512.0	3.80	11.35	41.05	1024.0	2.85	6.37	56.50	2048.0	2.07	3.36
180	1.67	30.75	355.6	3.17	7.88	41.05	711.1	2.37	4.42	56.50	1422.0	1.73	2.33
200	1.50	30.75	288.0	2.85	6.38	41.05	576.0	2.13	3.58	56.50	1152.0	1.55	1.89
210	1.43	30.75	261.2	2.71	5.79	41.05	522.5	2.03	3.25	56.50	1045.0	1.48	1.72
240	1.25	30.75	200.0	2.38	4.43	41.05	400.0	1.78	2.49	56.50	800.0	1.29	1.31

Figure 3.2: LOFAR effective area ($A_{\rm eff}$), full-width half-maximum ($FWHM$) and field of view (FOV) at different frequencies and for different station configurations, where D is the station diameter (van Haarlem et al., 2013).

construction of three additional stations (LOFAR 2.0 generation) in Latvia and Italy has already been planned, further expanding the size of this international facility (Figure 3.1). The LOFAR core consists in a strong concentration of 24 stations located within a radius of 2 km near the town of Exloo, in the Netherlands. This area was chosen because of its low population density and relatively low level of RFI. The core station distribution has been optimized to achieve the good instantaneous uv-coverage. At the heart of the core, a 320 m diameter island referred to as "the Superterp" contains six core stations that provide the shortest baselines in the array (Figure 3.3). The remaining 14 stations in the Netherlands are called remote stations. They are approximately arranged in a logarithmic spiral distribution over an area roughly 180 km in diameter around Exloo.

The fundamental receiving elements of LOFAR are two types of small, relatively low-cost antennas (Figure 3.3) that together cover the 10-240 MHz operating bandpass. Single antenna elements are connected via coaxial cables to the electronics housed in a cabinet located on the edge of each station, where the hardware used to perform the first data processing stage is located. The datastreams enter the digital electronics section which is mainly responsible for beam-forming. Further processing is done by the remote station processing boards utilizing low-cost, field programmable gate arrays. Following the beam-forming step, the data packets are streamed over the wide-area network to the correlator at the CEP facility. Here we provide a basic description of the two type of antennas, a more technical review can be found here[1].

- ◇ The Low Band Antennas (LBA) operates in the 30-80 MHz band, which cover the radio band from the ionospheric cutoff of the radio window near 10 MHz up to the onset of the commercial FM radio band at about 90 MHz. The LBA units consist of simple dual linear polarization droop dipoles connected to a molded cap on the top of a vertical shaft of PVC pipe. The wires are connected on a ground plane consisting of a metal mesh located above a foil sheet used to minimize the vegetation growth underneath the antenna. The resulting LBA element is shown in Fig. 7.3 (left panel). Despite this low-cost design, LBA

[1] http://old.astron.nl/radio-observatory/radio-observatory

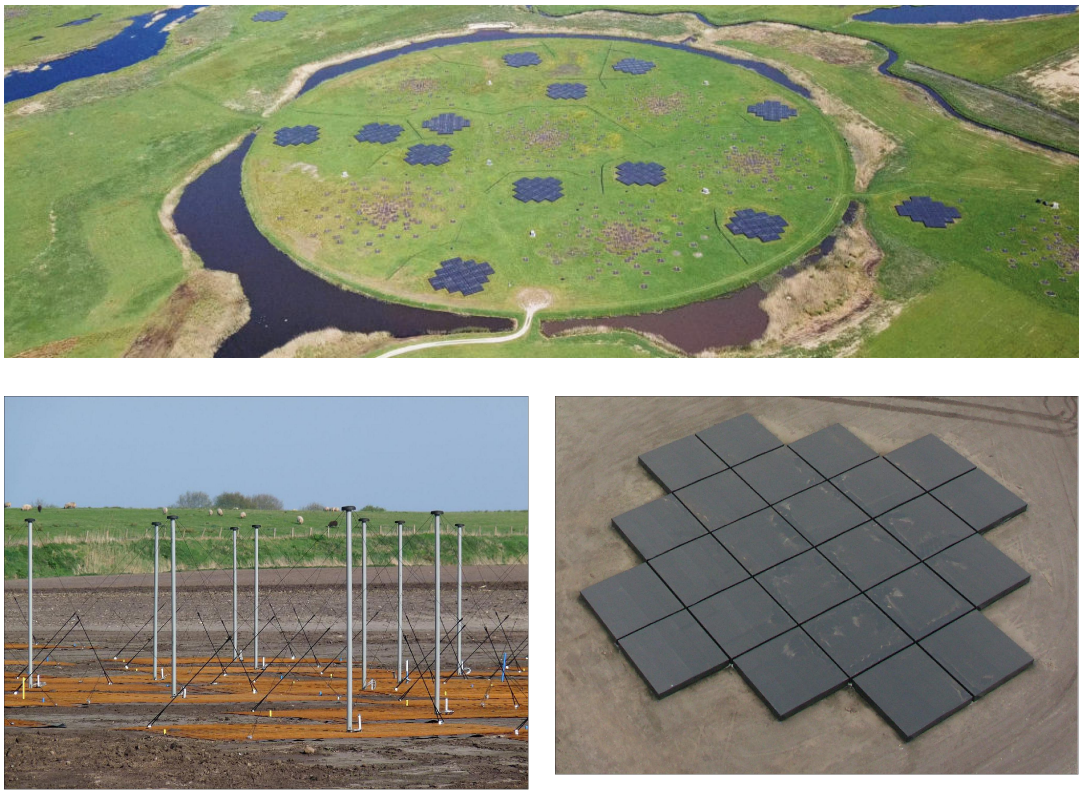

Figure 3.3: Pictures of the Superterp (top), and the LBA (bottom-left) and HBA (bottom-right) stations.

dipoles allow an innovative all-sky covering at the lowest frequency on short timescales, fundamental to study the large scale emission from the Galaxy and for the monitoring of radio transients;

- ◇ The High Band Antennas (HBA) cover the higher end of the LOFAR spectral response from 110 MHz to 250 MHz. This frequency range is limited to the range 110-240 MHz due to the high RFI contamination above 240 MHz. A different, low-cost design was necessary for HBA to minimize the contribution of the electronics to the system noise at this higher frequency. The HBA elements are grouped in 16 dual dipole antennas and arranged in a 4×4 grid to form a single HBA "tile". A single "tile beam" is created by combining the signals from these 16 antenna elements in phase for a given direction on the sky. A polypropylene foil layer shields the contents of the tile by bad weather conditions. In the core stations, HBA dipoles are distributed over two sub-stations of 24 tiles each that can be used in concert as a single station or independently. The advantage of the latter configuration is to provide a large number of short baselines within the core, hence a significantly more uniform uv-coverage. In addition, the dual HBA sub-stations result in the redundancy of many short baselines yielding additional diagnostics for identifying bad phase and gain solutions during the calibration process.

LOFAR is a pathfinder of SKA also for the management of data output, both in term of data rate and big data analysis and archiving. LOFAR observations produce an avarage of 13 Tbits/s of raw data, that entails an output volume is of the order of $\sim$ 10 TB for an 8 hrs observation (which is the standard duration of the LOFAR survey pointing, see following sections). Such amount of data requires specialized

facilities to be handled and stored. For this reason, the CEP is backed up by several data centers distributed in the LOFAR collaboration. Currently, the total amount of data stored is of the order of 100 PB, which may seem impressive, but it corresponds to only just the expected data output of SKA in a year.

3.2 Science with LOFAR

The science drivers for LOFAR determined the design, development and construction of the facility during its initial and commissioning phase, and have been divided into six Key Science Projects (KSP):

- *Epoch of Reionization:* aims at searching for the redshifted 21 cm line signal that marks the transition between the dark ages and the period after recombination when the Universe became neutral. This process possibly started at $z \sim 20-15$ and nished at $z \sim 6$. The redshift ranges $z \sim 30-20$ and $z \sim 12-6$ can be probed by LOFAR;
- *Cosmic Rays:* will allow to understand the origin of high-energy CRs at energies between $10^{15} - 10^{20.5}$ eV through the detection of air showers of secondary particles caused by interaction of CRs with the Earth atmosphere. Both the sites and processes for accelerating these energetic particles are still poorly known;
- *Solar Physics* and Space Weather: includes the denition of solar observing modes and the development of the necessary software infrastructure for solar and space weather studies;
- *Transients:* comprises the study of all time-variable astronomical radio sources, including pulsars, gamma-ray bursts, gravitational waves, X-ray binaries, radio supernovae, are stars, and even exoplanets. Thanks to the all-sky monitoring, LOFAR is expected to detect many new transient events, and to provide provide alerts to the international community for follow-up observations at other wavelengths;
- *Cosmic Magnetism of the Nearby Universe:* allows to study the polarized radio synchrotron emission to unveil the structure and strength of the magnetic elds of several objects,from the Milky Way, dwarf galaxies, galaxy halos, nearby galaxy clusters, and up to the intergalactic laments related to the formation of large-scale structures;
- *Surveys:* is one of the LOFAR science drivers since its inception. Due to its nature, the Surveys KSP touches a broad range of astrophysics topics, with possible cross-talks with the other KSPs. Four main science drivers have been identied for the proposed surveys:
  - Formation of massive galaxies, clusters and black holes using $z \geq 6$ radio galaxies as probes;
  - Non thermal emission and components in galaxy clusters;
  - Star formation processes in the early Universe using starburst galaxies as probes;
  - Exploration of new parameter space for serendipitous discovery.

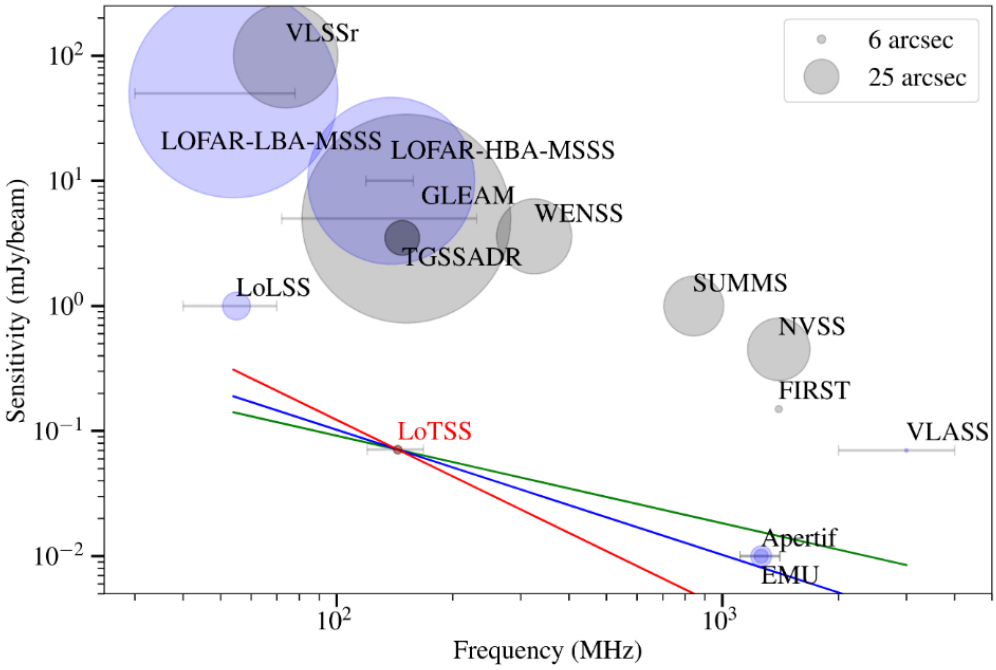

Figure 3.4: Image rms, frequency, and angular resolution (linearly proportional to the radius of the markers) of LoTSS-DR1 in comparison to a selection of existing wide-area completed (grey) and upcoming (blue) radio surveys. The horizontal lines show the frequency coverage for surveys with large fractional bandwidths. The green, blue, and red lines show an equivalent sensitivity to LoTSS for compact radio sources with spectral indices of -0.7,-1.0, and -1.5, respectively. (Shimwell et al., 2019).

3.3 LOFAR Two-metre Sky Survey

One of the main goals of LOFAR since its inception is to conduct wide and deep surveys (Figure 3.4). Currently the ongoing surveys are:

- ◇ LOFAR Two-meter Sky Survey (LoTSS Shimwell et al., 2017), is a sensitive, high-resolution survey of the northern sky at the frequency of 144 MHz. The survey is currently ongoing (almost 1/2 of the sky has been observed, see Figure A.5) and the first full-quality partial data release incorporating direction-dependent error correction has been recently published in Shimwell et al. (2019). A new release based on improved calibration procedures and covering about 5000 deg^2 area is planned for the second half of 2021;

- ◇ LOFAR LBA Sky Survey (LoLSS de Gasperin et al., in preparation), is the ultra-low frequency counterpart of LoTSS and will produce an unprecedented view of the sky at 54 MHz. The survey is currently ongoing;

- ◇ WEAVE-LOFAR a spectroscopic survey of the LoTSS sky with the WEAVE fibre spectrograph on the William Herschel Telescope. It will provide redshifts for the wide and deep tiers of LOTSS.

- ◇ LOFAR Deep fields: LoTSS is also taking repeated observations of northern hemisphere fields with the highest-quality multi-wavelength data over several-degree scales. These observations, taken with the same frequency coverage as the all-sky survey, will offer much higher sensitivity. The ultimate aim is to

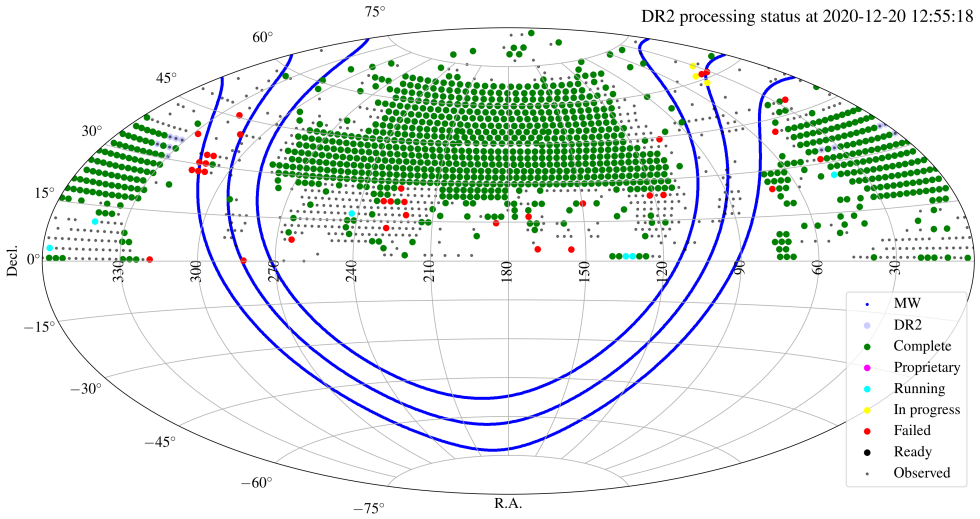

Figure 3.5: LOFAR Two-Metre Sky Survey DR2 processing status from https://lofar-surveys.org/status.html.

reach depths approaching 10 μJy beam^{-1} ($\sim$5 times deeper than the best all-sky LoTSS pointings) over combined sky areas of many tens of square degrees.

LoTSS is designed to push further into new territory by accomplishing its primary observational objectives, which are to reach a sensitivity of less than 100 μJy beam^{-1} at an angular resolution of $\sim$ 6 arcscond across the whole northern hemisphere, using the HBA system of LOFAR (Figure 3.4). The current status of the survey, and the upcoming progresses, are reported in Figure 3.5. The titanic output of the survey, in terms of brand-new, high-quality, low-frequency observation allows to carry out scientific studies in manifold directions. Indeed, the main scientific motivations for LoTSS are to explore the formation and evolution of massive black holes, galaxies, clusters of galaxies, and large-scale structure. The main contributes of LoTSS in these fields of research are summarized in Shimwell et al. (2019) and references therein.

Part of the results presented in this Thesis are the outcome of a direct involvement with LoTSS. By joining the SKP galaxy cluster working group, we had access to LoTSS observations of the relaxed cluster Abell 2626 and 2A0335+096 (in co-observation), which are presented in Chapters 5 and 6. Moreover, we actively contributed in two ongoing LoTSS projects. We developed the architecture of the LoTSS-PSZ2 cross-check catalog (see Chapter 4), which will provide the largest sample of clusters hosting diffuse radio sources with SZ masses. Moreover, we contributed to the final public release of the survey by developing a routine to automate the selection of the calibration region (see Section 3.3.1) for any LoTSS source.

3.3.1 LoTSS data processing

In our work we made use of HBA continuum images obtained in the LoTSS survey. Observations at low radio frequency require advanced calibration and specific processing techniques to obtain deep, high-fidelity images. The calibration challenges include the correction for the delay differences between antenna stations introduced by ionospheric distortions, which must be corrected direction-dependently being related to the free electron column density along each line of sight through the

ionosphere, and the time-varying station beam shape. Indeed, LOFAR stationary antenna units imply that sources are tracked across their motion in the sky by adjusting the delays between the dipole elements. Further errors are due to small differences in the station beam models and shapes. For a detailed discussion of the systematics effects inherent LOFAR data we refer to de Gasperin et al. (2018).

In order to be corrected for all the direction-dependent and independent errors, a specific pipeline, DDF-PIPELINE[2], has been designed to process LoTSS observations (Shimwell et al., 2019, and references therein). Here we report the stages of the calibration:

1. Direction-independent spectral deconvolution and imaging;
2. Sky model tesselation in 45 directions;
3. Direction-dependent calibration cycle 1;
4. Bootstrapping the flux density scale;
5. Direction-dependent spectral deconvolution and imaging cycle 1;
6. Direction-dependent calibration cycle 2;
7. Direction-dependent spectral deconvolution and imaging cycle 2;
8. Direction-dependent calibration cycle 3;
9. Direction-dependent spectral deconvolution and imaging cycle 3;
10. Facet-based astrometric correction.

Recently, an additional step, the extraction, has been developed to further improve the calibration of LoTSS data (van Weeren et al., 2020). In this step all sources are subtracted, apart from those in a specific, small (< 1 deg), user-defined region, from the visibility data. After the subtraction, the visibilites are phase-shifted at the center of the region of interest, to allow to optimally combine observations from multiple pointing centers with joint imaging and deconvolution. Eventually, the visibilites in the region of interest are self-calibrate to further improve the final results. In order to carry out a good self-calibration, the region of interest has to include, at least, one bright point source with a flux above 0.1 Jy. Our contribution was the developing of a routine that, for a given target, individuates the most suitable calibrators in the corresponding LoTSS pointing, and defines a proper square box that includes both the target and the calibrator.

3.4 A revolution for galaxy cluster studies

Here we briefly discuss the importance, and the potential, of the LOFAR observations, including those provided by LoTSS, in the study of galaxy clusters. Diffuse radio source are ideal candidates for low-frequency radio observations because of their steep spectral index ($\alpha < -1$, e.g. van Weeren et al., 2019, and references therein), which entails a significantly higher surface brightness at lower frequencies and, hence, an easier and more solid detection.

Low-frequency observations probe low-energy particle that have typical lifetimes of a factor ~ 3 longer than the high-energy particles traced by high-frequency

[2] https://github.com/mhardcastle/ddf-pipeline

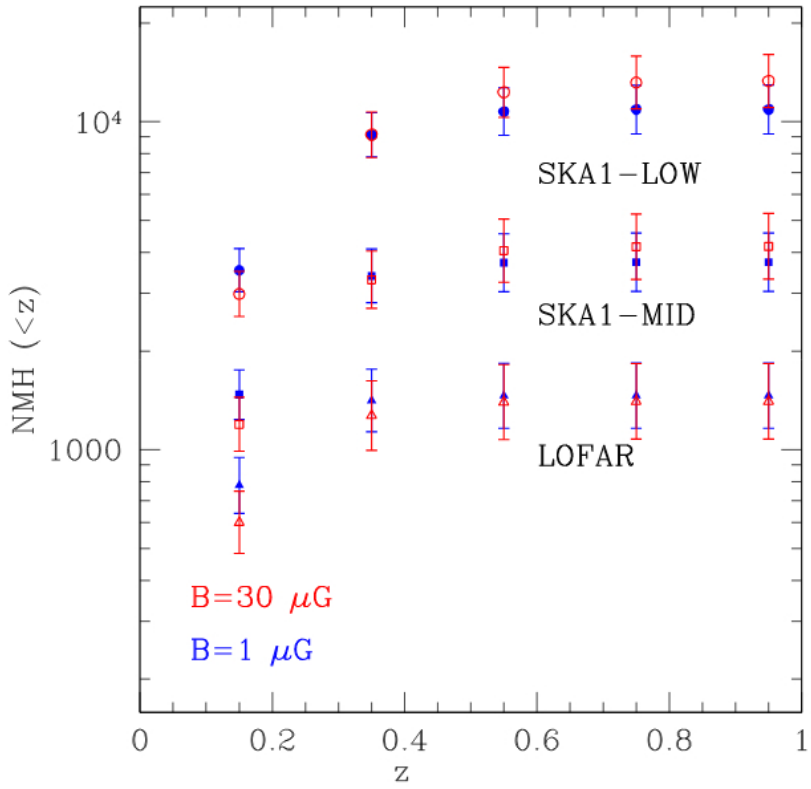

Figure 3.6: Integral number of radio mini-halo candidates observable at 140 MHz by LOFAR (triangles) and SKA1-LOW (circles), and at 1.4 GHz by SKA1-MID (squares) as a function of redshift, estimated by assuming two reference values of $B = 1\mu$G (blue) and $B = 30\mu$G (red) (Gitti et al., 2018).

radio emission. This difference in time-scales is crucial when we study the interaction between re-accelation processes and CRe, which are often invoked to explain the origin of large scale radio emission. A re-acceleration process, and re-energization in general, is effective only if the time-scale of the energy gain is smaller (or, at least, equal) to the time-scale of the energy losses. In other words, low-frequency observations have the potential to open a window on a class of new, low-efficiency processes related to the ICM micro-physics, in form of turbulence or gently compression of the radio plasma by the thermal gas (for a review Brunetti and Jones, 2014, and references therein).

For the case of giant radio halos, low-frequency observations allow to derive strong constraints on the re-acceleration of the radio-emitting CRe. The re-acceleration model predicts that while strong mergers would generate luminous radio halos, the events involving lower energies would produce fainter, steep-spectrum sources (e.g., Cassano, Brunetti, and Setti, 2006; Brunetti et al., 2008; Brunetti and Jones, 2014; Cassano et al., 2015). In this context, the detection of ultra-steep spectrum sources is a crucial test for this class of models (e.g., Wilber et al., 2018; Savini et al., 2018).

In general, for cluster scale radio emission it is becoming increasingly clear that the diffuse sources discovered at high frequency represent only the peak of the iceberg of the population of these objects because, in terms of energy and efficiency of the processes that generated them, they are the extreme cases (e.g., Cassano et al., 2015; Gitti et al., 2018). The fascinating prospective, and also the challenge posed

by the new frontier opened by LOFAR, is that the number of known diffuse radio sources is going to rise by order of magnitudes in the next years (Figure 3.6), thus permitting us, for the first time, to carry out detailed and solid statistical studies of the properties of radio sources in galaxy clusters.

In the following Chapters we are going to introduce the architecture of the LoTSS-PSZ2 automated catalog (Chapter 4), which will support the statistical, large-sample studies outlined in this Section, and then we will explore the brand-new LOFAR observations of the relaxed clusters Abell 2626 (Chapter 5) and 2A0335+096 (Chapter 6), concluding with the first low-frequency study of a jellyfish galaxy (Chapter 7).

Chapter 4

The LoTSS-PSZ2 cross-check catalog

4.1 Introduction

Radio studies of large samples of clusters can address fundamental questions, such as the number of diffuse radio sources and how the fractions evolves with redshift and cluster mass. Moreover, studies of large samples of radio halos can constrain the re-acceleration model by testing its key predictions: the connections between merging systems and radio halos, the evolution of halos fractions with the cluster mass, and the presence of faint, ultra steep-spectrum halos in systems with minor mergers (e.g., Brunetti et al., 2009; Cassano et al., 2010; Cuciti et al., 2015; Cassano et al., 2016).

The first statistical studies, specifically for giant radio halos, are have been carried out through the GMRT Radio Halo Survey (Venturi et al., 2007; Venturi et al., 2008; Kale et al., 2013; Kale et al., 2015) for a sample of X-ray selected clusters in the redshift range 0.2-0.4. The advent of cluster surveys based on the SZ effect has permitted to define unbiased mass-selected samples, which is less biased than X-ray selected samples toward relaxed systems (Rossetti et al., 2016; Rossetti et al., 2017; Andrade-Santos et al., 2017; Lovisari et al., 2017). Moreover, as discussed in Chapter 1, the total mass set the energy budget of galaxy clusters, thus it is a crucial quantities for these studies.

However, all these studies are limited by the sensitivity of previous radio telescopes (VLA, GMRT) and, most important, by the fact that the observations were generally carried out at high frequencies (600-1400 MHz). In this context, LoTSS represents a breakthrough by giving us, for the first time, the possibility to carry out statistical studies of large samples of diffuse radio sources at low frequencies (e.g., van Weeren et al., 2020; Osinga et al., 2020; Di Gennaro et al., 2020).

LoTSS clusters can be selected according to their mass to compose samples for statistical studies, where the mass can be inferred from the Planck 2nd Sunyaev-Zeldovich Source Catalog (PSZ2) provided by the Planck collaboration (Planck Collaboration et al., 2016). The PSZ2 catalog is the largest SZ-selected sample of galaxy clusters yet produced. It contains 1203 confirmed clusters, of which 858 are are in the northern sky and therefore are set to be observed by the LoTSS. In order to effectively carry out these studies, an efficient tool to organize the work of the LOFAR working group and to summarize all the information already available for each cluster can be highly useful.

4.2 Architecture

For this reason, in collaboration with the SKP staff we developed an automated cross-check catalog between the PSZ2 catalog and the LoTSS database, which tracks the status of each pointing of the survey from the observation scheduling to the data processing. Specifically, the catalog reports, for each one of the 858 PSZ2 cluster in the northern sky, the following details:

- ◇ PSZ2 name: the first identification of the cluster;
- ◇ J2000 coordinates expressed in degrees;
- ◇ Alternative names of the cluster: a string showing all the alternative names of the object from other catalogs (e.g. Abell);
- ◇ Redshift;
- ◇ M_{500}: Mass of the cluster within R_{500} expressed in solar masses;
- ◇ *Chandra* and *XMM-Newton* archival observations: two strings comprising observation ID, availability status and total exposure time in ks for each observation covering the cluster;
- ◇ LoTSS pointings: a list of all the LoTSS pointing covering the cluster;
- ◇ Observation, calibration and extraction status: for each interested LoTSS pointing, the status (not started, scheduled or done) of the three stages of the processing;
- ◇ Self-calibration status: if one or more extracted datasets are available, the status of the final self-calibration is reported;
- ◇ Image and image status: a link to the preview of the final, extracted and self-calibrated image of the cluster, and the final judgment on the quality/usability of the image after a visual inspection by the SKP staff;
- ◇ PI and project: information of the project PI which is working on the cluster and the statistical sample to which it belongs (if any).

To achieve this, we designed an architecture, which is schematized in Figure 4.1, composed of:

- ◇ a Python 3.0 software, called `archivist.py`, which reads the inputs information (PSZ2 name and coordinates) from a starting catalog, collects all the remaining information by querying several servers and provides and ordered output;
- ◇ a Google spreadsheet, which works both as primary input for `archivist.py` and front-end interface for the user;
- ◇ a Google Drive cloud storage to permit the online preview of the images, by also providing a backup storage for the catalog itself.

Google was naturally chosen as platform to develop the catalog because they provide public, flexible, and user-friendly Python APIs to manage both the spreadsheet and the cloud storage. Moreover, the Google spreadsheet itself offers a set of on-line, built-in tools to perform some basic operations on the dataset, as data filtering and

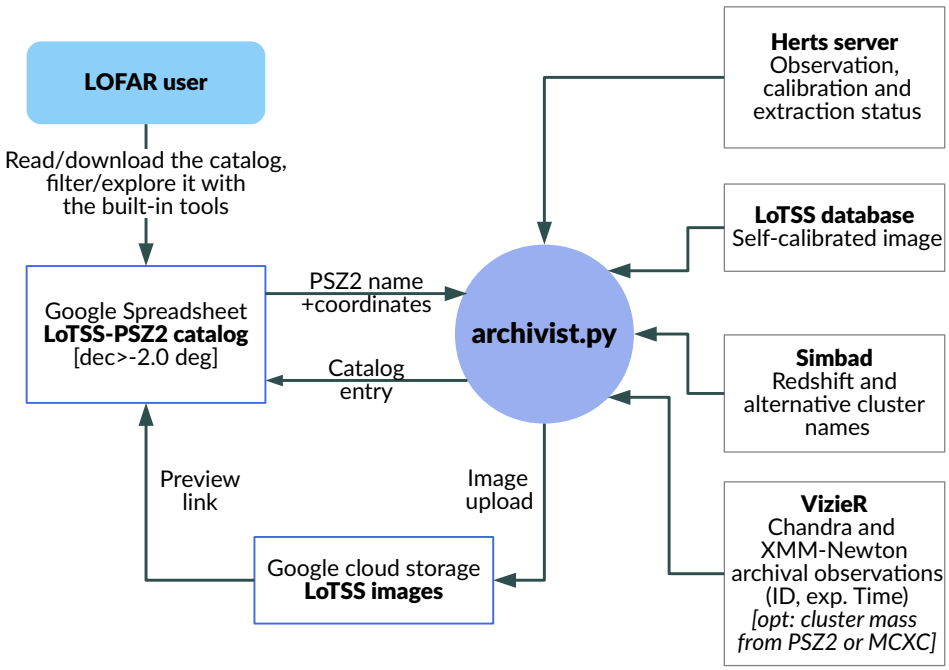

Figure 4.1: Infographic of the catalog.

averaging. The catalog is accessed through the Google spreadsheet web page.

Behind the curtain, `archivist.py` runs by reading information from the on-line catalog and using these information to collect the relevant details by querying several servers (Figure 4.1). The coordinates of each cluster are used to locate them on the LOFAR survey database hosted on the Herts server at the University of Hertfordshire and to retrieve the details about the observation and data processing status. If a self-calibrated image is present in the LOFAR server in Leiden, a copy of that image is uploaded on the Google cloud storage and a preview link is created. Then two queries are sent to Simbad and Vizier astronomy databases, through the `astropy` package (Astropy Collaboration et al., 2013), to collect the alternative names, the redshift and the archival X-ray observations of the cluster. Finally, `archivist.py` reports all these information on a string and upload it on the on-line spreadsheet (Figure 4.2). This operation is repeated for each one of the 858 PSZ2 clusters with declination above -2.0 degree, which is the nominal limit of LoTSS. On each run of `archivist.py`, the entries for each cluster are updated automatically, with the exception of the image status, PI and project voices which are modified manually by the SKP staff. In order to run the code, are necessary Google and Herts credentials and a direct access to the Leiden Sterrenwatch network with permissions to read the local disks where the images are stored.

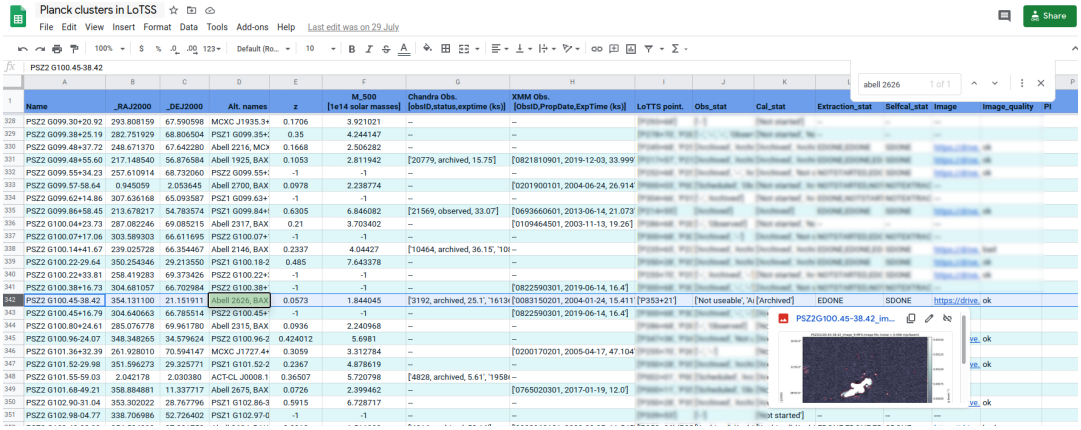

Figure 4.2: Example of the catalog entry for Abell 2626 (PSZ2 G100.45-38.42), including the survey image.

4.3 Results

The result is an on-line spreadsheet that can be easily accessed by everyone with a Google account (Figure 4.2). The catalog can be read on-line, or it can be downloaded in several formats (e.g., .txt, .xlsx, .csv) to be analyzed off-line. As mentioned before, the built-in tools allow to filter the catalog in smaller samples based on custom criteria, such as specific intervals in mass or redshift. These sub-samples can be inspected as separated databases which are keep updated together with the main database. The advantages of this architecture are double fold. On the one hand, this automated catalog can be easily updated to keep track of the progress of the LoTSS survey and the *Chandra* and *XMM-Newton* archive simply by running `archivist.py`. On the other hand, different cross-check catalogs can be produced simply by providing a different input catalog (e.g. Abell clusters or a custom one). In this case, the cluster mass can be collected from the PSZ2 or MXCX catalog with VizieR.

This catalog is already available and it is actively supporting the research of the SKP Galaxy cluster working group. Several mass- and redshift-selected subsamples, designed to study different aspects of the origin of diffuse radio emission with a solid statistical approach, have already been created. The study of large mass selected samples in the LoTSS DR2 area, which is going to covers 5700 square degrees of the northern sky by 2021 (see Figure 3.5 in Chapter 3), is ongoing as a collaboration between Bologna, Leiden and Hamburg. The overview provided by this catalog has also permitted to successfully plan observational proposals aimed to follow-up the current observations (e.g., accepted GMRT proposal 38025, 128h, PI Cuciti, with Ignesti). A complementary catalog, based on the same architecture and covering the MCXC clusters is already online.

Chapter 5

The great Kite in the sky

Based on Ignesti et al., 2018, A&A, 610 and Ignesti et al., 2020, A&A, 643, A172

5.1 Introduction

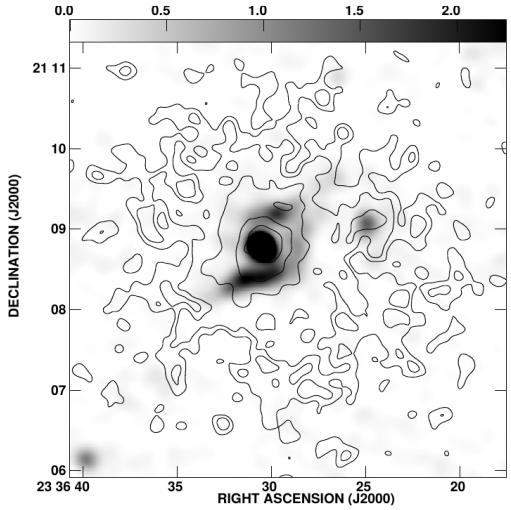

Figure 5.1: VLA at 1.4 GHz image of Abell 2626 with a resolution of 12.9×12.1 arcsec, with the *ROSAT* X-ray contours on top (Rizza et al., 2000).

Among the radio sources observed in galaxy clusters, the one at the center of the relaxed galaxy cluster Abell 2626 (z=0.0553, Struble and Rood, 1999, the adopted cosmology yields a luminosity distance of 246.8 Mpc and 1 arcsec = 1.1 kpc)[1] stands out for its unique properties. The discovery of diffuse radio emission at the center of the cluster surrounding the radio source 3C464 was reported for the first time by Rizza et al. (2000). In the first VLA image at 1.4 GHz, with a resolution of 12.9×12.1 arcsec, the source resembled an amorphous structure extended for ∼100 kpc around the central galaxy IC5338 (Figure 5.1). Due to tits position and size, it was originally classified as a MH (Gitti et al., 2004), the class of diffuse radio sources observed at the center of relaxed cluster which we discussed in Chapter 1.3.4.

In these VLA images the central radio source shows two symmetric substructures embedded in the diffuse emission around the central galaxy (Figure 5.2), which are uncommon for a MH. On the basis of a detailed analysis of the X-ray emission and the presence of two optical nuclei at the center of the galaxy, Wong et al. (2008a) suggested that these symmetric features could be the remnants of past activity of the central active galactic nucleus (AGN), where the precession of the AGN might have left two fossil plasma trails. This scenario was supported by the presence of two nuclei in the BCG IC5338, which could have provided the gravitational influences necessary to trigger the AGN precession.

[1] `http://www.astro.ucla.edu/#7Ewright/CosmoCalc.html`

Follow-up, deeper observations carried out with the Very Large Array (VLA) at 1.4 GHz in A+B configuration provided an high-resolution image at 1.5 arcsec that revealed that the source is not amorphous, but instead most of the emission comes from three elongated and collimated structures that were called "arcs" (Gitti, 2013a). The arcs are observed in the northward (N), westward (W) and southward (S) of the central galaxy, with a junction between the southern and western ones (Figure 5.4, top-right panel). The most puzzling features is the remarkably symmetric northern and southern arcs and their concavity, which is directed outward and earned this source the name of the "Kite". In these 1.4 GHz images the major and minor axis are 120 and 40 kpc, respectively. The minimum, projected distance of the arcs from the central AGN is $\sim$ 25 kpc. The discovery of the third arc suggested a more complex scenario than the one invoked by Wong et al. (2008a), which could have involved AGN activity by both the nuclei of IC 5538, or a combination of multiple phases of activity and the spin-flip of the black hole (e.g., Campanelli et al., 2007).

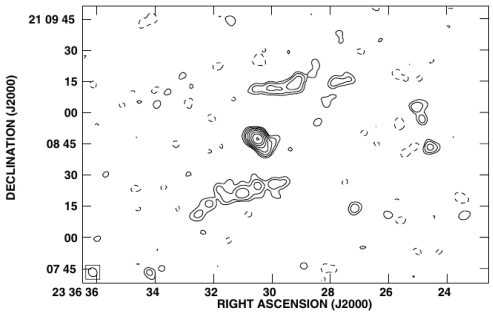

Figure 5.2: VLA image at 1.5 GHz of Abell 2626 from Gitti et al. (2004).

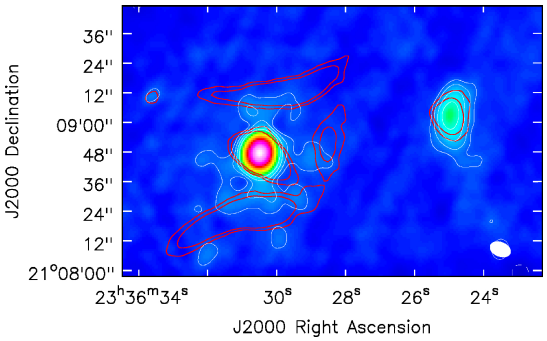

Figure 5.3: JVLA image at 5.5 GHz with a resolution of 4.9×4.4 arcsec (colormap and white contours), with the VLA 1.4 GHz image contours smoothed to a comparable resolution (red) (Ignesti et al., 2017).

New insights into its origin came from further radio observations at a different frequencies. By analyzing archival GMRT data at 610 MHz, Kale and Gitti (2017) discovered the presence of a fainter fourth arc on the east (E), thus completing the symmetry of the system (Figure 5.4, top-left panel). They produced a spectral index map between 610 MHz and 1.4 GHz with a resolution of 8.0×4.3 arcsec, measuring a spectral index in the arcs of $\alpha \sim -2.5$. The gravitational lensing was proposed as an alternative to the precession scenario because the symmetric arcs resembled the warped figures produced by this process.

Subsequently, Ignesti et al. (2017) presented JVLA images of the Kite obtained at 3.0 and 5.5 GHz in C-configuration, finding that the arcs have a steep spectral index $\alpha \sim -3$ up to 3 GHz, with no clear evidences of spectral index gradient along the arc length. These results severely constrained the jet-precession scenario because if the arcs were created gradually by the AGN, then a trend in spectral index was expected due the radiative ageing of the plasma. Moreover, the 5.5 GHz images revealed the presence of extended emission between the BCG and the arcs, thus supporting the scenario that that radio arcs were embedded in the MH (Figure 5.3). Ignesti et al. (2018) carried out a detailed study of the deepest *Chandra* observation available of the cluster, discovering a cold front at the center of the cluster and that the edge of the sloshing coincides remarkably well with the junction between the S and W arcs.

Subsequent studies confirmed the presence of a cavity in the ICM located beyond the S-W junction of the radio arcs and suggested that it was created by past AGN activity (Kadam et al., 2019). The discovery of the cold front, i.e. of the presence of sloshing, supported the idea that the arcs were the brightest part of an underlying MH, whose CRe had been re-energized by the compression and/or the turbulence (e.g., Mazzotta and Giacintucci, 2008; ZuHone et al., 2013b; Giacintucci et al., 2014a).

Recently, the LoTSS survey (see Chapter 3) provided a new observation at 144 MHz of this cluster made with LOFAR. As discussed in this Thesis, low-frequency observation explore the life-cycle of low-energy CRe, thus they can provide precious insights into the physics of diffuse radio emission. For this reason, we analyzed the new LOFAR data to solve the mystery of the origin of the Kite (Ignesti et al., 2020b).

In this Chapter we revisit the work carried out during the Ph.D. project, and presented in Ignesti et al. (2018) and Ignesti et al. (2020b), that contributed to solve the mystery of the Kite. We present the analysis that lead to the discovery of the cold fronts and the subsequent work in which we analyzed the new LOFAR data, which connected all the pieces of the puzzle, and we finally propose a new explanation for the origin of the source.

5.2 Data preparation

5.2.1 Radio data

In this work we present the analysis of the pointing P353+21 of the LoTSS survey (Shimwell et al., 2017; Shimwell et al., 2019). The observation was made using the Dutch High Band Antenna (HBA) array, which operates in the 120-168 MHz band, for a total observation time of 8.33 hrs. We reduced the dataset using the direction-dependent data-reduction pipeline DDF-PIPELINE[2] v. 2.2 developed by the LOFAR SKP, which we presented in Chapter 3. The data processing makes use of PREFACTOR (van Weeren et al., 2016; Williams et al., 2016; de Gasperin et al., 2019), KILLMS (Tasse, 2014; Smirnov and Tasse, 2015) and DDFACET (Tasse et al., 2018) to perform the calibration and imaging of the entire LOFAR field of view. Then, we performed additional phase and amplitude self-calibration cycles to correct the residual artifacts in a smaller region extracted from the observation and centered on the source following the procedure presented in van Weeren et al. (2020)

We produced images at different resolutions using WSCLEAN v2.6 (Offringa et al., 2014) and using several different Briggs weightings (Briggs and Cornwell, 1994), with `robust` going from 0 to -2, and multi-scale cleaning (Offringa and Smirnov, 2017). An inner uvcut of 80λ, corresponding to an angular scale of $43'$, was applied to the data to drop the shortest spacings where calibration is more challenging. Finally, we corrected for the systematic offset of the LOFAR flux density scale produced by inaccuracies in the LOFAR HBA beam model by multiplying it with a factor of 1.17 which aligns it with the flux-scale of the LoTSS-DR2 catalog that is calibrated off the NRAO VLA Sky Survey (NVSS) flux-scale. Following LoTSS

[2] `https://github.com/mhardcastle/ddf-pipeline`

(Shimwell et al., 2019), we adopt a conservative calibration error of 20%, which dominates the uncertainties on the LOFAR flux densities. The resulting images, with angular resolutions from 4 to 12 arcsec, are shown in Figure 5.4

We present here also the GMRT and the VLA images of Abell 2626 obtained from archival observations. We retrieved the archival GMRT observation of the cluster at 610 MHz, with a time on target of 95 mins, (observation 561, PI Clarke) and we processed it using the SPAM pipeline (see Intema et al., 2009; Intema et al., 2017, for details). For the VLA observation we used the calibrated dataset presented by Gitti (2013a). The images at 610 MHz and 1.4 GHz presented in this work were made using WSCLEAN to match the images presented in, respectively, Kale and Gitti (2017) and Gitti (2013a).

5.2.2 X-ray data

In this work we analyzed archival *Chandra* and *XMM-Newton* observations of Abell 2626 to produce images in the 0.5-2.0 keV band of the cluster. Specifically, we used the *Chandra* observations 3192 and 16136, for a total exposure time of 130 ks, and the *XMM-Newton* observations 0083150201 and 0148310101, for a total exposure time of 55 ks. We reprocessed the *Chandra* datasets with CIAO 4.10 and CALDB 4.8.1 to correct for known time-dependent gain and for charge transfer inefficiency. In order to filter out strong background flares, we also applied screening of the event files[3]. For the background subtraction, we used the CALDB "Blank-Sky" files normalized to the count rate of the source image in the 10-12 keV band. The data reduction of the XMM-Newton observations was performed using the Extended Source Analysis Software (ESAS) integrated in the Scientific Analysis System (SAS v16.1.0). Observation periods affected by soft proton flares were filtered out with the the mos-filter and pn-filter tasks. For each detector and observation we produced count images, background images, and exposure maps. These were combined to create a background-subtracted and exposure-corrected EPIC mosaic in the 0.5-2.0 keV band.

5.3 Image analysis and Results

At 144 MHz the source shows its striking, kite-like morphology at any resolution, ranging from 4 to 12 arcsec (Figure 5.4). The arcs are more extended along the major and minor axis than at higher frequencies, but their inner edges still have a projected distance of $\sim$ 25 kpc from the AGN and we detect extended emission between the AGN and the arcs. The LOFAR data reveal for the first time two large "plumes" of emission emerging from the ends of the arcs in in the south-east and north-west directions (Figure 5.4, middle and bottom-right panels), more than doubling the projected size of the Kite to $\sim$220 kpc ($\simeq 3.7'$). The new data also reveals two lobes of emission toward N-E and S-W. Finally, we observe extended emission associated with the galaxy JW100 (IC5337), which we are going to discuss in details in Chapter 7.

In Figure 5.5 we report the contours of the mid-resolution ($6.7'' \times 5.6''$, Figure 5.4 central panel) image where we label the various components of the radio emission observed by LOFAR. In this image we measure a 144 MHz flux density S_{144} =7.7$\pm$1.6

[3] http://cxc.harvard.edu/ciao/guides/acis_data.html

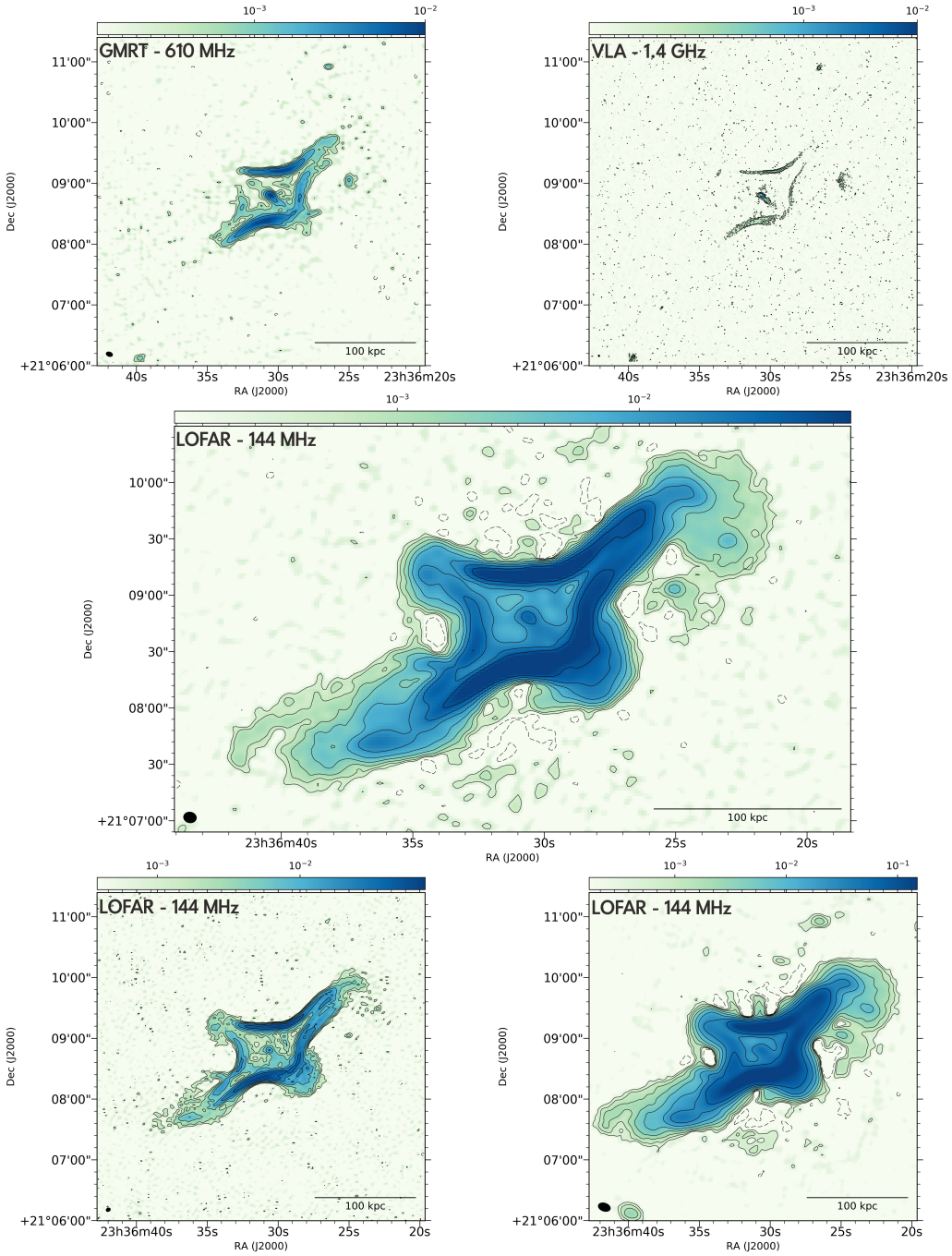

Figure 5.4: Images of the Kite at different frequencies involved in this work, the instrument and the frequency are reported in the labels. Top-left: GMRT image at 610 MHz, the RMS is 120 μJy beam^{-1} and the resolution is 6.2″×4.1″; Top-right: VLA A+B image at 1.4 GHz, the RMS is 13 μJy beam^{-1} and the resolution is 1.5″×1.4″. In both images the contours are at the -3, 3, 6, 12 and 24 σ levels. Middle: LOFAR image obtained with `robust=-0.75`, the final resolution is 6.7″×5.6″ and the RMS is 120 μJy beam^{-1}. The contours are at the -3, 3, 6, 12, 24, 48, 96, 192, 384 σ level; Bottom-left: LOFAR image obtained with `robust=-2`, the final resolution is 4.2″×3.2″ and the RMS is 380 μJy beam^{-1}. The contours are at the -3, 3, 6, 12, 24, 48, 96 σ level; Bottom-right: LOFAR image obtained with `robust=-0.25`, the final resolution is 12.2″×7.7″ and the RMS is 140 μJy beam^{-1}. The contours are at the -3, 3, 6, 12, 24, 48, 96, 192, 384 σ level. The surface brightness is reported in units of Jy beam^{-1}.

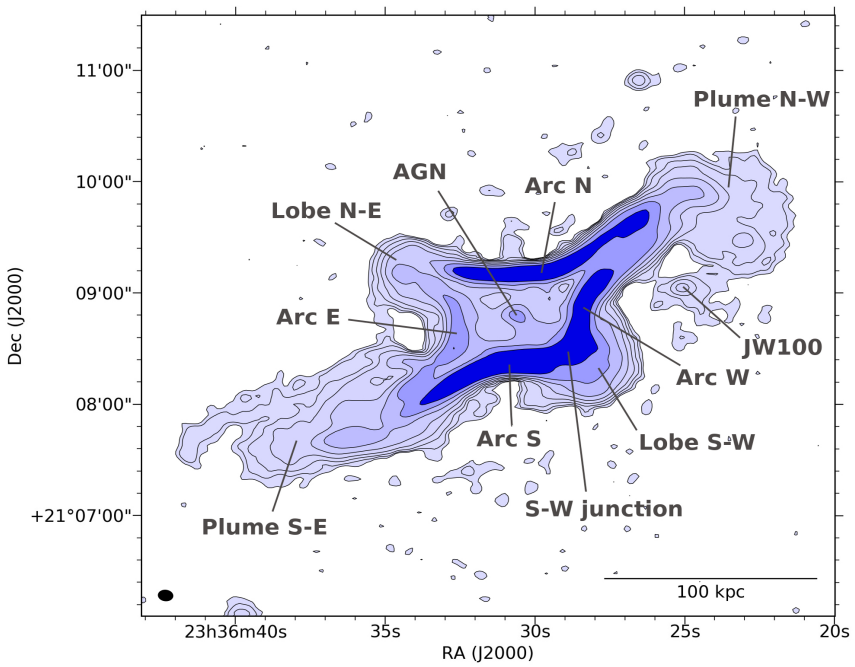

Figure 5.5: Contours of the LOFAR 144 MHz emission at a resolution of $6.7'' \times 5.6''$ (Figure 5.4, middle panel) color-coded for the surface brightness level. We label the main features studied in this work.

Jy for the whole source. The surface brightness contours show that the arcs, whose high brightness at low frequency ($> 100\sigma$) was expected due to their steep spectra (Kale and Gitti, 2017; Ignesti et al., 2017), dominate the total emission of the Kite.

5.3.1 Spectral index map

In order to probe the properties of the relativistic electrons, we combined the new LOFAR data with archival GMRT and VLA observation at 610 MHz and 1.4 GHz, respectively, to produce a resolved, 3-band spectral index map. First we produced new maps at the three frequencies using WSCLEAN with a `uniform` weighting for the visibilities and a uv-range of 200-46000 λ in order to match the same spatial scale in all wavelengths. The lower cut at 200 λ implies a largest recoverable angular scale of $\sim 20'$, hence it allows the detection of the complete structure of the Kite for each band. The resulting images were smoothed to a common resolution of $7'' \times 7''$. The resulting RMS noise of the LOFAR, GMRT and VLA maps are, respectively, 280, 150 and 35 μJy beam^{-1}.

We combined the three maps to produce a spectral index map and the corresponding error map. We compared the emission above the 3σ level of the LOFAR image with the emission above 2σ for the GMRT and VLA images to probe the steep-spectrum emission in the lobes. For each pixel of each map, we measured the flux density, S, and its associated error, $\sigma_S = [(f \times S)^2 + \mathrm{RMS}^2]^{1/2}$, where $f = 0.2$ is the calibration error (Shimwell et al., 2019). For each frequency, we extracted random values of the flux within the associated error by assuming a normal distribution. We fitted the three boot-strapped flux densities with a power-law spectrum $S(\nu) \propto \nu^{\alpha}$ to evaluate the spectral index. We repeated this procedure 500 times for each pixel, thus ending with a normal-like distribution of values of α whose skewness depends

on the relative uncertainties of the flux densities in each pixel. The final spectral index map in Figure 5.6 shows in each pixel the mean of these distributions, whereas the error map shows the standard deviations. This approach allows to get reliable errors on the spectral index that reflect the uncertainties of the three measurements.

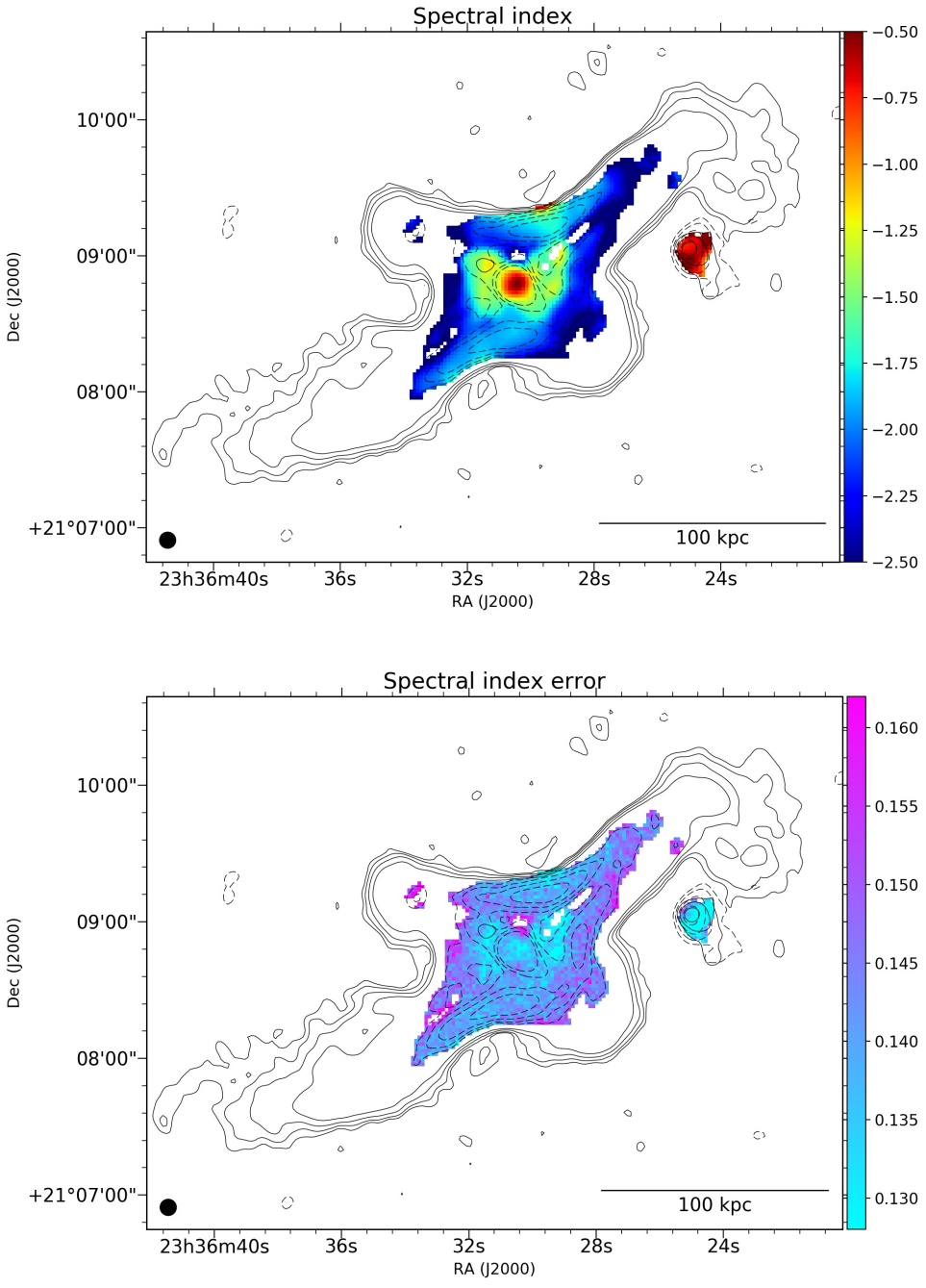

Figure 5.6: Spectral index map (top) and relative error map (bottom) obtained combining LOFAR, GMRT and VLA maps at, respectively, 144, 610 MHz and 1.4 GHz. The resolution is $7'' \times 7''$. We report the contours at the 3, 6, 12, 24 σ levels of the LOFAR (continuous, $\sigma = 280$ μJy beam^{-1}) and the VLA (dashed, $\sigma = 35$ μJy beam^{-1}) images produced with matching uv-range (200-46000 λ).

This spectral index map shows regions with different behaviours, in particular

we can distinguish two distinct regions. The central region within the arcs shows a flatter spectrum, $-1 < \alpha < -0.5$, likely dominated by the central AGN. In the arcs the spectral index is steeper, with $\alpha < -1.5$. Thanks to the resolution and sensitivity provided by the new LOFAR data, we observe, for the first time, a spatial gradient along the arcs N and S, where the spectrum steepens moving from the centers of the arcs to their ends. On the contrary, the arcs E and W do not show this trend, instead they exhibit more uniform and steeper spectra ($\alpha < -2$). Despite the low threshold in surface brightness at the higher frequencies, we could not map the spectral index of the lobes and the plumes. For the latter, we could derive only an upper limit for the spectral index $\alpha < -1.5$ by comparing their mean surface brightness at 144 MHz (in units of Jy beam^{-1}) with the 2σ level of VLA image.

Finally we used the LOFAR and VLA images produced for the spectral index analysis to estimate the integrated spectral index of the Kite. By comparing the total flux densities within the 3σ contours of the 144 MHz map, we estimated an integrated spectral index $\alpha = -2.0 \pm 0.4$ between 144 MHz and 1.4 GHz, that entails a k-corrected radio power at 144 MHz of $P_{144} = 4\pi D_L^2 S_{144}(1+z)^{-\alpha-1}$ $=6\times10^{25}$ W Hz^{-1}, where $D_L = 246.8$ Mpc is the Luminosity distance.

5.3.2 Point-to-point analysis

We performed a point-to-point analysis to explore the spatial correlation between the spectral index, α, and X-ray surface brightness, I_X, which is a proxy of the thermal plasma density. Observing (or not) a spatial correlation between the two quantities could potentially provide an insight into the intrinsic relation between the thermal plasma and the non-thermal ICM components, i.e. the magnetic field and the relativistic particles.

In this work we combined the observations of the cluster at 144, 610 MHz and 1.4 GHz with the *Chandra* X-ray image. By using the PT-REX code (see Appendix A), we sampled the region of the Kite where the 610 MHz emission is above the 3σ level with a grid whose cells are $12'' \times 12''$ in size to have a compromise between the signal-to-noise of each cell and the number of significant points. On the one hand, this sampling assures a reliable estimate of the spectral index for the low-band (144-610 MHz) of the spectrum in each cell. On the other hand, it introduces large uncertainties in the high-band (610 MHz-1.4 GHz) for those regions where the radio surface brightness at 1.4 GHz is below 3σ. The grid includes the central region (except the AGN and the jet-like feature which we excluded from this analysis), the arcs and part of the emission in the NW-SE direction (see Figure 5.7). For each cell of the grid, we measured the flux densities at the 3 frequencies and the I_X from the *Chandra* image of the cluster to produce the color-color plot (Figure 5.7).

We observe that the majority of the points are located below the 1:1 line, indicating a perfect power-law spectrum from 144 MHz to 1.4 GHz. This implies that the spectrum of the radio emission is steeper in the 610 MHz-1.4 GHz band than in the 144 MHz - 610 MHz one in most of the Kite, i.e. the synchrotron spectrum is mostly curved. This, in addition to the steep spectrum, indicates that the radio plasma of the Kite is radiatively old. We observe that, in general, the flattest-spectrum emission is associated with the regions with the brightest X-ray emission, as highlighted by the colorscale, and we estimated Spearman ranks between α and I_X of 0.5 and 0.7 for the

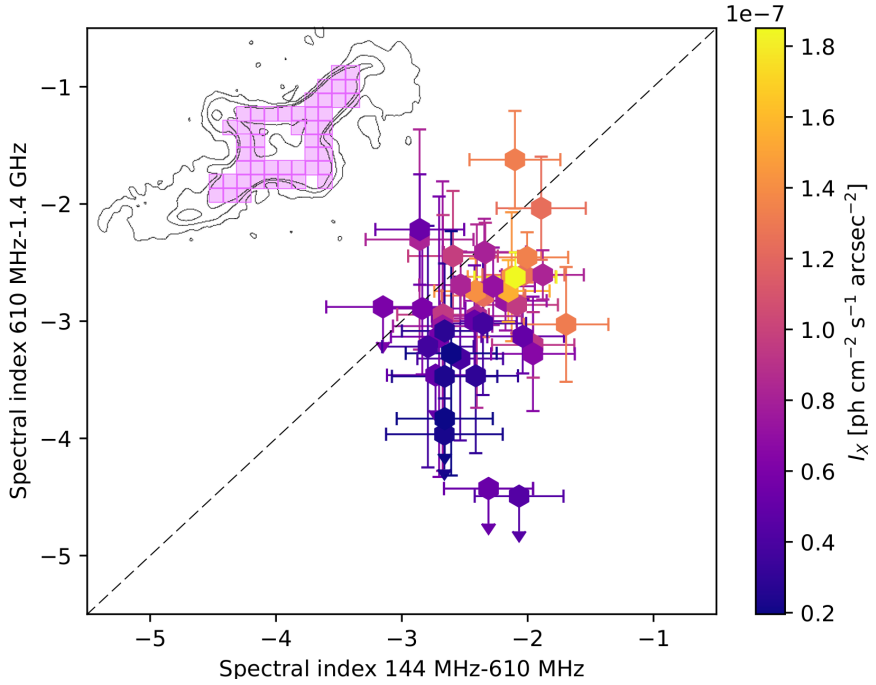

Figure 5.7: Spectral index in 610 MHz-1.4 GHz vs spectral index in 144 MHz-610 MHz band, color-coded for the X-ray surface brightness I_X. The values were measured in the cells of the green grid that is shown in the top-left corner, overlapped on the 3, 24, 96σ levels of the 144 MHz image involved in the spectral analysis. Cells where the relative error on the spectral index is greater than 50% are shown as upper limits.

low- and high-band, respectively. This indicates a spatial correlation between the slope of the synchrotron spectrum and the density of the thermal plasma along the arcs, that suggests a physical connection between the relativistic and thermal plasma which we are going to discuss in Section 5.4.

5.3.3 X-ray analysis

Residual maps

The cluster is relaxed and the I_X profile can be well described by a β-model profile (see Chapter 1.2.2). Therefore, by subtracting from the observed I_X a 2D β-model, fitted to the images, we can highlight substructures in the ICM, such as over-densities or depressions. We performed this analysis on both *Chandra* and *XMM-Newton* observations of the cluster using the package SHERPA (Freeman, Doe, and Siemiginowska, 2001). In both observations we masked the central AGN and the close spiral galaxy JW100, due to its extended X-ray emission not associated to the ICM emission. A detailed analysis of the X-ray emission of JW100 is going to be subject of Chapter 7, and it is presented in Poggianti et al. (2019b). The best fit parameters are core radius r_c= 13.36″, β = 0.45 for *Chandra* and r_c= 18.08″, β = 0.48 for *XMM-Newton*, the results are shown in Figure 5.8.

We found in both the observations an excess in surface brightness (red regions in Figure 5.8), which is extended from the center to the NE and crosses the northern part of the Kite, and is associated with a local excess of the thermal ICM density with respect to the mean gas density of the cluster. We observe also a depression in the SW direction (dashed ellipse in Figure 5.8) aligned with the jet-like features observed in the high-resolution observation at 1.4 GHz (Figure 5.4, top-right panel). The new

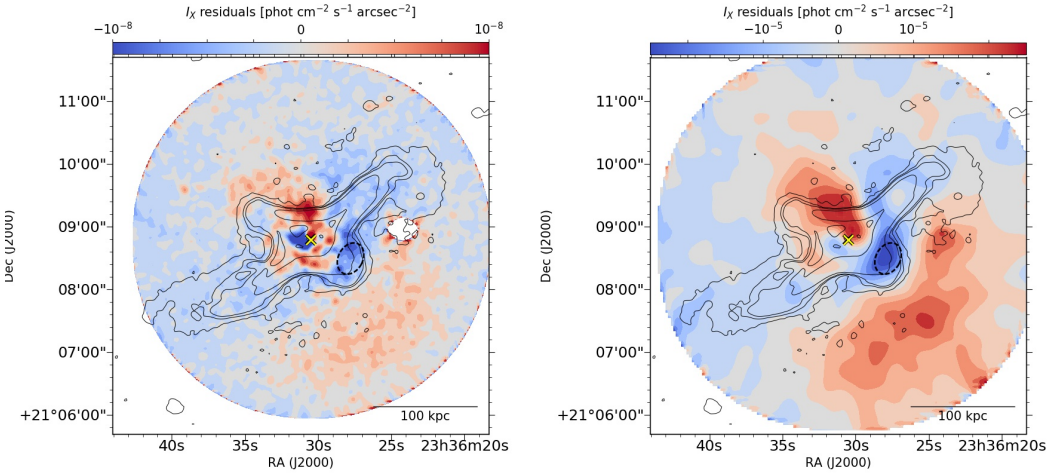

Figure 5.8: Comparison of the radio emission with the residual X-ray images produced with *Chandra* (left) and *XMM-Newton* (right) in the 0.5-2.0 keV band. Red indicates an excess with respect to the β-model, whereas blue is a deficit. The contours are the 3, 24, 48, 192σ of the image presented in Figure 5.4, middle panel. The images are smoothed with a gaussian filter of 2.5″ for *Chandra* and 15″ for *XMM-Newton*. the yellow cross and white mask indicate the position of, respectively, the AGN of IC5338 and the galaxy JW100. The black dashed ellipse indicate the position of the tentative cavity.

LOFAR data show, for the first time, that the radio plasma fills this structure, thus supporting the hypothesis suggested in Shin, Woo, and Mulchaey (2016) and Kadam et al. (2019) that it could be a radio-filled cavity. Kadam et al. (2019) also estimated an AGN mechanical power of 6.6×10^{44} erg s^{-1}, that, as we see in Chapter 1.3.2, is in the typical range for AGN radio-mode feedback in galaxy clusters. Therefore, we conclude that this radio-filled cavity indicates that the radio plasma could have been originally injected by the central AGN. Interestingly, the 144 MHz radio emission is extended toward N-E as well, but we do not observe evident depression in that region.

Spectral analysis

In order to investigate the nature of the spiral pattern that we found with the residual analysis, we carried out a spectral analysis of the cool core based on the *Chandra* observation 16139 (total exposure 110 ks, PI Sarazin), which is the deepest observation of the cluster currently available. We produced a spectral temperature map (Figure 5.9, top panel) by using the techniques described in O'Sullivan et al. (2011a). The map pixels are $\sim 5''$ (10 ACIS physical pixels) square. The value in each pixel is the best-fitting temperature obtained from an absorbed `apec` model fit to a spectrum extracted from a circular region centred on the pixel, with a radius chosen to ensure that it contains at least 1500 net counts. The effective resolution of the map is therefore determined by the size of the extraction regions, whose radii range from $\sim 5''$ in the cluster center to $\sim 20''$ in the outskirts. Since the spectral extraction regions are larger than the map pixels, individual pixel values are not independent and the maps are, thus, analogous to adaptively smoothed images, with more smoothing in regions of lower surface brightness.

This map shows that the ICM exhibits an inner cold region with $kT_{\rm cold}$ <2.8 keV and an outer hot region with $kT_{\rm hot}$ ∼3.4 keV. Remarkably, the edge of these regions coincides with the SW junction of the radio arcs observed at 1.4 GHz, whereas it results totally embedded in the 144 MHz emission. In the opposite direction, the cold

ICM is not confined to the inner part of Abell 2626, but it is elongated outside in a spiral-like shape that coincides with the northern spiral feature observed in the I_X residual map (Figure 5.8) and resembles the cold spirals often related to the sloshing of the ICM described in Chapter 1.3.3 (e.g., Markevitch and Vikhlinin, 2007). The temperature map also shows that the second brightest galaxy of the cluster, IC5337, is leaving a trail of cold plasma (kT ∼2.3 keV). This points out that the X-ray emission of this galaxy is not related to the ICM, as we discuss this in detail in Chapter 7.

The X-ray residual (Figure 5.8) and the spectral temperature (Figure 5.9, top) maps show that the ICM physical properties inside the 1.4 GHz SW radio arcs are different from outside, so we focused our analysis on the region across the SW junction to understand why. By following the geometry of the cold region observed in Figure 5.9, we divided the SW cluster region into several sectors. In these regions we extracted the background-subtracted, exposure-corrected I_X radial profiles and we fitted them with a broken power-law model (as described in Nulsen et al., 2005) in order to determine the position of the I_X jumps that we observe in the 2D residual map (Fig. 5.8). In two sectors to the south and to the west, which are shown in the bottom-left panel of Fig. 5.9 (top panels) labeled as 'Sector S' and ' Sector W', we detected I_X jumps located at distances from the core of 29.5 kpc and 26.4 kpc, respectively. They are associated to an ICM compression factor of $1.32^{+0.15}_{-0.13}$ (Sector S) and $1.37^{+0.19}_{-0.17}$ (Sector W), both detected above the 3σ level (Figure 5.9, central panels). We checked the solidity of our result by varying the extraction sectors (in both angular width and radial binning), always finding a density jump detection above 3σ.

We then divided the sectors into several annuli, which are reported in Figure 5.9 (bottom-left panel), to extract the ICM temperature, density and pressure radial profiles, by fitting the spectra of each annulus with both the projected `wabs·apec` and the de-projected `projct·wabs·apec` Xspec models, making sure to place the second and the third annuli across the I_X jump. We report the temperature and pressure profiles in Figure 5.9 (bottom panels). The profiles show that the I_X jumps coincide with a significant drop in the temperature toward the center, from $3.42^{+0.38}_{-0.28}$ keV to $2.50^{+0.19}_{-0.21}$ keV in Sector S and from $3.32^{+0.59}_{-0.36}$ keV to $2.31^{+0.29}_{-0.29}$ keV in Sector W. We observed the temperature drops in both the projected and de-projected profiles with a confidence level above 3σ. The pressure is instead continuous, thus indicating rough pressure balance across the front, which is a signature of the presence of a cold front. Therefore, we concluded that Abell 2626 shows a weak cold front which, interestingly, coincide with the 1.4 GHz radio emission, i.e. high-energy CRe, but, at the same time, it results embedded by the 144 MHz emission, i.e. the low-energy CRe.

5.4 Discussion

5.4.1 Morphology and spectral index of the Kite

Before delving into the discussion, here we summarize all the new features of the Kite discovered in our work. The LOFAR data show that the diffuse radio emission at 144 MHz is more extended than what we observe at higher frequencies (Figure 5.4, 5.10). LOFAR reveals two diffuse plumes at the ends of the arcs in the NW-SE direction. In the new images, we observe that the radio surface brightness outside

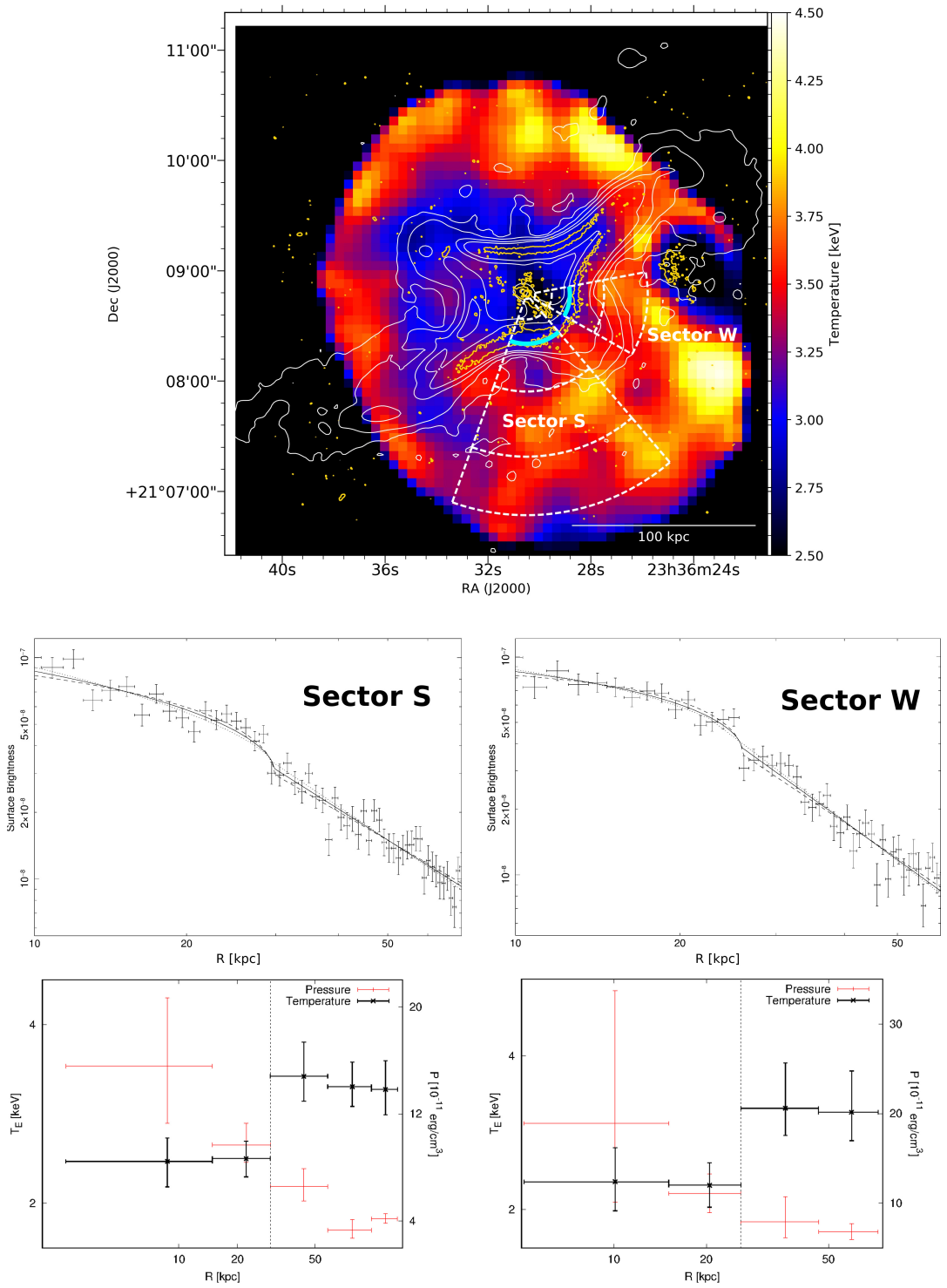

Figure 5.9: Top panel: Pseudo-temperature map in the 0.5-2.0 keV band with on top the contours of the 144 MHz (silver, resolution 6.7×5.6 arcsec) and 1.4 GHz (gold, resolution 1.5×1.4 arcsec resolution) radio emission, the sectors used to extract the spectral profiles (white dashed) and the position of the surface brightness jump (cyan). Central panels: Surface brightness radial profiles, expressed in units of counts px^{-2} s^{-1}, observed in the southern (left) and western (right) sectors. We report also the best-fit to the broken power-law model. The dashed lines show the upper and lower confidence bounds of the best-fit density ratios (corresponding to $1.32^{+0.15}_{-0.13}$ for the Sector S and to $1.37^{+0.19}_{-0.17}$ for the Sector W). Bottom panels: Projected temperature (black) and de-projected pressure (red) profiles measured in the sectors reported above. The black dashed line indicates the position of the front determined by the broken power-law fit to the surface brightness profiles shown in the upper panels.

the arcs drops by a factor ∼60 within ∼10 kpc, whereas in the plumes the emission declines more gradually in $\sim 50 - 60$ kpc. This indicates that in the arcs the non-thermal components (i.e. the magnetic field and relativistic electrons), which are traced by the radio emission, are efficently confined. The new observation also reveals that the cold front, which appears to delimit the high-frequency radio emission, is, at the same time, enveloped by the low-energy, radio-emitting plasma which fills the cavity located in front of the south-west jet observed at 1.4 GHz (Figure 5.8) and aligned along the major axis of IC5338 (Figure 5.10). But above all, the new observation shows that the S+W and N+E arcs compose two main structures which are almost symmetric with respect to the major axis (NW-SE).

The spectral index maps (Figure 5.6) shows that the Kite is a steep-spectrum source ($\alpha < -1.5$), in agreement with the previous results (Kale and Gitti, 2017; Ignesti et al., 2017), but we observe a spatial gradient along the arcs N and S, where the spectral index steepens from $\alpha \simeq -1.5$ their centers to $\alpha < -2$ toward their ends. Further insights into the properties of the Kite come from the residual maps (Figure 5.8) and the point-to-point analysis (Figure 5.7). The spectral index map (Figure 5.6) shows that the flattest regions of the arcs are located in the north and the south with respect to the central galaxy, while the residual X-ray maps (Figure 5.8) show that these regions coincide with an over-density of the thermal plasma, likely produced by the sloshing of the cool core. These two pieces of information are combined in the point-to-point analysis, where we observe that the flattest-spectrum emission comes from the regions with the brightest X-ray emission, i.e. the higher-density sloshing regions. The point-to-point analysis also reveals significant curvature in the spectrum, which is indicative of radiatively old plasma.

5.4.2 A new scenario for the origin of the Kite

Based on our results, we speculate on the origin of the Kite. On the one hand, on the basis of the exceptional morphology and spectral index trends, we claim that is very unlikely the Kite is a mini-halo. Moreover, the morphology revealed by LOFAR also discourages the lensing hypothesis (previously invoked in Kale and Gitti, 2017) because produce such a blend of collimated arcs and large plumes would require implausible combinations of lenses and scattering screens. On the other hand, in the new image at 144 MHz the Kite shows remarkable similarities with two specific classes of radio galaxies, the Z-shaped (e.g., Zier, 2005; Hardcastle et al., 2019) and X-shaped radio galaxies (e.g., Lal and Rao, 2007; Bruno et al., 2019; Cotton et al., 2020). The Kite shares the double-axis morphology with these radio sources, where the wings (i.e. the “plumes" of the Kite, see Figure 5.5) are more extended than the lobes. Moreover, the central, giant elliptical galaxy IC5338, is elongated in the same direction of the putative minor axis of the Kite from NE to SW. The extent of this is shown by the smoothed SDSS contours in the bottom panel of Figure 5.10, where a Gaussian kernel of width 1 arcsecond was used to improve sensitivity to the extended stellar emission and avoid confusion with surrounding point sources. Furthermore, the radio filled cavity (Figures 5.8) and the radio jets originating from the central AGN (Figure 5.10) are aligned along the same NE to SW axis.

Therefore, we suggest that originally the Kite was a radio galaxy whose central AGN produced the S-W cavity. In this framework, the peculiar, double-axis morphology of the Kite can be then explained by the backflow model (e.g., Leahy and

Williams, 1984; Hodges-Kluck and Reynolds, 2011). This hydrodynamical model, which is one of the possibilities that have been invoked to explain X-shaped radio galaxies, suggests that the plasma injected by the AGN along the jets can be redirected by the hot-spots or high-pressure environment back to the galaxy. In the case of axisymmetric backflow, Leahy and Williams (1984) noted that this process can cause the emission to grow in directions perpendicular to the angle at which the plasma impacts with the hot inter-stellar medium (ISM) of the galaxy. Therefore, for the case of the Kite, we suggest that the plasma was injected in the NE-SW direction, along the projected major axis of the IC5338 (Figure 5.10), to subsequently flow back and be redirected in the NW-SE directions to finally form the plumes. The lack of an AGN cavity toward NE could be due the presence of the northern over-density, that hide, via projection effects, any potential, smaller structure in that region.

However, there are several properties of the Kite that make this object peculiar and different from standard radio galaxies. First, the overall spectrum of the Kite ($\alpha < -1.5$) is steeper than the typical spectral index of active X-shaped radio galaxies ($\alpha > -1.5$, e.g., Lal and Rao, 2007), which indicates that the plasma is radiatively-old. The steep spectrum measured in the 144-610 MHz band (Figure 5.7) suggests that the break frequency of the spectrum, $\nu_{\rm br}$, is below 144 MHz and, hence, that we are observing only the radiatively-old part of the of the synchrotron spectrum. Therefore, by assuming a putative $\nu_{\rm br} < 100$ MHz and under the hypothesis that the local magnetic field, B, is in the range 5-15 μG, which are typical for radio galaxies (e.g., Croston et al., 2005), as discussed in Chapter 1.2.4 the radiative age of the arcs, $t_{\rm rad}$, can be estimated as:

$$t_{\rm rad} \simeq 3.2 \times 10^{10} \frac{B^{1/2}}{B^2 + B^2_{\rm CMB}} \left[(1+z)\nu_{\rm br}\right]^{-1/2} \ {\rm yr} \tag{5.1}$$

Under these assumptions, we determine the lower limit to the radiative age of the plasma to be between 5×10^7 and 2×10^8 yrs, which confirms that we are observing radio emission from old, fossil plasma. This time-scale is not far from the typical duty-cycle of an AGN ($\sim 10^8$ years, e.g., Morganti, 2017) and, thus, we suggest that the active phase that injected the relativistic plasma of the Kite likely ended recently.

Old radio plasma sitting in the center of clusters is expected to be uplifted due to buoyancy on a certain timescale. This provides complementary constraints to the age of the plasma in the Kite. The facts that the source preserves its X-shaped morphology and the plumes still sit at ~ 100 kpc from the central AGN implies that the plasma did not have enough time to evolve buoyantly. According to Churazov et al. (2001), the buoyant velocity of a bubble can be estimated as:

$$v_b \simeq v_k \sqrt{\frac{2V}{RSC}} \tag{5.2}$$

where v_k is the Keplerian velocity, which we approximate to the cluster dispersion velocity $\sigma_v \simeq 680$ km s^{-1} (Cava et al., 2009), S is the cross-section of the bubble, V its volume, R the distance from the central AGN and $C \sim 0.6$ is the drag coefficient.

By assuming the plumes as spherical bubbles with $r = 25$ kpc at a distance $R \simeq 100$ kpc from the AGN, Equation 5.2 gives us a reference buoyant velocity $v_b \sim 700$ km s^{-1}. This velocity entails a upper limit to the dynamical time-scale of

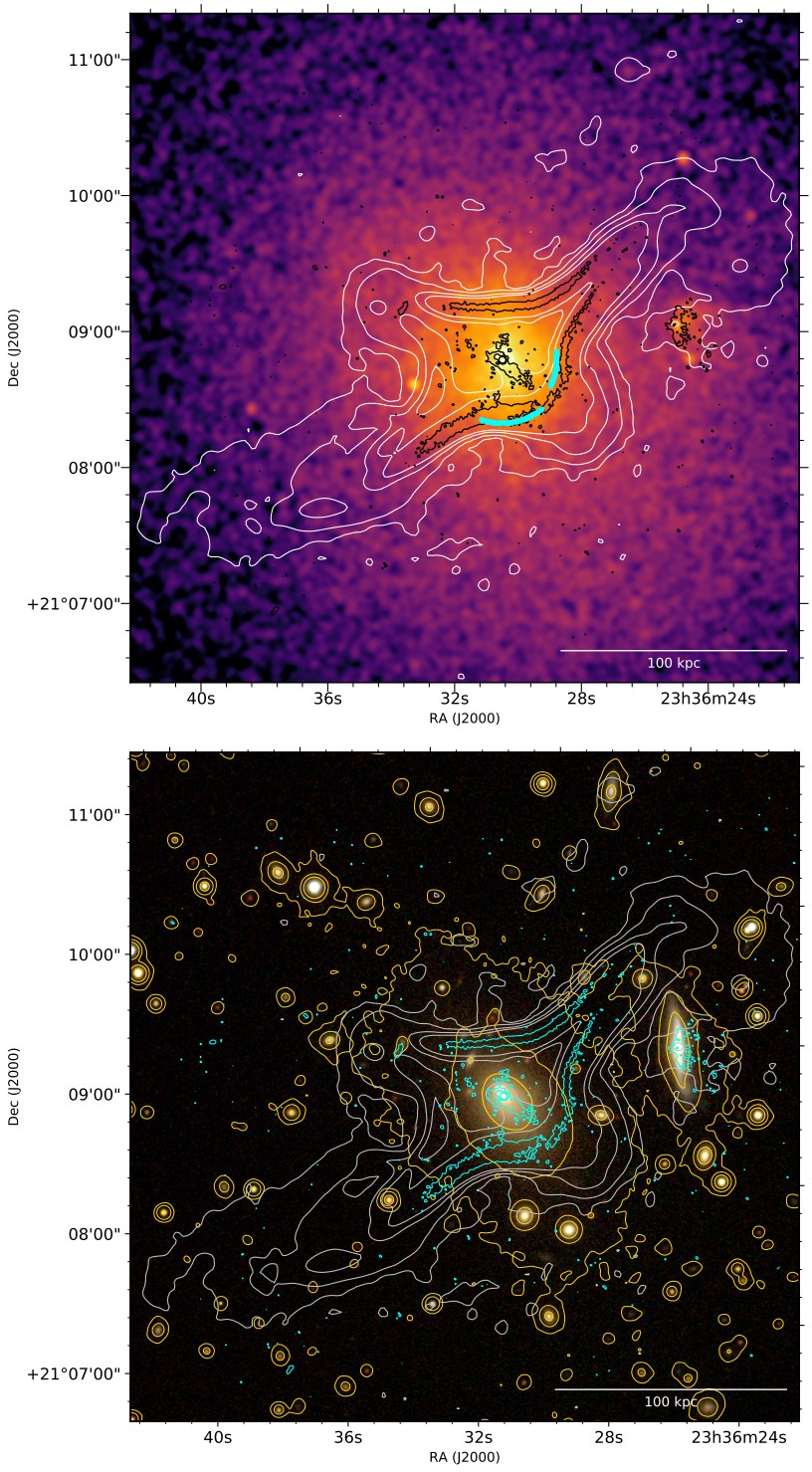

Figure 5.10: Top: *Chandra* X-ray image of Abell 2626 in the 0.5-2.0 keV band with the 3, 24, 96, 200σ level contours of the emission observed at 144 MHz in white (Figure 5.4, middle panel, $\sigma = 120$ μJy beam^{-1}) and the 3, 24, 96σ contours of the emission at 1.4 GHz in black (Figure 5.4, top-right panel, $\sigma = 13$ μJy beam^{-1}). In cyan is reported the position of the cold front observed in Ignesti et al. (2018); Bottom: Composite SDSS image from bands *i*, *r* and *g* with the 3, 24, 96, 200σ contours of the emission at 144 MHz in silver (Figure 5.4, middle panel), the 3, 24, 96σ contours of the emission at 1.4 GHz in cyan (Figure 5.4, top-right panel) and SDSS composite image smoothed with a Gaussian kernel of standard deviation 1 arcsecond at 6, 30, 150 times the RMS noise in the smoothed image (0.015 maggies) in yellow.

the plumes $< 1.5 \times 10^8 \, [\sin(\theta)]^{-1.5}$ yr, where θ is the angle between plumes and the line of sight, which is in agreement with previous constraints and suggests that the plasma is not significantly older than a typical AGN duty cycle ($\sim 10^8$ yrs).

Secondly, contrary to what is generally observed or expected in back-flowing radio galaxies, in the Kite the plumes have a projected length in the NW-SE direction that is almost double of the length of the jets, which we assumed originally directed in the NE-SW direction. This could be both due to local environmental properties (i.e. a stronger environmental pressure that restricted the expansion of the plasma in the jet direction) combined with bouyant motions of the radio plasma in the plume or complex projection effects due to a possible inclination of the Kite with respect to the plane of the sky. The latter hypothesis is partially supported by the spread of the color-color diagram (Figure 5.7), which could be due to the mixing of plasma with different radiative ages, hence spectral indices, along the line of sight.

Finally, the most obvious difference with X-shaped galaxies is that the arcs of the Kite are clearly detached from the central AGN (Figure 5.4, bottom-left panel) and, on the contrary to what is observed for X-shaped galaxies, the brightest part of the Kite are the arcs, where we observe also a gradient in spectral index and a spatial correlation between the α and the X-ray emission (Figure 5.7).

The role of the ICM dynamics

We interpreted the presence of edge-brightened features as indication of a role played by the ICM dynamics in the origin of this radio source. Interestingly, the radio spectral properties of the Kite resemble those of the radio phoenix sources, an exotic class of diffuse radio sources produced by the interplay of fossil radio plasma with shocks and/or ICM motions (e.g., Clarke et al., 2013; Mandal et al., 2020). Specifically, the arcs of the Kite resemble the complex, filamentary radio morphology of the radio phoenices, whose filaments have patchy distributions of increased surface brightness, and synchrotron emission typically that follow a curved spectra.

To tie together these scenarios, we speculate that after the end of the AGN activity, when the plumes were already formed, the sloshing of gas in the cool core has interacted with the fossil radio plasma (Figure 5.8, 5.10). The typical sloshing crossing-time is of the order of 10^8 years (e.g., Ascasibar and Markevitch, 2006). Therefore, according to our estimates, the Kite would be old enough to allow the sloshing to impact significantly on its radio emission. On the basis of the temperature maps presented in literature (Figure 5.9 (top panel), or Ignesti et al., 2018; Laganá, Durret, and Lopes, 2019; Kadam et al., 2019), we suggest that the ICM motion could have interacted with the fossil plasma mostly in the N-S direction. The motion of the thermal plasma could have enhanced the radio emissivity at the edges of the radio galaxy by compressing the relativistic plasma and producing the bright arcs of the Kite. The compression of radio plasma can efficiently enhance its radio emission by a factor δI of:

$$\delta I \propto x^{-\frac{2}{3}\delta+1} \tag{5.3}$$

where x is the compression factor and $\delta = 2\alpha - 1$ is the index of the electron spectrum $N_e(E) \propto E^{\delta}$ (e.g., Markevitch et al., 2005).

In the case of the Kite, by using a power-law spectrum instead of a curved spectrum, we can derive a first-order estimate of the effects of compression. For $\alpha < -1.5$, hence $\delta < -4$, even a small compression $x \simeq 1.2$ can results in a significant enhancement $\delta I > 2$. At the cold front, where the compression would be more evident, we measure $x = 1.32^{+0.15}_{-0.13}$ for Sector S and $x = 1.37^{+0.19}_{-0.17}$ for Sector W, whereas Kadam et al. (2019) measured slightly higher values of x (1.57 ± 0.08 and 2.06 ± 0.44). This compression would correspond to a $\delta I \gtrsim 3$, that is consistent with the surface brightness difference we observe in Figure 5.5 between the lobes ($\sim$10-20 σ) and the arcs ($> 100\sigma$).

The local increase of the magnetic field due to the compression impacts also on the spectrum of the emission by shifting the critical frequency of emission of the electrons at higher frequencies. For a curved synchrotron spectrum, as we observe here for the Kite, this compression can result in a flattening of the observed spectrum by moving the break frequency to higher values. This effect should be more noticeable where the ICM compression, and consequently also I_X, is stronger. This is in agreement with the point-to-point analysis (Figure 5.7), which shows that the flattening of the spectrum is most evident in the regions with the highest I_X, and, thus, it supports a scenario where the radio emission is driven by the local properties of the thermal ICM.

The role of the central AGN

The steep spectral index of the arcs and the color-color plot indicates that the arcs were formed after the end of the duty cycle, when the central AGN entered a low-activity state. Indeed IC5338 does not show properties of AGN emission from the optical (SDSS) or infrared (WISE) photometry, and it has a very low probability of being quasars (Clarke et al., 2019). However, an AGN coincident with IC5338 is clearly detected at 144 MHz (Figure 5.5), as well as at 1.4 GHz (Figure 5.4, top-right panel). We note at the center of the galaxy there are two compact cores shown in the SDSS image. The core to the SW is coincident with the 1.4 GHz radio emission observed by Gitti (2013a) (and shown by cyan contours in the right image of Figure 5.10) and it exhibits hard X-ray emission (Wong et al., 2008a), thus it is likely the host of the AGN. The presence of these two cores in close proximity suggests a merger event had occurred to form IC5338, and there may be significant ongoing tidal forces between the two cores. Evidence for a merger event helps to provide a mechanisms for the supply and accretion of gas onto the AGN in the SW core (e.g., Ellison et al., 2019, for a recent result).

The spectral index of the AGN (α =-0.8$\pm$0.1, Figure 5.6) indicates that the supermassive black hole is currently accreting material. Furthermore, at higher frequencies the VLA high-resolution observations presented by Gitti (2013a) (Figure 5.4, 5.10) show the existence of a small ($\sim$ 8 kpc), jet-like feature leaving the nucleus of the central galaxy, and, thus, confirming that the AGN has entered a new activity phase. The non-detection of an AGN in optical or infrared data hence suggests that it is just obscured by the accretion disk and potentially intra-cluster dust along the line of sight. Therefore, we can not exclude that the starting of a new duty cycle by the central AGN could have played a role in the origin of the Kite by launching shocks in the old radio plasma and/or by further compressing the fossil plasma from the inside in the NE-SW direction.

5.5 Summary and Conclusions

We presented the analysis of the *Chandra* and LOFAR observations of the galaxy cluster Abell 2626 and its puzzling central radio source, also known as the Kite, which has been previously classified as a radio MH. The *Chandra* data unveiled the sloshing core of Abell 2626 and revealed a close connection between the cold front and the radio emission, whereas the new LOFAR data have radically changed the general picture of the Kite. We detected new components of the radio emission in the form of plumes located at the ends of the arcs, which almost double the total length of the radio source to $\sim$ 220 kpc with respect to the higher frequencies images. We combined the new data with the archival datasets at 1.4 GHz and 610 MHz to map the spectral index of the Kite from 144 MHz to 1.4 GHz. We find that the spectral index of the arcs steepens at higher frequencies from $\alpha \simeq -1.5$ to $\alpha < -2$ with a steepening trend from their centers to their ends. Then we compared the radio and the X-ray emission and we found that the radio plasma fills a putative cavity located beyond the S-W junction of the arcs which is aligned along the major axis of IC5338. Finally, by performing a point-to-point analysis we found a spatial correlation between the spectral index and the X-ray surface brightness, which is a proxy of the local ICM thermal plasma density, where the flattest-spectrum parts of the arcs coincide with the brightest X-ray regions. This result highlights that the properties of the radio emission of the Kite are driven by the local properties of the thermal ICM.

On the basis of our findings, we propose that the Kite could be a relic radio galaxy whose lobes have been shaped by the motion of the gas sloshing in the cool core. Specifically, the morphology observed for the first time by LOFAR and the steep spectrum of the lobes ($\alpha < -2$) suggest that the Kite was originally an X-shaped radio galaxy, likely produced by the back-flow of the radio plasma injected by the AGN that was redirected by the galactic hot ISM along the plumes. The spectral index and the size of the lobes set the lower limit for age of the system between 5×10^7 and 2×10^8 years. The curved radio spectrum and the spatial connection with the cold front suggest that, subsequently after the end of the AGN activity, the fossil radio plasma has been compressed by the ICM motion that enhanced locally the emissivity of the radio arcs and flattened their spectral index. Such a combination of phenomena can also explain its uniqueness among the radio sources because only a very favorable combination of different mechanisms could have resulted in such a spectacular radio source. This scenario can be now tested with tailored numerical simulations, which can explore the physical boundaries of the back-flow and the ICM compression, and future, high-resolution observations at 144 MHz carried out with the LOFAR international stations, which could provide us images of the Kite with a resolution of $0.3''$.

Chapter 6

Stormy weather in 2A0335+096

Based on Ignesti et al., in preparation

6.1 Introduction

In this Chapter we will present the results of the LOFAR observation of the galaxy cluster 2A0335+096, a low redshift ($z = 0.035$, which entails a luminosity distance of 153.9 Mpc and an angular scale 1 arcsec = 0.694 kpc[1]), relatively low mass cluster ($M_{500} = 2.27 \times 10^{14}$ $M_{\odot}$ Planck Collaboration et al., 2014). This cluster hosts a MH included in the sample in which we studied the thermal and non-thermal connection (see Chapter 2 of this Thesis or Ignesti et al., 2020a).

The MH was first imaged at 1.4 GHz and 5.5 GHz by Sarazin, Baum, and O'Dea (1995). The central radio galaxy is a core-dominated, double-lobe source and another patch of extended emission, which is interpreted as a fossil lobe from an older AGN outburst, is detected at $\sim 25''$($\sim$18 kpc) from the cluster center (Bîrzan et al., 2020). The MH surrounds this structure extending for $\sim 100''$ ($\sim$ 70 kpc), thus making it one of the smallest MH known (Giacintucci et al., 2017; Giacintucci et al., 2019).

From the thermal point of view, 2A0335+096 has a central temperature of 3.6 keV and a central entropy of 7.1 keV cm^{-2}, which are amongst the lowest values observed in relaxed cluster hosting a MH (Cavagnolo et al., 2009; Giacintucci et al., 2017). In the X-ray band it present two cavities, which coincide with the radio lobes, and a cold front located at $\sim$40 kpc from the center, which points out that the cool core is sloshing in the gravitaional well (Mazzotta, Edge, and Markevitch, 2003; Ghizzardi et al., 2006; Sanders, Fabian, and Taylor, 2009). It is worth noticing that this is also one of the clusters with the lowest mass among those hosting a MH. 2A0335+096 hosts also the head-tail radio galaxy GB6 B0335+096 ($z = 0.038$), an FRI galaxy characterized by an extended radio tail produced during its motion in the ICM (for further details, see Sebastian, Lal, and Pramesh Rao, 2017).

The active environment in which we observe the MH, with the cavities produced by the AGN feedback and the sloshing, would entail a perturbed, turbulent ICM. Therefore, it suggested the possibility that the cluster may host extended, ultra steep-spectrum radio emission similar to that discovered by LOFAR in a few other cases (as we discussed in Chapters 1.2.4, 1.3.4, 3). Therefore, in order to explore this scenario, we obtained to observe the cluster with LOFAR in co-observing with the LoTSS during the observation cycle 14 (LC14011, PI Ignesti). In this Chapter we present the preliminary results and a comparison with GMRT data (Ignesti et al., in

[1] http://www.astro.ucla.edu/$#$7Ewright/CosmoCalc.html

preparation)

6.2 Data processing and analysis

6.2.1 Radio data

In this Chapter we present the analysis of the LOFAR observation LC11014 (PI Ignesti). The observation was carried out in co-observing with the LoTSS for a total observation time of 8.33 hrs, thus we followed the data processing routine described in Chapter 3. We reduced the dataset using the direction-dependent data-reduction pipeline DDF-PIPELINE v. 2.2 developed by the LOFAR Surveys Key Science Project[2] (see Chapter 3). The data processing makes use of PREFACTOR (van Weeren et al., 2016; Williams et al., 2016; de Gasperin et al., 2019), KILLMS (Tasse, 2014; Smirnov and Tasse, 2015) and DDFACET (Tasse et al., 2018) to perform the calibration and imaging of the entire LOFAR field of view. Then, we performed additional phase and amplitude self-calibration cycles to correct the residual artifacts in a smaller region extracted from the observation and centered on the source, where the direction-dependent errors are assumed to be negligible (see van Weeren et al., 2020, for further details on this procedure).

We produced images at different resolutions using WSCLEAN v2.6 (Offringa et al., 2014) and using several different Briggs weightings (Briggs and Cornwell, 1994), with `robust` going from -0.5 to -1.2, and multi-scale cleaning (Offringa and Smirnov, 2017). An inner uvcut of 80λ, corresponding to an angular scale of $43'$, was applied to the data to drop the shortest spacings where calibration is more challenging. We corrected for the systematic offset of the LOFAR flux density scale produced by inaccuracies in the LOFAR HBA beam model by multiplying it with a factor of 0.8284 which aligns it with the flux-scale of the point-sources mapped in the TGSS survey. Following LoTSS (Shimwell et al., 2019), we adopt a conservative calibration error of 20%, which dominates the uncertainties on the LOFAR flux densities. The resulting images, with resolutions between 6 and 50 arcseconds, are shown in Figure 6.1. 2A0335+096 has a declination of +10°, which resulted in a noise above 200 μJy beam^{-1}, which is $\times$2 higher than expected for a typical LoTSS 8hrs observation ($\sim$ 100 μJy beam^{-1}), and elliptical beams. We note the presence of artifacts surrounding the bright sources, such as the AGN of GB6 B0335+096 (Figure 6.1, panel b), which appear to be due ionospheric issues during the observation (see de Gasperin et al., 2018).

We present here also the GMRT image of 2A0335+095 obtained from an archival observation at 610 MHz (cycle 17, project 17016, PI Raychaudhury). The time on target is 75 mins, we processed the dataset using the SPAM pipeline (see Intema et al., 2009; Intema et al., 2017, for details). The images at 610 MHz presented in this work (Figure 6.1, panel a) were made using WSCLEAN. As a future development, we plan to include in this study also the VLA data at 1.4 and 5.5 GHz presented in Chapter 2. At this stage, we used the total flux density at 1.4 GHz reported in (Giacintucci et al., 2014b) to evaluate the spectral index of the MH, which is not detected in the GMRT image.

[2] `https://github.com/mhardcastle/ddf-pipeline`

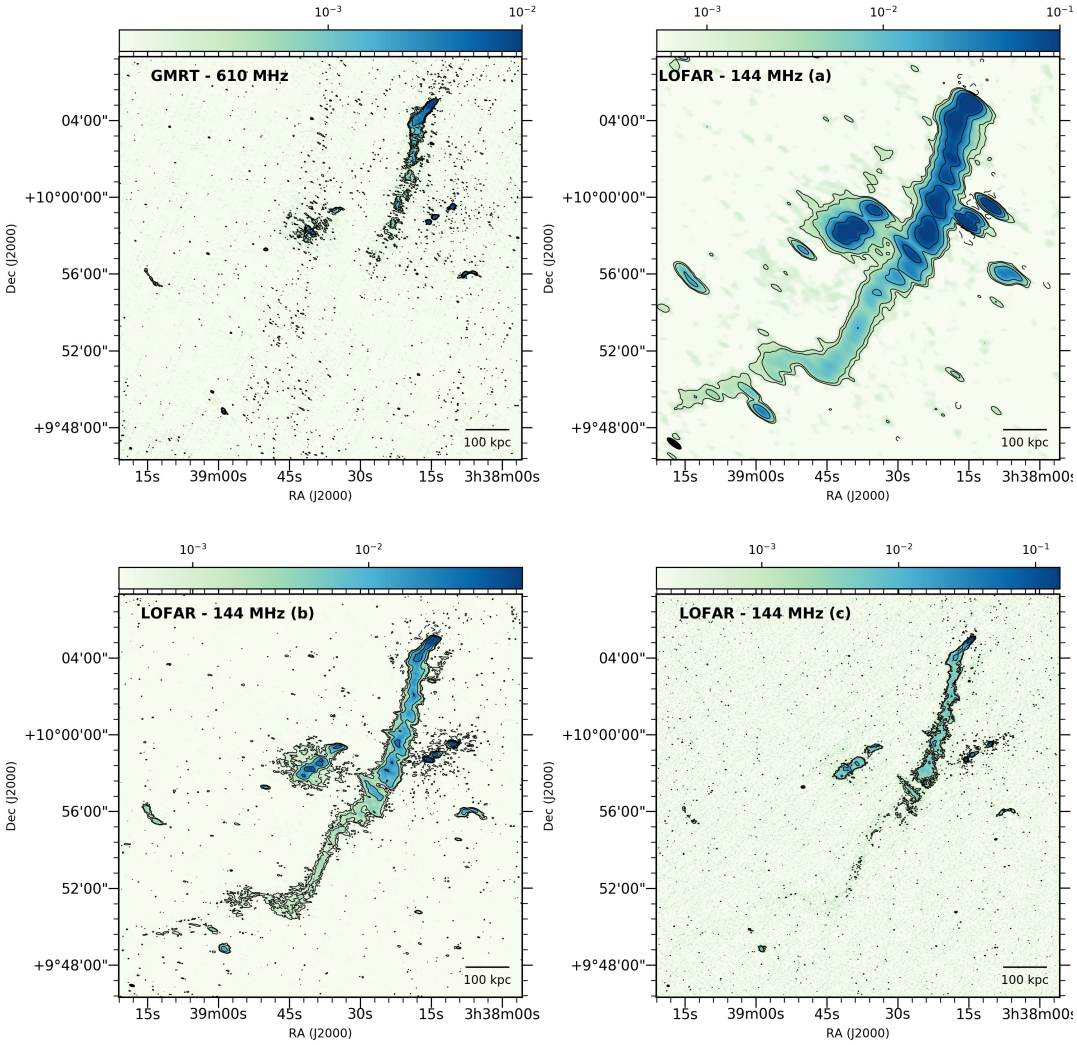

Figure 6.1: Multi-frequency view of 2A 0335+096. Top left: GMRT image at 610 MHz, σ=84 μJy beam^{-1}, resolution 5.90″ × 3.65″; Top right: LOFAR low-resolution image, σ=517 μJy beam^{-1}, resolution 51.53″ × 15.88″; Bottom left: LOFAR mid-resolution image, σ=231 μJy beam^{-1}, resolution 14.43″ × 5.05″; Bottom right: LOFAR high-resolution image, σ=400 μJy beam^{-1}, resolution 6.13″ × 3.82″; We report the -3, 3, 6, 24, 96σ levels in the LOFAR images and the -3, 3, 6, 12, 24σ in the GMRT image.

6.2.2 X-ray data

In this work we analyzed an archival *Chandra* observation of the cluster to produce an image in the 0.5-2.0 keV band of the cluster and to carry out a spectral analysis of the ICM emission. Specifically, we used the *Chandra* observation 7939 (PI Sanders), for a total exposure time of 49.5 ks. We reprocessed the *Chandra* datasets with CIAO 4.10 and CALDB 4.8.1 to correct for known time-dependent gain and for charge transfer inefficiency. In order to filter out strong background flares, we also applied screening of the event files[3]. For the background subtraction, we used the CALDB "Blank-Sky" files normalized to the count rate of the source image in the 10-12 keV band. We further processed the image with the GGM filter (Sanders et al., 2016) and the unsharp mask technique to search for edges in surface brightness (Figure 6.2).

[3] http://cxc.harvard.edu/ciao/guides/acis_data.html

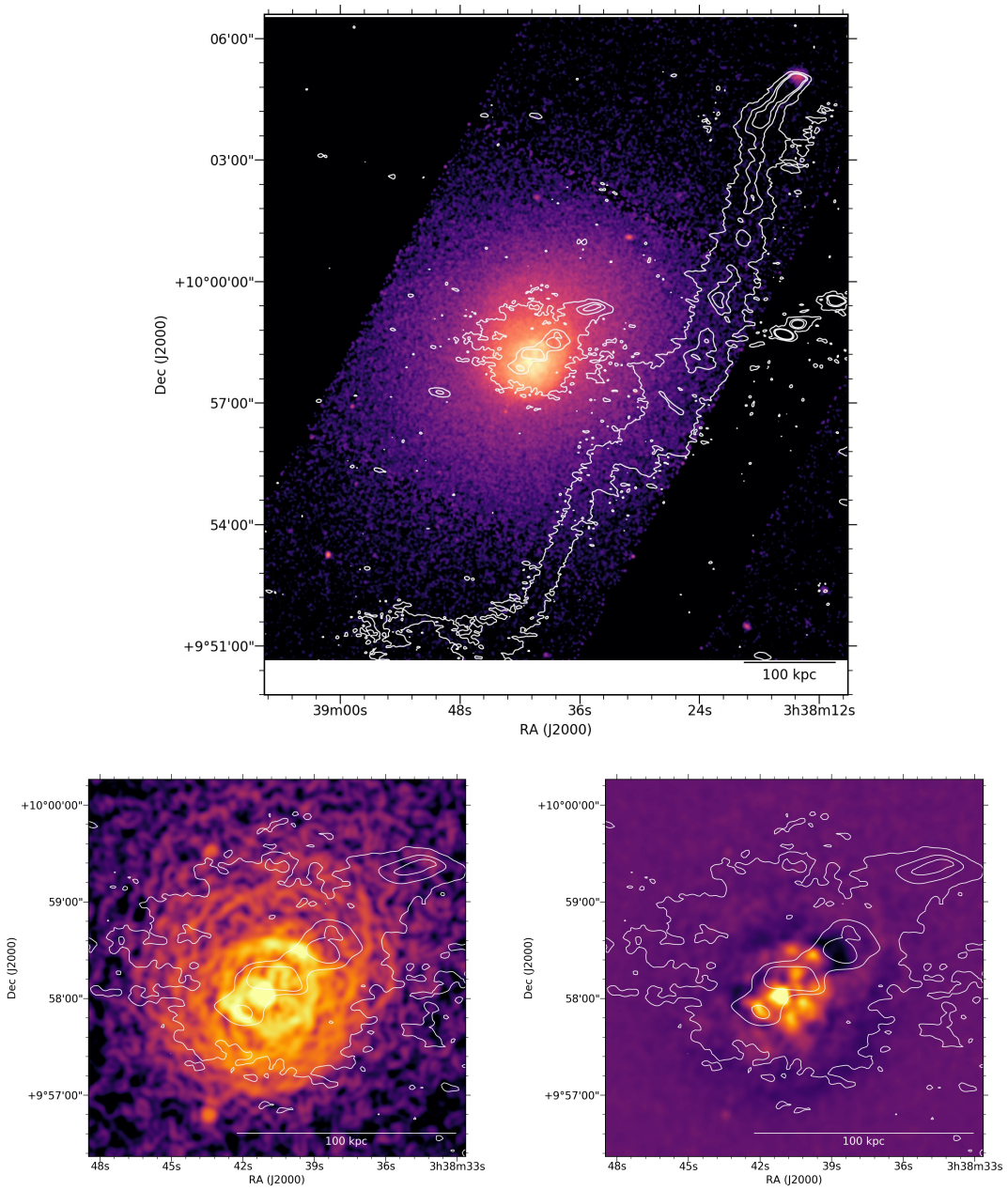

Figure 6.2: LOFAR contours of the mid-resolution image (panel b, Figure 6.1, σ=231 μJy beam^{-1}, resolution 14.43″ × 5.05″) at the 3, 24, 96σ levels on top of the background-subtracted, exposure corrected (top), the GGM-processed (bottom-left) and unsharp-masked (bottom-right, the negative residuals are reported in black) *Chandra* images in the 0.5-2.0 keV band.

6.2.3 Spectral index map

We combine the 144 and 610 MHz images to map the spectral index of the central source and the head tail galaxy. First we produced images in the same uv-range (80-54000 λ) to reliable compare fluxes on the same scales, then we smoothed both images to a resolution of 30″ and we regrid the GMRT image as the LOFAR one to be sure that each pixel covers the same angular direction. The final σ levels are 750 μJy beam^{-1} for the 144 MHz image and 410 μJy beam^{-1} for the 610 MHz one. The two images were compared on a pixel-by-pixel basis and the spectral index α was

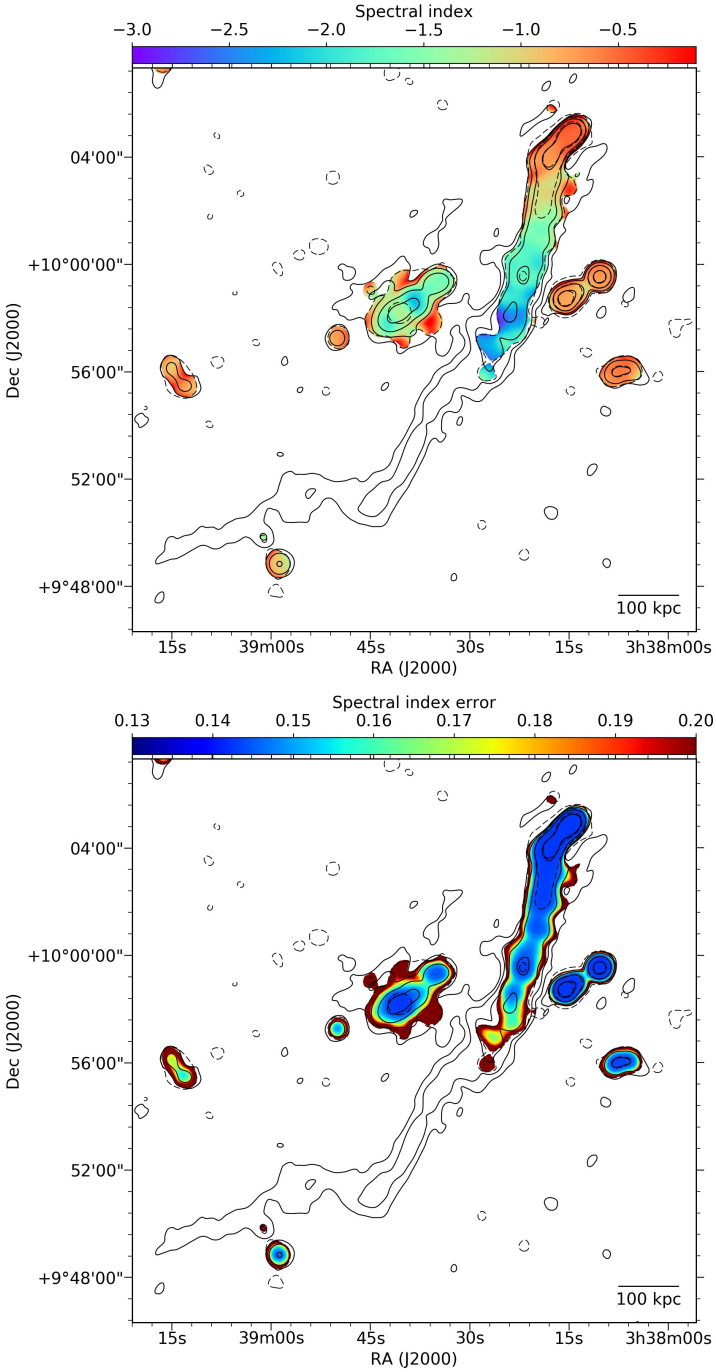

Figure 6.3: Spectral index map between 144 and 610 MHz (top) and corresponding error map (bottom). We report the 3, 12, 48, 192σ and the 3, 36, 144σ level of, respectively, the 144 (continue, σ=750 μJy beam^{-1}) and 610 (dashed, σ=410 μJy beam^{-1}) MHz images produced to map the spectral index.

computed as:

$$\alpha = \frac{\log\left(\frac{S_{610}}{S_{144}}\right)}{\log\left(\frac{610}{144}\right)} \pm \frac{1}{\log\left(\frac{610}{144}\right)} \sqrt{\left(\frac{\sigma_{S,610}}{S_{610}}\right)^2 + \left(\frac{\sigma_{S,144}}{S_{144}}\right)^2} \tag{6.1}$$

where S and $\sigma_S = [(f \cdot S)^2 + \sigma^2]^{1/2}$ (where $f = 0.2$ according to Shimwell et al., 2019) are the flux density and the corresponding error at the two frequencies, 144 and 610 MHz.

We computed the spectral index (and the corresponding error) in each pixel with a surface brightness above the 3σ levels, which give us a sensitivity to spectral index $\alpha > -0.5$. The results are shown in Figure 6.3, where we report the spectral index map and the corresponding error map. The next step will be to combine LOFAR and GMRT data with the VLA data appropriately imaged. We note that with the VLA images at 1.4 and 5.5 GHz, with a σ of 56 and 16 μJy beam^{-1} (Chapter 2)[4], we will be able to map the spectral index down to $\alpha \simeq -(1-1.1)$, which will permit a more detailed characterization of the synchrotron spectrum of the MH and the initial region of the radio tail within $\sim$ 100 kpc.

6.3 Discussion of the results

The new LOFAR observation probes, for the first time, the low-energy CRe of 2A0335. As discussed in Chapter 3, this allows us to explore the effects of low-efficiency phenomena, such as the ICM turbulent re-acceleration, on the evolution of the non-thermal plasma in the cluster. Here we use the new data to analyze the central source, which shows several components (Figure 6.4), and the radio galaxy GB6 B0335+096.

6.3.1 The central radio source

The combination of high resolution and sensitivity to large-scale emission of the new LOFAR data provides us a detailed view of the structure of the central radio source. In the mid-resolution LOFAR image (Figure 6.1, panel b, resolution $14.43'' \times 5.05''$), we can observe the bright central emission of the radio galaxy and its lobes with the MH underneath, whereas in the *Chandra* X-ray image we can see the cavity produced by the radio-mode AGN feedback at the center of the cluster coinciding with the northern radio lobe (Figure 6.2, bottom-right panel). In the high resolution image (Figure 6.1, panel c, resolution $6.13'' \times 3.82''$), we detect only the AGN-lobes system, plus another structure toward north-west that has been classified as a relic lobe (Giacintucci et al., 2019). Finally, at the lowest resolution of 51.53×15.88 arcsec (Figure 6.1, panel a, resolution $51.53'' \times 15.88''$), we can still recognize the morphology of the central radio galaxy and we observe a putative bridge between the central source and the radio tail, although it is likely an artifact given by the resolution of the image.

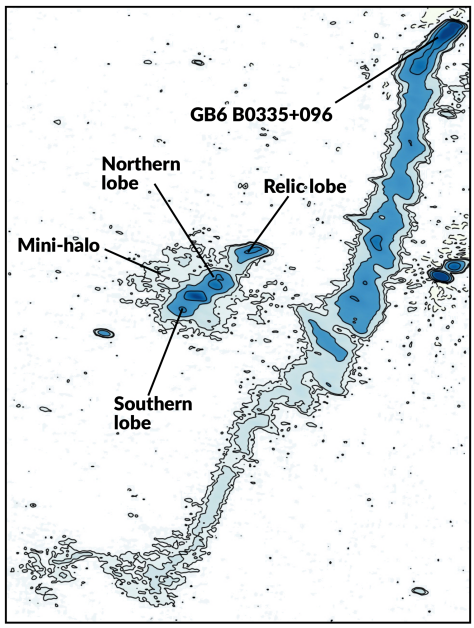

Figure 6.4: LOFAR contours of the mid-resolution image (panel b, Figure 6.1, σ=231 μJy beam^{-1}, resolution $14.43'' \times 5.05''$) where we label the components of the central source as referred in this work.

[4]The σ can possibly change due to the uv-cut and beam smoothing necessary to match the LOFAR uv-coverage.

Here we focus on the study of the diffuse radio emission, whereas a detailed analysis of a LOFAR observation of central AGN and its lobes can be found in Bîrzan et al. (2020). In the low-resolution LOFAR image (Figure 6.1, panel a), which is the deepest image we produced, we estimated the MH radius following Cassano et al. (2015), i.e. $R_{\rm MH} = \sqrt{R_{\rm min} \times R_{max}} = \sqrt{75'' \times 127''} = 97.6'' \simeq 67$ kpc. This is consistent with the observed radius at 1.4 GHz (70 kpc Giacintucci et al., 2014b), and generally smaller than the other MHs. However, due to the generally higher noise of the image due to the low declination of the cluster and the bright, extended radio galaxy at the center of the MH, we can not exclude that we are missing fainter and more extended emission.

In the mid and low-resolution images we measure a total flux density of 1.15±0.23 Jy within the 3σ contours. In order to estimate the flux density of the diffuse emission only, we subtracted from the total the flux density of the AGN-lobes system (0.75±0.15 Jy) and of the north-west relic lobe (0.17±0.03 Jy) measured within the 3σ contour of the high-resolution image (Figure 6.1, panel c), finding a net flux density of 0.23±0.05 Jy with a surface brightness, computed on the net area, of 9.3 mJy beam^{-1}. By multiplying the net surface brightness by the area of the radio galaxy and the relic lobe, we measure an additional 0.21±0.04 Jy that would be due to the diffuse emission, thus resulting in a total flux density of 0.44±0.09 Jy. By comparing this measure with the flux density of the MH at 1.4 GHz reported in Giacintucci et al. (2014b), which is 21.1±2.1 mJy, we estimated a spectral index $\alpha = -1.34 \pm 0.09$ between 144 and 1400 MHz. A more accurate measure will be possible by comparing LOFAR and VLA data by the means of images designed to match the uv-coverage and the baseline weights (Ignesti et al., in preparation).

We note that the MH in 2A0335+096 is at the low-end among the known MH also in terms of radio power at 1.4 GHz and cluster mass, as well as the size (Giacintucci et al., 2014b; Giacintucci et al., 2017), thus representing a sort of outstanding object in this sense. On the contrary, the k-index of the $I_{\rm radio} - I_{\rm X}$ correlation, both at 1.4 and 5.5 GHz, is above 1, thus in agreement with the others MH (see Chapter 2 or Ignesti et al., 2020a). Unfortunately the MH could not be reliably mapped in the new spectral index map (Figure 6.3) because of the low-quality of the GMRT observation, and we could map only the lobes and the relic lobe, which show an unusual steep spectrum $\alpha \simeq -1.5$. Interestingly, the GGM image presented in Figure 6.2 shows that the radio emission coincides with a bright, spiral-like edge in the X-ray surface brightness. Such a feature can be interpreted as evidence of sloshing of the cool core, in agreement with the previous results (Sarazin, Baum, and O'Dea, 1995), and is usually connected with the origin of the diffuse radio emission (e.g., Mazzotta and Giacintucci, 2008).

The new observation provided some insightful data that allow us to better define the nature of the MH and its interplay with the central AGN. The morphology (Figure 6.1) and spectral map (Figure 6.3) show steep-spectrum ($\alpha \simeq -1.5$), old radio lobes remnants of the past activity of the AGN. On the contrary, the surrounding diffuse radio emission shows a slightly flatter spectrum ($\alpha = -1.34 \pm 0.09$), thus suggesting that the CRe were not injected from the lobes and propagated on larger scales, and indicating the presence of a re-acceleration mechanisms acting on the 100 kpc scales. 2A0335+096 is a very active environment in that sense, with multiple possible sources of turbulence, as the AGN mechanical feedback and the sloshing, that can power the radio emission. The close connection between the radio emission

and the sloshing region suggests that the CRe are re-accelerated by the turbulence produced by the sloshing (e.g., Mazzotta and Giacintucci, 2008; Giacintucci et al., 2014a; Timmerman et al., 2020).

Alternatively, one might assume that, as shown in Chapter 2, the CRp generated by the AGN escape the lobes at late times (e.g., Ehlert et al., 2018) and propagate in the core generating CRe and, ultimately, diffuse radio (and γ-ray) emission. The current data do not allow us to check the presence of spectral steepening in the MH that might challenge this possibility (e.g., Brunetti and Jones, 2014) thus this remains a viable scenario.

6.3.2 GB6 B0335+096

The most striking feature discovered by LOFAR is the giant radio tail of GB6 B0335+096, which extends for almost 900 kpc, and is far more than what was observed in previous works (Sebastian, Lal, and Pramesh Rao, 2017). Interestingly, the high- and mid-resolution images (Figure 6.1, panels a, b) show a curvature of the radio tail within 100 kpc from the AGN. We detect hard X-ray 2-7 keV emission coming from the AGN in GB6 B0335+096 associated with flat-spectrum radio emission (Figure 6.5), which points out that the AGN is currently active.

However, the extent of this tail is surprising. The maximum life-time of low-energy CRe emitting at 144 MHz, which we can estimate by assuming the minimal energy loss magnetic field $B = B_{\rm CMB}/\sqrt{3} = 2.02$ μG, is $\tau \simeq 3 \times 10^8$ yrs (see Chapter 1.2.4). Under these favorable conditions, given the galactic velocity ($v_g = \sqrt{2} \times$ line-of-sight velocity $= 960$ km s^{-1}, Sebastian, Lal, and Pramesh Rao, 2017) the expected length of a radio-emitting trail left behind by the galaxy would be $l \simeq v \cdot \tau \simeq 300$ kpc, which is a factor ~ 3 shorter than we observe. Moreover, the actual difference is likely bigger because we can measure only the projected length of the tail, which is the lower-limit of this actual length. This difference could be explained by an exceptionally high galactic velocity, which is quite unrealistic, or an extended CRe life-time due to the action of some physical process taking place in the tail. Therefore, observing such a long component poses the same question as observing Mpc-scale diffuse radio emission: how is possible that CRe have survived that long in the ICM?

We investigated this issue by comparing the observations with simple numerical calculations of the expected emission of an aging radio plasma to estimate the flux density profile and the corresponding decline of the spectral index along the tail. In order to reliably compare the flux densities at 144 and 610 MHz, we used the images produced for the spectral analysis (Section 6.2.3) with matching uv-range (80-54000 λ) and resolution (30×30 arcsec). Based on the 3σ level of the 144 MHz emission, we used the PT-REX code (see Appendix A) to sample the tail with 19 boxes, $60'' \times 60''$ in size, which would correspond to 45×45 kpc at the galaxy redshift, and we measured the flux densities at 144 and 610 MHz in each of them, producing a profile of the emission along the tail (Figure 6.6). In this profile the 610 MHz emission is present up to box n. 8. Then we derived the spectral index profile by comparing the corresponding flux densities in each box. Where we do not detect emission above 3 σ at 610 MHz, we used the 2σ level of the GMRT image to derive an upper limit for the real spectral index. By assuming that the tail is parallel to the plane of the sky, this sampling can be roughly converted in a spatial scale, which sets a lower limit for

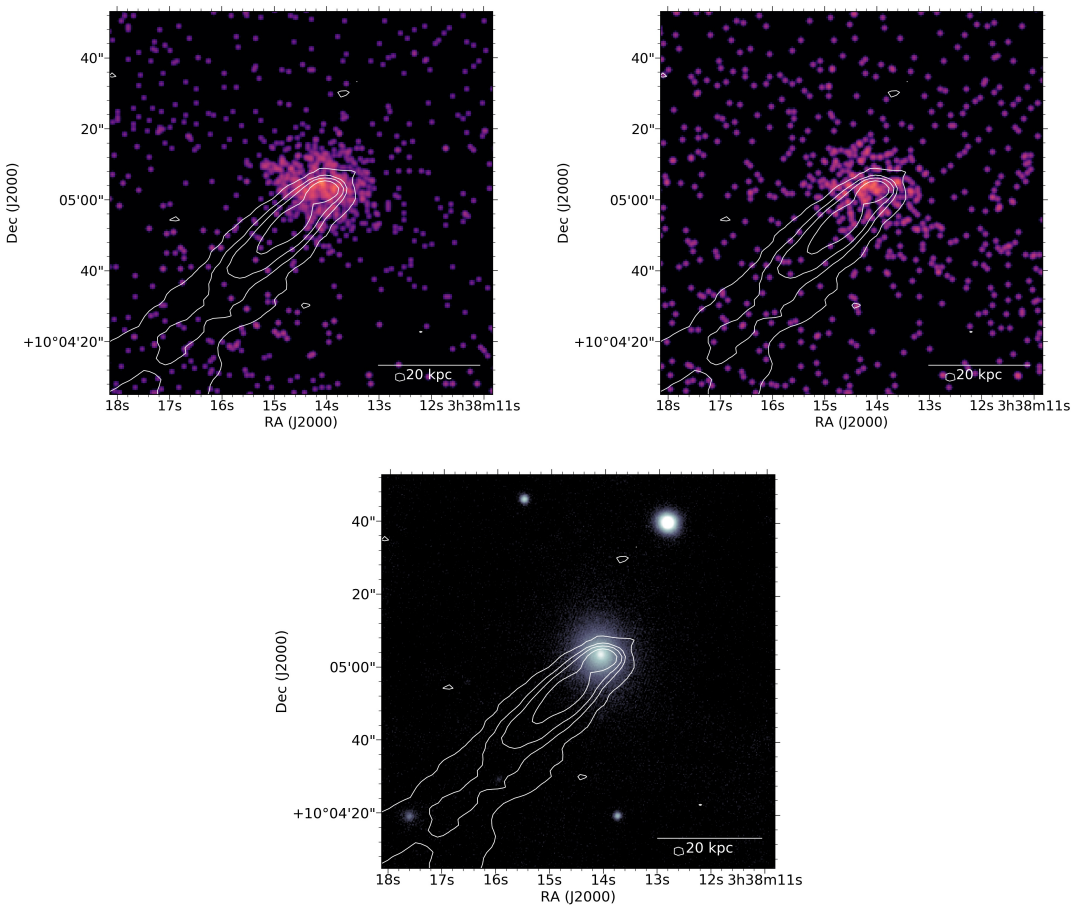

Figure 6.5: LOFAR contours of the high-resolution image (panel c, Figure 6.1, σ=400 μJy beam^{-1}, resolution 6.13″ × 3.82″) at the 3, 24, 48, 96σ levels on top of the *Chandra* 0.5-2.0 keV (top left), 2.0-7.0 (top right) and PanSTARR *r*-band (bottom) images.

its actual length. Under such assumption, we can assume that each box is 45 kpc afar from the next one and we can thus compute the distance of each box from the AGN and its position along the tail. Under the assumption that the plasma left behind by the galaxy does not have a proper motion, the time elapsed since the injection can be estimated as $\tau \simeq d/v_{\rm gal}$, where d is the distance from the AGN and $v_{\rm gal}$ is the galaxy velocity. It follows that the space grid defined by our sampling can be converted in a "time grid" with the dynamic age of each chunk of the radio tail.

In this framework we can compare the observations with the numerical prediction of the time evolution of the synchrotron emissivity of a radio plasma by taking into account only the radiative cooling of CRe, which we discussed in Chapter 1.2.4. Our estimate is conservative because we do not include the energy losses due to adiabatic expansion of the plasma, and we assume an uniform magnetic field in the tail. We computed numerically the synchrotron emissivity spectrum $j(k)$, where $k = \nu/\nu_{br}$, for $k = 0.1 - 10$ by assuming an injection index $\alpha = -0.6$, based on the spectral index observed at the beginning of the tail, and the minimal energy loss magnetic field $B = B_{\rm CMB}/\sqrt{3} \simeq 2$ μG.

To compare this model emissivity spectrum with our observation, we have first to derive the corresponding values of k at 144 and 610 MHz by evaluating the ν_{br} for

each box. This can be done starting from the radiative time of a relativistic particle population, $t_{\rm rad}$, which can be estimated as discussed in Chapter 1.2.4. Under the assumption that the radiative age of the plasma coincides with the time elapsed since the injection, i.e. $t_{\rm rad} \simeq \tau$, we can derive a putative ν_{br} for each chunk, and thus the corresponding values of k at the two frequencies, k_{144} and k_{610}.

By combining the synchrotron spectrum with the time-scale described by the break frequency, we can compare the observed spectrum with the prediction in the case of pure radiative ageing. Under the assumption that each cell defines a cylindrical section of the tail with a radius of 22.5 kpc and height of 45 kpc[5] and by using the flux density at 144 MHz measured in the first cell to normalize the model spectrum $j(k)$, we can produce the expected flux density and spectral index profiles along the tail.

We compared the observations with two set of simulations produced by assuming $v_{\rm gal} = 960$ and 1600 km s^{-1}. The former is computed by assuming that the line-of-sight velocity is $1/\sqrt{2}$ of the total velocity (Sebastian, Lal, and Pramesh Rao, 2017), the latter is an upper limit estimated by forcing the model to reproduce the spectral index decline within the first half of the tail. We note that both the velocity are higher than the cluster velocity dispersion $\sigma \simeq 600$ km s^{-1} (calculated on the basis of the $M_{500} = 2.27 \cdot 10^{14}$ $M_\odot$ and $R_{500} = 0.92$ Mpc reported in Giacintucci et al., 2017). Under our assumptions, the higher is the velocity of the galaxy the younger would be the age of the plasma in the tail, hence the emission (and the corresponding spectral index) would decline slower. Finally, to estimate the state of the ageing of the plasma, i.e. the change of ν_{br}, along the tail, we used the model synchrotron spectrum to sample the expected spectral index for values of ν_{br} within 1-5000 MHz. Then, by comparing via interpolation the observed spectral index with our predictions, we evaluated the break frequency profile along the tail. We report the observed and predicted profiles in Figure 6.6

However, neither of the two models can reproduce the observations. They both predicts that the flux density and the spectral index trends would be steeper than observed, with the emission that would fall below the detection limit within ∼500 kpc. In the first 500 kpc (i.e. where we still observe the 610 MHz emission), the tail shows several bright hotspots, which can be observed at both frequencies and they appear as a change of slope of the otherwise declining trend in flux density. Because we normalize the spectrum at the flux density observed at the begin of the tail, we expect these hotspots to be the main cause of the difference between the observations and the model. The question is if these features were produced by phases of higher AGN activity or by external processes affecting the tail. However, beyond 500 kpc the observed flux density differs from the model by more than 2 orders of magnitude, with the 144 MHz emission which declines dramatically slower than expected. Therefore we conclude that the simple ageing model, albeit the large galactic velocity and the minimal energy loss magnetic field, is not sufficient to reproduce the data and some other physical processes have to be included to contrast the radiative cooling of CRe.

[5]Such a rude assumption does not well describe the geometry at the end of the tail where it curves toward east (cells n. 10-15). However, more advanced geometrical models including the rotation of the cells would only marginally affect affect our conclusions, without changing the overwhelming difference between the observed and predicted flux densities in these regions.

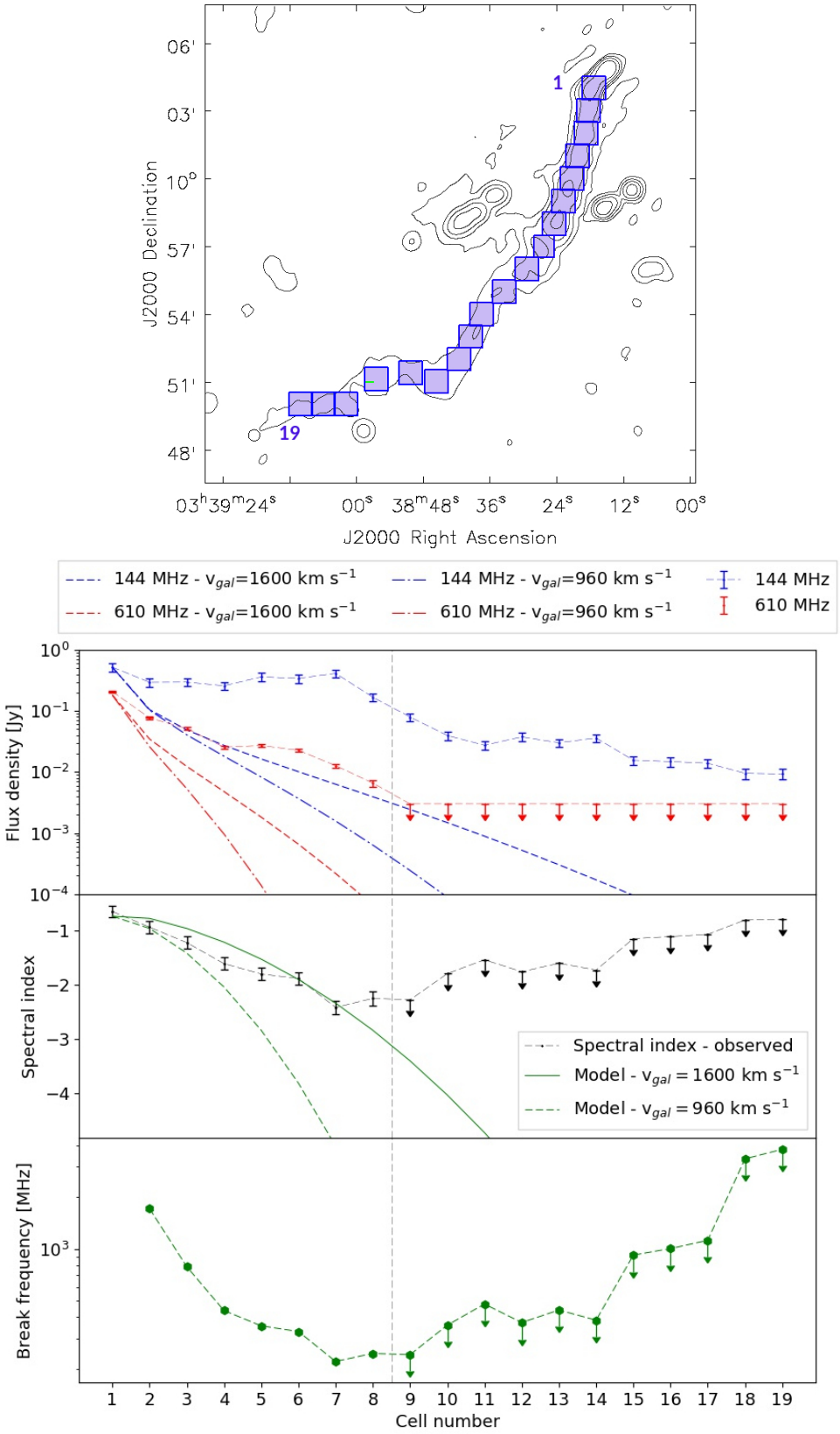

Figure 6.6: Top: 3, 48, 96, 192σ levels of the 144 MHz radio emission (σ=750 μJy beam^{-1}, resolution 30×30 arcsec) with the sampling cells on top; Bottom: Observed and modeled profiles of flux density (top), spectral index (midddle) and break-frequency (bottom).

The break frequency profile (Figure 6.6, bottom panel) shows a decline in the first half of the tail, then a sudden flatten in the cells 7, 8 and 9 at values of 250 MHz, and an apparent, inverted trend up to the end of the tail. Because the break frequency of the spectrum is an indicator of the plasma age (see Chapter 1.2.4), observing its values to be constant for $\sim$ 100 kpc (and likely way further, as suggested by the flatter decline of the 144 MHz emission beyond cell n. 9) suggests that in that region the radiative energy losses are balanced by some external process that is providing energy to the radiative electrons.

To explain these findings, mechanisms of re-energization can be invoked. One possibility is that micro-turbulence is generated in the tail by instabilities driven by the interplay of the tail with the external medium (i.e. gentle re-acceleration, de Gasperin et al., 2017). Alternatively, the observed profiles could be explained by a compression due to the interaction of the tail with a weak shock. This latter scenario would be characterized by the presence of a discontinuity in the X-ray surface brightness in the proximity of the tail. However, the GGM filter does not reveal any feature, neither we can search for it by extracting surface brightness profiles across the tail because, due to an unfortunate coincidence, the galaxy is placed along the edge of the CCD (Figure 6.2, left panel). Moreover, these phenomena would extend the radiative life of both the high- and low- energy CRe, i.e. would result in a strong flattening of the spectral index, thus resulting in extended (>500 kpc) emission at both frequencies. On the contrary, observing that the 144 MHz emission is far more extended than the 610 MHz one suggests that the re-energizing process is not efficient enough to compensate the energy losses observed at 610 MHz, but its time-scale is closer to the time-scale of the energy losses of the low-energy CRe, i.e. that we are dealing with a low-efficient phenomenon. Therefore, we tentatively suggest the ICM gentle re-acceleration as main process to power the low-energy CRe population, contrast the radiative cooling and explain the presence of 144 MHz emission at such a significant distance from the AGN.

6.4 Conclusions

Due to its capability to probe the low-energy CRe, LOFAR unveiled very interesting features in 2A0335+096. We focused our analysis on two aspects, the nature of the central extended radio emission and the puzzling properties of the radio tail of GB6 B0335+096. For the former, we could estimate for the first time the spectral index of the diffuse radio emission, $\alpha = -1.34 \pm 0.09$, which is flatter than the spectral index we observe in the lobes of the central radio galaxy ($\alpha = -1.5$). We conclude that the diffuse radio emission may be connected to the AGN (as primary source of CR), but the spectral index suggests that additional processes, either due to turbulent re-acceleration or hadronic cascade, played a role in the origin of the MH. On the basis of the connection we observe between the 144 MHz radio emission and the sloshing features highlighted by the GGM analysis, we suggest that the turbulent re-acceleration may have played a role. However, with the current data it is difficult to discriminate the two models.

For GB6 B0335+096, the new observation reveals that the radio tail is significantly more extended at low frequency than previously observed, hence posing the questions of how the relativistic particles could have survived longer than expected. In order to address this question, we studied the profiles of flux density and spectral

index along the tail trying to reproduce them with a simple ageing model. It clearly resulted that this was not possible, hence the role of re-acceleration mechanisms had to be invoked to explain the observation.

From this work emerged that 2A0335+096 is a very interesting system worth of future investigations. The central source could represent a laboratory to investigate both the fate of AGN bubbles, specifically the final phase when they reach the equilibrium with the surrounding medium, and the origin of diffuse emission. Furthermore, the tail of GB6 B0335+096 allows to explore the interplay between fossil plasma and ICM. These studies deserve to be carried out both by exploiting numerical simulation to test the existing models and by comparing these new LOFAR data with deeper radio observations at higher frequencies, such as the archival VLA observations of this cluster at 1.4 and 5.5 GHz. These observations will permit us to better constrain the spectrum of the MH, specifically searching for evidence of spectrum curvature that could rule out the hadronic scenario. In addition, we will be able to study the evolution of CRe in the first part of the tail, where we observe a curvature, by the means of 3-frequency color-color plot (Ignesti et al., in preparation).

Chapter 7

New windows on the ram-pressure stripping

Based on Poggianti et al., 2019, ApJ, Volume 887, Issue 2, article id. 155, Ignesti et al., 2020, A&A, 643, A172, and Müller et al., 2020, Nature Astronomy.

7.1 Introduction

In Chapter 1 we discussed how the ICM can affect the properties of the cluster galaxies. In this Chapter we will explore in details the effects of ICM ram pressure stripping, which is considered the most efficient mechanism to remove gas from galaxies in galaxy clusters (Boselli and Gavazzi, 2006). A multitude of observational studies have observed the smoking gun of this physical process at various wavelengths with different techniques, mostly HI, Hα narrow band imaging, UV/blue light, and, more recently, integral field spectroscopy (Kenney, van Gorkom, and Vollmer, 2004; Chung et al., 2007; Hester et al., 2010; Smith et al., 2010; Merluzzi et al., 2013; Yagi et al., 2010; Kenney et al., 2014; Fossati et al., 2016; Jáchym et al., 2017; Consolandi et al., 2017; Gullieuszik et al., 2017; Moretti et al., 2018; Fossati et al., 2019; Bellhouse et al., 2019). The most extreme examples of galaxies undergoing strong ram pressure are the so called *jellyfish galaxies* (Smith et al., 2010; Fumagalli et al., 2014; Ebeling, Ma, and Barrett, 2014). They are characterized by extraplanar, unilateral debris visible in the optical/UV light and striking tails of Hα ionized gas, where most of the Hα emission in the tails is due to photoionization by massive stars born in situ.

We present here an X-ray and radio analysis of the galaxy JW100 ($z = 0.06189$) in the galaxy cluster Abell 2626. JW100 (also known as IC5337) is an almost edge-on spiral galaxy in the cluster Abell 2626. Selected by Poggianti et al. (2016) as a stripping candidate, it is one of the jellyfish galaxies in the GAs Stripping Phenomena (GASP,[1] Poggianti et al., 2017a) sample. JW100 is characterized by one of the most striking ionized gas tails in the sample, and it is also the most massive galaxy of the GASP sample, with a stellar mass $3.2 \times 10^{11}\ M_{\odot}$ (Poggianti et al., 2017b). JW100 hosts a central AGN (Seyfert2), that is detectable both in X-rays (Wong et al., 2008b) and from MUSE emission-line ratios (Poggianti et al., 2017b). Poggianti et al. (2019a) computed JW100's current star formation rate (SFR) from the Hα luminosity corrected both for stellar absorption and for dust extinction using the Balmer decrement adopting the Kennicutt, 1998's relation ($SFR(M_{\odot}/\mathrm{yr}) = 4.6 \times 10^{-42} L_{\mathrm{H}\alpha}$ erg s^{-1}). They found a total (disk+tail) current star formation rate $SFR = 4.0 M_{\odot}\ \mathrm{yr}^{-1}$, of which 20% is in the tail. Its mass and SFR place JW100 about 0.4 dex below the SFR-mass relation for normal galaxies and ~ 0.65 dex below the relation for jellyfish

[1] http://web.oapd.inaf.it/gasp/index.html

galaxies (Vulcani et al., 2018), indicating that star formation has already decreased due to gas stripping.

Poggianti et al. (2019a) studied the optical ionization mechanisms in the tails of GASP galaxies, finding that the tail emission characteristics of the jellyfish galaxy JW100 are peculiar. At odds with the majority of the other jellyfish galaxies, star formation is not the obviously dominant ionization mechanism of the tail. According to the [OIII]5007/Hβ vs [OI]6300/Hff diagnostic diagram, it has only a few star-forming clumps in the tail and large amounts of ionized gas with an [OI]6300 line excess. A high [OI]6300/Hα ratio is usually interpreted as a sign of the presence of shocks (Rich, Kewley, and Dopita, 2011), and shock-heated molecular hydrogen has been observed with *Spitzer* in some cluster galaxies undergoing ram pressure stripping (Sivanandam, Rieke, and Rieke, 2010; Sivanandam, Rieke, and Rieke, 2014; Wong et al., 2014). The exact source of the [OI] excitation in jellyfish tails is currently unknown. Understanding why JW100 is so special in its tail ionization mechanism might be the key to understand under what conditions are stars forming in the tails, and when they are not. The interaction with the hot X-ray emitting ICM is expected to be crucial to set the conditions of the gas in the tails (e.g., Tonnesen, Bryan, and Chen, 2011). Such interaction might give rise to an X-ray tail, but so far there are only a few X-ray emitting ram pressure stripped tails observed (Sun et al., 2010). In this context, our findings provide new insights into the role played by the ICM, both as possible source of photo-ionizing photons and magnetized medium. Moreover, in this field of research these two bands are relatively less explored than the optical, infra-red and ultra-violet ones, thus our work is a precursor for future, similar analysis.

7.2 Data analysis

We present here the X-ray and radio analysis of JW100 in the galaxy cluster Abell 2626. We analyzed the *Chandra* observation 16136 and 3192 and LOFAR and VLA observations at 144 MHz and 1.4 GHz of the galaxy. The data processing does not differ from the one carried out for the whole cluster, so we refer to Chapter 5, Section 2 for the detailed description. Here we report only the data analysis that we carried out specifically for this source.

7.2.1 X-ray

Spectral analysis of the galaxy

We performed a spectroscopic analysis of the *Chandra* data with XSPEC v 12.10 (Arnaud, 1996). We defined the region of interest of the spectral analysis, i.e. the galaxy, based on the MUSE observation to include the disk and stripped tail. Then, we defined a control region to study the properties of the ICM at the galaxy clustercentric distance, i.e. the average thermal properties of the ICM surrounding JW100 at the same radial distance of the galaxy. The ICM of Abell 2626 has an almost spherical symmetry (e.g., Wong et al., 2008a; Ignesti et al., 2018; Kadam et al., 2019), thus, we expect all the thermal plasma at the same clustercentric distance of the galaxy to have similar properties[2]. To maximize the photons statistics, we used as control region a ring-shaped sector at the same distance of JW100. The galaxy region and

[2]We neglect here the possible, local increase in temperature due to the galactic Mach cone produced by its supersonic motion.

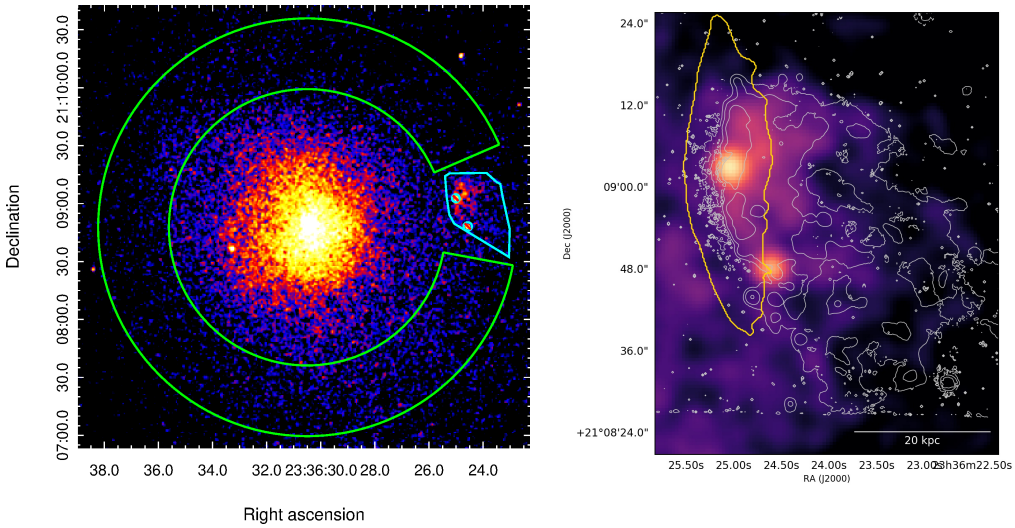

Figure 7.1: Left: Background-subtracted, exposure-corrected *Chandra* image of A2626 in the 0.5-2.0 keV band smoothed with a 1.5" gaussian beam, with the galaxy (cyan) and control (green) regions highlighted; Right: *Chandra* X-ray image in the 0.5-2.0 keV smoothed to 1.5 arcsec with the contorus of the Hα (silver) and stellar continuum (gold) emission.

the control region are shown in Figure 7.1 (left panel). We extracted a spectrum in each of the two regions using the CIAO task `specextract` and then binned to give at least 25 counts in each energy bin. Similarly, we extracted the background spectrum from the Blank-Sky files in the same regions. The point sources were removed or masked using circular regions with a radius 1.8", according to the *Chandra* PSF degradation far from the center of the observation, during the spectrum extraction. Spectra have been extracted separately from the two observations generating independent response matrices, and then, after background subtraction, fitted jointly in the energy range 0.5-7 keV. The control region spectrum was fitted with an absorbed thermal model (`phabs*apec`) and the results are reported in Table 7.1. We measure a temperature kT=3.5 $\pm$ 0.1 keV , a metallicity Z=0.36$\pm$0.04 solar and an electron density $n_e = 3.2 \cdot 10^{-3}$ cm^{-3}, that corresponds to a ICM density $\rho_{\rm ICM}$ of 5.8$\cdot$10^{-27} g cm^{-3}. The properties of the ICM we derive here are in agreement with previous results by Ignesti et al., 2018 and Kadam et al., 2019.

As a first result, we ruled out that a single thermal component (either only ISM or ICM) can reproduce the observed emission from JW100 because we found that the single-temperature model (`apec` model) does not produce a good fit, as shown by the final statistics presented in Table 7.2 (χ^2 =173.43, DOF=96). Therefore, we modeled the spectrum extracted in the galaxy region as the combination of two components. To model the cluster emission along the line of sight we used the absorbed, thermal, single-temperature component (`apec`) described above whose properties were fixed to that of the ICM measured in the control region (Table 7.1). Then, to model the galactic emission itself, we explored two different models:

- ◇ A single-temperature `apec` model, which is a simplified model where the galactic medium is a plasma emitting at a single temperature which is supposedly different from that of the local ICM;
- ◇ A multi-phase, multi-temperature `cemekl` model (Singh et al., 1996), where the plasma emission measure $EM = \int n_e n_{\rm H} dV$, i.e. the normalization of the

Table 7.1: Results of the X-ray spectral analysis in the control region.

Obs ID.	Exposure time [ks]	Bkg exp. time [ks]	Total counts [cnts]	Net rate [cnts s^{-1}]
16136	104.7	672.5	29992	0.266 (92.7 % total)
3192	23.68	461.5	8445	0.337 (94.4 % total)
Model		Parameters		χ^2, DOF, χ^2_R
`phabs*apec`		kT=3.50±0.10 keV, Z=0.36±0.04		499.02, 456, 1.0943

bolometric power emitted as thermal radiation, scales with the temperature as $EM \propto T^{\alpha}$ and the temperature has an upper limit $T_{\rm max}$. This model should be appropriate for a scenario in which the galactic X-ray emission comes from a multi-temperature plasma, that could be produced by the mixing of the hot ICM and the cold ISM triggered by the ISM stripping, the thermal conduction heating or the shock heating. In this case, we may expect the temperature of the emitting plasma to range from the temperature of the ICM (kT=3.5 $\pm$ 0.1 keV) to the temperature of the stripped ISM traced by the Hα emission (kT$< 10^{-3}$ keV).

The photon statistics was not sufficient to obtain a solid estimate of the metallicity of the plasma, so in both models we fixed it at the solar value, which is the metallicity of the stripped gas measured from the MUSE data. We report the results of the fits in Table 7.2 and the spectra with the best-fit models in Figure 7.2.

With the double `apec` model (χ^2 =93.58, DOF=95) we recover a temperature of $0.82^{+0.16}_{-0.05}$ keV for the galactic component, which is lower than that of the ICM. In the `apec+cemekl` model we fitted the data at first by setting the $\mathtt{T_{max}}$ parameter to match the temperature of the ICM (χ^2 =93.84, DOF=95), then by letting it free (χ^2 =87.18, DOF=94). In the second case we recovered an upper limit of the temperature $\mathtt{T_{max}}$=$1.2^{+0.50}_{-0.26}$ keV, which is lower than the ICM temperature. The two models (double `apec` vs `apec+cemekl`) are statistically indistinguishable and they fit equally well the observations. For each model we measured the unabsorbed X-ray luminosity in the 0.5-2.0, 0.5-10.0 and 0.3-10 keV bands associated to the galactic spectral component, listed in Table 7.2.

Search for the bow shock

JW100 has a line-of-sight velocity of 1807 km s^{-1} with respect to the cluster (Poggianti et al., 2017b) and, based on the orientation of the Hα tail we expect the total velocity to have also a significant trasversal component. From the values of the thermal properties of the ICM measured in the control region we estimate a local sound velocity $c_s \simeq 1.5 \cdot 10^4 T_{\rm ICM}^{1/2} \simeq 960$ km s^{-1}, thus the galaxy should be moving supersonically (with a tentative lower limit for the galaxy Mach number $\mathcal{M} \simeq 2$). Therefore, we may expect to observe two discontinuities in front of it, which are the leading edge of the shock, i.e. the bow shock, and the contact discontinuity that drives this shock. Measuring the jump temperature across the shock front could give us an independent measure of the galaxy Mach number, thus of its velocity with respect to the ICM. We note that bow shocks in front of jellyfish galaxies have never

Table 7.2: Results of the X-ray spectral analysis in the galactic region.

Obs ID.	Exposure time [ks]	Bkg exp. time [ks]	Total counts [cnts]	Net rate [cnts s^{-1}]
16136	104.7	672.5	2502	0.0228 (95.6 % total)
3192	23.68	461.5	632	0.0260 (97.4 % total)
Model		Parameters		χ^2, DOF, χ^2_R
`phabs*apec`		kT=1.99±0.14 keV Z=0.11±0.05		173.43, 96, 1.8066
`phabs*(apec+apec)`		kT=$0.82^{+0.14}_{-0.05}$ keV [Z=1.00] $L_{0.5-2.0}$=1.99 $L_{0.5-10.0}$=2.08 $L_{0.3-10.0}$=2.21		93.58, 95, 0.9851
`phabs*(apec+cemekl)`		[kT_{max}= 3.50 keV] [Z=1.00] α=$0.88^{+0.31}_{-0.32}$ $L_{0.5-2.0}$=3.40 $L_{0.5-10.0}$=4.54 $L_{0.3-10.0}$=5.00		93.84, 95, 0.9878
”		kT_{max}=$1.20^{+0.51}_{-0.26}$ keV [Z=1.00] α=$2.07^{+3.32}_{-0.98}$ $L_{0.5-2.0}$=2.31 $L_{0.5-10.0}$=2.47 $L_{0.3-10.0}$=2.68		87.36, 94, 0.9293

Frozen parameters are indicated in []. We report the luminosity, L, in the (0.5-2.0), (0.5-10.0), and (0.3-10.0) bands in units of 10^{41} erg s^{-1}.

been observed (but see Rasmussen, Ponman, and Mulchaey (2006) for the temperature jump in NGC 2276 in a galaxy group).

We performed a morphological analysis to search for a brightness discontinuity in front of the infalling galaxy by adopting several geometries, finding indications of a surface brightness jump at $\sim 6'' \sim 6$ kpc from the galaxy with a significance of 2σ (Figure 7.3). To have a spectroscopic confirmation, we further measured the temperature profile across the surface brightness jump. We extracted the spectra in the 0.5-7.0 keV band in the supposedly post-shock (orange) and pre-shock (blue) regions across the brightness edge (Figure 7.3) and we collected 1700 and 650 net photons in the outer and inner sectors, respectively. In order to measure the temperature jump, we model the ICM emission in front of the galaxy with an absorbed thermal model (`phabs*apec`). Our spectral results may suggest a temperature jump at the shock front ($kT_{\rm pre} = 4.33^{+0.30}_{0.20}$ keV, $kT_{\rm post} = 4.88^{+0.56}_{-0.39}$ keV), although given the uncertainties the pre-shock and post-shock regions are still consistent with being isothermal.

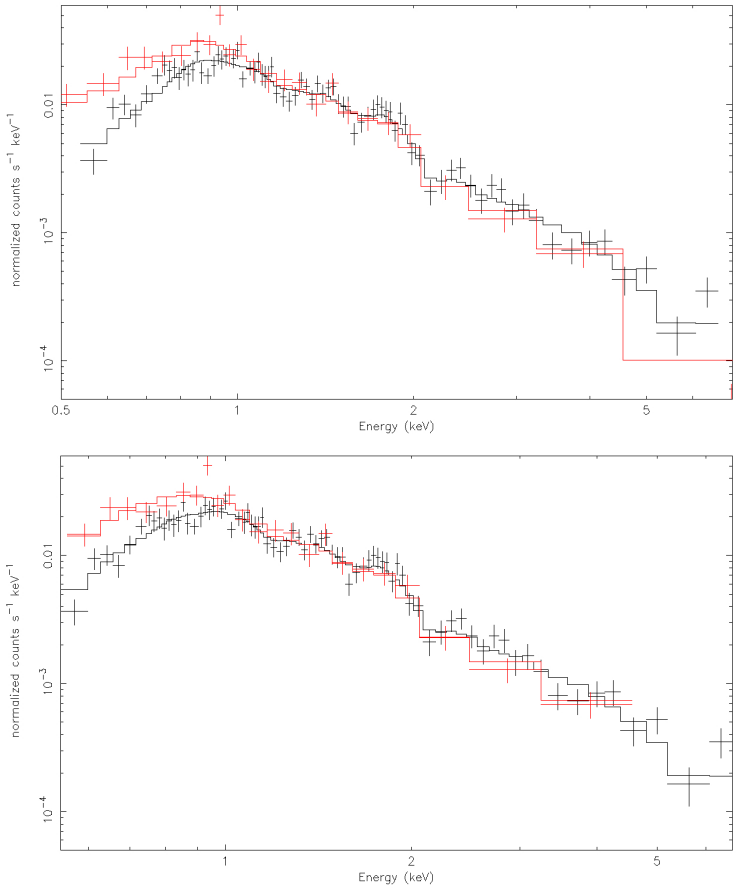

Figure 7.2: Spectrum of the galactic emission composed by combining the observation 16136 (black) and 3192 (red) and fitted with the `apec+apec` (left) and `apec+cemekl` (right) models.

From this analysis we therefore conclude that the *Chandra* data can neither confirm nor deny the existence of the shock front. This may be caused by the combination of the low data statistics and the complex morphology of the shock, as suggested by the Hα surface brightness distribution. We note that with the expected mach number $\mathcal{M} \gtrsim 2$ we would have a physical temperature jump around 2. However, projection effects would significantly decrease the jump and smear out the discontinuity.

The Hα-X-ray spatial correlation

The fact that the morphology of the X-ray gas in the disk follows exactly the morphology of the Hα gas suggests a physical link between these two components. Such connection is indeed expected in these object, as pointed out in the simulations by Tonnesen, Bryan, and Chen (2011), where the authors can reproduce the bright Hα and X-ray emission of the galaxy ESO 137-001, and argue that bright X-ray emission occurs when the stripped ISM is heated and mixed with the high-pressure ICM ($\geq 9 \times 10^{-12}$ erg cm^{-3}). The JW100 ICM pressure of $\sim 3 \times 10^{-11}$ erg cm^{-3} is above this threshold, and about twice the pressure around ESO137-001, hence we suggest that we are observing a similar process.

To further investigate the hypothesis of an interplay between hot ICM and cold ISM, we studied the spatial correlation between the tracers of these components, i.e.

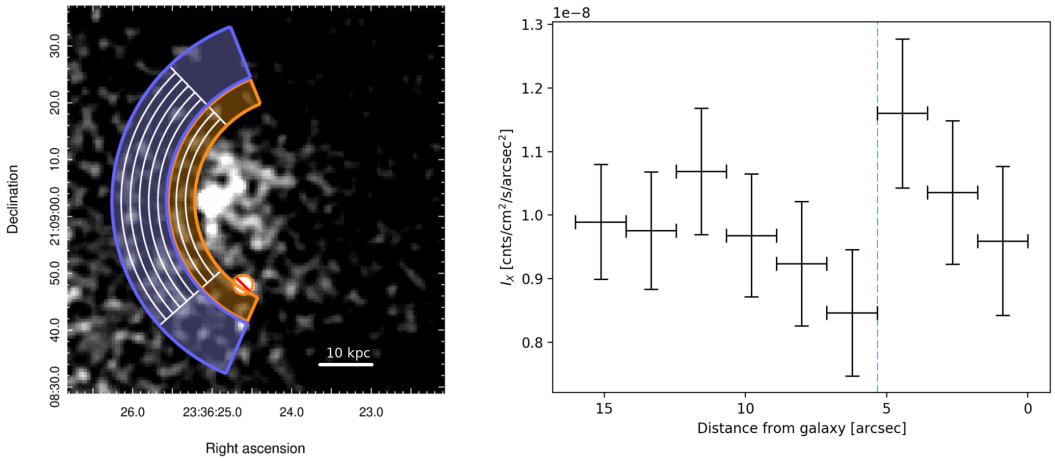

Figure 7.3: *Chandra* image of JW100 in the 0.5-2.0 keV band (left), with the sectors in which we extracted the surface brightness profile (white) and the spectra (blue and orange). The surface brightness profile (right) is taken from the galaxy to the cluster center. Note that the x-axis is inverted to match the pattern of the white sectors in the left panel. The vertical dashed line points out the location of the tentative discontinuity, which is located between the orange and the blue sectors.

the X-ray and Hα emission. We explored this by performing two different sampling of the Hα extended emission, which we corrected both for stellar absorption and dust extinction computed from the Balmer decrement. On the one hand, we sampled it according to the local, optical spectral properties derived with MUSE (see Poggianti et al., 2019b, for further details on the MUSE analysis). In this way we could discriminate the star forming regions from the LINERS ones, which we report respectively in red and blue in Figure 7.4. To estimate the X-ray surface brightness of each region, we extracted the corresponding spectra, where we removed the cluster contribute by using the surrounding ICM emission as the background, and, then, we fitted the spectra with an absorbed `apec` model. Due to the low statistics, we could not estimate the local properties of each region, so, under the basic assumption that the properties of the X-ray emitting plasma are the same all over the galaxy, we fixed the temperature and the metallicity to the values that we estimated for the whole galaxy (kT=0.82 keV, Z=1 $Z_\odot$) and we derived the luminosity in the 0.5-8.0 keV band from the fit normalizations, that we ultimately converted in surface brightness (Figure 7.4, top panels).

However, this approach allowed us to divide the galaxy in only 9 regions. In order to maximize the number of sampling cells, we exploited also a sampling based on the Hα surface brightness (Figure 7.4, bottom panels). We sampled the LINER emission in the Hα tail with 6 $\times$ 6 arcsec cells by using the PT-REX code (see Appendix 1), ending with 19 points to study the spatial correlation. We computed the X-ray surface brightness in units of `counts` s^{-1} `cm`$^{-2}$, similar to the analysis presented in Chapter 2. In this case we could not discriminate the ionization mechanism, but we had enough points to carry out a more detailed statistical analysis with the BCES algorithm (Akritas and Bershady, 1996).

Figure 7.4 presents some striking results. First of all, in both the analysis we found that the Hα and X-ray surface brightnesses correlate as $I_{H_\alpha} \propto I_X^k$, where I_{H_α} and I_X are the surface brightnesses of the two bands. This result confirms that the two phases occupy the same volume and, hence, it suggests a physical relation between

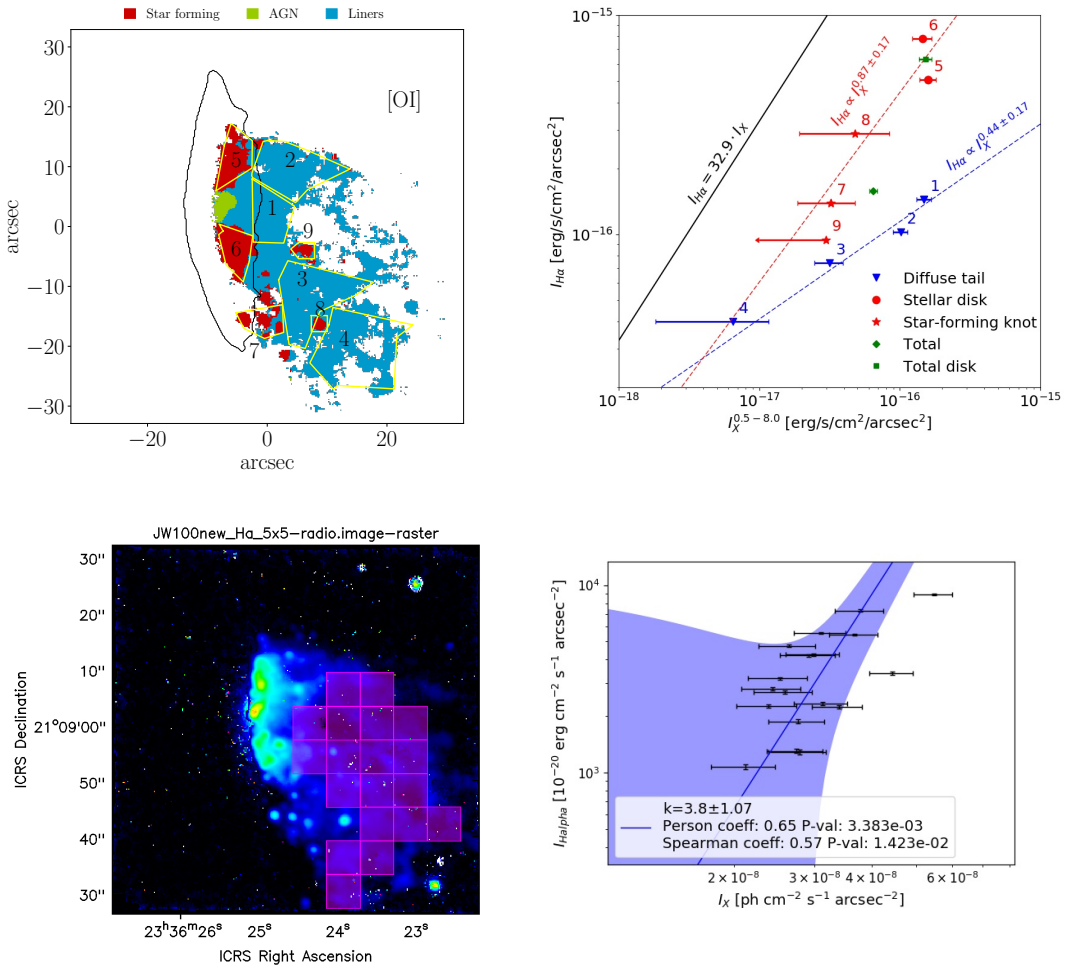

Figure 7.4: Spatial correlation between Hα and X-ray surface brightness where the sampling is based on the optical spectroscopy (top) and the Hα surface brightness (bottom). We report in the left panels the MUSE image with the corresponding sampling grids, including the cell labels and the optical spectral classifications in the top-left image (where the black contours points out the stellar disk), and in the right panels the $I_{\mathrm{H}\alpha}$ vs I_{X} plots. In the bottom-right panel we report also the 95% confidence interval of the fit.

the two emission processes. Interestingly, the correlation is different for star-forming regions and for regions with an [OI] excess, with $k = 0.87 \pm 0.17$ and $k = 0.44 \pm 0.17$ respectively. The finest sampling produced, instead, a much steeper correlation with $k = 3.8 \pm 1.1$, that could be due to the fact that we included in this analysis the low surface brightness region in the north-west part of the tail. In both cases the Spearman correlation coefficients are > 0.6, confirming the strong correlation between the two emissions.

7.2.2 Radio

A plethora of Abell 2626 radio images obtained with different instrument are available, which provide us a multi-frequency view of JW100 at 144 MHz (Ignesti et al., 2020b), 610 MHz (Kale and Gitti, 2017), 1.4 GHz (Gitti, 2013a) and 3.0 GHz (Ignesti

et al., 2017). Here we focus on the analysis of the 144 MHz and 1.4 GHz emission, based on the images presented in Chapter 5.

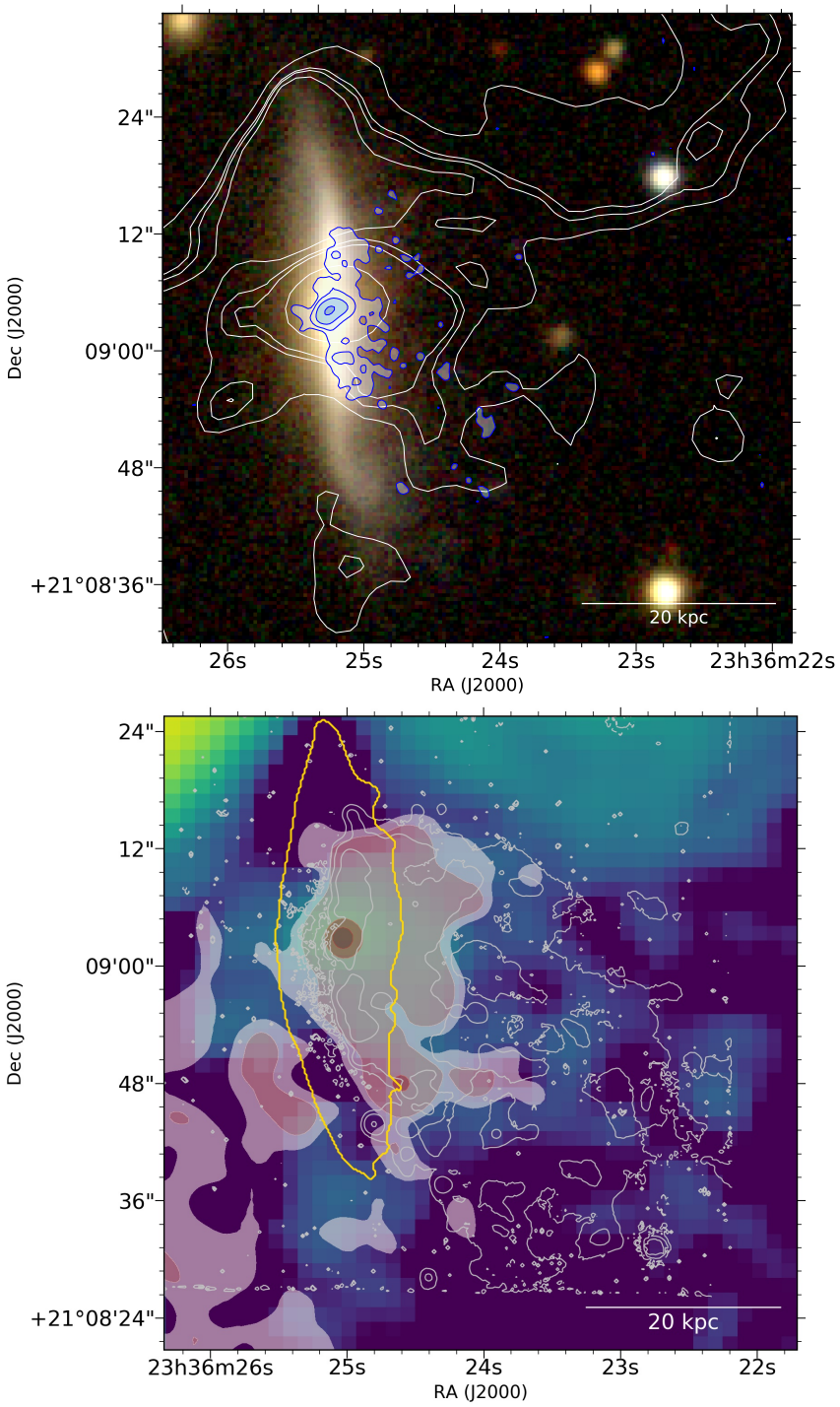

Figure 7.5: Top: Composite SDSS image of JW100 from bands *i*, *r* and *g*. The blue-filled contours are 3, 6, 12, 24 ×RMS levels of the 1.4 GHz image (RMS=13 μJy beam^{-1} , resolution 1.5″×1.4″), the white continuous contours are the 3, 5, 6, 12 ×RMS levels of the 144 MHz image (RMS=120 μJy beam^{-1}, resolution 6.7″×5.6″) presented in Ignesti et al. (2020b) (see Chapter 5); Bottom: Multi-wavelength view of JW100 comprising of LOFAR 144 MHz radio emission (color map), MUSE Hα and stellar continuum (silver and gold contours, respectively, from Poggianti et al., 2019b) and Chandra X-ray emission in the 0.5-2.0 keV band (red contours).

In the disk, the radio emission globally coincides with the location of the Hα

and X-ray emission (Figure 7.5). We observe a slight extension to the east of the ram pressure edge, coinciding with the galaxy center, that is most likely due to the radio continuum emission from the AGN, which is detected in the high-resolution images at 5 GHz presented in Gitti (2013a, Figure 4) and Ignesti et al. (2017, Figure 1). However, we note that the "radio" disk is truncated with respect of the optical disk. Outside of the disk, extended radio emission is detected at both frequency (for the tapered reconstructed images at 1.4 GHz where this component is more evident, see Figure 3 of Gitti, 2013b).

In order to probe the thermal or non-thermal origin of the radio emission, we estimated the spectral index of the tail between the two frequencies. At 144 MHz we measured a total flux density of 13.3±2.4 mJy, with 4.8±1.0 mJy associated with the AGN. By subtracting the AGN contribution, we estimated that the emission from the galaxy is 8.5±2.6 mJy. In order to to estimate the spectral index, we compared these values with the flux densities measured in the same regions in the 1.4 GHz map that we used for the spectral index analysis, thus with matching UV-range and resolution (see Chapter 4 for further details). We found that both the extended emission and the AGN have a spectral index $\alpha = -0.6 \pm 0.1$. We further estimated the spectral index between 1.4 and 5.5 GHz using the VLA maps presented in Ignesti et al. (2017, , Figure 1). At 5.5 GHz we do not observe diffuse radio emission in the tail, so by considering the 3σ level, we could estimate only a lower limit for the spectral index $\alpha < -0.5$, which is in agreement with the estimate between 144 MHz and 1.4 GHz.

We compared our results with the findings of Tabatabaei et al. (2016), which fitted the 1-10 GHz spectral energy distribution of nearby galaxies using a Bayesian Markov Chain Monte Carlo technique in order to disentangle the thermal and non-thermal contributions to the radio emission (e.g., Condon, 1992). They measured a total spectral index (combination of thermal and non-thermal components) ranging from -0.5 to -1.0. Then, by assuming $\alpha = -0.1$ for the thermal radio emission, they estimated a mean thermal fraction at 1.4 GHz of 10-13%. Therefore, the spectral index we measured ($\alpha \simeq -0.6$) entails that the radio emission is mostly ($\sim$ 90%) non-thermal, thus indicating that we are mainly observing synchrotron emission of relativistic electrons diffused in the tail of JW100.

The principal source of non-thermal radio emission in galaxies is the synchrotron emission of relativistic electrons accelerated by supernovae explosions (e.g., Condon, 1992), thus the non-thermal radio luminosity should scale with the galaxy SFR. For the case of JW100, the expected $L_{1.4GHz}$ associated with the SFR (4 $M_\odot$ yr^{-1}) can be derived by using the Bell et al., 2003 calibration:

$$SFR = 3.25 \times 10^{-22} \left(\frac{L_{1.4\,\mathrm{GHz}}}{[\mathrm{W\ Hz^{-1}}]} \right)\ M_\odot\ \mathrm{yr}^{-1} \tag{7.1}$$

The resulting radio luminosities are 2.5·10^{21} W Hz^{-1} and 9.8·10^{21} W Hz^{-1} for the tail and the disk, respectively. These values are consistent with the observed $L_{1.4GHz}$, which are 5.7±1.2 and 11.2±0.8×10^{21} W Hz^{-1} respectively, thus suggesting that the star formation is the main source of radio emission. However, we cannot exclude a contribution of other sources, such as stripping of relativistic electrons from the galaxy due to ICM winds. On the other hand, the k-corrected, monochromatic radio power at 144 MHz of the extended emission is 7.7×10^{22} W Hz^{-1}. The observed spectral index down to 144 MHz ($\alpha < -0.5$) suggests that, at lower frequencies, we

are observing the oldest/weakest electrons produced by the supernovae explosions. Interestingly, at the end of the tail we observe radio emission at 144 MHz without a counterpart at 1.4 GHz, which points out the presence of steep-spectrum emission in that region.

7.3 Discussion

7.3.1 Origin of the X-ray emission

The galactic X-ray emission is extended on a scale $\geq$ a dozen kpc, and it is clearly detected above the local cluster emission (see Figure 7.1). We do not observe, instead, any anisotropic features in the X-ray emission that may suggest the presence of jets powered by AGN. Despite the statistical degeneracy between the models we tested, overall the spectral analysis revealed that the X-ray emission is mostly thermal and it is produced by a warm plasma with a temperature $\sim$1 keV, which is not consistent with neither the ISM ($kT < 10^{-3}$ keV) or the ICM (kT=3.5 keV).

The X-ray emitting plasma might have different origins, such as star formation within the tail or interplay between ICM and ISM, which, for the case of stripped galactic tail (or, in general, for any cold cloud embedded in a hot wind), is indeed predicted by several numerical simulations (e.g., Tonnesen, Bryan, and Chen, 2011; Scannapieco and Brüggen, 2015; Gronke and Oh, 2018; Sparre, Pfrommer, and Ehlert, 2020; Kanjilal, Dutta, and Sharma, 2020). In this latter scenario the evolution and the thermal properties of the stripped clouds are driven by the complex balance between the ISM heating (which can be due to conduction, shock heating, or complex hydrodynamical interactions such as the evolution of instabilities) and ICM cooling. This interplay would lead to the formation of a mixing layer between ISM and ICM with a temperature in between that of these two phases, which is in agreement with our findings. However, the details of this complex process are still unclear. We note that, in principle, a third scenario would be possible, i.e. extended X-ray emission due to the stripping of the galactic hot corona during the infalling. However, this tenue structure would dissipate very rapidly in the ICM ($\sim$15 Myr), thus disfavouring this scenario. Therefore, we do not discuss it in this Section, but a detailed discussion can be found in the Appendix of Poggianti et al. (2019b).

The star-formation scenario

Concerning the first hypothesis, in the presence of SF, the dominant contribution to the X-ray emission is expected from high-mass X-ray binaries, that have a lifetime of a few 10^7 yr and dominate over the emission of low-mass X-ray binaries when there is vigorous ongoing SF. A smaller contribution arises from the hot ISM ionized by supernovae and massive stars. Each of these contributions, and the sum of the two, correlate well with other SFR indicators, such as Hα and UV emission (e.g., Ranalli, Comastri, and Setti, 2003; Mineo et al., 2014). To test whether the observed X-ray luminosity of JW100 is compatible with the SFR measured from the optical lines, we use the $L_X - SFR$ calibration from Mineo et al. (2014), which we adapted by converting from a Salpeter to a Chabrier IMF and from 0.5-8.0 keV to 0.5-10.0 keV

assuming a factor 1.11, that is:

$$SFR = 1.32 \times 10^{-40} \left(\frac{L_{X(0.5-10)}}{[\mathrm{erg\ s^{-1}}]} \right) \ M_{\odot}\ \mathrm{yr}^{-1} \tag{7.2}$$

With this calibration, the X-ray luminosity of JW100[3] (see Table 7.2) would correspond to SFR=28±5 $M_{\odot}\, yr^{-1}$ (model `apec+apec`), SFR=60±11 (model `apec+cemekl` with T_{max} fixed), or SFR=33±6 $M_{\odot}\, yr^{-1}$ (model `apec+cemekl` without T_{max} fixed). Even excluding the region of the disk where the X-ray and Hα contours are compressed by ram pressure, where the X-ray luminosity could be boosted, the derived SFR would still be very high, ranging between 21±4 and 46±9 $M_{\odot}\, yr^{-1}$. In the range 0.5-10keV, $\sim$ 50% of the counts come from the tail and assuming the shape of the spectrum in the tail is similar to the total one this should correspond to a tail SFR between $\sim$14±3 and $\sim$30±7 $M_{\odot}\, yr^{-1}$ depending on the X-ray model adopted.

The X-ray-based SFR values are much higher than those measured from the dust-corrected, absorption corrected Hα luminosity ($4M_{\odot}\, yr^{-1}$ total,$\sim$ $1M_{\odot}\, yr^{-1}$ in the tail, Poggianti et al., 2019b) even under the most generous assumptions. The scatter in the $L_X - SFR$ relation in Mineo et al. (2014) is not able to account for the low Hα-based SFRs, which is a factor between 6 and 30 lower than the X-ray-based values. Using the $L_X - SFR$ relation in the 0.5-2 keV band from Ranalli, Comastri, and Setti (2003), transformed from a Salpeter to a Chabrier IMF, yields slightly lower X-ray-based SFR (between 14 and 24 $\sim$ $1M_{\odot}\, yr^{-1}$) than with the Mineo calibration, but these values are still higher than the Hα-based SFR by a factor between 4 and 6. It is interesting to note that comparing the total X-ray emission (having excluded the AGN) and the 1.4 GHz emission, the X-ray emission of JW100 is more than an order of magnitude too high for its radio continuum emission, according to the relation shown in Figure 1 of Mineo et al. (2014). Thus, while the radio continuum and the Hα emission produce consistent estimates of the star formation, the X-ray emission has a significant excess. We conclude that it is necessary to invoke an additional source of X-ray emission other than the sources linked with ongoing star formation.

The ICM-ISM interplay scenario

We explore the possibility that the X-ray emission of JW100 could arise as consequence of the ICM-ISM interplay. In this case, the warm plasma would be composed either by heated ISM (either due to shock heating, thermal conduction from the ICM, mixing of the ISM and the ICM), cooled ICM onto the colder, stripped ISM, or a mixing of the two. Assessing the dominant process between heating and cooling is crucial to understand the evolution of the star formation in the tail. On the one hand, the cooling could actively enhance the star formation by providing an additional source of cold gas. On the other hand, an efficient heating of the ISM would prevent the formation of molecular gas and ultimately quench the formation of new stars.

The pure, thermal ICM cooling scenario can be tested by considering the Field length for a static cold cloud immersed in a hot medium, $\lambda_F = [\kappa(T)T/n^2\Lambda(T)]^{1/2}$,

[3]We remind the Reader that X-ray point sources (AGN and candidate ULX) have already been excluded from the calculation of the X-ray luminosities.

where κ is the thermal conductivity, T and n are the temperature and number density of the hot gas and Λ is the cooling function. This is a measure of the balance between the cloud energy gain by conduction and the energy loss by radiation (see McKee and Begelman (1990)). For a cloud size larger that λ_F, radiative cooling dominates and the hot ICM condenses on the cloud. Numerically, $\lambda_F \sim 136\phi_c^{1/2}T_{e,7}^{7/4}n_e^{-1}\Lambda_{-23}^{-1/2}$ pc $\approx$ 450 kpc for the ICM surrounding JW100 (McKee and Begelman, 1990). For this estimate we have adopted $n_e \sim 3\times10^{-3}$ cm^{-3} and $T \sim 3.5$ keV from the X-ray analysis above. The factor $\phi_c \leq 1$, which describes the suppression of the conductivity in a magnetized plasma, has been set ~ 1. The value for λ_F, much larger than the size of the JW100 cold ISM, makes the cooling scenario unpalatable, unless $\phi_c \ll 1$.

Therefore, the remaining scenarios are the pure ISM heating or the ISM-ICM mixing. Unfortunately, all the spectral models we tested are statistically indistinguishable (Table 7.2), thus we can not discern between a single-temperature model (that could favorite the idea that the X-ray emission comes solely from heated ISM) and the multi-temperature model (which could describe a mixing of cold ISM and hot ICM). The X-ray plasma metallicity would be a key probe to discern the models, because in the ISM-ICM mixing scenario (or in the ICM cooling one) we would expect the metallicity to be lower ($Z \simeq 0.1-0.3\ Z_\odot$, similar to the ICM metallicity we report in Table 7.1) than that of the heated stripped gas, whose MUSE metallicity is solar and supersolar. However, the existing X-ray data do not allow us to estimate the metallicity of the X-ray emitting gas, and longer *Chandra* exposures are needed. Another possibility to further explore this problematic is to analyze XMM-Newton observation of this object because the better spectral resolution and effective area could end in a better characterization of the X-ray spectral properties of the galaxy. The XMM-Newton study of JW100, and other jellyfish galaxies, is going to be object of a follow-up work.

Insights from the Hα-X spatial correlation

In general, we observe a positive correlation between X-ray and Hα surface brightness (Figure 7.4), that indicates that the warm, X-ray emitting medium closely follows the spatial distribution of the stripped ISM. This result indicates that the X-ray emission arises due to local, small scale (<6 kpc, which is the smallest sampling scale we adopted) processes taking place in the stripping ISM. This is in agreement the idea that the high-energy emission is a consequence of the local interplay between ICM and ISM along the stripped tail and that it could be produced by the interface between the two components which envelopes the stripped ISM (e.g. Gronke and Oh, 2018; Sparre, Pfrommer, and Ehlert, 2020; Kanjilal, Dutta, and Sharma, 2020).

Interestingly, the spectral-based analysis shows that LINER regions are located to the bottom-right with respect to the SF regions, i.e. that, for similar I_X, SF regions have an higher $I_{H\alpha}$ than LINER ones. Moreover, the Hα-X surface brightness relation of even strongly star forming regions falls on the left with respect to the prediction, which entails that the X-ray emission cannot be fully explained by the expected emission due to SF under standard conditions. All the star-forming regions present an excess of X-ray emission compared to the SFR calibration commonly used in the literature, represented by the solid black line in Figure 7.4. At this point we can only speculate on the possible origin for the discrepancy between the star-forming points and the standard SFR relation line in Figure 7.4:

- ◇ The standard SFR calibrations may not apply under the extraordinary physical conditions in which stars form in the tail (IMF, different timescales probed by the two indicators etc);
- ◇ There could be an additional source of X-ray emission due to ISM heating even along the line of sight of star-forming regions (though its relative importance should be lower than in the [OI]-excess regions). This is clearly possible, but the effect should be conspicuous, because the observed X-ray surface brightness of star-forming regions is a factor 5-8 higher than expected from the Hα and, in order to reconcile the two SFR estimates, the majority of the X-ray flux should arise from the ICM-ISM mixing. This effect might be seen from another point of view. The main, underlying relation in Figure 7.4 (top panels) might be the one traced by the blue points, in which the emission in Hα and X arise from exactly the same process, e.g. ISM-ICM mixing. The star-forming points would lie *above* this relation due to an excess of Hα flux due to star formation.

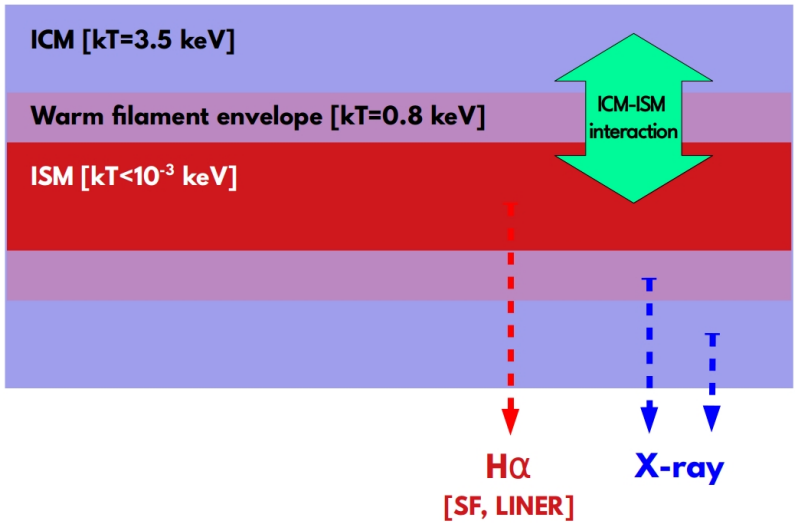

Figure 7.6: Sketch of the scenario outlined by our findings, where the warm, X-ray emitting plasma (violet) forms between the stripped ISM filament (red) and the ICM (blue), producing different emissions.

Therefore, our data are consistent with the X-ray emission of JW100 coming from warm regions that envelope the cold ISM produced by the ISM-ICM mixing or thermal heating of the ISM due to the ICM, or shock heating (Figure 7.6). This warm envelope could play the role of the additional source of ionization/excitation of the stripped gas, causing the different optical line ratios, in particular the [OI], that has been claimed by Poggianti et al. (2019a) to explain the exceptional LINER emission of JW100.

On the basis of this, we speculate that the LINER emission is tracing those regions of the tail that have been more affected by the ISM-ICM interplay. This speculation can be tested in the future both via observations and numerical simulations. On the one hand, it will be crucial searching for extended X-ray emission in those jellyfish galaxies with extended LINER emission in their tail (such as JO201 and JO194 from the GASP sample, Poggianti et al., 2019a). On the other hand, MUSE optical

spectra can be compared with the predicted optical signatures expected from a cold cloud embedded in a hot plasma, with properties similar to the ones we inferred from the X-ray spectral analysis.

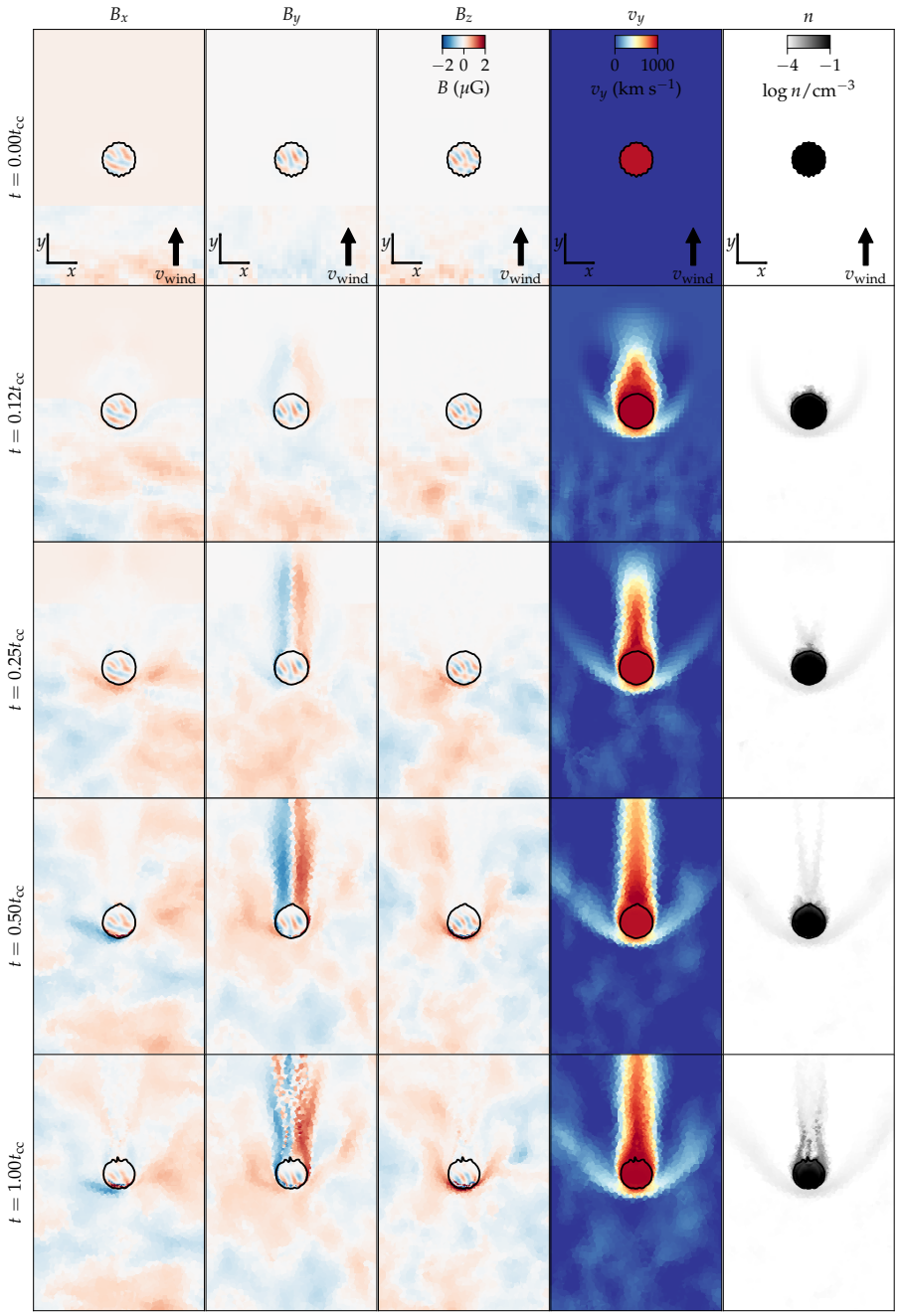

Figure 7.7: Initial time evolution of magnetic field components, the vertical velocity and the gas density in the simulation with a turbulent wind. This demonstrates the formation of a magnetic draping layer that enables condensation and accretion of hot ICM onto the tail and hence magnetic field alignment with the filamentary tail. Each panel measures 300 kpc × 450 kpc. We refer to Müller et al. (2021) for furhter details about the simulations

7.3.2 Radio emission as probe of ISM-ICM interplay

The extended radio emission of JW100 does not seem to be related to the complex scenario described above because the observed luminosity is in agreement with the

SFR (see Section 7.2.2). However, a significant insight recently came from the study of the jellyfish galaxy JO206 presented by Müller et al. (2021). JO206 shows an high degree of polarized emission ($\sim$ 50%), which indicates that the magnetic field of the galaxy is extremely ordered along the stripped tail. The presence of an ordered magnetic field can be explained by the action of the ICM accretion, that would be able to deposit layers of magnetized plasma onto the galaxy (Sparre, Pfrommer, and Ehlert, 2020). Accretion of draped magnetised plasma from the hot wind that condenses onto the external layer of the tail, which is then adiabatically compressed and sheared by the velocity difference of the cold tail and the wind can explain the high degree of fractional polarisation and ordered magnetic field (Figure 7.7). These magnetised cold filaments in the jellyfish tail are then "lit up" by the synchrotron emission from cosmic ray electrons that are accelerated in supernova remnants in the interstellar medium and the star-forming tail. The streaming of electrons along the ordered magnetic field would result also in a steepening of the spectral index along the tail due to their radiative energy losses during the travel. Finally, such an ordered magnetic field may prevent heat and momentum exchange (e.g. Vijayaraghavan and Sarazin, 2017), and favor in-situ star formation in the tail. In this scenario, star formation in the tail should be a self-regulating process, achieving a balance with the magnetic field in a sort of feedback: a strong and widespread star-formation activity would disrupt the ordered magnetic field, which in turn is fundamental to allow the star-formation process to continue.

Transposed to the case of JW100, this scenario has obvious connections with our results. The draping of hot ICM onto the cold ISM would be consistent with the ICM-ISM interplay that we invoked to explain the observed spectral properties. However, it would favour the ICM cooling scenario over the ISM heating. This, apparently, contradicts our speculation based on the Field length, which in turn disfavours the ICM cooling. This could be reconciled by considering that, if the scenario proposed for JO206 is valid also for JW100, then the presence of an ordered magnetic field "shielding" the galaxy would suppress the thermal conduction perpendicular to the magnetic field stripped tail directions (i.e. toward the surrounding ICM) and, hence, it would overturn the estimate of the Field length by significantly enhancing the suppression of the conductivity. The ICM draping is in agreement also with the spatial correlation that we observe between the X-ray and Hα emission, where, under this hypothesis, the former would be produced by the ICM drapes left onto the stripped ISM. Another striking prediction of this model is the presence of steep-spectrum radio emission produced by the streaming of CRe, injected by supernovae, along the ordered magnetic field. This could be in agreement with the 144 MHz emission that we observe without 1.4 GHz counterpart, i.e. with a spectral index significantly steeper than -0.6.

However, further testing is required before directly connect the ICM draping hypothesis to the results of the X-ray analysis. The temperature we measure ($\sim$0.8 keV) is lower than that of the ICM (3.5 keV), hence even by assuming that the draping is able to deposit the hot plasma over the stripped ISM, an additional cooling phase is required to match the temperatures. An important step to further explore this scenario would be to obtain deep *Chandra* observations of JO206 to check if 1) this galaxy show extended X-ray emission and 2) the thermal properties of such emission resembles those we found in JW100.

7.4 Conclusions and future prospects

We presented a multi-wavelength analysis of the jellyfish galaxies JW100. In particular, we studied the radio and X-ray emissions, which are still unexplored for these galaxies, obtaining some valuable insights into the physics of the ram-pressure stripping. On the one hand, the X-ray analysis revealed that the extended X-ray emission is produced by a warm ($kT \simeq 1$ keV) medium, whereas the study of the spatial correlation showed that this warm medium is closely connected to the cold, stripped tail traced by the Hα emission. On the other hand, the radio analysis revealed that the extended radio emission can be associated with the SFR, for the most part. However, the low-frequency image revealed also the presence of steep-spectrum components located at the end of the tail.

We suggest that our findings could be the result of the accretion of hot, magnetized drapes of ICM onto the galaxy (as suggested by Sparre, Pfrommer, and Ehlert, 2020; Müller et al., 2021). We speculate that this process kicked-off the interplay of the ICM and the ISM over the stripped tail, which can explain both the presence of a warm, X-ray emitting envelope following the ISM, and the additional source of ionization in the tail which produced the large LINER emission observed by MUSE.

Investigating this process is crucial because it can push forward our understanding of the thermal impact of the stripping, as a possible catalyst or obstacle for the star formation, and of origin of magnetic field in these galaxies, with several implications for the galaxy evolution. From the observational point of view, these studies can be carried out by expanding the samples of jellyfish galaxies with deep, multi-wavelength data to study their radio and X-ray properties. The studies presented in Poggianti et al. (2019b) and Müller et al. (2021), in that sense, represent pilot studies to plan future observations.

Finally, we showed that low-frequency LOFAR observations, by probing the steep-spectrum emission at the end of the tails, can be a keystone also in the study of jellyfish galaxies. For this reason, we are planning to explore deeply the low-frequency side of the jellyfish galaxies by analysing the LoTSS observations (GASP-LOFAR MoU, PI Ignesti, Poggianti, McGee). In this context, low-frequency observations can unveil two unexplored fields of research. On the one hand, LOFAR observations can probe the low-frequency radio emission of the oldest relativistic electrons injected by supernovae. By measuring the spectral index of their synchrotron emission, it will be possible to infer the radiative age of these relativistic particles, hence to estimate the time elapsed since the supernovae explosions that produced them. Measuring this will provide a crucial constraint on the time-scale of the star formation in these objects. On the other hand, the large-scale, ordered magnetic field which would be originated by accreting magnetized ICM during the stripping, in combination with the injection of relativistic electrons by supernovae, would result in extended, steep-spectrum radio emission enveloping the stripped filaments. The study of these structures, which could be carried out only with LOFAR due to its unprecedented sensitivity and resolution at low frequencies, will drive forward our understanding of the origin of large-scale magnetic field in the tail of jellyfish galaxies.

Chapter 8

Conclusions

In this Thesis we tackled a series of open questions in the study of relaxed galaxy clusters by focusing on the interplay between relativistic and thermal plasma. Our analysis was based on a multi-wavelength approach which combined radio and X-ray observations of our targets. We also developed new methods and suggested new approaches to provide further insights in this field. Here we summarize the main results of the Thesis:

- ◇ **New insights from the radio and X-ray spatial correlation.**
  We studied, for the first time, the spatial correlation between radio (mini-halo) and X-ray emission in relaxed clusters by means of the point-to-point analysis (Chapter 2). For these studies we developed a new technique, the Monte Carlo point-to-point analysis, which combines randomly-generated point-to-point analysis to probe the parameter space of the spatial correlation. This new tool, which we included in the software PT-REX developed during this Ph.D. Thesis (Appendix A), allows to extend the point-to-point analysis to small or poorly resolved sources, such as radio mini-halos, thus expanding the horizons of the spatial correlation studies.

  We found a clear evidence of spatial correlation between the two emissions, with the radio surface brightness I_R, which traces cosmic rays and magnetic fields, having a distribution that declines more rapidly with radius than the X-ray brightness I_X. These results have two main implications. First, we found that the spatial correlation discriminates between mini and giant halos, where the former have a generally super-linear (more peaked) I_R-I_X scaling and the latter are instead sub-linear (less peaked). This suggests that the radio-X spatial correlation may highlight an intrinsic physical differences between these sources. Second, our studies have been used to test the hadronic scenario. Our results point to the central AGNs as the natural sources of cosmic rays in relaxed clusters. Following this hypothesis, we demonstrated that the proton-proton collisions can efficiently fill the ICM within a few hundred kpc from the BCG with relativistic particles, which could either produce directly the radio emission or be the seed for a subsequent re-acceleration, without violating the Fermi-LAT detection limits.

- ◇ **New discoveries with LOFAR.**
  The works presented in this Ph.D. Thesis exemplify how the new facilities, such as LOFAR, are revolutionizing our understanding of non-thermal plasma in galaxy clusters. Sensitive, low-frequency observations are probing the properties of low energy cosmic rays electrons, thus unveiling new phenomenologies and suggesting new physical mechanisms in the ICM. These mechanisms affect the life-cycle of the cosmic rays and, therefore, of the cluster radio sources.

Specifically, in our works we studied the LOFAR observations of two relaxed clusters, Abell 2626 and 2A0335+096 (Chapters 5 and 6). Our studies indicated that the dynamics and the micro-physics of the ICM are able to extend the lifetime of the relativistic plasma ejected by the radio galaxies, and to model it into complex structures. These results are part of a larger upsurge of new results that have been achieved in the past few years thanks to LOFAR and the LoTSS observations.

However, the true potential of these new instruments lies in the possibility to detect thousands of new sources, thus allowing us to carry out, for the first time, statistical studies of large sample of diffuse radio sources. We contributed in this ambitious project, which will involve the LOFAR community for the next years, by developing the infrastructure of the LoTSS-PSZ2 automated catalog (Chapter 4).

◇ **New windows on the ram pressure stripping physics.**
Radio and X-ray are still relatively poorly explored for ram pressure stripping studies. Our results on the jellyfish galaxy JW100 (Chapter 7) showed that they can instead provide important insights into the physics of this process, which is crucial for the cluster galaxies evolution. On the one hand, we carried out a deep spectral analysis of the X-ray emission of the galaxy, and, for the first time, we studied the spatial correlation between the X-ray and optical Hα emission. We found that the X-ray emission is produced by an envelope of warm plasma formed in the interface between the stripped ISM and the ICM. The presence of a warm plasma enveloping the tail can explain the peculiar optical spectral properties of jellyfish galaxies. From the thermal point of view, we found that the stripped tails of these galaxies resembles the cold filaments observed at the center of relaxed clusters, thus imply that they could be produced by similar processes. In this context, due to the parallels between the case of jellyfish galaxies and the more general case of the evolution of cold clouds subjected to an hot wind, our findings can help constraining future numerical simulations aimed to explore this complex problem.

On the other hand, JW100 represented the first study of the low-frequency radio emission of a jellyfish galaxy. We observe that the low-frequency radio emission follows the stripped Hα tail and extends beyond the high-frequency emission, thus suggesting the presence of steep-spectrum radio emission at the end of the tail. Recent high-frequency polarimetric observations, assisted by detailed numerical simulations, found that these features can be explained by the presence of an ordered magnetic field produced by the draping of the ICM onto the galaxy, and highly ordered along the tail. Our findings demonstrate that, by probing the steep-spectrum emission, low-frequency observations can provide complementary constraints for this complex process, thus pushing forward our understanding of the physics of ram pressure stripping.

Overall, our results outline the path for future developments. The fascinating possibility, emerged in our work, that the I_R-I_X spatial correlation could reliably discriminate mini and giant radio halos needs to be tested on larger samples. If confirmed, it will be crucial in the next-generation statistical studies, when, thank to the potential of the new observatories, the number of diffuse radio source will increase dramatically. Our results in the studies of ram pressure stripping can be instead developed

on shorter terms. Our findings encourage to explore the radio and X-ray emission of other jellyfish galaxies, and provide the basis to design future survey studies of these objects. A first important step in this direction has already been done by designing a first sample of jellyfish galaxies to be observed with LOFAR within the LoTSS survey.

We are at the sunrise of a golden age for radio astronomy due to the arrival of facilities such as LOFAR, uGMRT, ngVLA, MeerKAT, and, ultimately, SKA. These next generation instruments, combined with the new and incoming X-ray observatories such as *eROSITA* or *ATHENA*, will assure great progresses in the studies of galaxy clusters. In this exciting context, hopefully the results presented in this Thesis can contribute to push forward our understanding of these complex ecosystems.

Appendix A

PT-REX, the Point-to-point TRend eXtractor

A.1 Introduction

In this Appendix we present the Point-to-point TRend Extractor (PT-REX), a tool designed to easily evaluate the spatial correlataion between different emissions, which has been largely employed in this Thesis (see Chapters 2, 5, 6 and 7). Complex astrophysical systems are characterized by multi-wavelength emission. It follows that the only way to have a comprehensive understanding of their nature is to combine the information derived from as many observations as possible. In the case of extended sources, the study of the spatial correlation between emissions at different wavelengths is the key to understand the physical connection between the processes that are taking place in the source. Observing a positive spatial correlation indicates that the two components responsible for the emissions occupy the same volume, whereas the relative scaling may provide some insights into the physical link between them.

These studies can been carried out by using the point-to-point (ptp) analysis which is, basically, the comparison of surface brightness measured by two different observation made by sampling the extended source with a grid. Under the assumption that each cell of the grid cover the same space of the celestial sphere in each observation, the ptp analysis is more flexible than a comparison between surface brightness radial profiles because it can be seamlessly performed on asymmetrical sources and it can be more responsive to the presence of substructures embed in the extended emission, because their signals are not “blended" together by the azimuthal averaging[1]. Therefore, performing a ptp analysis can offer an additional insight into the nature of a source.

[1]The drawback is that, contrary to radial profile which can be easily interpreted by assuming a spherical symmetry of the system, understanding the physical meaning of a ptp trend could be not trivial, especially for non-spherical objects.

A.2 PT-REX

PT-REX is flexible python script to easily carry out the ptp analysis on every kind of extended radio source. PT-REX handles most of the operations with the the Common Astronomy Software Applications (CASA) packages v.5.6 and 6.0 (McMullin et al., 2007) developed by the National Radio Astronoly Observatory. We integrated the CASA tools with a variety of Python libraries from Astropy and Scipy. The code is structured in a series of tasks to handle the individual steps of a ptp analysis independently, from defining a grid to sample the radio emission to accurately analyze the data with several statistical method.

Figure A.1: The logo of PT-REX.

A.2.1 Data preparation

PT-REX works by combining radio and X-ray images of an extended source. In order to have reliable results, input images must have matching coordinates systems. Radio images can be produced with any preferred software, provided that they include information about the beam size and the pixel/arcsec scale in their header to be read with CASA task `imhead`. Concerning the X-ray images, multiple observations can be combined together to improve the count statistic. The X-ray images can be provided as a single exposure-corrected and background-subtracted image in units of surface brightness (e.g., photons cm^{-2} s^{-1}) or by providing the count, background and exposure images separately. CASA region files, which are necessary to define the grid and the masks (see Section A.2.2 and A.2.5) can be defined while running PT-REX by using the CASA `viewer`. Finally, ancillary information about the calibration error of the radio images and the preferred statistic method (see Section A.2.6) have to provided before running the analysis.

A.2.2 Sampling algorithm

The core of the ptp analysis is the sampling of the diffuse emission. We developed a simple algorithm that converts a rectangular region provided by the user into a grid. The region is intended to include the source which is going to be sampled, and thus we refer to is as region of interest. The boundaries of the sampling grid, as cell size, lower threshold in surface brightness to be sampled and regions to exclude, have to be provided at the begin of the analysis. In order to have a reliable reconstruction of the radio flux density, the cell size has to be large at least as the beam of the radio image. A larger cell-seize can be adopted to increase the signal-to-noise ratio of each cell in the two observation. However, for a given source larger cells entail a lower number of points to finally study the spatial correlation, which can eventually impact in the study. A rule of the thumb is that 15 cells, at least, are necessary to sample the diffuse emission to assure a reliable outcome of the analysis, so a compromise between resolution of the grid and signal-to-noise has to be found. Finally, the threshold defines the lowest value of surface brightness that is going to be sampled by the grid and it is expressed in unit of Jy $beam^{-1}$.

The sampling algorithm is quite straightforward and it described in Figure A.2. After a preliminary check on the cell-size, the region of interest is converted in a

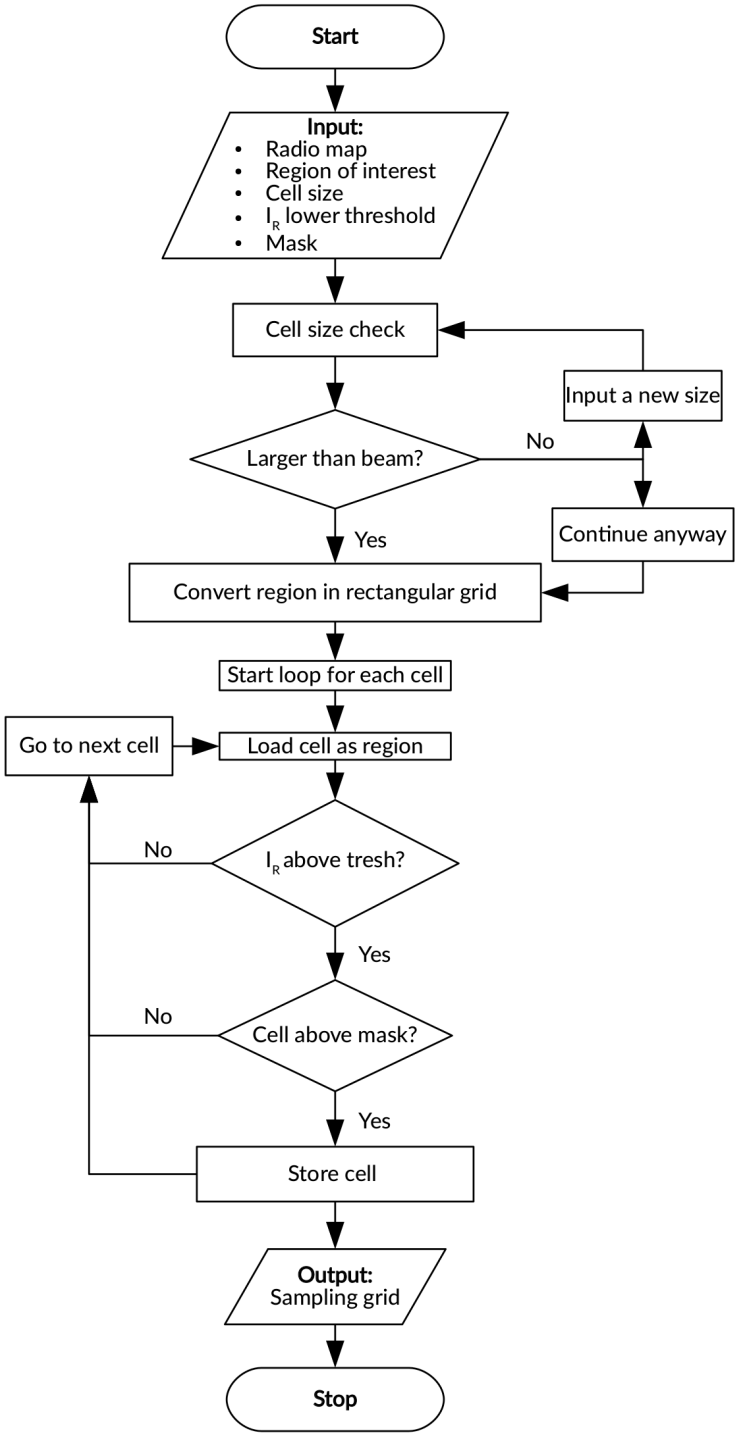

Figure A.2: Flowchart of sampling algorithm.

rectangular grid. At this step, the coordinates of each cell are defined in the pixel units of the radio image. Then the radio surface brightness and the position with respect of the mask are evaluated for each cell of the grid, starting from the bottom-left to the top-right. These checks are done with the CASA task `imstat`. All those cells that do not meet the requirements are excluded, whereas the others are converted in J2000 coordinates and finally stored in a region file, which is the final output of the routine. Every sampling grid can be loaded on the top of the radio image by using the CASA `viewer` and it can be further modified manually to better adapt to the

science case. After having defined a sampling grid, we can use it to compare radio and X-ray emission.

A.2.3 Single-mesh analysis

We define a single-mesh ptp (SMptp) analysis a ptp analysis carried out by using only a mesh to sample the radio emission. It is composed of two steps: first the radio and X-ray surface brightness are measured in each cell, then they are compared in a $I_R - I_X$ plot to evaluate the spatial correlation. We present the flowchart of the process in Figure A.3. The routine that collect the values of I_R and I_X is quite simple. For a given sampling grid, which was previously created by using the sampling algorithm, I_R and I_X are evaluated for each of its cell. For the radio image, the flux density in each cell is measured with the CASA task `imstat` and the converted in I_R by dividing for the area of the cell, Ω_c, in units of arcsec^2. The associated error, σ_R, is computed as:

$$\sigma_R = \frac{\sqrt{(f \cdot S)^2 + \left(\mathrm{RMS} \cdot \sqrt{\Omega_c/\Omega_B}\right)^2}}{\Omega_c} \tag{A.1}$$

where f and RMS are, namely, the calibration error and the RMS of the radio image provided by the user, S is the flux density measured in the cell and Ω_B is the beam area. As for the X-ray images, When several X-ray observations of the same cluster are involved, the total I_X of a cell is computed as:

$$I_X = \frac{\sum N_{\mathrm{cnt,i}} - \sum N_{\mathrm{bkg,i}}}{\sum q_{\mathrm{exp,i}}} \frac{1}{\Omega_c} = \frac{\sum S_{X,i} \cdot q_{\mathrm{exp,i}}}{\sum q_{\mathrm{exp,i}}} \frac{1}{\Omega_c}, \tag{A.2}$$

where

$$S_{X,i} = \frac{N_{\mathrm{cnt,i}} - N_{\mathrm{bkg,i}}}{q_{\mathrm{exp,i}}} \tag{A.3}$$

is the flux measured for the i-th X-ray observation, Ω_c is the angular area of the cell in units of arcsec^2, and $N_{\mathrm{cnt,i}}$, $N_{\mathrm{bkg,i}}$ (in units of counts), and $q_{\mathrm{exp,i}}$ (in units of counts cm^2 s photons^{-1}) are, respectively, the values measured on the counts, the background, and the exposure map of the i-th X-ray observation. When no background or exposure maps are provided, their values are set to, respectively, 0 and 1 for each cell[2]. We derive the associated errors on $S_{X,i}$ by assuming a Poisson error for $N_{\mathrm{cnt,i}}$ and $N_{\mathrm{bkg,i}}$ and computing the error propagation of Eq. A.2. During this phase, the sampling is further refined by excluding all these cells that measure negative values of I_R and I_X or upper limits in radio and X-ray, i.e. those values with relative uncertainties greater than 100%.

Once the values of I_R and I_X have been stored, the fitting can begin. We fit the I_R-I_X distribution with a power-law relation as:

$$I_R = A \cdot I_X^k \tag{A.4}$$

We propose a set of different fitting algorithms to measure k and its associated error σ_k (see Section A.2.6). We also provide a direct estimate of the linear correlation in the logarithmic space by estimating the Spearman and Pearson ranks with the

[2]This entails that, by providing only the count image, this procedure is valid for every other kind of observation where the signal can be divided into counts, e.g. an optical image. This makes PT-REX virtually able to compare radio emission with other kinds of emissions, as well as the X-ray emission.

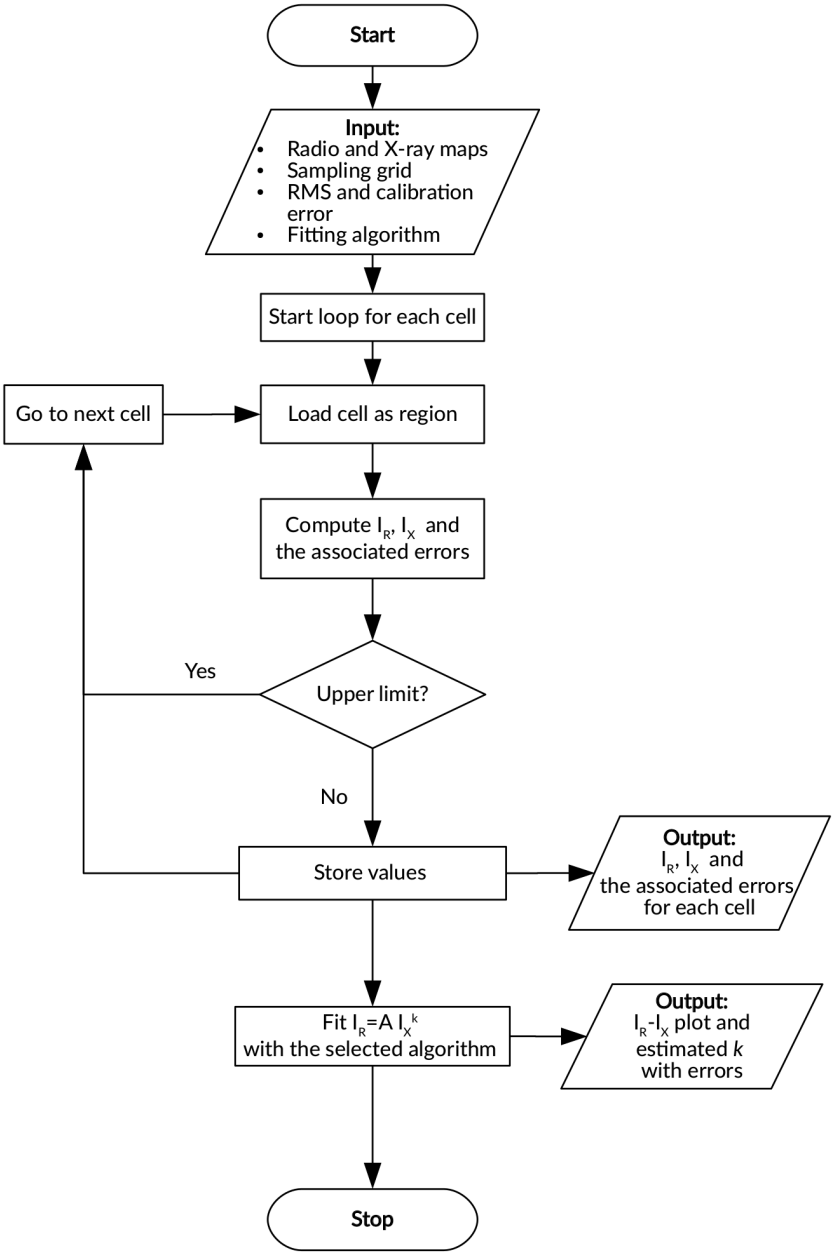

Figure A.3: Flowchart of the SMptp routine.

`scipy` library. At the end of this routine a data file with I_R and I_X and relative errors is produced as output. These values can be used for further analysis, e.g. to be examined with a fitting method which is not included in PT-REX (for example LIRA, Sereno, 2016) or, by combining multiple SMptp analysis of the same object observed at different radio frequencies, to study the spatial correlation between spectral index and I_X. In addition to the data file, PT-REX produce a simple plot with the data and the best-fit line together with the interval which has the 95% chance of containing the true regression line. At this point we hope we have convinced the Reader that the SMptp analysis is a fast and solid approach to evaluate the trend between radio and X-ray emission. However, its reliability is limited by the assumption that the sampling grid provides an unambiguous reconstruction of the real surface brightness of the source. Such an assumption is valid for those sources that can be sampled by large number of cell, i.e. whose radio emission is well resolved by the observation,

but it may not be true for the other smaller or poorly-resolved objects. In the next section we discuss how the ptp analysis can be extended also to these cases.

A.2.4 Monte-Carlo analysis

Extended sources may encompass smaller substructures (e.g. bright filaments embed in the extended emission or surface brightness gradients). If the resolution of the observation is sufficient to fully resolve them, i.e. the angular resolution is lower than half of the angular scale of these features, the result of the SMptp analysis will not depend on the sampling grid because the surface brightness will be reliably reconstructed by every possible grid. Otherwise, if these substructures can not be properly sampled by the observation/grid, the resulting SMptp analysis will be fatally biased by the choice of the sampling grid. In this latter case, a more complex approach is required to estimate the spatial trend.

The major feature introduced by PT-REX is the possibility to use an automatic, randomly-generated sampling routine to combine several SMptp analysis into a Monte Carlo ptp (MCptp) analysis. By repeating several cycles of SMptp analysis with randomly-generated grids[3], we can probe the parameter space of k to reliably estimate the correlation. This routine makes uses of the sampling algorithm and the SMptp routine presented in the previous sections. We present the flowchart of the process in Figure A.4. After setting the number of Monte Carlo iterations (N), the region of interest, the cell-size and the $I_{\rm R}$ lower threshold are set, the python function `numpy.random` is used to generate a number N of coordinates (x, y) within the region of interest. These coordinates are used to define N different, rectangular regions centered in (x, y) and large enough to include the region of interest. Then these N regions are converted in sampling grids by using the sampling algorithm and used to carry out a SMptp analysis to measure $k \pm \sigma_k$.
At the endd of each cycle, a random value k_b is extracted from a normal distribution centered in k with sigma σ_k and is finally stored. This procedure enables us to transpose the error of the fit in the following step. After all the N different grids have been exploited, the result of the MCptp analysis, k, is computed as:

$$k = \bar{k}_{\rm b} \pm \sigma_{k_{\rm b}} \tag{A.5}$$

where $\bar{k}_{\rm b}$ and $\sigma_{k_{\rm b}}$ are the mean and the standard deviation of the distribution of bootstrapped k_b obtained at the end of each cycle. An histogram of the k_b distribution is produced in output, which may contain useful information about the source. On the one hand, observing a dispersion significantly larger than the SMptp uncertainties indicates that the random sampling affected the estimate, which is sign of a poor sampling of the radio emission. On the other hand, an asymmetrical distribution may indicate the presence of a secondary component in the radio source. For instance, low-brightness, weakly-correlated components or strong X-ray point-sources embed in the radio emission can produce a negative skewness in the distribution, whereas the presence of point sources with a strong radio and X-ray emission can induce a positive skewness.

MCptp analysis is advised for those sources that can be sampled with < 30 cells. We suggest setting the number N to a minimum of 100 to adequately probe the

[3]It follows that the MCptp is more time-consuming than the SMptp.

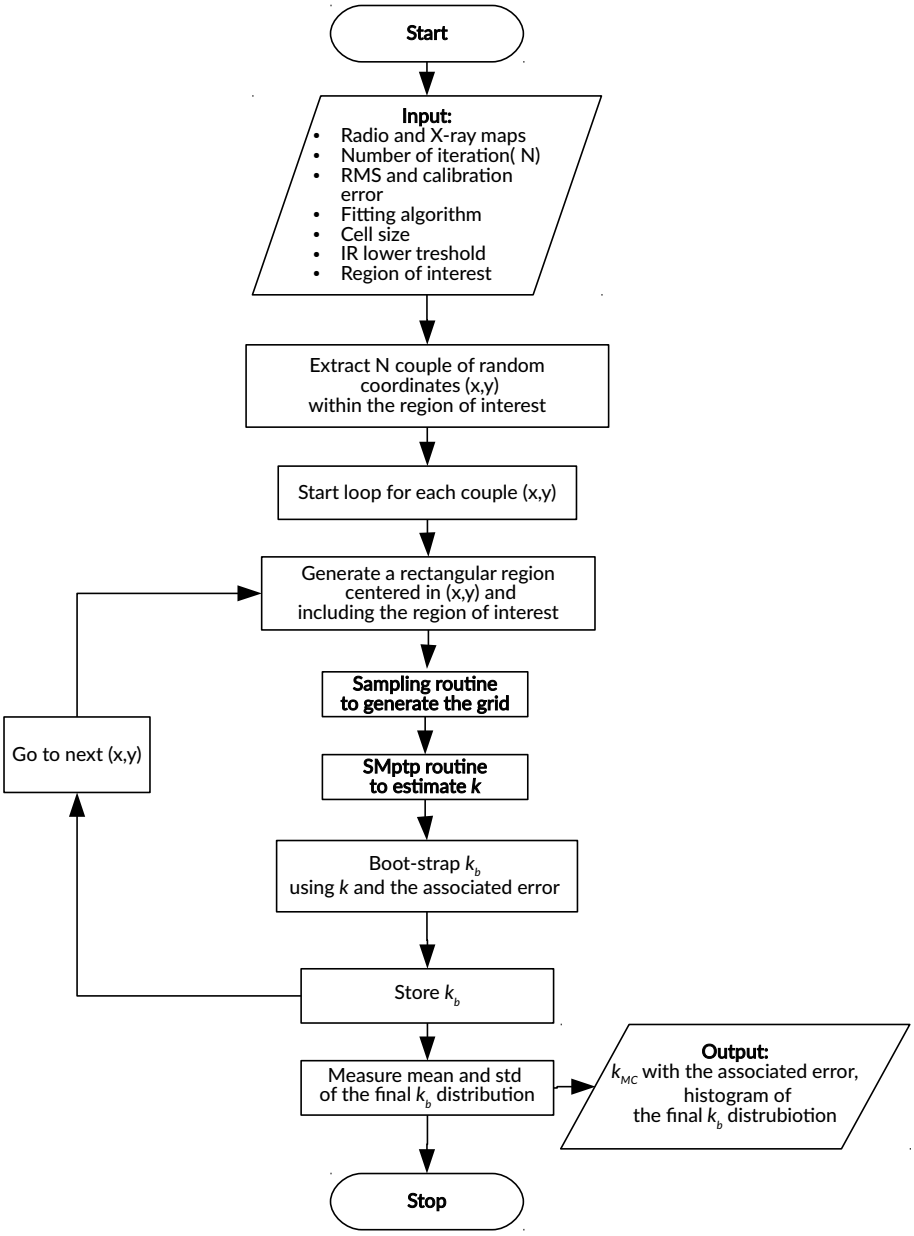

Figure A.4: Flowchart of the MCptp routine.

parameter space of k.A scientific application of MCptp analysis to study radio mini-halos in galaxy clusters is presented in Ignesti et al. (2020a).

A.2.5 Generate a mask

Field sources and those embed in the radio emission not associated with the extended source (e.g. central radio galaxies) can jeopardize the results of the ptp analysis. When the subtraction of those sources from the data is not possible, they can be masked and excluded from the ptp analysis. PT-REX includes a tool that allows the user to produce masks for the analysis simply by providing the regions intended

to be excluded. The regions are used to define a matrix with the same size of the radio image that allows the sampling routine to recognize and exclude any unwanted sources. Typically, there are two kind of sources that have to be masked:

- ◇ Those embed in the extended emission, as physically located within the source but whose emission is not related it, or background and foreground sources along the line of sight;
- ◇ Those that are outside the diffuse emission but within the region of interest;

As a simple rule of the thumb, we suggest to define carefully the regions to be masked within the source. On the on hand, define a mask that exceeds the size of the unwanted source can lead the sampling routine to exclude a number of cells larger than the necessary, and thus to reduce the number of point to evaluate the spatial correlation. On the other hand, a mask smaller than the source cold not contain its contribute in the surface brightness, thus jeopardizing the analysis. As for the sources close to the region of interest, they can be problematic during a MCptp analysis. At the begin of the cycle a new region of interest is defined and some of them can be erroneously included and sampled. So we suggest to adopt large masks to safely account for their presence within $2\times$, both in width and in height, the size of the region of interest.

A.2.6 Fitting algorithms

Fitting $I_R \propto I_X^k$ is a crucial part of the ptp analysis, and different scientific problems may require different statistic methods to evaluate the trend. For this reason, PT-REX includes a range of fitting algorithms:

- ◇ *Least squares (LS):* data can be fitted with a power-law relation $I_R = A \cdot I_X^k$ by using the least-squares method with the `scipy.optimize.curve_fit` method. Only the uncertainties on I_R are taken into account. This method estimates the best-fitting parameter of the power-law which minimize the distance from the data, under the assumption that the data intrinsically follow a power-law distribution and the scatter is only due to observational errors. Due to its assumptions, this method can be biased by outliers that can pivot the fit. For a physical point of view, the assumption of an intrinsic, perfect correlation between the two quantities may be questionable. In a complex, physical system the apparent correlation between two quantities can depend on a third, unknown factor. In this case, an internal scatter of the data is expected regardless of the quality of the observations and, thus, the base assumptions of this method can lead to biases in the scientific conclusions. Therefore, although we include this method for the sake of completeness because it has been largely used in literature, we advise to use it cautiously;
- ◇ *BCES orthogonal and bisector:* The fitting method is the bivariate correlated errors and intrinsic scatter (BCES) presented in Akritas and Bershady (1996). The BCES regression offers several advantages compared to ordinary least squares fitting, as measurement errors on both variables and it can account for an intrinsic internal scatter of the data. The fitting is performed by the `bces` module[4]. By default, we assume the errors on I_R and I_X to not correlate. We included in PT-REX both the orthogonal method, which is advised when it is not

[4] `https://github.com/rsnemmen/BCES`

clear which variable should be treated as the independent one, and the bisector method, which compute the best-fit as the bisector line between the two BCES fit $I_R|I_X$ and $I_X|I_R$;

- ◇ *LinMix:* this is a Bayesian method to account for measurement errors in linear regression introduced in Kelly (2007). This method allows for heteroscedastic and possibly correlated measurement errors and intrinsic scatter in the regression relationship. The method is based on deriving a likelihood function for the measured data, especially for the case when the intrinsic distribution of the independent variables can be approximated using a mixture of Gaussian functions. LinMix incorporates multiple independent variables, nondetections, and selection effects (e.g., Malmquist bias). We implemented this algorithm with the `linmix` module[5]. This method derives a likelihood function for the data, thus the best-fit slope is estimated from the mean of the posterior distribution. To run this method, a number of chains for the bayesian algorithm, `n_chain`, and the number of gaussian to build the prior, `K`, has to be defined by the user. This method is significantly more time-consuming than the other options. We advise to use it when a large number of cells is involved and the chose of the lower threshold is expected to impact on the fit.

A detailed discussion about the best fitting strategy to adopt for different science cases could be found in Isobe et al. (1990), Akritas and Bershady (1996), Kelly (2007), and Hogg, Bovy, and Lang (2010).

A.3 Application to a scientific case

We present here the application of PT-REX to study the radio MH in the RX J1347.5-1145 galaxy cluster. The morphology of the mini-halo in RX J1347.5-1145 is not spherical but, instead, is elongated, with the brightest part located toward north with a fainter extension toward south. Also the X-ray emission exhibits an elliptical shape, although more symmetric than the radio emission, with the major axis aligned along northwest-southeast. Finally, two large extended radio sources are placed side by side with the mini-halo. The complex morphology of the system is not suited to be analyzed with radial profiles, hence is a perfect candidate for the ptp analysis. Whereas a detailed discussion of the nature of these objects, and the insights we can obtain through the ptp analysis, are presented in Chapters 1 and 2, here we use this MH to exemplify the outcomes of the different analysis tools included in PT-REX.

We combined the VLA observation at 1.4 GHz presented in Gitti et al. (2007) (RMS=0.04 mJy beam^{-1}, beam 17.7″ × 13.6″) with an X-ray image in the 0.5-2.0 keV band produced from the archival *Chandra* observation 2222 (PI Khan, exposure time 100 ks), which we processed following the standard analysis procedure[6]. We used the 3σ level contours to define the region of interest, which indicates to PT-REX the size and the position of the radio source, and the mask (Figure A.5). Note how we tried to carefully define the mask within the region of interest, in contrast to the more crude approach adopted outside the region. Then we define a first grid to sample the emission above the 3σ level of the radio image. The beam area is 273.6 arcsec^2 (23 pixel^2), so we use cell with a 17.5″ size and a total area of 289 arcsec^2 (25 pixel^2). The

[5] `https://github.com/jmeyers314/linmix`
[6] `https://cxc.cfa.harvard.edu/ciao/threads/index.html`

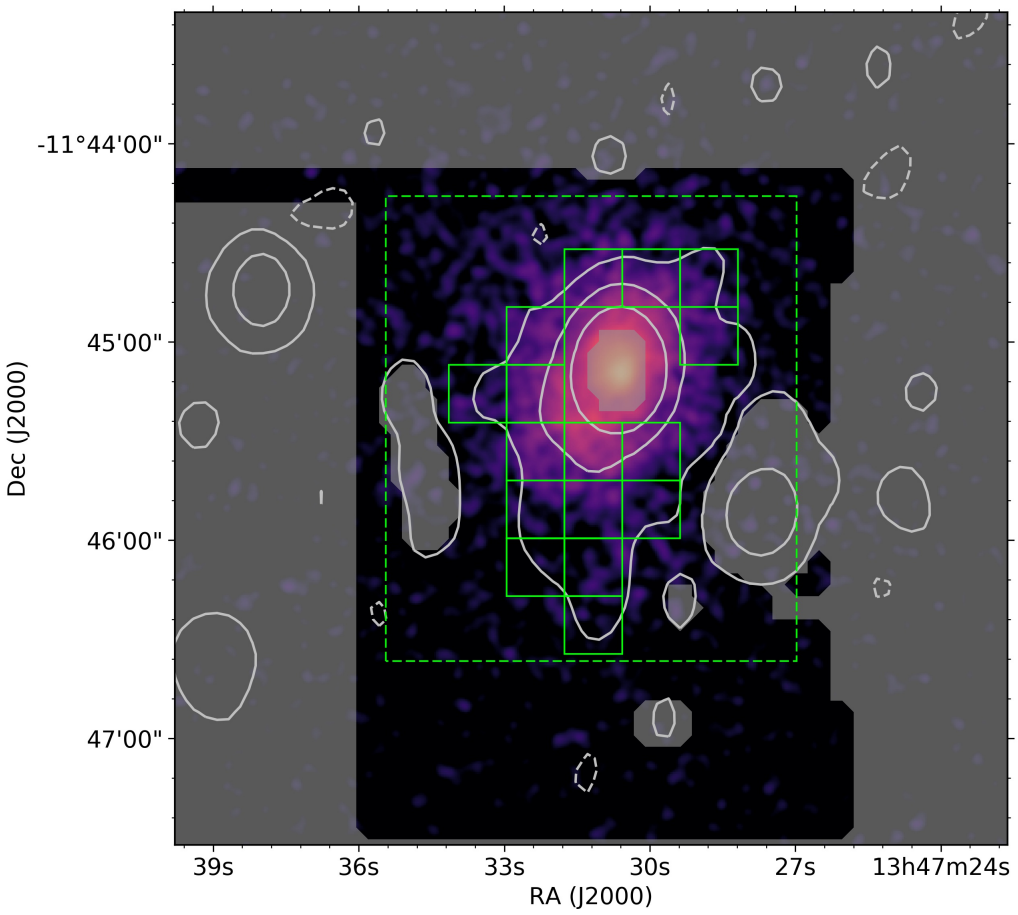

Figure A.5: X-ray image of RXJ1347.5-1145 in the 0.5-2.0 keV band with the -3, 3, 24, 96σ level countours of the radio image (1σ= 0.04 mJy beam^{-1}). We report here the region of interest (green, dashed), a random sampling grid (green, continuous) and the mask (grey).

resulting grid shown in Figure A.5 is composed of 16 cells. The final Spearman and Pearson rank are 0.79 and 0.8, respectively, which indicate a strong linear correlation and, hence, that the ICM component responsible of the radio and X-ray occupy the same volume as expected in radio mini-halos. In Figure A.6 we report the resulting SMptp analysis carried out with the algorithms implemented in PT-REX. Albeit the large errors, they are all consistent within 1 σ and indicate a sub-linear correlation between radio and X-ray emission. However, the low number of cells indicates that the source is poorly resolved, so our results may be biased by the grid which we used. So we performed also a MCptp analysis to test this possibility and to explore the parameter space of k. We present here the results of 500 iterations of MCptp analysis carried out with the BCES orthogonal fit. We used the mask and region of interest presented in Figure A.5 with the same cell size and threshold adopted for the SMptp analysis. In Figure A.1 we report the mean and the standard deviation of the final distribution and of the first 50, 100 and 200 iterations.

In Table A.1 we report the results of the all the ptp analysis carried out. All the method produced estimates of k that are in agreement within 1σ, although the MCptp estimates a slightly steeper trend. The uncertainties of the MCptp analysis decrease with the increase of the number of iterations, which indicates that the routine has converged to a final estimate of k. The uncertainties of the MCptp are also larger than the SMptp, regardless of the fitting method. This indicate that the

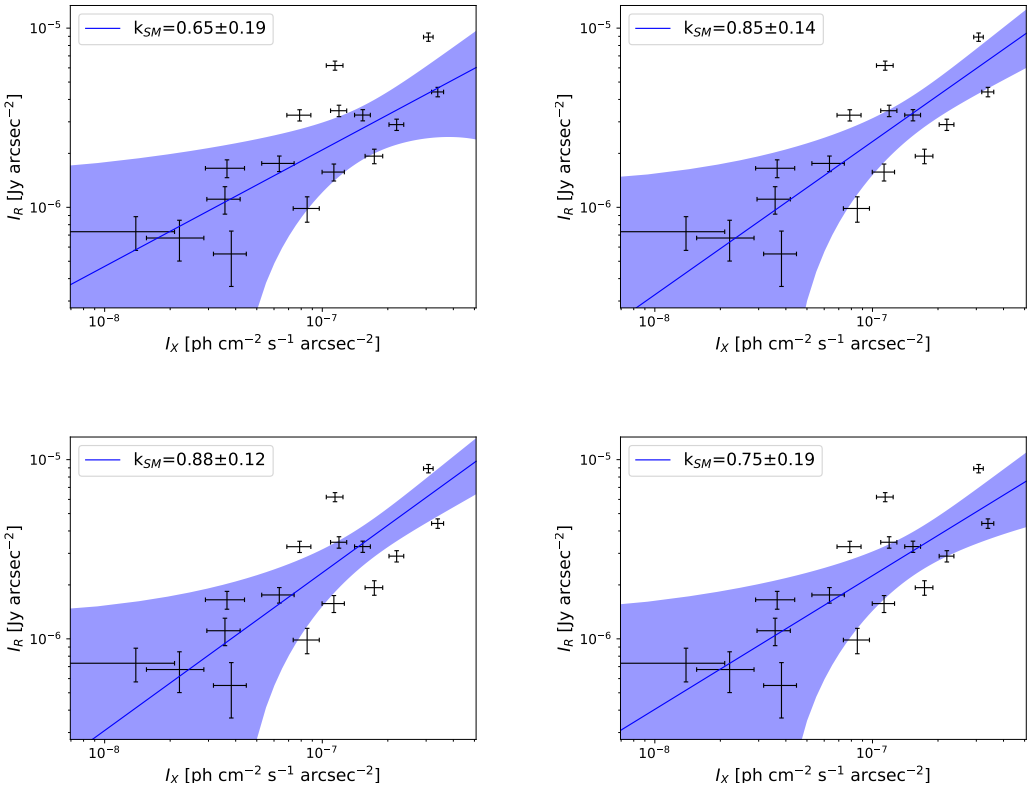

Figure A.6: Results of the SMptp analysis carried out with the grid shown in Figure A.5 with the different fitting algorithm: Least squares (top-left), BCES orthogonal (top-right), BCES bisector (bottom-left), LinMix (bottom-right). We report the 95% confidence interval.

random sampling has significantly affected the estimate of k, i.e. it confirms the presence of some kind of sub-structures embed in the radio emission which is not properly resolved by the observation. We can therefore conclude that the ptp analysis estimated a linear correlation between radio and X-ray emission in RXJ1347.5-1145 and suggests that higher-resolution observations may be requested to reveal the real morphology of this radio source. The scientific interpretation of this result in the context of origin of the radio emission is not trivial and it is beyond the scope of this Appendix. Here we just mention that this result is in agreement with the results presented in Chapter 2.

Another application of PT-REX can be found in Bruno et al. (2021) where the ptp analysis was used to disentangle the several components of the diffuse radio source observed in MACS 1149.5+2223 with LOFAR (Figure A.7). The ptp analysis revealed that the source is composed of an halo, in which we observe a strong, sub-linear correlation between radio and X-ray emission , which is in agreement with previous results for giant radio halos (see Chapter 2), and a relic, which contrary to the halo does not show correlation between the two emission. This result points out a completely different connection between the thermal and non-thermal plasma in the two sources, and we refer to Bruno et al. (2021) for a detailed discussion.

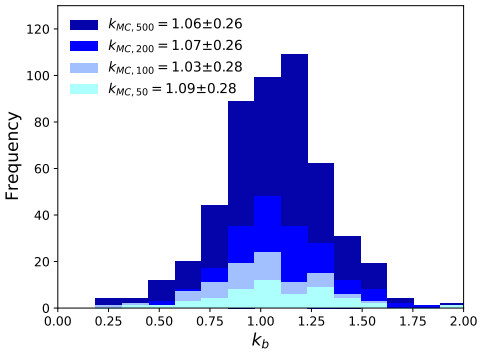

SMptp: fitting method	k
Least squares	0.66±0.19
BCES orthogonal	0.85±0.14
BCES bisector	0.88±0.12
LinMix	0.75±0.19
MCptp: number of iterations	k
50	1.09±0.28
100	1.03±0.28
200	1.07±0.26
500	1.06±0.26

Table A.1: Left: Histogram with the distribution of k produced by 500 iterations of the MCptp routine. We individually report the mean and standard deviation of the first 50, 100, 200 iterations and of the total distribution.; Right: Results of the different ptp analysis.

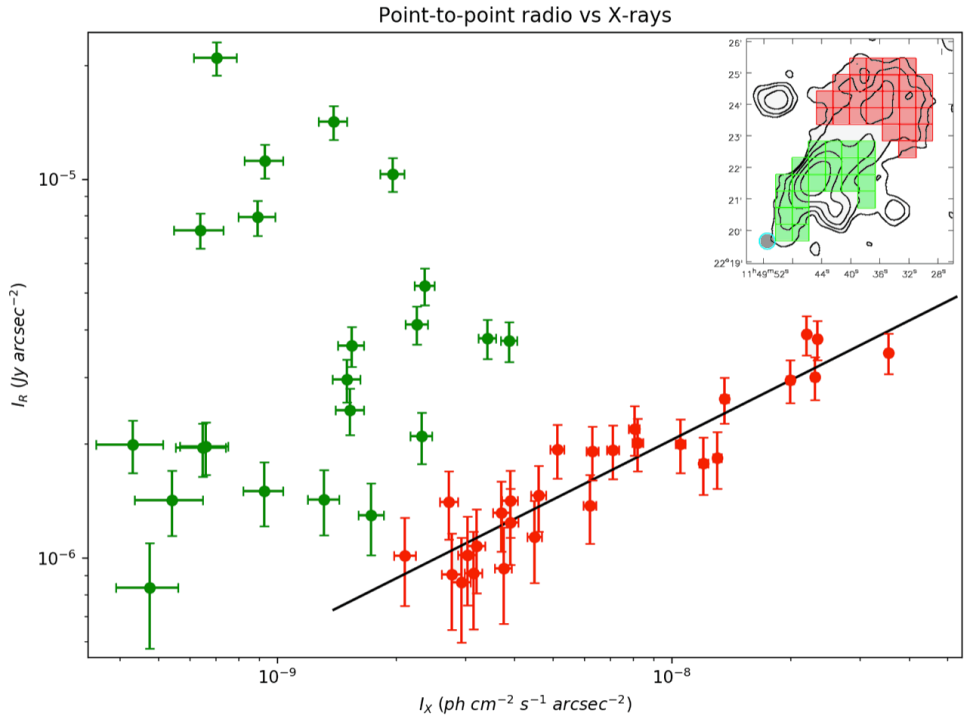

Figure A.7: Ptp analysis of MACS 1149.5+2223 from Bruno et al. (2021). In the top-right corner we report the contorus of the radio emission and the sampling grid used for the halo (red) and the relic (green).

Bibliography

Akritas, M. G. and M. A. Bershady (Oct. 1996). "Linear Regression for Astronomical Data with Measurement Errors and Intrinsic Scatter". In: *APJ* 470, p. 706. DOI: 10.1086/177901. eprint: astro-ph/9605002.

Andrade-Santos, Felipe et al. (July 2017). "The Fraction of Cool-core Clusters in X-Ray versus SZ Samples Using Chandra Observations". In: *APJ* 843.1, 76, p. 76. DOI: 10.3847/1538-4357/aa7461. arXiv: 1703.08690 [astro-ph.CO].

Arnaud, K. A. (1996). "XSPEC: The First Ten Years". In: *Astronomical Data Analysis Software and Systems V*. Ed. by G. H. Jacoby and J. Barnes. Vol. 101. Astronomical Society of the Pacific Conference Series, p. 17.

Arnaud, M. (June 2009). "The beta-model of the intracluster medium. Commentary on: Cavaliere A. and Fusco-Femiano R., 1976, AA, 49, 137". In: *A&A* 500, pp. 103–104. DOI: 10.1051/0004-6361/200912150.

Ascasibar, Y. and M. Markevitch (Oct. 2006). "The Origin of Cold Fronts in the Cores of Relaxed Galaxy Clusters". In: *APJ* 650, pp. 102–127. DOI: 10.1086/506508. eprint: astro-ph/0603246.

Astropy Collaboration et al. (Oct. 2013). "Astropy: A community Python package for astronomy". In: *A&A* 558, A33, A33. DOI: 10.1051/0004-6361/201322068. arXiv: 1307.6212 [astro-ph.IM].

Barcons, X. et al. (Mar. 2017). "Athena: ESA's X-ray observatory for the late 2020s". In: *Astronomische Nachrichten* 338.153, pp. 153–158. DOI: 10.1002/asna.201713323.

Beck, A. M. et al. (Nov. 2013). "Strong magnetic fields and large rotation measures in protogalaxies from supernova seeding". In: *MNRAS* 435.4, pp. 3575–3586. DOI: 10.1093/mnras/stt1549. arXiv: 1308.3440 [astro-ph.GA].

Begelman, M. C., R. D. Blandford, and M. J. Rees (Apr. 1984). "Theory of extragalactic radio sources". In: *Reviews of Modern Physics* 56, pp. 255–351. DOI: 10.1103/RevModPhys.56.255.

Bell, Eric F. et al. (Dec. 2003). "The Optical and Near-Infrared Properties of Galaxies. I. Luminosity and Stellar Mass Functions". In: *APJs* 149.2, pp. 289–312. DOI: 10.1086/378847. arXiv: astro-ph/0302543 [astro-ph].

Bellhouse, Callum et al. (2019). "GASP. XV. A MUSE view of extreme ram-pressure stripping along the line of sight: physical properties of the jellyfish galaxy JO201". In: *MNRAS* 485.1, pp. 1157–1170. DOI: 10.1093/mnras/stz460. arXiv: 1902.04486 [astro-ph.GA].

Bennett, C. L. et al. (June 1996). "Four-Year COBE DMR Cosmic Microwave Background Observations: Maps and Basic Results". In: *APJl* 464, p. L1. DOI: 10.1086/310075. arXiv: astro-ph/9601067 [astro-ph].

Binney, J. and S. Tremaine (1987). *Galactic dynamics*. Ed. by Binney, J. & Tremaine, S.

Bîrzan, L. et al. (Oct. 2008). "Radiative Efficiency and Content of Extragalactic Radio Sources: Toward a Universal Scaling Relation between Jet Power and Radio Power". In: *APJ* 686, pp. 859–880. DOI: 10.1086/591416. arXiv: 0806.1929.

Bîrzan, L. et al. (June 2020). "LOFAR observations of X-ray cavity systems". In: *MNRAS* 496.3, pp. 2613–2635. DOI: 10.1093/mnras/staa1594. arXiv: 2006.09708 [astro-ph.GA].

Biviano, A. (Jan. 2002). "Tracing the Cluster Internal Dynamics with Member Galaxies (Invited Speaker)". In: *Tracing Cosmic Evolution with Galaxy Clusters*. Ed. by Stefano Borgani, Marino Mezzetti, and Riccardo Valdarnini. Vol. 268. Astronomical Society of the Pacific Conference Series, p. 127.

Blasi, Pasquale and Sergio Colafrancesco (Nov. 1999). "Cosmic rays, radio halos and nonthermal X-ray emission in clusters of galaxies". In: *Astroparticle Physics* 12, pp. 169–183. DOI: 10.1016/S0927-6505(99)00079-1.

Blumenthal, G. R. et al. (Oct. 1984). "Formation of galaxies and large-scale structure with cold dark matter". In: *Nature* 311, pp. 517–525. DOI: 10.1038/311517a0.

Boehringer, H. and G. E. Morfill (1988). "On the Dynamical Role of Cosmic Rays in Cooling Flows in Clusters of Galaxies". In: *The Astrophysical Journal* 330, p. 609. DOI: 10.1086/166497.

Bonafede, A. et al. (2010). "The Coma cluster magnetic field from Faraday rotation measures". In: *Astronomy and Astrophysics* 513, A30, A30. DOI: 10.1051/0004-6361/200913696. arXiv: 1002.0594 [astro-ph.CO].

Bonafede, A. et al. (2011). "Fractional polarization as a probe of magnetic fields in the intra-cluster medium". In: *A&A* 530, A24, A24. DOI: 10.1051/0004-6361/201016298. arXiv: 1103.0277 [astro-ph.CO].

Borgani, S. (May 2006). "Cosmology with clusters of galaxies". In: *ArXiv Astrophysics e-prints*. eprint: arXiv:astro-ph/0605575.

Borgani, S. et al. (Oct. 2002). "The effect of non-gravitational gas heating in groups and clusters of galaxies". In: *MNRAS* 336, pp. 409–424. DOI: 10.1046/j.1365-8711.2002.05746.x. eprint: arXiv:astro-ph/0205471.

Boselli, A. and G. Gavazzi (Apr. 2006). "Environmental Effects on Late-Type Galaxies in Nearby Clusters". In: 118, pp. 517–559. DOI: 10.1086/500691. eprint: astro-ph/0601108.

Botteon, A., F. Gastaldello, and G. Brunetti (June 2018). "Shocks and cold fronts in merging and massive galaxy clusters: new detections with Chandra". In: *MNRAS* 476.4, pp. 5591–5620. DOI: 10.1093/mnras/sty598. arXiv: 1707.07038 [astro-ph.HE].

Botteon, A. et al. (July 2020). "The Beautiful Mess in Abell 2255". In: *APJ* 897.1, 93, p. 93. DOI: 10.3847/1538-4357/ab9a2f. arXiv: 2006.04808 [astro-ph.GA].

Braginskii, S. I. (Jan. 1965). "Transport Processes in a Plasma". In: *Reviews of Plasma Physics* 1, p. 205.

Bravi, L., M. Gitti, and G. Brunetti (Jan. 2016). "Do radio mini-halos and gas heating in cool-core clusters have a common origin?" In: *MNRAS* 455, pp. L41–L45. DOI: 10.1093/mnrasl/slv137. arXiv: 1509.06911.

Briggs, D. S. and T. J. Cornwell (1994). "CLEAN /MEM deconvolution errors: semi-compact sources". In: *Very High Angular Resolution Imaging*. Ed. by J. G. Robertson and W. J. Tango. Vol. 158. IAU Symposium, p. 212.

Brüggen, M. (Nov. 2013). "Magnetic field amplification by cosmic ray-driven turbulence - I. Isotropic CR diffusion". In: *MNRAS* 436.1, pp. 294–303. DOI: 10.1093/mnras/stt1566. arXiv: 1308.5230 [astro-ph.HE].

Brunetti, G. and P. Blasi (Nov. 2005). "Alfvénic reacceleration of relativistic particles in galaxy clusters in the presence of secondary electrons and positrons". In: *MNRAS* 363.4, pp. 1173–1187. DOI: 10.1111/j.1365-2966.2005.09511.x. arXiv: astro-ph/0508100 [astro-ph].

Brunetti, G. and T. W. Jones (Mar. 2014). "Cosmic Rays in Galaxy Clusters and Their Nonthermal Emission". In: *International Journal of Modern Physics D* 23, 1430007, p. 30007. DOI: 10.1142/S0218271814300079. arXiv: 1401.7519 [astro-ph.CO].

Brunetti, G. and A. Lazarian (Jan. 2011). "Acceleration of primary and secondary particles in galaxy clusters by compressible MHD turbulence: from radio haloes to gamma-rays". In: *MNRAS* 410, pp. 127–142. DOI: 10.1111/j.1365-2966.2010.17457.x. arXiv: 1008.0184.

Brunetti, G., S. Zimmer, and F. Zandanel (Dec. 2017). "Relativistic protons in the Coma galaxy cluster: first gamma-ray constraints ever on turbulent reacceleration". In: *MNRAS* 472.2, pp. 1506–1525. DOI: 10.1093/mnras/stx2092. arXiv: 1707.02085 [astro-ph.HE].

Brunetti, G. et al. (Oct. 2008). "A low-frequency radio halo associated with a cluster of galaxies". In: *Nature* 455.7215, pp. 944–947. DOI: 10.1038/nature07379. arXiv: 0810.4288 [astro-ph].

Brunetti, G. et al. (Nov. 2009). "On the evolution of giant radio halos and their connection with cluster mergers". In: *A&A* 507, pp. 661–669. DOI: 10.1051/0004-6361/200912751. arXiv: 0909.2343 [astro-ph.CO].

Brunetti, Gianfranco (July 2004). "Non-thermal phenomena in galaxy clusters". In: *IAU Colloq. 195: Outskirts of Galaxy Clusters: Intense Life in the Suburbs*. Ed. by Antonaldo Diaferio, pp. 148–154. DOI: 10.1017/S174392130400033X. arXiv: astro-ph/0404507 [astro-ph].

Bruno, L. et al. (2019). "Multifrequency JVLA observations of the X-shaped radio galaxy in Abell 3670". In: *A&A* 631, A173, A173. DOI: 10.1051/0004-6361/201936240.

Bruno, L. et al. (Mar. 2021). "The LOFAR and JVLA view of the distant steep spectrum radio halo in MACS J1149.5+2223". In: *arXiv e-prints*, arXiv:2103.10110, arXiv:2103.10110. arXiv: 2103.10110 [astro-ph.CO].

Burns, J. O. (Jan. 1990). "The radio properties of cD galaxies in Abell clusters. I - an X-ray selected sample". In: *AJ* 99, pp. 14–30. DOI: 10.1086/115307.

Burns, J. O. et al. (Apr. 1992). "Where have all the cluster halos gone?" In: *APJl* 388, pp. L49–L52. DOI: 10.1086/186327.

Campanelli, Manuela et al. (Mar. 2007). "Spin flips and precession in black-hole-binary mergers". In: 75.6, 064030, p. 064030. DOI: 10.1103/PhysRevD.75.064030. arXiv: gr-qc/0612076 [gr-qc].

Carilli, C. L. and G. B. Taylor (2002). "Cluster Magnetic Fields". In: *Annual Review of Astronomy and Astrophysics* 40, pp. 319–348. DOI: 10.1146/annurev.astro.40.060401.093852. eprint: astro-ph/0110655.

Carlstrom, John E., Gilbert P. Holder, and Erik D. Reese (Jan. 2002). "Cosmology with the Sunyaev-Zel'dovich Effect". In: *Annual Review of Astronomy and Astrophysics* 40, pp. 643–680. DOI: 10.1146/annurev.astro.40.060401.093803. arXiv: astro-ph/0208192 [astro-ph].

Cassano, R., G. Brunetti, and G. Setti (July 2006). "Statistics of giant radio haloes from electron reacceleration models". In: *MNRAS* 369.4, pp. 1577–1595. DOI: 10.1111/j.1365-2966.2006.10423.x. arXiv: astro-ph/0604103 [astro-ph].

Cassano, R., M. Gitti, and G. Brunetti (Aug. 2008). "A morphological comparison between giant radio halos and radio mini-halos in galaxy clusters". In: *A&A* 486, pp. L31–L34. DOI: 10.1051/0004-6361:200810179. arXiv: 0806.1817.

Cassano, R. et al. (Oct. 2010). "On the Connection Between Giant Radio Halos and Cluster Mergers". In: *APJl* 721, pp. L82–L85. DOI: 10.1088/2041-8205/721/2/L82. arXiv: 1008.3624 [astro-ph.CO].

Cassano, R. et al. (Apr. 2015). "Cluster Radio Halos at the crossroads between astrophysics and cosmology in the SKA era". In: *Advancing Astrophysics with the Square Kilometre Array (AASKA14)*, p. 73. arXiv: 1412.5940 [astro-ph.CO].

Cassano, R. et al. (Sept. 2016). "Can giant radio halos probe the merging rate of galaxy clusters?" In: *A&A* 593, A81, A81. DOI: 10.1051/0004-6361/201628414. arXiv: 1606.07293 [astro-ph.CO].

Cava, A. et al. (Mar. 2009). "WINGS-SPE Spectroscopy in the WIde-field Nearby Galaxy-cluster Survey". In: *A&A* 495, pp. 707–719. DOI: 10.1051/0004-6361:200810997. arXiv: 0812.2022.

Cavagnolo, K. W. et al. (May 2009). "Intracluster Medium Entropy Profiles for a Chandra Archival Sample of Galaxy Clusters". In: *APJs* 182, pp. 12–32. DOI: 10.1088/0067-0049/182/1/12. arXiv: 0902.1802 [astro-ph.CO].

Cavaliere, A. and R. Fusco-Femiano (May 1976). "X-rays from hot plasma in clusters of galaxies". In: *A&A* 49, pp. 137–144.

— (Nov. 1978). "The Distribution of Hot Gas in Clusters of Galaxies". In: *A&A* 70, p. 677.

Chung, A. et al. (Apr. 2007). "Virgo Galaxies with Long One-sided H I Tails". In: *APJl* 659, pp. L115–L119. DOI: 10.1086/518034. eprint: astro-ph/0703338.

Churazov, E. et al. (June 2001). "Evolution of Buoyant Bubbles in M87". In: *APJ* 554, pp. 261–273. DOI: 10.1086/321357. eprint: arXiv:astro-ph/0008215.

Churazov, E. et al. (Dec. 2020). "Tempestuous life beyond R_500: X-ray view on the Coma cluster with SRG/eROSITA. I. X-ray morphology, recent merger, and radio halo connection". In: *arXiv e-prints*, arXiv:2012.11627, arXiv:2012.11627. arXiv: 2012.11627 [astro-ph.HE].

Clarke, A. O. et al. (Sept. 2019). "Identifying galaxies, quasars, and stars with machine learning: A new catalogue of classifications for 111 million SDSS sources without spectra". In: *arXiv e-prints*, arXiv:1909.10963, arXiv:1909.10963. arXiv: 1909.10963 [astro-ph.GA].

Clarke, T. E. et al. (Aug. 2013). "Chandra View of the Ultra-steep Spectrum Radio Source in A2443: Merger Shock-induced Compression of Fossil Radio Plasma?" In: *APJ* 772.2, 84, p. 84. DOI: 10.1088/0004-637X/772/2/84. arXiv: 1306.3879 [astro-ph.CO].

Condon, J. J. (Jan. 1992). "Radio emission from normal galaxies." In: *Annual Review of Astronomy and Astrophysics* 30, pp. 575–611. DOI: 10.1146/annurev.aa.30.090192.003043.

Consolandi, G. et al. (Oct. 2017). "MUSE sneaks a peek at extreme ram-pressure events. III. Tomography of UGC 6697, a massive galaxy falling into Abell 1367". In: *A&A* 606, A83, A83. DOI: 10.1051/0004-6361/201731218. arXiv: 1707.06241.

Cotton, W. D. et al. (May 2020). "Hydrodynamical Backflow in X-shaped Radio Galaxy PKS 2014-55". In: *MNRAS*. DOI: 10.1093/mnras/staa1240. arXiv: 2005.02723 [astro-ph.GA].

Croston, J. H. et al. (June 2005). "An X-Ray Study of Magnetic Field Strengths and Particle Content in the Lobes of FR II Radio Sources". In: *APJ* 626.2, pp. 733–747. DOI: 10.1086/430170. arXiv: astro-ph/0503203 [astro-ph].

Croston, J. H. et al. (June 2013). "The Hot and Energetic Universe: AGN feedback in galaxy clusters and groups". In: *arXiv e-prints*, arXiv:1306.2323, arXiv:1306.2323. arXiv: 1306.2323 [astro-ph.HE].

Cuciti, V. et al. (Aug. 2015). "Occurrence of radio halos in galaxy clusters. Insight from a mass-selected sample". In: *A&A* 580, A97, A97. DOI: 10.1051/0004-6361/201526420. arXiv: 1506.03209 [astro-ph.CO].

de Gasperin, F. et al. (Aug. 2018). "The effect of the ionosphere on ultra-low-frequency radio-interferometric observations". In: *A&A* 615, A179, A179. DOI: 10.1051/0004-6361/201833012. arXiv: 1804.07947 [astro-ph.IM].

de Gasperin, F. et al. (2019). "Systematic effects in LOFAR data: A unified calibration strategy". In: *A&A* 622, A5, A5. DOI: 10.1051/0004-6361/201833867. arXiv: 1811.07954 [astro-ph.IM].

de Gasperin, Francesco et al. (Oct. 2017). "Gentle reenergization of electrons in merging galaxy clusters". In: *Science Advances* 3, e1701634. DOI: 10.1126/sciadv.1701634.

Di Gennaro, Gabriella et al. (Nov. 2020). "Fast magnetic field amplification in distant galaxyclusters". In: *arXiv e-prints*, arXiv:2011.01628, arXiv:2011.01628. arXiv: 2011.01628 [astro-ph.CO].

Diaferio, Antonaldo and Margaret J. Geller (May 1997). "Infall Regions of Galaxy Clusters". In: *APJ* 481.2, pp. 633–643. DOI: 10.1086/304075. arXiv: astro-ph/9701034 [astro-ph].

Domainko, W. et al. (Oct. 2004). "Feedback from intra-cluster supernovae on the ICM in cooling flow galaxy clusters". In: *A&A* 425, pp. L21–L24. DOI: 10.1051/0004-6361:20040178. eprint: arXiv:astro-ph/0405493.

Donahue, Megan et al. (June 2015). "Ultraviolet Morphology and Unobscured UV Star Formation Rates of CLASH Brightest Cluster Galaxies". In: *APJ* 805.2, 177, p. 177. DOI: 10.1088/0004-637X/805/2/177. arXiv: 1504.00598 [astro-ph.GA].

Donnert, J. et al. (Jan. 2010). "Radio haloes from simulations and hadronic models - I. The Coma cluster". In: *MNRAS* 401.1, pp. 47–54. DOI: 10.1111/j.1365-2966.2009.15655.x. arXiv: 0905.2418 [astro-ph.CO].

Doria, A. et al. (July 2012). "A Chandra-VLA Investigation of the X-Ray Cavity System and Radio Mini-Halo in the Galaxy Cluster RBS 797". In: *APJ* 753, 47, p. 47. DOI: 10.1088/0004-637X/753/1/47. arXiv: 1204.6191 [astro-ph.CO].

Dutson, K. L. et al. (2013). "A stacked analysis of brightest cluster galaxies observed with the Fermi Large Area Telescope". In: *MNRAS* 429.3, pp. 2069–2079. DOI: 10.1093/mnras/sts477. arXiv: 1211.6344 [astro-ph.HE].

Ebeling, H., C.-J. Ma, and E. Barrett (Apr. 2014). "Spectroscopic Redshifts of Galaxies within the Frontier Fields". In: *APJs* 211, 21, p. 21. DOI: 10.1088/0067-0049/211/2/21. arXiv: 1402.3769.

Ebeling, Harald and Boris S. Kalita (Sept. 2019). "Jellyfish: Ram Pressure Stripping As a Diagnostic Tool in Studies of Cluster Collisions". In: *APJ* 882.2, 127, p. 127. DOI: 10.3847/1538-4357/ab35d6. arXiv: 1907.12781 [astro-ph.GA].

Edge, A. C. (Dec. 2001). "The detection of molecular gas in the central galaxies of cooling flow clusters". In: *MNRAS* 328.3, pp. 762–782. DOI: 10.1046/j.1365-8711.2001.04802.x. arXiv: astro-ph/0106225 [astro-ph].

Ehlert, K. et al. (2018). "Simulations of the dynamics of magnetized jets and cosmic rays in galaxy clusters". In: *MNRAS* 481.3, pp. 2878–2900. DOI: 10.1093/mnras/sty2397. arXiv: 1806.05679 [astro-ph.CO].

Ellison, Sara L. et al. (Aug. 2019). "A definitive merger-AGN connection at z $\sim$ 0 with CFIS: mergers have an excess of AGN and AGN hosts are more frequently disturbed". In: *MNRAS* 487.2, pp. 2491–2504. DOI: 10.1093/mnras/stz1431. arXiv: 1905.08830 [astro-ph.GA].

Ettori, S., L. Lovisari, and M. Sereno (Dec. 2020). "From universal profiles to universal scaling laws in X-ray galaxy clusters". In: *A&A* 644, A111, A111. DOI: 10.1051/0004-6361/202038586.

Ettori, Stefano (Nov. 2000). "β-model and cooling flows in X-ray clusters of galaxies". In: *MNRAS* 318.4, pp. 1041–1046. DOI: 10.1046/j.1365-8711.2000.03664.x. arXiv: astro-ph/0005224 [astro-ph].

Ettori, Stefano et al. (Aug. 2013). "Mass Profiles of Galaxy Clusters from X-ray Analysis". In: 177.1-4, pp. 119–154. DOI: 10.1007/s11214-013-9976-7. arXiv: 1303.3530 [astro-ph.CO].

Fabian, A. C. (Sept. 2012). "Observational Evidence of Active Galactic Nuclei Feedback". In: *Annual Review of Astronomy and Astrophysics* 50, pp. 455–489. DOI: 10.1146/annurev-astro-081811-125521. arXiv: 1204.4114 [astro-ph.CO].

Fabian, A. C., C. R. Canizares, and H. Boehringer (Apr. 1994). "Mergers, cooling flows, and evaporation revisited". In: *APJ* 425, pp. 40–42. DOI: 10.1086/173959.

Fabian, A. C. et al. (Feb. 2006). "A very deep Chandra observation of the Perseus cluster: shocks, ripples and conduction". In: *MNRAS* 366, pp. 417–428. DOI: 10.1111/j.1365-2966.2005.09896.x. eprint: arXiv:astro-ph/0510476.

Fanaroff, B. L. and J. M. Riley (May 1974). "The morphology of extragalactic radio sources of high and low luminosity". In: *MNRAS* 167, 31P–36P.

Fasano, Giovanni et al. (Oct. 2000). "The Evolution of the Galactic Morphological Types in Clusters". In: *APJ* 542.2, pp. 673–683. DOI: 10.1086/317047. arXiv: astro-ph/0005171 [astro-ph].

Feretti, L. and G. Giovannini (Jan. 1996). "Diffuse Cluster Radio Sources (Review)". In: *Extragalactic Radio Sources*. Ed. by Ron D. Ekers, C. Fanti, and L. Padrielli. Vol. 175, p. 333.

Feretti, L. et al. (July 2001). "The giant radio halo in Abell 2163". In: *A&A* 373, pp. 106–112. DOI: 10.1051/0004-6361:20010581. arXiv: astro-ph/0104451.

Feretti, Luigina and Tiziana Venturi (2002). "Radio Galaxies and Their Environment". In: *Merging Processes in Galaxy Clusters*. Ed. by L. Feretti, I. M. Gioia, and G. Giovannini. Vol. 272, pp. 163–195. DOI: 10.1007/0-306-48096-4_6.

Fossati, M. et al. (Jan. 2016). "MUSE sneaks a peek at extreme ram-pressure stripping events - II. The physical properties of the gas tail of ESO137-001". In: *MNRAS* 455, pp. 2028–2041. DOI: 10.1093/mnras/stv2400. arXiv: 1510.04283.

Fossati, Matteo et al. (2019). "MUSE sneaks a peek at extreme ram-pressure stripping events - IV. Hydrodynamic and gravitational interactions in the Blue Infalling Group". In: *MNRAS* 484.2, pp. 2212–2228. DOI: 10.1093/mnras/stz136. arXiv: 1901.03334 [astro-ph.GA].

Freeman, Peter, Stephen Doe, and Aneta Siemiginowska (2001). "Sherpa: a mission-independent data analysis application". In: ed. by Jean-Luc Starck and Fionn D. Murtagh. Vol. 4477. Society of Photo-Optical Instrumentation Engineers (SPIE) Conference Series, pp. 76–87. DOI: 10.1117/12.447161. arXiv: astro-ph/0108426 [astro-ph].

Fujita, Yutaka and Yutaka Ohira (2013). "Radio mini-halo emission from cosmic rays in galaxy clusters and heating of the cool cores". In: *Monthly Notices of the Royal Astronomical Society* 428.1, pp. 599–608. DOI: 10.1093/mnras/sts050. arXiv: 1209.4639 [astro-ph.CO].

Fumagalli, M. et al. (Dec. 2014). "MUSE sneaks a peek at extreme ram-pressure stripping events - I. A kinematic study of the archetypal galaxy ESO137-001". In: *MNRAS* 445, pp. 4335–4344. DOI: 10.1093/mnras/stu2092. arXiv: 1407.7527.

Gaspari, M., M. Ruszkowski, and S. Peng Oh (2013). "Chaotic cold accretion on to black holes". In: *MNRAS* 432, pp. 3401–3422. DOI: 10.1093/mnras/stt692. arXiv: 1301.3130 [astro-ph.CO].

Gavazzi, G. et al. (Dec. 1995). "The radio and optical structure of three peculiar galaxies in A 1367." In: *A&A* 304, p. 325.

Ghirardini, V. et al. (Aug. 2017). "On the evolution of the entropy and pressure profiles in X-ray luminous galaxy clusters at z > 0.4". In: *A&A* 604, A100, A100. DOI: 10.1051/0004-6361/201630209. arXiv: 1704.01587 [astro-ph.CO].

Ghirardini, V. et al. (Dec. 2020). "Discovery of a Supercluster in the eROSITA Final Equatorial Depth Survey: X-ray Properties, Radio Halo, and Double Relics". In: *arXiv e-prints*, arXiv:2012.11607, arXiv:2012.11607. arXiv: 2012.11607 [astro-ph.CO].

Ghizzardi, S., M. Rossetti, and S. Molendi (June 2010). "Cold fronts in galaxy clusters". In: *A&A* 516, A32, A32. DOI: 10.1051/0004-6361/200912496. arXiv: 1003.1051 [astro-ph.CO].

Ghizzardi, S. et al. (Jan. 2006). "Searching for Sharp Surface Brightness Discontinuities: A Systematic Study of Cold Fronts in Galaxy Clusters". In: *The X-ray Universe 2005*. Ed. by A. Wilson. Vol. 604. ESA Special Publication, p. 717. arXiv: astro-ph/0511445 [astro-ph].

Ghizzardi, Simona, Sabrina De Grandi, and Silvano Molendi (Oct. 2014). "Metal distribution in sloshing galaxy clusters: the case of A496". In: *A&A* 570, A117, A117. DOI: 10.1051/0004-6361/201424016. arXiv: 1407.6814 [astro-ph.CO].

Giacintucci, S. et al. (2005). "Spectral properties and origin of the radio halo in A3562". In: *A&A* 440.3, pp. 867–879. DOI: 10.1051/0004-6361:20053016. arXiv: astro-ph/0505614 [astro-ph].

Giacintucci, S. et al. (Jan. 2011). "A radio minihalo in the extreme cool-core galaxy cluster RXC J1504.1-0248". In: *A&A* 525, pp. L10+. DOI: 10.1051/0004-6361/201015882. arXiv: 1011.3141 [astro-ph.HE].

Giacintucci, S. et al. (Nov. 2014a). "Mapping the Particle Acceleration in the Cool Core of the Galaxy Cluster RX J1720.1+2638". In: *APJ* 795, 73, p. 73. DOI: 10.1088/0004-637X/795/1/73. arXiv: 1403.2820.

Giacintucci, S. et al. (Jan. 2014b). "New Detections of Radio Minihalos in Cool Cores of Galaxy Clusters". In: *APJ* 781, 9, p. 9. DOI: 10.1088/0004-637X/781/1/9. arXiv: 1311.5248.

Giacintucci, Simona et al. (June 2017). "Occurrence of Radio Minihalos in a Mass-limited Sample of Galaxy Clusters". In: *APJ* 841, 71, p. 71. DOI: 10.3847/1538-4357/aa7069.

Giacintucci, Simona et al. (2019). "Expanding the Sample of Radio Minihalos in Galaxy Clusters". In: *APJ* 880.2, 70, p. 70. DOI: 10.3847/1538-4357/ab29f1. arXiv: 1906.07087 [astro-ph.HE].

Giodini, S. et al. (Aug. 2013). "Scaling Relations for Galaxy Clusters: Properties and Evolution". In: 177.1-4, pp. 247–282. DOI: 10.1007/s11214-013-9994-5. arXiv: 1305.3286 [astro-ph.CO].

Gitti, M. (Nov. 2013a). "The puzzling radio source in the cool core cluster A2626". In: *MNRAS* 436, pp. L84–L88. DOI: 10.1093/mnrasl/slt118. arXiv: 1308.5825 [astro-ph.CO].

— (Nov. 2013b). "The puzzling radio source in the cool core cluster A2626". In: *MNRAS* 436, pp. L84–L88. DOI: 10.1093/mnrasl/slt118. arXiv: 1308.5825.

Gitti, M., F. Brighenti, and B. R. McNamara (2012). "Evidence for AGN Feedback in Galaxy Clusters and Groups". In: *Advances in Astronomy* 2012, 950641. DOI: 10.1155/2012/950641. arXiv: 1109.3334 [astro-ph.CO].

Gitti, M., G. Brunetti, and G. Setti (May 2002). "Modeling the interaction between ICM and relativistic plasma in cooling flows: The case of the Perseus cluster". In: *A&A* 386, pp. 456–463. DOI: 10.1051/0004-6361:20020284. eprint: arXiv:astro-ph/0202279.

Gitti, M., L. Feretti, and S. Schindler (Mar. 2006). "Multifrequency VLA radio observations of the X-ray cavity cluster of galaxies RBS797: evidence of differently oriented jets". In: *A&A* 448, pp. 853–860. DOI: 10.1051/0004-6361:20053998. eprint: arXiv:astro-ph/0510613.

Gitti, M. et al. (Apr. 2004). "Particle acceleration in cooling flow clusters of galaxies: The case of Abell 2626". In: *A&A* 417, pp. 1–11. DOI: 10.1051/0004-6361:20031750. eprint: arXiv:astro-ph/0311275.

Gitti, M. et al. (Aug. 2007). "Discovery of diffuse radio emission at the center of the most X-ray-luminous cluster RX J1347.5-1145". In: *A&A* 470, pp. L25–L28. DOI: 10.1051/0004-6361:20077658. arXiv: 0706.3000.

Gitti, M. et al. (Sept. 2013). "A candidate supermassive binary black hole system in the brightest cluster galaxy of RBS 797". In: *A&A* 557, L14, p. L14. DOI: 10.1051/0004-6361/201322401. arXiv: 1308.5851 [astro-ph.CO].

Gitti, M. et al. (2015). "The SKA view of cool-core clusters: evolution of radio mini-halos and AGN feedback". In: *in proceedings of "Advancing Astrophysics with the Square Kilometre Array", PoS(AASKA14)076*, 76, p. 76. arXiv: 1412.5664.

Gitti, M. et al. (2018). "Radio-continuum surveys with SKA and LOFAR: a first look at the perspectives for radio mini-halos". In: *A&A* 617, A11, A11. DOI: 10.1051/0004-6361/201832749. arXiv: 1806.05751 [astro-ph.CO].

Gopal-Krishna et al. (Feb. 2012). "On the origin of X-shaped radio galaxies". In: *Research in Astronomy and Astrophysics* 12.2, pp. 127–146. DOI: 10.1088/1674-4527/12/2/002. arXiv: 1008.0789 [astro-ph.CO].

Govoni, F. et al. (Apr. 2001). "A comparison of radio and X-ray morphologies of four clusters of galaxies containing radio halos". In: *A&A* 369, pp. 441–449. DOI: 10.1051/0004-6361:20010115.

Gronke, Max and S. Peng Oh (Oct. 2018). "The growth and entrainment of cold gas in a hot wind". In: *MNRAS* 480.1, pp. L111–L115. DOI: 10.1093/mnrasl/sly131. arXiv: 1806.02728 [astro-ph.GA].

Gullieuszik, M. et al. (Sept. 2017). "GASP. IV. A Muse View of Extreme Ram-pressure-stripping in the Plane of the Sky: The Case of Jellyfish Galaxy JO204". In: *APJ* 846, 27, p. 27. DOI: 10.3847/1538-4357/aa8322. arXiv: 1708.09035.

Gursky, H. et al. (Aug. 1971). "A Strong X-Ray Source in the Coma Cluster Observed by UHURU". In: *APJl* 167, p. L81. DOI: 10.1086/180765.

Hallman, Eric J. and Maxim Markevitch (Aug. 2004). "Chandra Observation of the Merging Cluster A168: A Late Stage in the Evolution of a Cold Front". In: *APJl* 610.2, pp. L81–L84. DOI: 10.1086/423449. arXiv: astro-ph/0406322 [astro-ph].

Hardcastle, M. J. et al. (2019). "NGC 326: X-shaped no more". In: *MNRAS* 488.3, pp. 3416–3422. DOI: 10.1093/mnras/stz1910. arXiv: 1907.03274 [astro-ph.GA].

Hester, J. A. et al. (June 2010). "IC 3418: Star Formation in a Turbulent Wake". In: *APJl* 716, pp. L14–L18. DOI: 10.1088/2041-8205/716/1/L14. arXiv: 1006.5746 [astro-ph.GA].

Hlavacek-Larrondo, J. et al. (Apr. 2012). "Extreme AGN feedback in the MAssive Cluster Survey: a detailed study of X-ray cavities at z0.3". In: *MNRAS* 421, pp. 1360–1384. DOI: 10.1111/j.1365-2966.2011.20405.x. arXiv: 1110.0489 [astro-ph.CO].

Hlavacek-Larrondo, J. et al. (Nov. 2013). "Probing the Extreme Realm of Active Galactic Nucleus Feedback in the Massive Galaxy Cluster, RX J1532.9+3021". In: *APJ* 777. DOI: 10.1088/0004-637X/777/2/163.

Hlavacek-Larrondo, J. et al. (May 2015). "X-Ray Cavities in a Sample of 83 SPT-selected Clusters of Galaxies: Tracing the Evolution of AGN Feedback in Clusters of Galaxies out to z=1.2". In: *APJ* 805.1, 35, p. 35. DOI: 10.1088/0004-637X/805/1/35. arXiv: 1410.0025 [astro-ph.HE].

Hoang, D. N. et al. (2019). "Radio observations of the merging galaxy cluster Abell 520". In: *A&A* 622, A20, A20. DOI: 10.1051/0004-6361/201833900. arXiv: 1811.09713 [astro-ph.HE].

Hodges-Kluck, Edmund J. and Christopher S. Reynolds (May 2011). "Hydrodynamic Models of Radio Galaxy Morphology: Winged and X-shaped Sources". In: *APJ* 733.1, 58, p. 58. DOI: 10.1088/0004-637X/733/1/58. arXiv: 1103.4863 [astro-ph.CO].

Hoekstra, Henk et al. (Aug. 2013). "Masses of Galaxy Clusters from Gravitational Lensing". In: 177.1-4, pp. 75–118. DOI: 10.1007/s11214-013-9978-5. arXiv: 1303.3274 [astro-ph.CO].

Hogg, David W., Jo Bovy, and Dustin Lang (Aug. 2010). "Data analysis recipes: Fitting a model to data". In: *arXiv e-prints*, arXiv:1008.4686, arXiv:1008.4686. arXiv: 1008.4686 [astro-ph.IM].

Hu, E. M., L. L. Cowie, and Z. Wang (Dec. 1985). "Long-slit spectroscopy of gas in the cores of X-ray luminous clusters." In: *APJs* 59, pp. 447–498. DOI: 10.1086/191081.

Hudson, D. S. et al. (Apr. 2010). "What is a cool-core cluster? a detailed analysis of the cores of the X-ray flux-limited HIFLUGCS cluster sample". In: *A&A* 513, A37, A37. DOI: 10.1051/0004-6361/200912377. arXiv: 0911.0409 [astro-ph.CO].

Ignesti, A. et al. (July 2017). "New JVLA observations at 3 GHz and 5.5 GHz of the "Kite" radio source in Abell 2626". In: *A&A* 604, A21, A21. DOI: 10.1051/0004-6361/201730964. arXiv: 1705.01787.

Ignesti, A. et al. (Mar. 2018). "The mystery of the "Kite" radio source in Abell 2626: Insights from new Chandra observations". In: *A&A* 610. DOI: 10.1051/0004-6361/201731380.

Ignesti, A. et al. (Aug. 2020a). "Radio and X-ray connection in radio mini-halos: Implications for hadronic models". In: *A&A* 640, A37, A37. DOI: 10.1051/0004-6361/201937207. arXiv: 2006.09254 [astro-ph.HE].

Ignesti, A. et al. (Nov. 2020b). "The great Kite in the sky: A LOFAR observation of the radio source in Abell 2626". In: *A&A* 643, A172, A172. DOI: 10.1051/0004-6361/202039056. arXiv: 2009.11210 [astro-ph.GA].

Intema, H. T. et al. (2009). "Ionospheric calibration of low frequency radio interferometric observations using the peeling scheme. I. Method description and first results". In: *A&A* 501.3, pp. 1185–1205. DOI: 10.1051/0004-6361/200811094. arXiv: 0904.3975 [astro-ph.IM].

Intema, H. T. et al. (Feb. 2017). "The GMRT 150 MHz all-sky radio survey. First alternative data release TGSS ADR1". In: *A&A* 598, A78, A78. DOI: 10.1051/0004-6361/201628536.

Isobe, Takashi et al. (Nov. 1990). "Linear Regression in Astronomy. I." In: *APJ* 364, p. 104. DOI: 10.1086/169390.

Jáchym, P. et al. (Apr. 2017). "Molecular Gas Dominated 50 kpc Ram Pressure Stripped Tail of the Coma Galaxy D100". In: *APJ* 839, 114, p. 114. DOI: 10.3847/1538-4357/aa6af5. arXiv: 1704.00824.

Jacob, Svenja and Christoph Pfrommer (2017a). "Cosmic ray heating in cool core clusters - I. Diversity of steady state solutions". In: *MNRAS* 467.2, pp. 1449–1477. DOI: 10.1093/mnras/stx131. arXiv: 1609.06321 [astro-ph.GA].

Jacob, Svenja and Christoph Pfrommer (May 2017b). "Cosmic ray heating in cool core clusters - II. Self-regulation cycle and non-thermal emission". In: *MNRAS* 467.2, pp. 1478–1495. DOI: 10.1093/mnras/stx132. arXiv: 1609.06322 [astro-ph.GA].

Jones, C. and W. Forman (Jan. 1984). "The structure of clusters of galaxies observed with Einstein". In: *APJ* 276, pp. 38–55. DOI: 10.1086/161591.

Kadam, S. K. et al. (2019). "Merging cold front and AGN feedback in the peculiar galaxy cluster Abell 2626". In: *MNRAS* 484.3, pp. 4113–4126. DOI: 10.1093/mnras/stz144. arXiv: 1901.03550 [astro-ph.GA].

Kaiser, N. (Sept. 1986). "Evolution and clustering of rich clusters". In: *MNRAS* 222, pp. 323–345.

— (Dec. 1991). "Evolution of clusters of galaxies". In: *APJ* 383, pp. 104–111. DOI: 10.1086/170768.

Kale, R. and M. Gitti (Mar. 2017). "Discovery of a fourth arc in Abell 2626 at 610 MHz with the GMRT: spectral properties and possibilities for the origin". In: *MNRAS* 466, pp. L19–L23. DOI: 10.1093/mnrasl/slw227. arXiv: 1611.03160.

Kale, R. et al. (Sept. 2013). "The Extended GMRT Radio Halo Survey. I. New upper limits on radio halos and mini-halos". In: *A&A* 557, A99, A99. DOI: 10.1051/0004-6361/201321515. arXiv: 1306.3102 [astro-ph.CO].

Kale, R. et al. (July 2015). "The Extended GMRT Radio Halo Survey. II. Further results and analysis of the full sample". In: *A&A* 579, A92, A92. DOI: 10.1051/0004-6361/201525695. arXiv: 1503.02415 [astro-ph.CO].

Kanjilal, Vijit, Alankar Dutta, and Prateek Sharma (Nov. 2020). "Growth and structure of multiphase gas in the cloud-crushing problem with cooling". In: *MNRAS*. DOI: 10.1093/mnras/staa3610. arXiv: 2009.00525 [astro-ph.GA].

Kelly, Brandon C. (Aug. 2007). "Some Aspects of Measurement Error in Linear Regression of Astronomical Data". In: *APJ* 665.2, pp. 1489–1506. DOI: 10.1086/519947. arXiv: 0705.2774 [astro-ph].

Kenney, J. D. P., J. H. van Gorkom, and B. Vollmer (June 2004). "VLA H I Observations of Gas Stripping in the Virgo Cluster Spiral NGC 4522". In: *AJ* 127, pp. 3361–3374. DOI: 10.1086/420805. eprint: astro-ph/0403103.

Kenney, J. D. P. et al. (Jan. 2014). "Transformation of a Virgo Cluster Dwarf Irregular Galaxy by Ram Pressure Stripping: IC3418 and Its Fireballs". In: *APJ* 780, 119, p. 119. DOI: 10.1088/0004-637X/780/2/119. arXiv: 1311.5501.

Kennicutt Jr., R. C. (1998). "Star Formation in Galaxies Along the Hubble Sequence". In: *Annual Review of Astronomy and Astrophysics* 36, pp. 189–232. DOI: 10.1146/annurev.astro.36.1.189. eprint: arXiv:astro-ph/9807187.

King, I. (Oct. 1962). "The structure of star clusters. I. an empirical density law". In: *AJ* 67, pp. 471–+. DOI: 10.1086/108756.

Kirkpatrick, C. C. et al. (Dec. 2009). "Direct Evidence for Outflow of Metal-Enriched Gas Along the Radio Jets of Hydra A". In: *APJl* 707, pp. L69–L72. DOI: 10.1088/0004-637X/707/1/L69. arXiv: 0909.2252 [astro-ph.GA].

Kokotanekov, G. et al. (Oct. 2018). "Signatures of multiple episodes of AGN activity in the core of Abell 1795". In: *A&A* 618, A152, A152. DOI: 10.1051/0004-6361/201833222. arXiv: 1807.11520 [astro-ph.GA].

Kolokythas, Konstantinos et al. (Dec. 2018). "The Complete Local-volume Groups Sample - II. A study of the central radio galaxies in the high-richness sub-sample". In: *MNRAS* 481.2, pp. 1550–1577. DOI: 10.1093/mnras/sty2030. arXiv: 1807.11095 [astro-ph.GA].

Kravtsov, Andrey V. and Stefano Borgani (Sept. 2012). "Formation of Galaxy Clusters". In: *Annual Review of Astronomy and Astrophysics* 50, pp. 353–409. DOI: 10.1146/annurev-astro-081811-125502. arXiv: 1205.5556 [astro-ph.CO].

Laganá, T. F., F. Durret, and P. A. A. Lopes (Apr. 2019). "Physical properties of the X-ray gas as a dynamical diagnosis for galaxy clusters". In: *MNRAS* 484.2, pp. 2807–2830. DOI: 10.1093/mnras/stz148. arXiv: 1901.03851 [astro-ph.CO].

Lal, Dharam Vir and A. Pramesh Rao (Jan. 2007). "Giant Metrewave Radio Telescope observations of X-shaped radio sources". In: *MNRAS* 374.3, pp. 1085–1102. DOI: 10.1111/j.1365-2966.2006.11225.x. arXiv: astro-ph/0610678 [astro-ph].

Lauer, Tod R. et al. (Dec. 2014). "Brightest Cluster Galaxies at the Present Epoch". In: *APJ* 797.2, 82, p. 82. DOI: 10.1088/0004-637X/797/2/82. arXiv: 1407.2260 [astro-ph.GA].

Leahy, J. P. and A. G. Williams (Oct. 1984). "The bridges of classical double radio sources." In: *MNRAS* 210, pp. 929–951. DOI: 10.1093/mnras/210.4.929.

Liu, Ang et al. (Nov. 2018). "Spatial distribution of metals in the ICM: evolution of the iron excess in relaxed galaxy clusters". In: *MNRAS* 481.1, pp. 361–372. DOI: 10.1093/mnras/sty2294. arXiv: 1808.06742 [astro-ph.CO].

Lovisari, Lorenzo et al. (Sept. 2017). "X-Ray Morphological Analysis of the Planck ESZ Clusters". In: *APJ* 846.1, 51, p. 51. DOI: 10.3847/1538-4357/aa855f. arXiv: 1708.02590 [astro-ph.CO].

Mandal, S. et al. (Feb. 2020). "Revived fossil plasma sources in galaxy clusters". In: *A&A* 634, A4, A4. DOI: 10.1051/0004-6361/201936560. arXiv: 1911.02034 [astro-ph.CO].

Mantz, Adam B. et al. (Dec. 2016). "Weighing the giants- V. Galaxy cluster scaling relations". In: *MNRAS* 463.4, pp. 3582–3603. DOI: 10.1093/mnras/stw2250. arXiv: 1606.03407 [astro-ph.CO].

Markevitch, M. and A. Vikhlinin (May 2007). "Shocks and cold fronts in galaxy clusters". In: *Physics Reports* 443, pp. 1–53. DOI: 10.1016/j.physrep.2007.01.001. eprint: arXiv:astro-ph/0701821.

Markevitch, M. et al. (July 2005). "Bow Shock and Radio Halo in the Merging Cluster A520". In: *APJ* 627.2, pp. 733–738. DOI: 10.1086/430695. arXiv: astro-ph/0412451 [astro-ph].

Mazzotta, P., A. C. Edge, and M. Markevitch (Oct. 2003). "A Chandra Study of the Complex Structure in the Core of 2A 0335+096". In: *APJ* 596, pp. 190–203. DOI: 10.1086/377633. arXiv: astro-ph/0303314 [astro-ph].

Mazzotta, P. and S. Giacintucci (Mar. 2008). "Do Radio Core-Halos and Cold Fronts in Non-Major-Merging Clusters Originate from the Same Gas Sloshing?" In: *APJl* 675, pp. L9–L12. DOI: 10.1086/529433. arXiv: 0801.1905.

Mazzotta, P. et al. (July 2001). "Chandra Observation of RX J1720.1+2638: a Nearly Relaxed Cluster with a Fast-moving Core?" In: *APJ* 555, pp. 205–214. DOI: 10.1086/321484.

McDonald, M. et al. (Sept. 2013). "The Growth of Cool Cores and Evolution of Cooling Properties in a Sample of 83 Galaxy Clusters at 0.3 z 1.2 Selected from the SPT-SZ Survey". In: *APJ* 774, 23, p. 23. DOI: 10.1088/0004-637X/774/1/23. arXiv: 1305.2915 [astro-ph.CO].

McDonald, M. et al. (May 2018). "Revisiting the Cooling Flow Problem in Galaxies, Groups, and Clusters of Galaxies". In: *APJ* 858.1, 45, p. 45. DOI: 10.3847/1538-4357/aabace. arXiv: 1803.04972 [astro-ph.HE].

McDonald, Michael (Dec. 2011). "Optical Line Emission in Brightest Cluster Galaxies at 0 < z < 0.6: Evidence for a Lack of Strong Cool Cores 3.5 Gyr Ago?" In: *APJl*

742.2, L35, p. L35. DOI: 10.1088/2041-8205/742/2/L35. arXiv: 1110.5904 [astro-ph.CO].

McKee, Christopher F. and Mitchell C. Begelman (Aug. 1990). "Steady Evaporation and Condensation of Isolated Clouds in Hot Plasma". In: *APJ* 358, p. 392. DOI: 10.1086/168995.

McMullin, J. P. et al. (Oct. 2007). "CASA Architecture and Applications". In: *Astronomical Data Analysis Software and Systems XVI*. Ed. by R. A. Shaw, F. Hill, and D. J. Bell. Vol. 376. Astronomical Society of the Pacific Conference Series, p. 127.

McNamara, B. R. and P. E. J. Nulsen (Sept. 2007). "Heating Hot Atmospheres with Active Galactic Nuclei". In: *Annual Review of Astronomy and Astrophysics* 45, pp. 117–175. DOI: 10.1146/annurev.astro.45.051806.110625. arXiv: 0709.2152.

— (May 2012). "Mechanical feedback from active galactic nuclei in galaxies, groups and clusters". In: *New Journal of Physics* 14.5, 055023, p. 055023. DOI: 10.1088/1367-2630/14/5/055023. arXiv: 1204.0006 [astro-ph.CO].

McNamara, B. R. et al. (May 2000). "Chandra X-Ray Observations of the Hydra A Cluster: An Interaction between the Radio Source and the X-Ray-emitting Gas". In: *APJl* 534, pp. L135–L138. DOI: 10.1086/312662. eprint: arXiv:astro-ph/0001402.

McNamara, B. R. et al. (Oct. 2016). "A Mechanism for Stimulating AGN Feedback by Lifting Gas in Massive Galaxies". In: *APJ* 830.2, 79, p. 79. DOI: 10.3847/0004-637X/830/2/79. arXiv: 1604.04629 [astro-ph.GA].

McNamara, Brian R. and Robert W. O'Connell (Dec. 1989). "Star formation in cooling flows in clusters of galaxies." In: *AJ* 98, pp. 2018–2043. DOI: 10.1086/115275.

Meneghetti, M. et al. (May 2010). "Weighing simulated galaxy clusters using lensing and X-ray". In: *A&A* 514, A93, A93. DOI: 10.1051/0004-6361/200913222. arXiv: 0912.1343 [astro-ph.CO].

Merluzzi, P. et al. (Feb. 2013). "ACCESS - V. Dissecting ram-pressure stripping through integral-field spectroscopy and multiband imaging". In: *MNRAS* 429, pp. 1747–1773. DOI: 10.1093/mnras/sts466. arXiv: 1211.6532.

Mineo, S. et al. (Jan. 2014). "X-ray emission from star-forming galaxies - III. Calibration of the L_X-SFR relation up to redshift z $\approx$ 1.3". In: *MNRAS* 437.2, pp. 1698–1707. DOI: 10.1093/mnras/stt1999. arXiv: 1207.2157 [astro-ph.HE].

Mittal, R. et al. (July 2009). "AGN heating and ICM cooling in the HIFLUGCS sample of galaxy clusters". In: *A&A* 501, pp. 835–850. DOI: 10.1051/0004-6361/200810836. arXiv: 0810.0797.

Moretti, A. et al. (Apr. 2018). "GASP. V. Ram-pressure stripping of a ring Hoag's-like galaxy in a massive cluster". In: *MNRAS* 475, pp. 4055–4065. DOI: 10.1093/mnras/sty085. arXiv: 1802.07294.

Morganti, Raffaella (Sept. 2017). "Archaeology of active galaxies across the electromagnetic spectrum". In: *Nature Astronomy* 1, pp. 596–605. DOI: 10.1038/s41550-017-0223-0.

Müller, Ancla et al. (Jan. 2021). "Highly ordered magnetic fields in the tail of the jellyfish galaxy JO206". In: *Nature Astronomy* 5, pp. 159–168. DOI: 10.1038/s41550-020-01234-7. arXiv: 2009.13287 [astro-ph.GA].

Murgia, M. et al. (June 2009). "Comparative analysis of the diffuse radio emission in the galaxy clusters A1835, A2029, and Ophiuchus". In: *A&A* 499, pp. 679–695. DOI: 10.1051/0004-6361/200911659. arXiv: 0901.1943 [astro-ph.CO].

Neronov, Andrii and Ievgen Vovk (Apr. 2010). "Evidence for Strong Extragalactic Magnetic Fields from Fermi Observations of TeV Blazars". In: *Science* 328.5974, p. 73. DOI: 10.1126/science.1184192. arXiv: 1006.3504 [astro-ph.HE].

Nulsen, P. E. J. et al. (May 2005). "The Powerful Outburst in Hercules A". In: *APJl* 625, pp. L9–L12. DOI: 10.1086/430945. eprint: arXiv:astro-ph/0504350.

O'Dea, C. P. and F. N. Owen (June 1985). "The global properties of a representative sample of 51 narrow-angle-tail radio sources in the directions of Abell clusters." In: *AJ* 90, pp. 954–972. DOI: 10.1086/113802.

Offringa, A. R. and O. Smirnov (Oct. 2017). "An optimized algorithm for multi-scale wideband deconvolution of radio astronomical images". In: *MNRAS* 471.1, pp. 301–316. DOI: 10.1093/mnras/stx1547. arXiv: 1706.06786 [astro-ph.IM].

Offringa, A. R. et al. (2014). "WSCLEAN: an implementation of a fast, generic wide-field imager for radio astronomy". In: *MNRAS* 444.1, pp. 606–619. DOI: 10.1093/mnras/stu1368. arXiv: 1407.1943 [astro-ph.IM].

Olivares, V. et al. (Nov. 2019). "Ubiquitous cold and massive filaments in cool core clusters". In: *A&A* 631, A22, A22. DOI: 10.1051/0004-6361/201935350. arXiv: 1902.09164 [astro-ph.GA].

Osinga, E. et al. (Nov. 2020). "Diffuse Radio Emission from Galaxy Clusters in the LOFAR Two-metre Sky Survey Deep Fields". In: *arXiv e-prints*, arXiv:2011.08249, arXiv:2011.08249. arXiv: 2011.08249 [astro-ph.HE].

O'Sullivan, E. et al. (Mar. 2011a). "A deep Chandra observation of the poor cluster AWM 4 - II. The role of the radio jets in enriching the intracluster medium". In: *MNRAS* 411, pp. 1833–1842. DOI: 10.1111/j.1365-2966.2010.17812.x. arXiv: 1010.0610 [astro-ph.CO].

O'Sullivan, E. et al. (July 2011b). "Heating the Hot Atmospheres of Galaxy Groups and Clusters with Cavities: The Relationship between Jet Power and Low-frequency Radio Emission". In: *APJ* 735, pp. 11–+. DOI: 10.1088/0004-637X/735/1/11. arXiv: 1104.2411 [astro-ph.CO].

Owers, Matt S., Paul E. J. Nulsen, and Warrick J. Couch (Nov. 2011). "Minor Merger-induced Cold Fronts in Abell 2142 and RXJ1720.1+2638". In: *APJ* 741.2, 122, p. 122. DOI: 10.1088/0004-637X/741/2/122. arXiv: 1109.5692 [astro-ph.CO].

Pakmor, Rüdiger, Federico Marinacci, and Volker Springel (Mar. 2014). "Magnetic Fields in Cosmological Simulations of Disk Galaxies". In: *APJl* 783.1, L20, p. L20. DOI: 10.1088/2041-8205/783/1/L20. arXiv: 1312.2620 [astro-ph.GA].

Parekh, Viral et al. (Mar. 2015). "Morphology parameters: substructure identification in X-ray galaxy clusters". In: *A&A* 575, A127, A127. DOI: 10.1051/0004-6361/201424123. arXiv: 1411.6525 [astro-ph.CO].

Pasini, T. et al. (Nov. 2019). "A BCG with Offset Cooling: Is the AGN Feedback Cycle Broken in A2495?" In: *APJ* 885.2, 111, p. 111. DOI: 10.3847/1538-4357/ab4808. arXiv: 1910.05363 [astro-ph.GA].

Peebles, P. J. E. (1980). *The large-scale structure of the universe*.

— (1993). *Principles of Physical Cosmology*.

Peterson, J. R. and A. C. Fabian (Apr. 2006). "X-ray spectroscopy of cooling clusters". In: *Physics Reports* 427, pp. 1–39. DOI: 10.1016/j.physrep.2005.12.007. eprint: arXiv:astro-ph/0512549.

Peterson, J. R. et al. (June 2003). "High-Resolution X-Ray Spectroscopic Constraints on Cooling-Flow Models for Clusters of Galaxies". In: *APJ* 590, pp. 207–224. DOI: 10.1086/374830. eprint: arXiv:astro-ph/0210662.

Pfrommer, C. and T. A. Enßlin (Jan. 2004). "Constraining the population of cosmic ray protons in cooling flow clusters with γ-ray and radio observations: Are radio mini-halos of hadronic origin?" In: *A&A* 413, pp. 17–36. DOI: 10.1051/0004-6361:20031464.

Pfrommer, Christoph (Apr. 2008). "Simulating cosmic rays in clusters of galaxies - III. Non-thermal scaling relations and comparison to observations". In: *MNRAS*

385.3, pp. 1242–1256. DOI: 10.1111/j.1365-2966.2008.12957.x. arXiv: 0707.1693 [astro-ph].

Pillepich, Annalisa et al. (Jan. 2018). "Simulating galaxy formation with the IllustrisTNG model". In: *MNRAS* 473.3, pp. 4077–4106. DOI: 10.1093/mnras/stx2656. arXiv: 1703.02970 [astro-ph.GA].

Planck Collaboration et al. (Dec. 2011a). "Planck early results. I. The Planck mission". In: *A&A* 536, A1, A1. DOI: 10.1051/0004-6361/201116464. arXiv: 1101.2022 [astro-ph.IM].

Planck Collaboration et al. (Dec. 2011b). "Planck early results. XI. Calibration of the local galaxy cluster Sunyaev-Zeldovich scaling relations". In: *A&A* 536, A11, A11. DOI: 10.1051/0004-6361/201116458. arXiv: 1101.2026 [astro-ph.CO].

Planck Collaboration et al. (Nov. 2014). "Planck 2013 results. XXIX. The Planck catalogue of Sunyaev-Zeldovich sources". In: *A&A* 571, A29, A29. DOI: 10.1051/0004-6361/201321523. arXiv: 1303.5089 [astro-ph.CO].

Planck Collaboration et al. (Sept. 2016). "Planck 2015 results. XXVII. The second Planck catalogue of Sunyaev-Zeldovich sources". In: *A&A* 594, A27, A27. DOI: 10.1051/0004-6361/201525823. arXiv: 1502.01598 [astro-ph.CO].

Poggianti, B. M. et al. (June 1999). "The Star Formation Histories of Galaxies in Distant Clusters". In: *APJ* 518, pp. 576–593. DOI: 10.1086/307322. eprint: astro-ph/9901264.

Poggianti, B. M. et al. (Mar. 2016). "Jellyfish Galaxy Candidates at Low Redshift". In: *AJ* 151, 78, p. 78. DOI: 10.3847/0004-6256/151/3/78. arXiv: 1504.07105.

Poggianti, B. M. et al. (July 2017a). "GASP. I. Gas Stripping Phenomena in Galaxies with MUSE". In: *APJ* 844, 48, p. 48. DOI: 10.3847/1538-4357/aa78ed. arXiv: 1704.05086.

Poggianti, B. M. et al. (Aug. 2017b). "Ram-pressure feeding of supermassive black holes". In: *Nature* 548, pp. 304–309. DOI: 10.1038/nature23462. arXiv: 1708.09036.

Poggianti, B. M. et al. (Feb. 2019a). "GASP XIII. Star formation in gas outside galaxies". In: *MNRAS* 482, pp. 4466–4502. DOI: 10.1093/mnras/sty2999. arXiv: 1811.00823.

Poggianti, Bianca M. et al. (Dec. 2019b). "GASP XXIII: A Jellyfish Galaxy as an Astrophysical Laboratory of the Baryonic Cycle". In: *APJ* 887.2, 155, p. 155. DOI: 10.3847/1538-4357/ab5224. arXiv: 1910.11622 [astro-ph.GA].

Predehl, P. et al. (Oct. 2020). "The eROSITA X-ray telescope on SRG". In: *arXiv e-prints*, arXiv:2010.03477, arXiv:2010.03477. arXiv: 2010.03477 [astro-ph.HE].

Press, W. H. and P. Schechter (Feb. 1974). "Formation of Galaxies and Clusters of Galaxies by Self-Similar Gravitational Condensation". In: *APJ* 187, pp. 425–438. DOI: 10.1086/152650.

Rafferty, D. A. et al. (Nov. 2006). "The Feedback-regulated Growth of Black Holes and Bulges through Gas Accretion and Starbursts in Cluster Central Dominant Galaxies". In: *APJ* 652, pp. 216–231. DOI: 10.1086/507672. eprint: arXiv:astro-ph/0605323.

Rajpurohit, K. et al. (2018). "Deep VLA Observations of the Cluster 1RXS J0603.3+4214 in the Frequency Range of 1-2 GHz". In: *APJ* 852.2, 65, p. 65. DOI: 10.3847/1538-4357/aa9f13. arXiv: 1712.01327 [astro-ph.GA].

Rajpurohit, K. et al. (Dec. 2020). "Physical insights from the spectrum of the radio halo in MACS J0717.5+3745". In: *arXiv e-prints*, arXiv:2012.14373, arXiv:2012.14373. arXiv: 2012.14373 [astro-ph.GA].

Ranalli, P., A. Comastri, and G. Setti (Feb. 2003). "The 2-10 keV luminosity as a Star Formation Rate indicator". In: *A&A* 399, pp. 39–50. DOI: 10.1051/0004-6361:20021600. arXiv: astro-ph/0211304 [astro-ph].

Rasmussen, Jesper, Trevor J. Ponman, and John S. Mulchaey (July 2006). "Gas stripping in galaxy groups - the case of the starburst spiral NGC 2276". In: *MNRAS* 370.1, pp. 453–467. DOI: 10.1111/j.1365-2966.2006.10492.x. arXiv: astro-ph/0604549 [astro-ph].

Rich, J. A., L. J. Kewley, and M. A. Dopita (June 2011). "Galaxy-wide Shocks in Late-merger Stage Luminous Infrared Galaxies". In: *APJ* 734, 87, p. 87. DOI: 10.1088/0004-637X/734/2/87. arXiv: 1104.1177.

Richard-Laferrière, A. et al. (Oct. 2020). "On the relation between mini-halos and AGN feedback in clusters of galaxies". In: *MNRAS* 499.2, pp. 2934–2958. DOI: 10.1093/mnras/staa2877. arXiv: 2007.01306 [astro-ph.GA].

Rizza, E. et al. (Jan. 2000). "X-Ray and Radio Interactions in the Cores of Cooling Flow Clusters". In: *AJ* 119, pp. 21–31. DOI: 10.1086/301167. eprint: arXiv:astro-ph/9910129.

Roediger, E. et al. (Feb. 2013). "Kelvin-Helmholtz Instabilities at the Sloshing Cold Fronts in the Virgo Cluster as a Measure for the Effective Intracluster Medium Viscosity". In: *APJ* 764.1, 60, p. 60. DOI: 10.1088/0004-637X/764/1/60. arXiv: 1211.4874 [astro-ph.CO].

Rossetti, M. et al. (Aug. 2013). "Abell 2142 at large scales: An extreme case for sloshing?" In: *A&A* 556, A44, A44. DOI: 10.1051/0004-6361/201321319. arXiv: 1305.2420 [astro-ph.CO].

Rossetti, M. et al. (Apr. 2016). "Measuring the dynamical state of Planck SZ-selected clusters: X-ray peak - BCG offset". In: *MNRAS* 457.4, pp. 4515–4524. DOI: 10.1093/mnras/stw265. arXiv: 1512.00410 [astro-ph.CO].

Rossetti, M. et al. (June 2017). "The cool-core state of Planck SZ-selected clusters versus X-ray-selected samples: evidence for cool-core bias". In: *MNRAS* 468.2, pp. 1917–1930. DOI: 10.1093/mnras/stx493. arXiv: 1702.06961 [astro-ph.CO].

Rudnick, Lawrence (Jan. 2019). "The Stormy Life of Galaxy Clusters: astro version". In: *arXiv e-prints*, arXiv:1901.09448, arXiv:1901.09448. arXiv: 1901.09448 [astro-ph.GA].

Rybicki, G. B. and A. P. Lightman (1979). *Radiative processes in astrophysics*. Ed. by Rybicki, G. B. & Lightman, A. P.

Ryu, D. et al. (May 2012). "Magnetic Fields in the Large-Scale Structure of the Universe". In: 166.1-4, pp. 1–35. DOI: 10.1007/s11214-011-9839-z. arXiv: 1109.4055 [astro-ph.CO].

Sanders, J. S., A. C. Fabian, and G. B. Taylor (Jan. 2005). "A Chandra observation of the disturbed cluster core of Abell 2204". In: *MNRAS* 356, pp. 1022–1028. DOI: 10.1111/j.1365-2966.2004.08526.x.

— (2009). "Feedback through multiple outbursts in the cluster 2A 0335+096". In: *MNRAS* 396.3, pp. 1449–1459. DOI: 10.1111/j.1365-2966.2009.14892.x. arXiv: 0904.1374 [astro-ph.CO].

Sanders, J. S. et al. (Aug. 2016). "Detecting edges in the X-ray surface brightness of galaxy clusters". In: *MNRAS* 460, pp. 1898–1911. DOI: 10.1093/mnras/stw1119. arXiv: 1605.02911.

Santos-Lima, R. et al. (Feb. 2014). "Magnetic Field Amplification and Evolution in Turbulent Collisionless Magnetohydrodynamics: An Application to the Intracluster Medium". In: *APJ* 781.2, 84, p. 84. DOI: 10.1088/0004-637X/781/2/84. arXiv: 1305.5654 [astro-ph.CO].

Santos-Lima, R. et al. (Mar. 2017). "Features of collisionless turbulence in the intracluster medium from simulated Faraday rotation maps - II. The effects of instabilities feedback". In: *MNRAS* 465.4, pp. 4866–4871. DOI: 10.1093/mnras/stw3050. arXiv: 1611.10183 [astro-ph.HE].

Sarazin, C. L. (Jan. 1986). "X-ray emission from clusters of galaxies". In: *Reviews of Modern Physics* 58, pp. 1–115. DOI: 10.1103/RevModPhys.58.1.

— (1988). *X-ray emission from clusters of galaxies*. Ed. by Sarazin, C. L.

Sarazin, Craig L. (2002). "The Physics of Cluster Mergers". In: *Merging Processes in Galaxy Clusters*. Ed. by L. Feretti, I. M. Gioia, and G. Giovannini. Vol. 272, pp. 1–38. DOI: 10.1007/0-306-48096-4_1.

Sarazin, Craig L., Stefi A. Baum, and Christopher P. O'Dea (Sept. 1995). "Unusual Radio Structures in the Cooling Flow Cluster 2A 0335+096". In: *APJ* 451, p. 125. DOI: 10.1086/176205.

Savini, F. et al. (Aug. 2018). "First evidence of diffuse ultra-steep-spectrum radio emission surrounding the cool core of a cluster". In: *MNRAS* 478, pp. 2234–2242. DOI: 10.1093/mnras/sty1125.

Savini, F. et al. (2019). "A LOFAR study of non-merging massive galaxy clusters". In: *A&A* 622, A24, A24. DOI: 10.1051/0004-6361/201833882. arXiv: 1811.08410 [astro-ph.CO].

Scannapieco, Evan and Marcus Brüggen (June 2015). "The Launching of Cold Clouds by Galaxy Outflows. I. Hydrodynamic Interactions with Radiative Cooling". In: *APJ* 805.2, 158, p. 158. DOI: 10.1088/0004-637X/805/2/158. arXiv: 1503.06800 [astro-ph.GA].

Sebastian, Biny, Dharam V. Lal, and A. Pramesh Rao (Oct. 2017). "Giant Metrewave Radio Telescope Observations of Head-Tail Radio Galaxies". In: *AJ* 154, 169, p. 169. DOI: 10.3847/1538-3881/aa88d0.

Sereno, Mauro (Jan. 2016). "A Bayesian approach to linear regression in astronomy". In: *MNRAS* 455.2, pp. 2149–2162. DOI: 10.1093/mnras/stv2374. arXiv: 1509.05778 [astro-ph.IM].

Sereno, Mauro et al. (June 2017). "CLUMP-3D: three-dimensional lensing and multi-probe analysis of MACS J1206.2-0847, a remarkably regular cluster". In: *MNRAS* 467.4, pp. 3801–3826. DOI: 10.1093/mnras/stx326. arXiv: 1702.00795 [astro-ph.CO].

Shimwell, T. W. et al. (Feb. 2017). "The LOFAR Two-metre Sky Survey. I. Survey description and preliminary data release". In: *A&A* 598, A104, A104. DOI: 10.1051/0004-6361/201629313.

Shimwell, T. W. et al. (2019). "The LOFAR Two-metre Sky Survey. II. First data release". In: *A&A* 622, A1, A1. DOI: 10.1051/0004-6361/201833559. arXiv: 1811.07926 [astro-ph.GA].

Shin, J., J.-H. Woo, and J. S. Mulchaey (Dec. 2016). "A Systematic Search for X-Ray Cavities in Galaxy Clusters, Groups, and Elliptical Galaxies". In: *APJs* 227, 31, p. 31. DOI: 10.3847/1538-4365/227/2/31. arXiv: 1610.03487.

Simionescu, A. et al. (June 2010). "Metal transport by gas sloshing in M87". In: *MNRAS* 405.1, pp. 91–99. DOI: 10.1111/j.1365-2966.2010.16450.x. arXiv: 1002.0395 [astro-ph.CO].

Singh, K. P. et al. (July 1996). "ROSAT Observations of Five Chromospherically Active Stars". In: *AJ* 112, p. 221. DOI: 10.1086/118003.

Sivanandam, Suresh, Marcia J. Rieke, and George H. Rieke (2010). "A Warm Molecular Hydrogen Tail due to Ram-pressure Stripping of a Cluster Galaxy". In: *APJ* 717.1, pp. 147–162. DOI: 10.1088/0004-637X/717/1/147. arXiv: 0912.0075 [astro-ph.CO].

— (2014). "Tracing Ram-pressure Stripping with Warm Molecular Hydrogen Emission". In: *APJ* 796.2, 89, p. 89. DOI: 10.1088/0004-637X/796/2/89. arXiv: 1410.0688 [astro-ph.GA].

Smirnov, O. M. and C. Tasse (2015). "Radio interferometric gain calibration as a complex optimization problem". In: *MNRAS* 449.3, pp. 2668–2684. DOI: 10.1093/mnras/stv418. arXiv: 1502.06974 [astro-ph.IM].

Smith, R. J. et al. (Nov. 2010). "Ultraviolet tails and trails in cluster galaxies: a sample of candidate gaseous stripping events in Coma". In: *MNRAS* 408, pp. 1417–1432. DOI: 10.1111/j.1365-2966.2010.17253.x. arXiv: 1006.4867.

Sparre, Martin, Christoph Pfrommer, and Kristian Ehlert (Oct. 2020). "Interaction of a cold cloud with a hot wind: the regimes of cloud growth and destruction and the impact of magnetic fields". In: *MNRAS* 499.3, pp. 4261–4281. DOI: 10.1093/mnras/staa3177. arXiv: 2008.09118 [astro-ph.GA].

Spitzer, L. Jr. (1956). *Physics of Fully Ionized Gases, 1956*. Ed. by Spitzer, L. Jr.

Springel, Volker et al. (June 2005). "Simulations of the formation, evolution and clustering of galaxies and quasars". In: *Nature* 435.7042, pp. 629–636. DOI: 10.1038/nature03597. arXiv: astro-ph/0504097 [astro-ph].

Struble, M. F. and H. J. Rood (Nov. 1999). "A Compilation of Redshifts and Velocity Dispersions for ACO Clusters". In: *APJs* 125, pp. 35–71. DOI: 10.1086/313274.

Subramanian, Kandaswamy, Anvar Shukurov, and Nils Erland L. Haugen (Mar. 2006). "Evolving turbulence and magnetic fields in galaxy clusters". In: *MNRAS* 366.4, pp. 1437–1454. DOI: 10.1111/j.1365-2966.2006.09918.x. arXiv: astro-ph/0505144 [astro-ph].

Sun, M. et al. (Jan. 2010). "Spectacular X-ray Tails, Intracluster Star Formation, and ULXs in A3627". In: *APJ* 708, pp. 946–964. DOI: 10.1088/0004-637X/708/2/946. arXiv: 0910.0853.

Sunyaev, R. A. and Ya. B. Zeldovich (Nov. 1972). "The Observations of Relic Radiation as a Test of the Nature of X-Ray Radiation from the Clusters of Galaxies". In: *Comments on Astrophysics and Space Physics* 4, p. 173.

Sutherland, R. S. and M. A. Dopita (Sept. 1993). "Cooling functions for low-density astrophysical plasmas". In: *APJs* 88, pp. 253–327. DOI: 10.1086/191823.

Tabatabaei, F. S. et al. (Feb. 2016). "An Empirical Relation between the Large-scale Magnetic Field and the Dynamical Mass in Galaxies". In: *APJl* 818.1, L10, p. L10. DOI: 10.3847/2041-8205/818/1/L10. arXiv: 1512.08145 [astro-ph.GA].

Tasse, C. (2014). "Nonlinear Kalman filters for calibration in radio interferometry". In: *A&A* 566, A127, A127. DOI: 10.1051/0004-6361/201423503. arXiv: 1403.6308 [astro-ph.IM].

Tasse, C. et al. (2018). "Faceting for direction-dependent spectral deconvolution". In: *A&A* 611, A87, A87. DOI: 10.1051/0004-6361/201731474. arXiv: 1712.02078 [astro-ph.IM].

Tchernin, C. et al. (June 2018). "Reconstruction of the two-dimensional gravitational potential of galaxy clusters from X-ray and Sunyaev-Zel'dovich measurements". In: *A&A* 614, A38, A38. DOI: 10.1051/0004-6361/201629364. arXiv: 1802.07118 [astro-ph.CO].

Timmerman, R. et al. (Sept. 2020). "Very Large Array observations of the mini-halo and AGN feedback in the Phoenix cluster". In: *arXiv e-prints*, arXiv:2009.13238, arXiv:2009.13238. arXiv: 2009.13238 [astro-ph.CO].

Tonnesen, Stephanie, Greg L. Bryan, and Rena Chen (Apr. 2011). "How to Light it Up: Simulating Ram-pressure Stripped X-ray Bright Tails". In: *APJ* 731.2, 98, p. 98. DOI: 10.1088/0004-637X/731/2/98. arXiv: 1103.3273 [astro-ph.CO].

Vacca, V. et al. (2010). "The intracluster magnetic field power spectrum in Abell 665". In: *A&A* 514, A71, A71. DOI: 10.1051/0004-6361/200913060.

van Gorkom, Jacqueline H. (Jan. 2004). "Interaction of Galaxies with the Intracluster Medium". In: *Clusters of Galaxies: Probes of Cosmological Structure and Galaxy Evolution*. Ed. by J. S. Mulchaey, A. Dressler, and A. Oemler, p. 305. arXiv: astro-ph/0308209 [astro-ph].

van Haarlem, M. P. et al. (Aug. 2013). "LOFAR: The LOw-Frequency ARray". In: *A&A* 556, A2, A2. DOI: 10.1051/0004-6361/201220873. arXiv: 1305.3550 [astro-ph.IM].

van Weeren, R. J. et al. (Mar. 2016). "LOFAR Facet Calibration". In: *The Astrophysical Journal Supplement Series* 223, 2, p. 2. DOI: 10.3847/0067-0049/223/1/2.

van Weeren, R. J. et al. (2019). "Diffuse Radio Emission from Galaxy Clusters". In: 215.1, 16, p. 16. DOI: 10.1007/s11214-019-0584-z. arXiv: 1901.04496 [astro-ph.HE].

van Weeren, R. J. et al. (Nov. 2020). "LOFAR observations of galaxy clusters in HETDEX". In: *arXiv e-prints*, arXiv:2011.02387, arXiv:2011.02387. arXiv: 2011.02387 [astro-ph.CO].

Vazza, F. et al. (Dec. 2014). "On the amplification of magnetic fields in cosmic filaments and galaxy clusters". In: *MNRAS* 445.4, pp. 3706–3722. DOI: 10.1093/mnras/stu1896. arXiv: 1409.2640 [astro-ph.CO].

Venturi, T. et al. (Mar. 2007). "GMRT radio halo survey in galaxy clusters at z = 0.2-0.4. I. The REFLEX sub-sample". In: *A&A* 463, pp. 937–947. DOI: 10.1051/0004-6361:20065961. eprint: arXiv:astro-ph/0610271.

Venturi, T. et al. (June 2008). "GMRT radio halo survey in galaxy clusters at z = 0.2-0.4. II. The eBCS clusters and analysis of the complete sample". In: *A&A* 484, pp. 327–340. DOI: 10.1051/0004-6361:200809622. arXiv: 0803.4084.

Vijayaraghavan, Rukmani and Craig Sarazin (Oct. 2017). "The Evaporation and Survival of Cluster Galaxies' Coronae. II. The Effectiveness of Anisotropic Thermal Conduction and Survival of Stripped Galactic Tails". In: *APJ* 848.1, 63, p. 63. DOI: 10.3847/1538-4357/aa8bb3. arXiv: 1706.00021 [astro-ph.GA].

Vogelsberger, M. et al. (May 2014). "Properties of galaxies reproduced by a hydrodynamic simulation". In: *Nature* 509, pp. 177–182. DOI: 10.1038/nature13316. arXiv: 1405.1418.

Voit, G. M. (Apr. 2005). "Tracing cosmic evolution with clusters of galaxies". In: *Reviews of Modern Physics* 77, pp. 207–258. DOI: 10.1103/RevModPhys.77.207. eprint: arXiv:astro-ph/0410173.

Voit, G. Mark, Scott T. Kay, and Greg L. Bryan (Dec. 2005). "The baseline intracluster entropy profile from gravitational structure formation". In: *MNRAS* 364.3, pp. 909–916. DOI: 10.1111/j.1365-2966.2005.09621.x. arXiv: astro-ph/0511252 [astro-ph].

Völk, H. J. and A. M. Atoyan (Sept. 2000). "Early Starbursts and Magnetic Field Generation in Galaxy Clusters". In: *APJ* 541.1, pp. 88–94. DOI: 10.1086/309395. arXiv: astro-ph/0005185 [astro-ph].

Vulcani, B. et al. (Jan. 2018). "GASP. VII. Signs of Gas Inflow onto a Lopsided Galaxy". In: *APJ* 852, 94, p. 94. DOI: 10.3847/1538-4357/aa992c.

Walker, S. A. et al. (June 2017). "Is there a giant Kelvin-Helmholtz instability in the sloshing cold front of the Perseus cluster?" In: *MNRAS* 468, pp. 2506–2516. DOI: 10.1093/mnras/stx640. arXiv: 1705.00011.

Walker, S. A. et al. (June 2020). "Is there an enormous cold front at the virial radius of the Perseus cluster?" In: *arXiv e-prints*, arXiv:2006.14043, arXiv:2006.14043. arXiv: 2006.14043 [astro-ph.HE].

Werner, N. et al. (Apr. 2013). "The Nature of Filamentary Cold Gas in the Core of the Virgo Cluster". In: *APJ* 767.2, 153, p. 153. DOI: 10.1088/0004-637X/767/2/153. arXiv: 1211.6722 [astro-ph.CO].

White, D. A. et al. (Aug. 1994). "A ROSAT HRI obseravtion of the Abell 478 cluster of galaxies." In: *MNRAS* 269, pp. 589–606. DOI: 10.1093/mnras/269.3.589.

Widrow, Lawrence M. et al. (May 2012). "The First Magnetic Fields". In: 166.1-4, pp. 37–70. DOI: 10.1007/s11214-011-9833-5. arXiv: 1109.4052 [astro-ph.CO].

Wilber, A. et al. (Jan. 2018). "LOFAR discovery of an ultra-steep radio halo and giant head-tail radio galaxy in Abell 1132". In: *MNRAS* 473, pp. 3536–3546. DOI: 10.1093/mnras/stx2568.

Williams, W. L. et al. (2016). "LOFAR 150-MHz observations of the Boötes field: catalogue and source counts". In: *MNRAS* 460.3, pp. 2385–2412. DOI: 10.1093/mnras/stw1056. arXiv: 1605.01531 [astro-ph.CO].

Wirth, A., L. Smarr, and J. S. Gallagher (Apr. 1982). "Dumbbell galaxies and precessing radio jets." In: *AJ* 87, pp. 401–404. DOI: 10.1086/113135.

Wong, K.-W. et al. (July 2008a). "XMM-Newton and Chandra Observations of Abell 2626: Interacting Radio Jets and Cooling Core with Jet Precession?" In: *APJ* 682, pp. 155–174. DOI: 10.1086/588272. arXiv: 0803.1680.

— (July 2008b). "XMM-Newton and Chandra Observations of Abell 2626: Interacting Radio Jets and Cooling Core with Jet Precession?" In: *APJ* 682, pp. 155–174. DOI: 10.1086/588272. arXiv: 0803.1680.

Wong, O. Ivy et al. (2014). "The Search for Shock-excited H_2 in Virgo Spirals Experiencing Ram Pressure Stripping". In: *APJ* 783.2, 109, p. 109. DOI: 10.1088/0004-637X/783/2/109. arXiv: 1401.6223 [astro-ph.GA].

Xie, C. et al. (Apr. 2020). "The discovery of radio halos in the frontier fields clusters Abell S1063 and Abell 370". In: *A&A* 636, A3, A3. DOI: 10.1051/0004-6361/201936953. arXiv: 2001.04725 [astro-ph.HE].

Xue, Y.-J. and X.-P. Wu (Nov. 2000). "Properties of the double β model for intracluster gas". In: *MNRAS* 318, pp. 715–723. DOI: 10.1046/j.1365-8711.2000.03753.x. eprint: astro-ph/0006131.

Yagi, M. et al. (Dec. 2010). "A Dozen New Galaxies Caught in the Act: Gas Stripping and Extended Emission Line Regions in the Coma Cluster". In: *AJ* 140, pp. 1814–1829. DOI: 10.1088/0004-6256/140/6/1814. arXiv: 1005.3874.

Zhuravleva, I. et al. (Nov. 2014). "Turbulent heating in galaxy clusters brightest in X-rays". In: *Nature* 515, pp. 85–87. DOI: 10.1038/nature13830. arXiv: 1410.6485 [astro-ph.HE].

Zier, C. (Dec. 2005). "Orientation and size of the 'Z' in X-shaped radio galaxies". In: *MNRAS* 364.2, pp. 583–592. DOI: 10.1111/j.1365-2966.2005.09586.x. arXiv: astro-ph/0507129 [astro-ph].

ZuHone, J., M. Markevitch, and G. Brunetti (Jan. 2011). "Testing the Connection Between Radio Mini-Halos and Core Gas Sloshing with MHD Simulations". In: *ArXiv e-prints*. arXiv: 1101.4627 [astro-ph.HE].

ZuHone, J. A., M. Markevitch, and R. E. Johnson (July 2010). "Stirring Up the Pot: Can Cooling Flows in Galaxy Clusters be Quenched by Gas Sloshing?" In: *APJ* 717, pp. 908–928. DOI: 10.1088/0004-637X/717/2/908. arXiv: 0912.0237 [astro-ph.CO].

ZuHone, J. A., J. Zavala, and M. Vogelsberger (Sept. 2019). "Sloshing of Galaxy Cluster Core Plasma in the Presence of Self-interacting Dark Matter". In: *APJ* 882.2, 119, p. 119. DOI: 10.3847/1538-4357/ab321d. arXiv: 1901.11140 [astro-ph.CO].

ZuHone, J. A. et al. (Jan. 2013a). "Cold Fronts and Gas Sloshing in Galaxy Clusters with Anisotropic Thermal Conduction". In: *APJ* 762.2, 69, p. 69. DOI: 10.1088/0004-637X/762/2/69. arXiv: 1204.6005 [astro-ph.CO].

ZuHone, J. A. et al. (Jan. 2013b). "Turbulence and Radio Mini-halos in the Sloshing Cores of Galaxy Clusters". In: *APJ* 762, 78, p. 78. DOI: 10.1088/0004-637X/762/2/78. arXiv: 1203.2994 [astro-ph.CO].

ZuHone, J. A. et al. (Mar. 2015). "Testing Secondary Models for the Origin of Radio Mini-Halos in Galaxy Clusters". In: *APJ* 801, 146, p. 146. DOI: 10.1088/0004-637X/801/2/146. arXiv: 1403.6743.

Zuhone, John A. and E. Roediger (June 2016). "Cold fronts: probes of plasma astrophysics in galaxy clusters". In: *Journal of Plasma Physics* 82.3, 535820301, p. 535820301. DOI: 10.1017/S0022377816000544. arXiv: 1603.08882 [astro-ph.HE].

Zwicky, F. (1933). "Die Rotverschiebung von extragalaktischen Nebeln". In: *Helvetica Physica Acta* 6, pp. 110–127.